
Doctoral

Science

2011-7

The Preparation and Characterisation of Silver Nanomaterials and Their Application in Sensing Techniques

Aoife Power

Technological University Dublin

Follow this and additional works at: <https://arrow.tudublin.ie/sciendoc>

 Part of the [Chemistry Commons](#)

Recommended Citation

Power, A. (2011). *The Preparation and Characterisation of Silver Nanomaterials and Their Application in Sensing Techniques*. Doctoral Thesis. Technological University Dublin. doi:10.21427/D7M88K

This Theses, Ph.D is brought to you for free and open access by the Science at ARROW@TU Dublin. It has been accepted for inclusion in Doctoral by an authorized administrator of ARROW@TU Dublin. For more information, please contact arrow.admin@tudublin.ie, aisling.coyne@tudublin.ie, vera.kilshaw@tudublin.ie.

The Preparation and Characterisation of Silver Nanomaterials and their application in Sensing Techniques.

Aoife Power BSc.



A thesis presented to the Dublin Institute of Technology for the award of Ph.D.

Prepared under the supervision of Dr. Anthony Betts and Prof. John Cassidy

School of Chemical and Pharmaceutical Sciences

Dublin Institute of Technology Kevin St.

July 2011

Declaration

Declaration

I certify that this thesis which I now submit for examination for the award of PhD., is entirely my own work and has not been taken from the work of others, save and to the extent that such work has been cited and acknowledged within the text of my work.

This thesis was prepared according to the regulations for postgraduate study by research of the Dublin Institute of Technology and has not been submitted in whole or in part for another award in any Institute.

The work reported on in this thesis conforms to the principles and requirements of the Institute's guidelines for ethics in research.

The Institute has permission to keep, lend or copy this thesis in whole or in part, on condition that any such use of the material of the thesis be duly acknowledged.

Signature

Date

Acknowledgements

Acknowledgements

I would like to thank my two supervisors Dr. Anthony Betts and Prof. John Cassidy for their guidance and encouragement over the course of this work.

I also wish to thank everyone in the School of Chemistry and the FOCAS Institute, particularly the technical staff whose assistance was invaluable through out the past number of years.

Thanks to the ABBEST PhD Scholarship Programme of the Dublin Institute of Technology for funding.

Thanks to Noreen O' Mahoney and Deirdre Carr of MetPro, who kindly supplied VCI component samples for study.

Special thanks to all the staff, postgrads and postdocs I've had the pleasure of working with, I won't name you as no doubt someone important would be forgotten, however I would particularly like to express my gratitude to all the members of the applied electrochemistry group, honorary and otherwise.

Finally last but by no means least I wish to thank my family, Pat, Maeve, (or Mam and Dad), Aislinn, Enda, Sorcha and Cillian, and my friends especially the 'Scientists' for all your encouragement and support.

.

Abstract

Abstract

In this work the impact of nanomaterial, specifically silver nanostructures, on sensing techniques is investigated. The work can be divided in to three sections, preparation and characterisation of silver nanoparticles, their application as a nanocomposite based chemiresistor humidity sensing device and finally their application within the surface enhanced (resonance) Raman spectroscopy, SE(R)RS, technique.

In the first study silver nanoparticles were prepared as aqueous colloidal dispersions. The colloids were of either a defined diameter (average diameter ~ 20 nm) with high silver loading or lower loaded colloids of tuneable morphology and hence optical properties.

In a subsequent study the high load colloid when cast on platinum interdigital electrodes as a nanocomposite coating proved to be useful as a humidity sensor. The sensor gave a reversible, selective and rapid response which was proportional to humidity levels within the range of 10% RH to 60% RH. An investigation into the mechanism of the sensor's response was conducted and the response was found to correlate well with a second order Langmuir adsorption model.

The final study was multi faceted as it first determined the suitability of the tuneable colloids as SE(R)RS substrates using a number of probe molecules. A clear sensing trend was observed, where the Raman signal emitted was significantly enhanced by the addition of silver nanoparticles. This prompted an additional investigation where both colloids were again cast as films (fabricating alternative SERS substrates) to determine the degree outside factors could influence the enhancement seen by the SERS technique. The suitability of the SERS substrates in a real world application was investigated, with SERS being used to monitor the action mechanism of components of a commercially available volatile corrosion inhibitor.

Table of Contents

Declaration.....i

Acknowledgements.....ii

Abstract.....iii

Table of Contents.....iv

Table of Figuresviii

1. General Introduction.....1

1.1 Nanotechnology.....1

1.2 Appeal of nanomaterials.....1

1.3 Fabrication at the nanoscale.....3

1.4 Colloidal preparation4

1.5 Colloidal stability.....4

1.6 Electrostatic stabilisation.....6

1.7 Steric stabilisation.....12

1.8 Silver nanoparticles.....14

1.9 Sensing16

1.10 Nanomaterials and sensing.....17

1.11 Nanocomposites.....17

1.12 Electro-optical properties of silver nanomaterials.....18

1.13 Origin of plasmons.....19

1.14 Optical Sensors23

1.15 Optical Absorption24

1.16 Optical Emission (Luminescence).....25

1.17 Elastic and inelastic scattering.....27

1.18 Raman scattering.....28

1.19 Raman spectroscopy29

1.20 Surface Enhanced Raman spectroscopy, SERS31

1.21 SERS enhancement mechanisms.....33

1.22 Chemiresistor Sensors.....35

1.23 Humidity36

1.24 Commercial humidity sensors.....36

1.25 Humidity Sensing Materials38

Table of Contents

1.26 Impedance Spectroscopy	38
1.27 Overview of Study.....	44
1.28 References.....	45
2. Synthesis and Characterisation of Silver Nanoparticles.....	53
2.1 Introduction.....	53
2.2 Experimental.....	56
2.2.1 Reagents.....	56
2.2.2 Apparatus.....	56
2.3 Silver nanocomposite / colloid synthesis.....	56
2.3.1 Silver nanocomposite / colloid recipe.....	57
2.3.2 High load silver nanocomposite / colloid preparation	58
2.4 High load silver nanocomposite colloid characterisation.....	58
2.4.1 UV-Vis analysis – Perkin Elmer, Lambda 900 Spectrometer.....	58
2.4.2 Jobs Method.....	59
2.4.3 Dynamic light scattering, DLS – Malvern nano series Zetasizer.....	59
2.4.3.1 Zeta potential.....	60
2.4.4 Transmission electron microscopy, TEM – JEOL, 100CX Transmission Electron Microscope.....	61
2.4.5 X-Ray Diffraction, XRD – Siemens Diffractometer, Model D500.....	63
2.4.5.1 Scherrer equation.....	63
2.5.1 Colloids of tuneable optical properties.....	64
2.5.2.1 ‘Seed’ production.....	64
2.5.2.2 Preparation of coloured colloids.....	64
2.5.2.3 UV-Vis analysis – Perkin Elmer, Lambda 900 Spectrometer.....	65
2.5.2.4 Dynamic light scattering, DLS – Malvern nano series Zetasizer.....	66
2.5.2.5 Electron microscopy – JEOL, 100CX Transmission Electron Microscope / Hitachi, SU 6600 FESEM.....	68
2.5.2.5.1 Shape of silver nanostructures of tuneable colloids.....	70
2.5.2.6 Colloid Stability.....	71
2.6 Alternative colloid recipes.....	72
2.7 Conclusions.....	75
2.8 References.....	77

Table of Contents

3. Humidity Sensor	79
3.1 Introduction.....	79
3.2 Experimental.....	80
3.3 Humidity measurements.....	83
3.4 Cyclic Voltammetry.....	89
3.5 Electrochemical Impedance Spectroscopy, EIS.....	90
3.6 Sensing mechanism.....	94
3.7 Application of other composite films.....	95
3.8 Conclusions.....	96
3.8 References.....	97
4. Surface enhanced resonance Raman spectroscopy with tuneable silver colloids	99
4.1 Introduction.....	99
4.2 Experimental.....	100
4.2.1 SERRS measurements.....	101
4.2.2 Dye and colloid interaction.....	108
4.3 Sensing Trend.....	109
4.4 Conclusions.....	117
4.5 References.....	118
5. Effect of potential modulation of chemically synthesised Ag nanoparticles on SERS	120
5.1 Introduction.....	120
5.2 Experimental.....	121
5.2.1 Materials.....	121
5.2.2 Preparation of SERS substrates.....	121
5.2.2.1 Atomic Force Microscope analysis – MFP – 3D BIO AFM.....	122
5.2.3 SERS measurements.....	123
5.2.3.1 SERS measurements experimental setup.....	124
5.3 Effectiveness of ‘roughened’ silver as SERS substrate.....	124
5.3.1 Impact of added electrolyte.....	127
5.4 Carbon – silver nanoparticles SERS surfaces.....	128
5.4.1 Development of the Carbon – silver nanoparticles SERS surfaces.....	130

Table of Contents

5.4.2 C – AgNP SERS surfaces – colloid dilution.....	131
5.4.3 C – AgNP SERS surfaces – spin coated.....	133
5.5 Conclusions.....	135
5.6 References.....	136
6. A study of Volatile Corrosion Inhibitor release using SERS.....	137
6.1 Introduction.....	137
6.2 Experimental.....	138
6.2.1 Materials.....	138
6.2.2 Apparatus.....	138
6.3.1 FTIR Analysis – Perkin Elmer spectrum 100 FTIR with Universal ATR sampling accessory.....	139
6.3.2 NMR Analysis – Bruker 400 MHz Ultra Shield.....	139
6.3.3 Characterisation of MetPro samples.....	139
6.4 Preparation of SERS surfaces.....	140
6.5 Raman spectra of neat compounds.....	140
6.6 SERS analysis of compounds.....	142
6.6.1 Dissociation rate of compounds	142
6.6.2 Dissociation kinetics	147
6.6.3 Diffusion Model.....	151
6.6.4 Adsorption of benzotriazole onto SERS surface.....	153
6.7 Conclusions.....	156
6.8 References.....	157
7. General Conclusion & Future Work.....	158
7.1 References.....	161
Appendices.....	162
Appendix A.....	162
Appendix B.....	165
Appendix C.....	180

Table of Figures and Tables

Chapter 1

Figure 1.1: Size comparison scale – macro to nano.....	2
Figure 1.2: Three types of stability of a skittle, (A) metastable, (B) unstable, (C) stable.....	5
Figure 1.3: Stern layer.....	10
Figure 1.4: Double layer of a nanoparticle.....	11
Figure 1.5: Schematic of steric stabilisation.....	13
Table 1.1: Summary of major findings of T.M. Tolaymat's <i>et al.</i> review.....	15
Figure 1.6: Schematic representation of the plasmon oscillation for a spherical metallic nanoparticle, irradiated by light, the oscillating electric field causes the conduction electrons to oscillate coherently.....	19
Figure 1.7: Jablonski diagram, a schematic representation of the electronic and vibronic (rotational/vibrational) energy levels of a molecule.....	24
Figure 1.8: Different types of scatter.....	27
Figure 1.9: An assortment of SERS active nanostructures.....	31
Figure 1.10: Silver nanostructures fabricated through metal deposition.....	32
Figure 1.11. A sine wave voltage applied to an electrochemical cell and the current response as a function of time.....	39
Figure 1.12: Bode Plot with One Time Constant.....	40
Figure 1.13: Vector representation, polar coordinates (A) and Complex Plane representation, Cartesian coordinates, (B) both specify the same point.....	41
Figure 1.14. Nyquist plot magnitude and phase.....	42

Chapter 2

Figure 2.1: Chemical colloid synthesis.....	53
Figure 2.2: Marble in a box model.....	57
Figure 2.3: UV-Vis spectrum of stable aqueous colloidal Ag polymer mixture, with λ max of 391 nm.....	58
Figure 2.4: Graphical representation of the findings of Jobs method analysis, stoichiometry of AgNO_3 and NaBH_4 shown to be approximately 1:1.....	59

Table of Figures

Figure 2.5a: Distribution of particle diameters within the Ag PVA colloid determined by DLS.....	60
Figure 2.5b Zeta potential distribution of the aqueous based Ag PVA colloid.....	61
Figure 2.6a: TEM image of silver nanoparticles stabilised with PVA.....	62
Figure 2.6b: Break down of average diameters of silver nanoparticles for 250 TEM measurements analysed with ImageJ.....	62
Figure 2.7: XRD pattern recorded from a drop-coated film of nanocomposite on glass substrate.....	63
Figure 2.8: Colloids of tuneable optical properties.....	64
Table 2.1: Summary of volumes of 0.001 M AgNO ₃ and the resulting colloids.....	65
Figure 2.9: UV-Vis spectrum of stable aqueous colloidal Ag Seed solution, with λ max of 393 nm.....	65
Figure 2.10: UV-Vis spectra of aqueous coloured Ag colloids.....	66
Figure 2.11 a: Distribution of particle diameters within the 'seed' Ag colloid.....	67
Figure 2.11 b: Distribution of particle diameters within the Blue Ag colloid.....	67
Figure 2.11 c: Combined graphical representation of the distribution of particle diameters of the nanoparticles in the coloured Ag colloids.....	68
Table 2.2: Summary of Colloids UV-Vis λ max's and DLS results.....	68
Figure 2.12a : A TEM image of silver nanoparticle (seed colloid) with an average diameter range of \sim 9 nm.....	69
Figure 2.12b : A STEM image of silver nanoparticles (blue colloid) with an average diameter range of 58 – 60 nm.....	70
Figure 2.13: UV-Vis spectra of aqueous colloidal Ag polymer mixture over a 6 month period, colloid was stored at room temperature 18 ± 2 °C in the dark.....	71
Figure 2.14: UV-Vis spectra of blue colloid over a 6 month period, colloid was stored at room temperature 18 ± 2 °C in the dark.....	72
Figure 2.15: Zeta potential distribution of the methanol based Ag PVA colloid.....	73
Figure 2.16: Distribution of particle diameters within the Triton stabilised Ag colloid.....	73
Figure 2.17: UV-Vis spectra of methanol dispersed colloidal Ag Triton stabilised mixture over a 6 month period, colloid was stored at room temperature 18 ± 2 °C in the dark.....	74

Table of Figures

Figure 2.18: Distribution of particle diameters within the PVC stabilised Ag colloid.....74

Figure 2.19: UV-Vis spectra of PVC stabilised methanol dispersed Ag colloid over a 6 month period, colloid was stored at room temperature 18 ± 2 °C in the dark.....75

Chapter 3

Figure 3.1: A range of the various applications of humidity sensors in industry.....80

Figure 3.2: Schematic of BVT Technologies CC2.W* (*) conductometric sensor substrates, A= 4.00 ± 0.05 mm, B & C = 3.00 ± 0.05 mm.....81

Figure 3.3: BVT Technologies interdigital electrodes, bare (left) and with nanocomposite sensing coating (right).....82

Figure 3.4: Bubbler apparatus schematic, the Dreschel flasks typically held a volume of 40 cm^382

Figure 3.5: Representative plot of sensor's response to a change in environment.....84

Figure 3.6: Sensor's response to exposure to various solvent vapours, summarised in table 3.1.....85

Figure 3.7: Magnification of the sensor's base line response of the results displayed in figure 3.5, illustrating the negligible response of certain test solvent (T.S.) vapours..85

Table 3.1: Summary of sensor's response during exposure to different vapours.....86

Figure 3.8: Graphical representation of sensor's response to increasing % RH over time at a constant temperature of 23.1 °C.....86

Figure 3.9: The sensor's response to repeated exposures to varying % RH at set time intervals.....88

Figure 3.10: Responses of four different sensors prepared separately. The slopes for the lines are 5.4, 5.5, 7.2 and 8.2 (mV/%RH).....89

Figure 3.11: Cyclic voltammograms of sensing coating in both dry and humid conditions, initial E = 0.5 V, high E = 0.5 V, low E = -0.5 V with a scan rate of 0.1 V/s.....90

Figure 3.12: Schematic of EIS experimental set up.....91

Figure 3.13: Nyquist plot of effect of humidity on the impedance of the sensing coating.....91

Figure 3.14: Bode plot of effect of humidity on the impedance of the sensing coating.....92

Table of Figures

Figure 3.15: Modified Randles Circuit Model.....	92
Table 3.2: Summary of sensor's modelled response during EIS at different %RH levels.....	93
Figure 3.16: Calibration curve of sensor coatings Impedance.....	94
Figure 3.17: PVC stabilised sensor coatings response to exposure to various solvent vapours.....	95

Chapter 4

Figure 4.1a: Molecular structures of Crystal Violet, Malachite Green and Rhodamine 6G.....	101
Figure 4.1b: Absorption spectra of probe dyes, Crystal Violet, Malachite Green and Rhodamine 6G.....	102
Figure 4.2a: Raman Spectra of 3.33×10^{-5} M Cr.V. mixed with each colloid with excitation by the 660 nm laser.	103
Figure 4.2b: Raman Spectra of 3.33×10^{-5} M Cr.V. mixed with each colloid with excitation by the 532 nm laser.....	104
Figure 4.3a: Raman Spectra of M.G. 3.33×10^{-5} M mixed with each colloid with excitation by the 660 nm laser.....	105
Figure 4.3b: Raman Spectra of 3.33×10^{-5} M Cr.V. mixed with each colloid with excitation by the 532 nm laser.....	106
Figure 4.3c: Raman Spectra of R6G 3.33×10^{-5} M mixed with each colloid with excitation by the 660 nm laser.....	107
Figure 4.3d: Comparison of MG spectra (with best colloid enhancement) at the different excitation wavelengths with $[Ag] = 11 \times 10^{-5}$ M.....	108
Figure 4.4: Effect of the Dye on the particle size range of the colloidal nanoparticles, (a) silver colloid (blue) $[Ag] = 1 \times 10^{-5}$ M, (b) silver colloid (blue) $[Ag] = 1 \times 10^{-5}$ M with excess crystal violet $[Cr.V.] = 5 \times 10^{-5}$ M.....	108
Figure 4.5: Raman Spectra of 3.33×10^{-5} M Cr.V. with increasing concentrations of the blue colloid's NPs with excitation by the 660 nm laser.....	110
Figure 4.6: Observed Raman spectra emission trend of 3.33×10^{-5} M Cr.V. with increasing concentrations of the blue colloid's NPs with excitation by the 660 nm laser.....	110
Table 4.1: Probe molecules Raman spectra peak assignation.....	111

Table of Figures

Figure 4.7: Raman Spectra of 3.33×10^{-5} M MG with increasing concentrations of the blue colloid's NPs with excitation by the 660 nm laser.....	111
Figure 4.8: Observed Raman spectra emission trend of 3.33×10^{-5} M MG with increasing concentrations of the blue colloid's NPs with excitation by the 660 nm laser.....	112
Figure 4.9: Raman Spectra of 3.33×10^{-5} M R6G with increasing concentrations of the blue colloid's NPs with excitation by the 660 nm laser.....	113
Figure 4.10: Observed Raman spectra emission trend of 3.33×10^{-5} M R6G with increasing concentrations of the blue colloid's NPs with excitation by the 660 nm laser.....	114
Figure 4.11: Raman Spectra of 3.33×10^{-7} M Cr.V. with increasing concentrations of the blue colloid's NPs with excitation by the 660 nm laser.....	115
Figure 4.12: Observed Raman spectra emission trend of 3.33×10^{-7} M Cr.V. with increasing concentrations of the blue colloid's NPs with excitation by the 660 nm laser.....	116

Chapter 5

Figure 5.1: Silver (left) and carbon (right) SERS electrodes, scale in cm.....	122
Figure 5.2.a: Morphology of polished silver SERS substrate.....	123
Figure 5.2.b: Morphology of roughened silver SERS substrate.....	123
Figure 5.3: Schematic of spectrochemical cell employed for Raman Spectroscopy.....	124
Figure 5.4: Spectra of 5×10^{-5} M Crystal Violet, 1% laser strength, 5 s exposure time and accumulation of 20, silver SERS substrate.....	125
Figure 5.5: Spectra of 5×10^{-5} M Crystal Violet, 1% laser strength, 5 s exposure time and accumulation of 20, silver SERS substrate, with different applied potentials... ..	126
Figure 5.6: Spectra of 5×10^{-5} M Crystal Violet, 1% laser strength, 5 s exposure time and accumulation of 20, silver SERS substrate with different applied potentials in the presence of an electrolyte (0.1M KNO_3).....	127
Figure 5.7: Spectra of 5×10^{-5} M Crystal Violet, 1% laser strength, 5 s exposure time and accumulation of 20, with C – AgNP (blue colloid) SERS surface and different applied potentials.....	129
Figure 5.8: Spectra of 5×10^{-5} M Crystal Violet, 1% laser strength, 5 s exposure time and accumulation of 20, with C – AgNP (100% high load colloid – 20nm diameter nanostructures) SERS surface and different applied potentials.....	130

Table of Figures

Figure 5.9: Spectra of 5×10^{-5} M Crystal Violet, 1% laser strength, 5 s exposure time and accumulation of 20, with C – AgNP (10% high load colloid - 20nm diameter nanostructures) SERS surface and different applied potentials.....	131
Figure 5.10: Spectra of 5×10^{-5} M Crystal Violet, 1% laser strength, 5 s exposure time and accumulation of 20, with C – AgNP (1% high load colloid) SERS surface and different applied potentials.....	132
Figure 5.11: Spectra of 5×10^{-5} M Crystal Violet, 1% laser strength, 5 s exposure time and accumulation of 20, with C – AgNP (100% high load colloid - 20nm diameter nanostructures – spin coated) SERS surface and different applied potentials.....	133
Figure 5.12: Comparison of enhancement by different substrate/techniques.....	134

Chapter 6

Figure 6.1: Raman spectra of neat MetPro compounds, laser strength 10%, exposure time 20s, accumulation 5 and excitation wavelength 660nm.....	140
Table 6.1: VCI components Raman spectra peak assignation.....	141
Figure 6.2: Graphical representation of changes in intensity of the SERS spectra of 50% w/v benzotriazole in $CDCl_3$ over a set time period, laser strength 1 %, exposure time 20s, accumulation 5 and excitation wavelength 660nm.....	142
Figure 6.3: Graphical representation of changes in intensity of the SERS spectra of octanoic acid over a set time period, laser strength 1 %, exposure time 20s, accumulation 5 and excitation wavelength 660nm.....	143
Figure 6.4: Graphical representation of changes in intensity of the SERS spectra of monoethanolamine 90% over a set time period, laser strength 1 %, exposure time 20s, accumulation 5 and excitation wavelength 660nm.....	144
Figure 6.5: Graphical representation of changes in intensity of the SERS spectra of diethanolamine 88% over a set time period, laser strength 1 %, exposure time 20s, accumulation 5 and excitation wavelength 660nm.....	145
Figure 6.6: Graphical representation of changes in intensity of the SERS spectra of triethanolamine 90% over a set time period, laser strength 1 %, exposure time 20s, accumulation 5 and excitation wavelength 660nm.....	146
Figure 6.7: Desorption of 50% w/v benzotriazole in $CDCl_3$ over a set time period.....	147
Figure 6.8: Modelling of desorption of 50% w/v benzotriazole in $CDCl_3$ over a set time period.....	147

Table of Figures

Figure 6.9: Desorption of monoethanolamine 90% over a set time period.....	148
Figure 6.10: Modelling of desorption of monoethanolamine 90% over a set time period.....	148
Figure 6.11: Desorption of diethanolamine 88% over a set time period.....	149
Figure 6.12: Modelling of desorption of diethanolamine 88% over a set time period.....	149
Figure 6.13: Desorption of triethanolamine 90% over a set time period.....	150
Figure 6.14: Modelling of desorption of triethanolamine 90% over a set time period.....	150
Figure 6.15: Desorption of octanoic acid over a set time period.....	151
Figure 6.16: Modelling of desorption of octanoic acid over a set time period.....	151
Figure 6.17: Schematic of fabricated sealed diffusion/condensation container with quartz window.....	154
Figure 6.18: Graphical representation of changes in intensity of the SERS spectra of Benzotriazole over a set time period, laser strength 1 %, exposure time 20s, accumulation 5 and excitation wavelength 660nm.....	155
Figure 6.19: Condensation of benzotriazole over a set time period.....	156

Chapter 7

Figure 7.1: Some of the major contributors to current SERS research.....	159
--	-----

1. General Introduction

1.1 Nanotechnology

“There’s plenty of room at the bottom”; this statement by Richard Feynman in 1959 during a presentation to a meeting of the American Physical Society, is widely accepted as the spark that initiated the present ‘*nano*’ age ¹.

Nano, “dwarf” in Greek, is defined as one billionth, it follows that the nanoscale is measured in nanometres, or 10^{-9} m. To put this in perspective; the average strand of a human hair is roughly 75,000 nm in diameter, or from the other extreme 1 nm is the length of 10 hydrogen atoms lined up end to end.

Nanotechnology can be difficult to define, as its definition is often engineered to suit the researcher and their field; this resulted in a need of a general working definition, which the national nanotechnology initiative (NNI) established ². Nanotechnology is thus defined as possessing the following features;

- Nanotechnology involves research and technology development at the 1 nm to 100 nm range.
- Nanotechnology creates and uses structures that have novel properties because of their small size.
- Nanotechnology builds on the ability to control or manipulate at the atomic scale.

1.2 Appeal of nanomaterials

According to the definition above a clear emphasis is placed on size. This is because nanomaterials/nanostructures often exhibit novel and considerably different physical and chemical properties in comparison to their bulk counterparts ³⁻⁴ and herein lies their appeal. These properties often arise as a result of the physical size (and thus high surface to volume ratio) of the particles themselves. This phenomenon is primarily due to the scale of the ‘nano world’ (figure 1.1), the area “between the realm of individual atoms and molecules (where quantum mechanics rules) and the ‘macro world’ (where the bulk properties of materials emerge from the collective behaviour of trillions of atoms.)” and affords the ‘nano world’ a flexibility where set laws of the

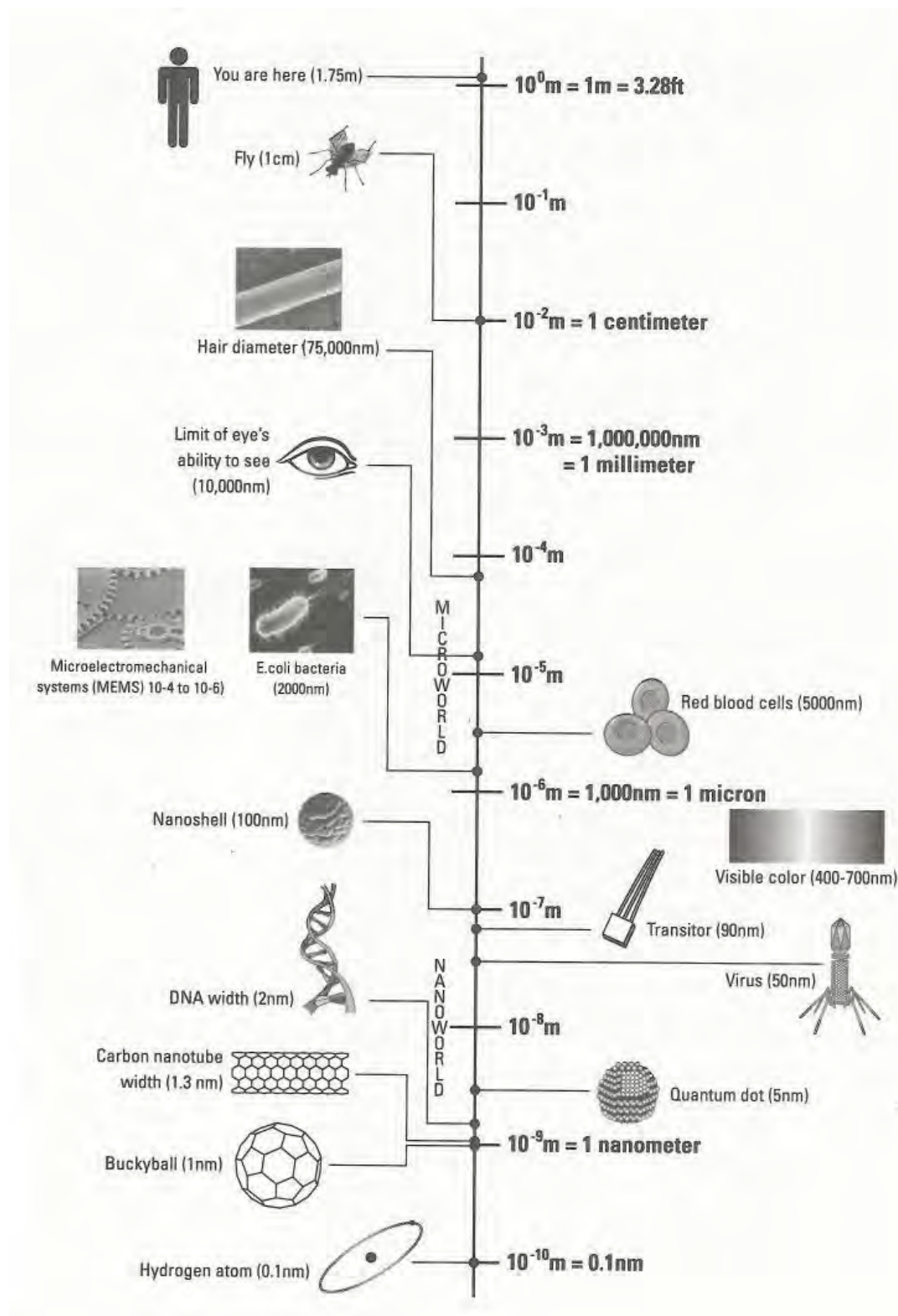


Figure 1.1: Size comparison scale – macro to nano ⁵

macro scale may be manipulated and distorted to suit a project's design ⁶. This inbuilt flexibility is the key driving force behind a 'nano' revolution, allowing researchers of multiple disciplines massive scope for the development of both new materials and

techniques. This gives nanotechnology the potential to significantly impact on multiple aspects of modern life whether as a result of the production of superior lightweight materials, advanced computing, medicine (diagnostics and treatments), or energy production⁷⁻⁸.

The influence of scale is most clearly illustrated by changes in the physical properties of metallic nanostructures. For example gold nanoparticles not only display a ruby colour⁹⁻¹⁰ rather than the yellow of bulk gold, but the optical absorbance spectra of these gold nanostructures is also size dependent; spherical nanoparticles of diameter 22, 48 and 99 nm have λ_{\max} 's of 520, 540 and 580 nm respectively¹¹.

So the size of nanostructures (particularly metallic) has a significant impact on their properties; this is also true of the shape/morphology of the nanoparticle/structure. Therefore the ability to reliably tailor the morphology of nanostructures (and hence their very nature) has become increasingly important.

Being able to control the size and shape of the nanoparticle influences its properties and ultimate use. This has directed research focus on the development of reliable fabrication methodologies of nanostructures with controlled morphologies¹²⁻¹⁵.

1.3 Fabrication at the nanoscale

Nanostructures can be produced by one of two methods 'top down' or 'bottom up'. The distinction between the two techniques is that conventional manufacturing processes are "top down," where a material is produced in bulk and then shaped into a finished part through a variety of processes (e.g., casting, moulding, rolling, forging, extruding, machining, and etching fine features such as in electronic circuits). In these processes, the positioning of each atom is not individually controlled during the operation resulting in defects and impurities.

Top down techniques are most evident in the computer industry with the fabrication of microprocessors by lithography now the standard operating practice for industry leaders such as Intel¹⁶⁻¹⁷. Alternatively, bottom up "atom by atom" manufacturing processes involve self-assembly, in which the position of individual atoms are controlled during fabrication by inducing conditions for the self-organised growth of structures to produce the desired material¹⁸⁻¹⁹.

There are several synthetic routes available in the bottom up technique including photochemistry, thermochemistry, sonochemistry, biochemistry, electrochemistry and wet chemistry²⁰⁻²⁶. Bottom – up techniques are often the preferred synthetic route

for nanostructures synthesis; this has been attributed to the surface deficiencies associated with particles prepared by the top – down route²⁷. A common bottom up fabrication technique in the literature, (and the method of preparation utilised in this study), for the preparation of metallic nanoparticles is synthesis via the preparation of a colloid.

Colloids “consist of a dispersed phase (or discontinuous phase) distributed uniformly in a finely divided state in a dispersion medium (or continuous phase)”. The dimensions of the dispersed phase in the ‘simple’ colloids (a clear distinction between the two phases is possible) prepared in this study are within the range of 1 – 100 nm. As a result, the colloids have a large surface to volume ratio, which gives the colloid’s particles different physicochemical properties, as the influence of the particle’s surface chemistry increases^{28 - 30}. Synthesis via colloidal dispersion allows the specific control of the morphology of the nanoparticles/structures by directing their self-assembly through variation of the synthesis parameters.

1.4 Colloidal preparation

Chemical reduction is the most common method for the preparation of metal colloids in aqueous or organic solvents^{31 - 32}. Common reducing agents include borohydrides, citrates, ascorbates and elemental hydrogen³³.

The major route reported in the literature is by the production of colloidal dispersions²⁷ using chemical – reduction methods³⁴, which classically involve the reduction of the metal by chemical means. This technique’s popularity is due to the relative ease of production; the advantages being mild reaction conditions, low energy consumption, and simple separation procedures coupled with high yields, good stability and relatively short reaction times³⁵.

1.5 Colloidal stability

Although the fundamental principles of thermodynamics maintain that a system at constant temperature should spontaneously change to lower its free energy, colloidal systems often remain stable at an elevated energy state. This is because, for a system to undergo the change necessary to move to a lower energy state, a mechanism for the change must be available.

D.H. Everett provides a simple demonstration of a system, which remains stable at a higher energy state using a skittle as an example²⁸ (figure 1.2). “The free (or

potential) energy of the pin may be measured, relative to the surface, by the product $mg\Delta h$, where m is the mass of the skittle; g is the acceleration due to gravity, and Δh the height of the centre of gravity of the pin above the surface. In the configuration shown in figure 1.2 A the skittle has a higher free energy than that in the flat position (figure 1.2 C). The tendency to fall to the position of lower free energy cannot, however, manifest itself unless the pin is sufficiently disturbed (e.g. by the impact of a ball) so that it reaches the intermediate configuration shown in figure 1.2 B.” An increase in the systems energy is necessary therefore for the system to progress from the higher metastable equilibrium state (figure 1.2 A) to lower (figure 1.2 C) energy state of stable equilibrium.

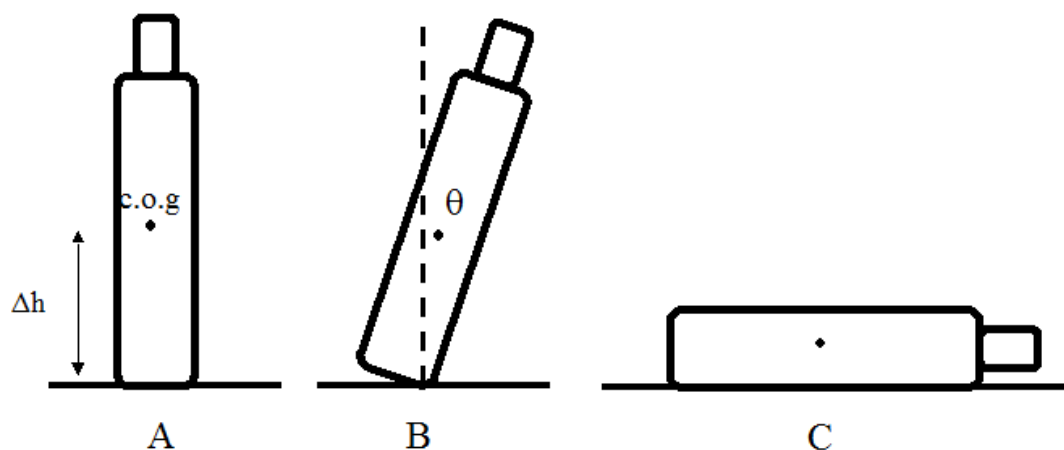


Figure 1.2: Three types of stability of a skittle, (A) metastable, (B) unstable, (C) stable ²⁸.

Therefore it is useful to consider the stability of colloids in terms of the free energy of a colloidal dispersion, primarily because of the large interfacial area between the dispersed phase and the surrounding dispersion medium. This results in the dispersed phases' molecules contributing to the thermodynamic properties of the system, particularly its free energy and determining its overall stability. Surface chemistry therefore, plays a significant role in the manner in which colloids are stabilised.

Colloidal particles in a dispersion medium always show Brownian motion and hence collide with each other frequently. The stability of colloids is thus determined by the interaction between the particles during such a collision. There are two basic interactions: one being attractive and the other repulsive. When attraction dominates, the particles will adhere to each other and finally the entire dispersion may coalesce.

When repulsion dominates, the system will be stable and remain in a dispersed state³⁶. Van der Waals forces are the primary source of attraction between colloidal particles. These forces are always present between particles of similar composition. Therefore, a colloidal dispersion is said to be stable only when a sufficiently strong repulsive force counteracts the van der Waals attraction.

The Deryagin-Landau-Verwey-Overbeek (DLVO) theory^{37 - 38} states that the stability of a particle in solution is dependent upon its total potential energy function V_T . This theory recognizes that V_T is the balance of several competing contributions:

$$V_T = V_A + V_R + V_S \quad 1.1$$

V_S (the potential energy due to the solvent) usually only makes a marginal contribution to the total potential energy over the last few nanometres of separation. More important is the balance between Van der Waals attractive (V_A) and electrical double layer repulsive (V_R) forces.

The stability of a colloidal system therefore, is determined by the sum of V_A and V_R that exist between particles as they approach each other due to Brownian motion. This theory proposes that an energy barrier resulting from the repulsive force prevents two particles approaching one another and adhering together. Therefore, if the particles have a sufficiently high repulsion, the dispersion will resist flocculation and the colloidal system will be stable. However, if a repulsion mechanism does not exist then flocculation or coagulation will eventually take place. To maintain the stability of the colloidal system, DLVO theory states that the repulsive forces between the particles must be dominant. The colloid's stability is maintained by electrostatic stabilisation, steric stabilisation or a combination of the two.

1.6 Electrostatic stabilisation

If a colloidal particle is brought within a short distance of another particle, they are attracted to each other by the van der Waals force. If there is no counteracting force, the particles will aggregate and the colloidal system will be destabilised. Colloidal stability is achieved due to repulsion forces between the particles balancing or exceeding the attraction forces.

The dispersed particles in aqueous colloids are often electrically charged; this charge contributes to the colloid's overall stability.

Coulomb's fundamental law of electrostatics states that the force of attraction or repulsion between two charged particles in a vacuum is inversely proportional to the square of the distance between them (equation 1.2)

$$F = \frac{q_1 q_2}{(4\pi\epsilon_0 d^2)} \quad 1.2$$

where ϵ_0 is the permittivity of free space. In a colloid, where a medium surrounds both charged particles, the force is reduced and is dependent upon the permittivity, or dielectric constant, ϵ , of the dispersion medium. Hence the work required to bring two charges together from an infinite separation to d is (equation 1.3).

$$\Delta W = -\int_{\infty}^d F dh = \frac{q_1 q_2}{(4\pi\epsilon d)} \quad 1.3$$

Electrostatic stabilisation therefore, is due to the presence of an electric double layer, which surrounds each dispersed particle in the colloid.

The double layer model describes the ionic environment in the vicinity of a charged surface. The electrical state of a surface depends on the spatial distribution of free (electronic or ionic) charges in its environment, i.e., where there is a charged surface, there must be a balancing counter charge. The distribution of charge in the system is usually idealised as an electrochemical double – layer. Current models of the electrical double – layer are based on the premise that one layer of the double-layer is a fixed charge or surface charge attached to the particle or solid surface, while the other layer is distributed diffusely in the liquid in contact with the particle.

The resulting solid – liquid interface may be described by a number of theories of which, the Helmholtz double layer is the simplest. It states that the surface charge, Φ_0 , is neutralised by the presence of oppositely charged counter ions at a set increment d from the charged surface. The distance, d , will be that to the centre of the counter ions, i.e. their radius. However the Helmholtz theoretical treatment does

not adequately explain all the features, since it hypothesizes rigid layers of opposite charges.

In the Guoy Chapman model of the double layer, Gouy suggested that the interfacial potential at the charged surface could be attributed to the presence of a charge of given sign at the surface, and to an equal number of ions of opposite charge in the solution. In other words, counter ions are not rigidly held, but tend to diffuse into the liquid phase until the counter potential set up by their departure restricts this tendency. The kinetic energy of the counter ions will, in part, affect the thickness of the resulting diffuse double layer. Gouy and, independently, Chapman developed theories of this *diffuse double layer* in which the change in concentration of the counter ions near a charged surface follows the Boltzmann distribution (equation 1.4)

$$n = n_0 \exp\left(-\frac{ze\Psi}{k_B T}\right) \quad 1.4$$

where n_0 is the bulk concentration, Ψ is potential, z is the charge on the ion, e is the charge on a proton and k_B is the Boltzmann constant.

However, the derivation assumes that activity is equal to molar concentration, this is a sufficient approximation for the bulk solution, but is not true near a charged surface. Since the double layer is diffuse, rather than a rigid double layer, it is necessary to consider the volume charge density rather than surface charge density when studying the Coulombic interactions between charges. The volume charge density, ρ , of any volume, i , can be expressed as

$$\rho_i = \sum z_i e n_i \quad 1.5$$

The Coulombic interaction between charges can, then, be expressed by the Poisson equation. For plane surfaces, this can be expressed as

$$\frac{d^2\Psi}{dx^2} = -\frac{4\pi\rho}{d} \quad 1.6$$

where Ψ varies from Ψ_0 at the surface to 0 in bulk solution. Thus, we can relate the charge density at any given point to the potential gradient away from the surface. Combining the Boltzmann distribution with the Poisson equation and integrating under appropriate limits yields the electric potential as a function of distance from the surface. The thickness of the diffuse double layer, therefore, may be expressed as

$$\lambda_{double} = \left[\frac{\epsilon_r kT}{4\pi e^2 \sum n_i z_i^2} \right]^{\frac{1}{2}} \quad 1.7$$

and at room temperature this can be simplified as

$$\lambda_{double} = \frac{3.3 \times 10^6 \epsilon_r}{z c^{\frac{1}{2}}} \quad 1.8$$

where ϵ_r is the dielectric constant of the solvent and c is concentration. This equation predicts that, the double layer thickness decreases with increasing valence and concentration.

Further modification of the Gouy – Chapman model by Stern provided a better approximation of reality than the Helmholtz theory.

Stern, stated that unlike Helmholtz theory (which assumes that ions behave as point charges and that there are no physical limits for the ions in their approach to the surface.), that ions do indeed have finite size and so cannot approach the surface closer than a few nanometres. Therefore the first ions of the Gouy-Chapman Diffuse Double Layer are not at the surface, but at some distance δ away from the surface, this distance is usually taken as the radius of the ion (figure 1.3). The potential and concentration of the diffuse part of the layer is low enough to justify treating the ions as point charges.

Stern also assumed that it is possible that some of the ions are specifically adsorbed by the surface in the plane δ , and this layer has become known as the Stern Layer. Therefore, the potential will drop by $\Psi_0 - \Psi_\delta$ over the "molecular condenser" (ie. the Helmholtz Plane).

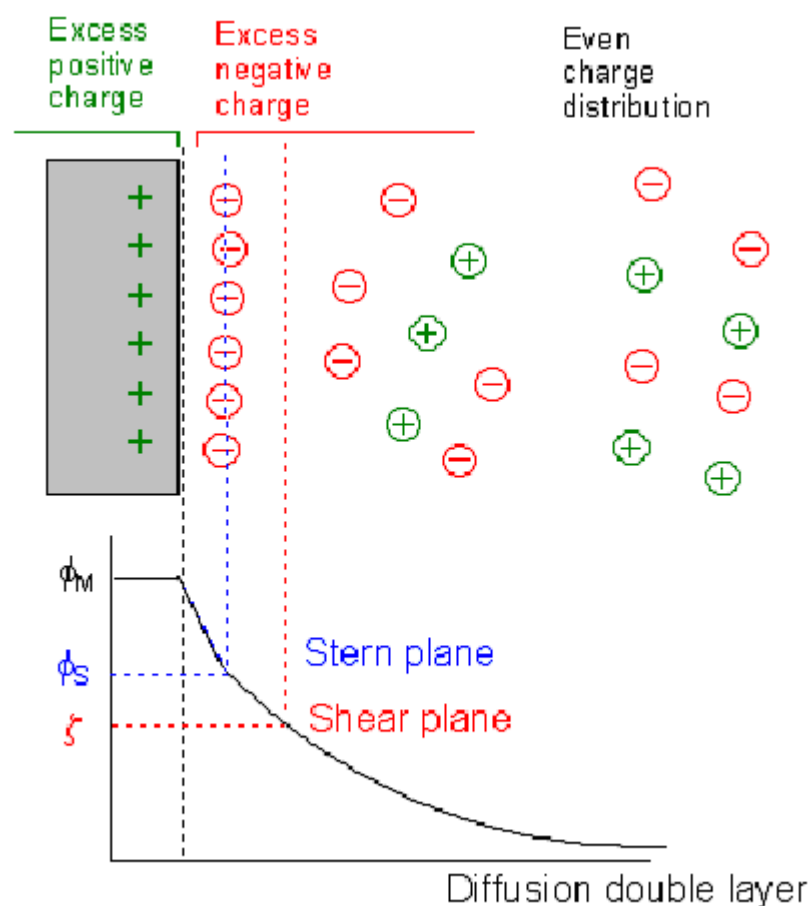


Figure 1.3: Stern layer.

Within a colloidal dispersion the double layer is formed in order to neutralize the charged surface of the nanostructures (figure 1.4) and, in turn, causes an electrokinetic potential between the surface of a nanoparticle and any point in the mass of the dispersion medium. The magnitude of the surface potential is related to the surface charge and the thickness of the double layer. Away from the surface, the potential drops off roughly linearly in the Stern layer and then exponentially through the diffuse layer, approaching zero at the imaginary boundary of the double layer. The potential curve is useful because it indicates the strength of the electrical force between particles and the distance at which this force comes into play.

A charged particle will move with a fixed velocity in a voltage field. This phenomenon is called electrophoresis. The particle's mobility is related to the dielectric constant and viscosity of the suspending liquid and to the electrical potential at the boundary between the moving particle and the liquid. The relationship between zeta potential and surface potential depends on the amount of ions in the solution. The

zeta potential is related to the mobility of the particle and although it is an intermediate value, Zeta potential is sometimes considered to be more significant than surface potential as far as electrostatic repulsion is concerned and is therefore used as a measure of electrostatic stability (particles with zeta potentials of $\geq \pm 30$ mV are normally considered stable).

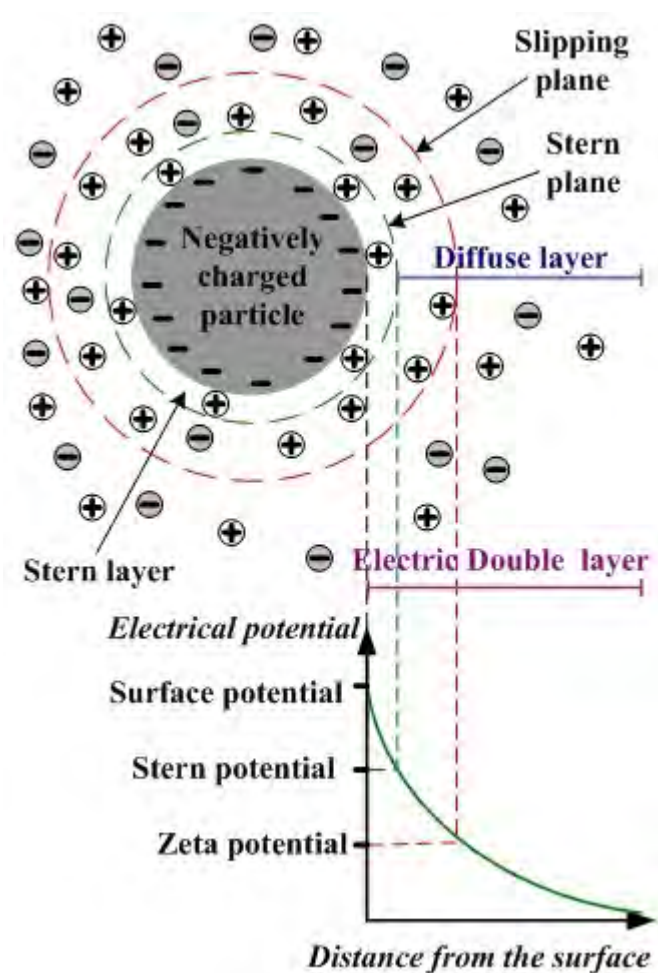


Figure 1.4: Double layer of a nanoparticle.

Coulombic repulsion is an effective method of colloidal stabilisation, however it is limited to dispersion media with low ionic strengths. This is because the thickness of the double layer depends, on the ionic strength (equation 1.9) of the dispersion medium.

$$I = \frac{1}{2} \sum z_i^2 c_i \quad 1.9$$

Where z_i is the charge and c_i is the molar concentration of the ions, for 1:1 electrolytes, the ionic strength is equal to the concentration. Here we will use the concentration c to represent ionic strength. At low ionic strengths (electrolyte $c = 10^{-3}$ M), the thickness of the double layer is about 5 – 10 nm, which is of the same order as the attractive Van der Waals forces between particles.

However the thickness of the double layer is reduced significantly with increasing the ionic strength. At ionic strengths for electrolyte $c > 10^{-1}$ M, the thickness of the double layer is less than 1 nm. In that case, the range of double layer electrostatic repulsion is usually insufficient to counterbalance the Van der Waals attraction³⁹. As a result colloids are highly sensitive to the ionic strength of the dispersion medium.

1.7 Steric stabilisation

The stability of many colloids of both natural and man-made origin can be improved by the presence of macromolecules or polymers, e.g. fatty acids in milk are stabilised by the presence of casein.

Polymers increase viscosity of a colloidal dispersion, altering the sedimentation behaviour. This, coupled with their high molecular weights, results in only a small concentration being necessary to achieve this. Originally this method of stabilisation was referred to as protection because on addition, these macromolecules in essence form a protective coating around each colloidal particle by attaching (grafting or chemisorption) to the surfaces of the particles (figure 1.5), which prevents them from aggregating. However, following systematic studies with a variety of synthetic polymers acting as the capping agents (where the polymers possess chain dimensions that are comparable to, or in excess of, the range of the attractive Van der Waals forces³⁹), the mechanism of stabilisation has been illuminated and renamed as steric stabilisation. Here the presence of the ‘protecting’ agent affects the inter-particle forces by either influencing the particles’ attractive (van der Waals) forces or introducing a repulsive force between the particles^{28, 40}. For example, poly vinyl alcohol (PVA) is a commonly used steric polymer stabiliser. It works by partially adsorbing to the particle surface, while the remainder of the macromolecule solvates

and expands away from the interface, preventing other particles from approaching.²⁷
41-45



Figure 1.5: Schematic of steric stabilisation.

Electrostatic and steric stabilization can be combined as electrosteric stabilisation where the electrostatic component is either a net charge on the particle's surface and/or charges associated with the polymer attached to the surface.

Steric stabilisation has several distinct advantages over electrostatic stabilisation:

- Steric stabilised colloids are relatively insensitive to the presence of electrolytes, whereas for 1:1 electrolytes ($I \approx c_i$), a charge-stabilized dispersion will be unstable once the electrolyte's concentration exceeds 10^{-1} M.
- Steric stabilisation is equally effective in both aqueous and non-aqueous dispersion media. Charge stabilization is less effective in non-aqueous dispersion media than in aqueous media. This is due to the low relative dielectric constant (< 10) of most non-aqueous media. As a result, steric stabilisation is generally preferred for non-aqueous colloids.
- Steric stabilisation is independent of a colloid's solids content. While for charge stabilised non-aqueous colloids, the thickness of the double layers can be so large, (due to the low dielectric constant of the dispersion medium), that the preparation of high solids dispersions can force the particles too close together leading to coagulation. Whereas in aqueous based colloids, preparation of charge-stabilized particles at high solids dispersions is often

difficult because of interactions between the double layers surrounding individual particles.

- Reversibility of flocculation. The coagulation of charge - stabilized particles by the addition of electrolyte is often irreversible. In contrast, flocculation of sterically stabilized dispersions can usually be reversed spontaneously by mere dilution of the concentration. This is because sterically stabilised dispersions may be thermodynamically stable while charge stabilised dispersions are only thermodynamically metastable. As a consequence, for charge - stabilised dispersions, the coagulated state represents a lower energy state and the coagulation can be reversed only after input of work into the system.

Electrosteric stabilization, a combination of these two stabilisation mechanisms is used in this study.

1.8 Silver nanoparticles

In this study silver nanoparticles were synthesised, characterised and applied, as both a sensing device and as the basis of a spectroscopic analytical technique. Why silver? As mentioned in the previous section metallic nanoparticles often display novel properties. This is particularly true of silver, a relatively inexpensive noble metal¹⁰. One of silver's most desirable properties has been its anti microbial action. Ionic silver (Ag^+) has long been considered a useful antimicrobial, effective against a broad range of microorganisms, with low concentrations documented to have therapeutic activity. "Silver has been described as being 'oligodynamic' because of its ability to exert a bactericidal effect at minute concentrations"^{46 - 47}. Consequently, this has resulted in extensive study of silver nanoparticles, which in turn has resulted in the production of a range of commercially available healthcare products including silver-coated catheters, anti-microbial paints, municipal water systems and wound dressings e.g. Hydrofiber[®] dressing^{48 - 50}.

Antimicrobial effects however useful are not the only string to silver's bow; *nano* silver also displays novel electro-optical (discussed further in section 1.12), magnetic and catalytic properties^{51 - 54} that have encouraged its application in a wide variety of research.

Another highly active area of nano silver research, according to the volume of research published, is its application in sensing ⁵⁵ with silver nanostructures being utilised as DNA detectors ⁵⁶, gas sensors (such as ammonia sensors) ⁵⁷ and as herbicide biosensors ⁵⁸ among others.

T.M. Tolaymat *et al.* ²⁷ describe the properties, synthesis and application of silver nanoparticles detailed in the available literature at the time of writing.

Synthesis Parameter	Reported Preference	%	Reasoning
Salt Precursor	Silver Nitrate	83	<ul style="list-style-type: none"> • Relative low cost • High chemical stability compared to alternatives
Solvent	Water	80	<ul style="list-style-type: none"> • Produces stable and mobile nanoparticles • Low cost • Readily available
Reducing Agent	<ul style="list-style-type: none"> • Sodium Borohydride (23 %) • Sodium Citrate (10 %) 	33	<ul style="list-style-type: none"> • Traditional reduction agents • Established wet chemical methodologies • Readily available • Low energy/cost • Well defined effects
Stabilising Agent	<ul style="list-style-type: none"> • Polymers (29 %) • Sodium Citrate (27 %) 	56	<ul style="list-style-type: none"> • Dependent on stabilisation mechanism (electrostatic (citrate) / steric (polymer)) • Both relatively low cost • Both have dual role in synthesis process <ul style="list-style-type: none"> - Citrate as a reduction agent - Polymer directs morphology
Particle Morphology (Shape)	Spherical	90	<ul style="list-style-type: none"> • Preparation methodology driven • Most thermodynamically stable
Particle Morphology (Size Range)	1 - 10 nm	45.5	Linked to choice of <ul style="list-style-type: none"> • Choice of reduction and stabilising agents • Desired application <ul style="list-style-type: none"> - Biological effects are most potent at smaller size ranges - Whereas larger particles are more effective for applications such as SERS

Table 1.1: Summary of major findings of T.M. Tolaymat's *et al.* review ²⁷ (% refers to the proportional of articles considered in the review)

The authors found that the major route of fabrication was bottom up (with wet chemistry the dominant technique, entailing the chemical reduction of a silver salt),

with less than 4 % of the articles reviewed utilising the alternative top down methods and document the salt precursors and agents used in the fabrication of the silver nanoparticles, the morphology of the particles, their resulting properties (singularly or within nanocomposites) and hence the possible applications of the nanomaterials of which their findings are summarised in table 1.1. The authors conclude that the literature confirms the potential of silver nanomaterials, in a wide range of applications, from medical (exploiting silver's antimicrobial properties) to sensing devices (capitalising on nano silver's unique optical properties).

1.9 Sensing

Analytical chemistry and analytical techniques are essential tools in the investigation of the world surrounding us ⁵⁹. Since any intellectual information structure capable of producing theories is dependent upon a reliable input of data the quality of this information is important ⁶⁰. A sensor is a device, which measures a chemical or physical quantity and converts it into a signal that can be read by an observer or by an instrument, thus sensors can be classified according to the type of energy transfer that they detect, for example, electromagnetic and chemical ⁶¹.

The following qualities are essential for an effective sensor.

- **Selectivity:** the ability to detect one specific species even in the presence of a number of other chemical species.
- **Reproducibility:** it is key that the sensor can be trusted to give the same signal/output value for a certain set of conditions over the course of its lifetime.
- **Accuracy:** giving a correct concentration of the species being detected, ensuring that the output value that the sensor provides is as close as possible to the true value.
- **Sensitivity or the limit of detection (LOD):** the minimum signal that can be interpreted as a meaningful measurement, and

- Limit of quantitation (LOQ): the signal, at which quantitative results can be reported with a high degree of confidence, should be known.
- Reversibility: ideally the sensing process should proceed equally well in both the forward or reverse direction i.e. when the analyte is removed the sensor's response should return to the baseline.
- Stability: the sensor should retain its characteristics when tested or used under varying conditions and environments.
- Linearity: over the desired measurement range the sensor's response should be linearly proportional to the concentration of analyte^{61 - 62}.

1.10 Nanomaterials and sensing

A significant quantity of the unique properties (both physical and chemical) of nano silver can be exploited in the sensing domain, particularly by improving an individual sensors' sensitivity, selectivity or stability.

Research to augment one of these facets has resulted in multiple advances in sensing devices and techniques, such as, the production of innovative sensing materials^{62 - 63} improved data analysis (e.g. pattern recognition, fast Fourier transform, and wavelet transform),^{63 - 64}, and sensor fabrication^{65 - 66}.

Nanoscience therefore has an active role in many aspects of sensor development, specifically in terms of exploiting the miniaturisation and unique applications afforded by the nanoscale. In this instance metallic nanostructures are notable precursors with the use of nanostructured materials in particulate, film or composite form increasing rapidly³.

Because the size and therefore the properties of the nanoparticles can be varied, a wide range of sensors has been developed^{67 - 68}.

1.11 Nanocomposites

A nanocomposite is a matrix to which nanoparticles have been added to improve a particular property of the material. The difference in optical, catalytic or conductive

properties between nanocomposites and their constituent components depends largely on the chemical nature of each component and how the components interact. This interaction depends strongly on characteristics of each component, i.e. interface, size, shape and structure. In extreme cases, where there is no or little interaction between the components, the composites' properties should be equivalent to a simple sum of the properties of the individual elements. In cases where the interaction between the constituents is strong, the properties of the composite system can differ substantially from the simple sum of the properties of the individual components. The characteristics of the individual components are lost and new features arise as a result of the strong interaction⁶⁹⁻⁷⁰.

*H. Chik and J. M. Xu*⁷¹ have described a fabrication method that not only allows the addition of a variety of materials, including metals, semiconductors, and carbon nanotubes to an anodised aluminium oxide porous membrane but also, through tuning of the synthesis parameters, controls the nanomaterials morphology.

This enabled the authors to engineer the physical properties of the composite by determining the shape, size, composition and doping of the nanostructures, as well as new properties produced by their interaction with the matrix itself. Some of these properties and functions were not intrinsic to the individual nano-elements but were due to the collective behaviour of the nanostructures within the membrane. The novel nanocomposite platform described potentially offers a wide range of applications in various fields including electronics, optics, mechanics and biotechnologies.

Work by *J. Li and J.Z. Zhang*⁶⁹, highlights the ability to capitalise on the unique properties of nanoparticles, through their incorporation into composites. The authors also noted that the composites' properties could be tailored by controlling the nanostructures' morphology and optical interfaces. This affords the nanocomposite multiple potential applications in different fields, including bio-labelling (silica-coated CdSe/ZnS core/shell quantum dots), light energy conversion (nano doped silicon in photovoltaic cells) and hygienic materials (the addition of antibacterial copper or silver ions into plastics and paints).

1.12 Electro-optical properties of silver nanomaterials

When light interacts with the surface of a metal; the free electrons of the metal move in a background of fixed positive ions, which ensure overall neutrality of the system.

This movement of electrons forms a plasma; the free electron plasma. The optical response of the plasma governs the optical response of the metal itself.⁷¹⁻⁷²

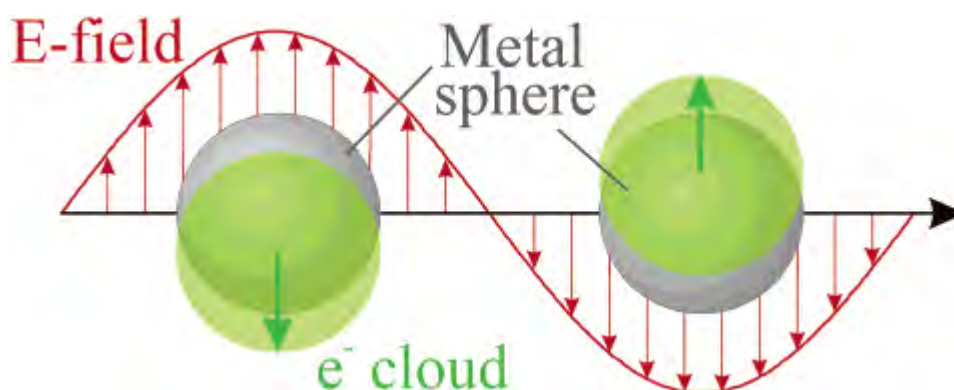


Figure 1.6: Schematic representation of the plasmon oscillation for a spherical metallic nanoparticle, irradiated by light, the oscillating electric field causes the conduction electrons to oscillate coherently.⁹

1.13 Origin of plasmons

When an external electro-magnetic field such as light is applied to a metal, the conduction electrons move collectively so as to screen the perturbed charge distribution in what is known as plasma oscillation. The Surface Plasmon Resonance (SPR) is therefore a collective excitation mode of the plasma localised near the metal surface (LSPR). In the case of a metal nanoparticle, the surface plasmon mode is 'restricted' due to the small dimensions to which the electrons are confined, i.e. the surface plasmon mode must conform to the boundaries of the dimensions of the nanoparticle²⁴. Therefore the resonance frequency of the surface plasmon oscillation of the metal nanoparticle is different from the plasma frequency of the bulk metal.

Among the metal nanoparticles known to exhibit LSPR, silver nanoparticles have an especially strong LSPR.

These unique surface plasmons determined by the nanoparticle's own physical properties, can be observed in the electromagnetic spectrum^{9, 73 - 75}. Surface interactions can alter the optical properties and influence the spectral profile of the light scattered by the LSPR of the metal nanoparticles. This feature can be employed as an indicator in sensing interactions. Particle size may be determined using Mie theory, which solves Maxwell's equations⁷⁶. Mie theory can also describe the spectra

of colloids of spherical particles of arbitrary size (extinction = scattering + absorption).

Silver colloids (nanoparticles) have been extensively characterised by UV – Vis spectroscopy because they exhibit an intense absorption band in this region, known as the surface plasmon absorption band (SPAB), which is a product of the colloid's nanoparticles physical properties, including their size, shape, surrounding dielectric medium, coupling of the colloids and adsorbed solutes.

The colloids SPAB may also be used to monitor the size of nanoparticles. There is also experimental information concerning the interpretation of the absorption spectra for ionic silver clusters. It should be noted that a number of factors could affect the properties of the SPAB of a silver colloid; these include the synthesis process, aggregation of the nanoparticles, adsorption of metallic ions or protective polymers onto the nanoparticles' surfaces or changes to the particle's morphology and/or electron density.

The formal solution of the problem of the light absorption and scattering by small particles is described by the Mie theory^{4, 77 – 78}, whose complete mathematical basis developed the theory of absorption and scattering of light by spherical nanoparticles. When a beam of light irradiates a metallic nanoparticle, the oscillating electric field causes a collective excitation of the conduction electrons, the LSPR/SPAB, this displacement of electrons results in the polarisation of the nanoparticle. The absorbance of the colloid may in the case of non – aggregated spherical silver nanoparticles, with clean surfaces be calculated using,

$$A = lC_{ext} \frac{C_{Ag}}{101.273 r^3} \quad 1.10$$

where r is the particle radius, C_{ext} is the extinction cross section of a single particle in nm^2 , l is the optical path length in nm and C_{Ag} is the concentration of Ag^0 in g cm^{-3} . The extinction cross section of the colloid's spherical particles in a dispersion medium of refractive index N can be calculated as

$$C_{ext} = 2 \frac{\pi}{k^2} \sum_{n=1}^{\infty} (2n+1) \Re(a_n + b_n) \quad 1.11$$

where, $k = 2\pi N/\lambda$, \Re is the real part of the scattering coefficients a_n and b_n , which are dependent on the particle's radius.

When the particle size is smaller than the mean free path of the conduction electrons (52 nm for silver), the magnitude of the real $\varepsilon'(\omega)$ and imaginary parts $\varepsilon''(\omega)$ of the dielectric function of the particle is also affected,

$$\varepsilon'(\omega, r) = \varepsilon'_{bulk} + \frac{\omega_p^2}{(\omega^2 + \omega_d^2)} - \frac{\omega_p^2}{(\omega^2 + \omega_r^2)} \quad 1.12$$

$$\varepsilon''(\omega, r) = \varepsilon''_{bulk} + \frac{i\omega_p^2\omega_r}{[\omega(\omega^2 + \omega_r^2)]} - \frac{i\omega_p^2\omega_d}{[\omega(\omega^2 + \omega_d^2)]} \quad 1.13$$

where ω is the light frequency, ω_p , the plasmon frequency and ω_d is the bulk metal damping constant. ω_r , the metal particle damping constant (or the inverse of the collision time for conduction electrons), can be calculated by

$$\omega_r = \omega_d + B \frac{v_f}{r} \quad 1.14$$

where v_f is the electron velocity at the Fermi level and B is a constant.

Usually the calculations of absorption spectra of metallic nanoparticles are presented as the extinction cross – section or extinction efficiency of a single nanoparticle, but for experimental UV – Vis results of metallic colloids (their optical properties), it is more useful to be able to interpret the absorption spectra themselves. As the fundamental characteristics of SPAB, such as peak position, maximum absorbance and bandwidth at half – maximum absorption are heavily influenced by the particle size, morphology and surrounding medium. For example, where the plasmon absorption peak shifts to higher wavelengths as the particle size increases, as described by equation 1.15

$$A(C_{ext}, r) = a \frac{C_{ext}}{r^3} \quad 1.15$$

where a is a constant. It also states that the absorbance increases as C_{ext} increases, while an increase in the particle radius decreases the absorbance and that the position of the plasmon peak and the shape of the absorption band is determined by C_{ext} .

This is evident throughout the literature where spherical silver nanoparticles possess a single plasmon peak between $\sim 390 - 480$ nm whereas triangular silver nanostructures may display a number of peaks over a greater absorbance range, with their out of plane dipole band generally around 330 nm and the in plane dipole plasmon band at $\sim 550 - 630$ nm⁷⁹⁻⁸¹.

Recent advances in nanoscience and nanotechnologies have fuelled a renewed interest in the interaction of metals and light (plasmonics); with particular emphasis on the fabrication and application of plasmon supporting substrates. These surface plasmons can be observed in the electromagnetic spectrum, their energy being determined by the morphology and dielectric constant of the metal particle^{9, 73-75}.

SERS substrates can be classified into three categories⁸²

- metallic nanoparticles in suspension; utilising the simplest methodology, reproducibility and potential sampling challenges. Suspensions are widely used due to their effective performance, good stability and ease of fabrication
- metallic nanoparticles immobilized on solid substrates generated by immobilising the nanostructures on planar platforms. Adhesion of the particles to the support is usually very poor, which has led to the development of immobilisation techniques to improve the integrity and the performance of the substrate's stability
- nanostructures fabricated directly on solid substrates, which includes nanolithography and template synthesis of nanostructures

Currently SERS is one of the most sensitive analytical techniques available, and is rapidly developing into an analytical tool in numerous fields, with a wide range of applications. For example in biomedical research, where *Picorel et al.*⁸³ used SERS to examine the complex structure of three different protein complexes, and their orientations on an electrochemically roughened Ag electrode. Whereas other groups such as *Vo-Dinh's* and *Bartlett's* have used SERS for DNA detection using a variety of substrates^{84–88}.

A number of SERS substrates obtained by immobilizing particles onto a solid support have shown potential in environmental monitoring. For example, sol–gels doped with nanostructures⁸⁰ and permeability-selective polymer coated metal nanoparticles⁹⁰ not only provided large surface areas to trap environmental pollutants and bring them close to the metallic surface, but their inherent protective coating improved their stability and shelf life, SERS substrates consisting of C-18 alkylsilane and short chain thiol modified nanostructures⁹¹ can selectively adsorb organic molecules.

*J. Shi et al.*⁷⁷, summarised a range of chemical sensors that apply the optical principles of nanomaterials for the detection of multiple chemical and biochemical analytes. These include colorimetric biosensors based on gold nanoparticles, gas sensing semi-conductors which exhibit changes to their optical transmittance when exposed to gases such as NO, and CO and optical humidity sensors based on changes in cobalt oxide films' absorbance in the visible wavelength.

1.14 Optical Sensors

The interaction of light and matter can be measured in a multitude of ways; the principle techniques are absorption, emission or scattering. The manner in which a molecule interacts with light is governed by the energy levels of the molecule, which is dictated by the movement of the compound's atoms (motional energy states, e.g. vibrational) or the movement of electrons (electronic energy levels) within the system⁷¹.

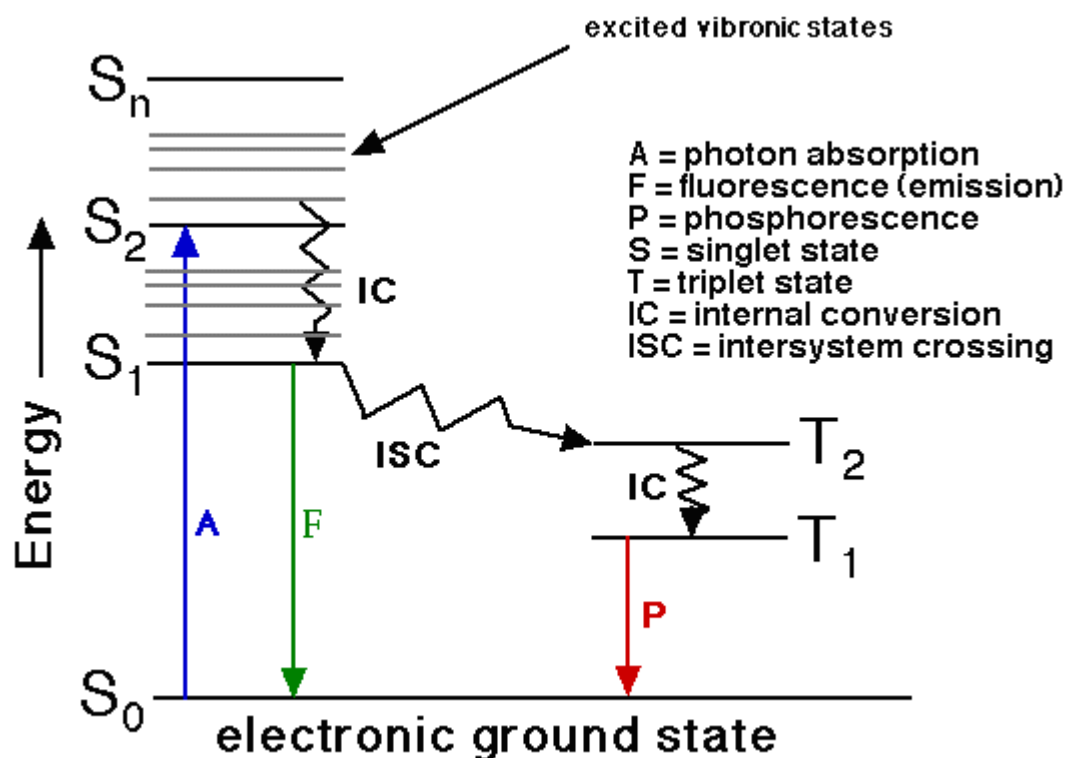


Figure 1.7: Jablonski diagram, a schematic representation of the electronic and vibronic (rotational/vibrational) energy levels of a molecule.⁹³

Figure 1.7, illustrates the transitions which can occur between molecular states due to a molecule's interaction with light. These include electronic, (between two electronic states) and vibronic transitions. These transitions may be further classified as either radiative or non-radiative transitions.

Radiative transitions are a consequence of the molecules interaction with a photon and are considered dipole allowed; they involve the absorption or emission of a photon, whereas non-radiative transitions are a product of the molecule's interaction with the surrounding environment.

Optical processes primarily involve the absorption and emission of photons, these include:

1.15 Optical Absorption

There are two major types of optical absorption, where a molecule is excited to a higher energy state via its interaction with a photon,

- Electronic absorption, an electron is excited to a higher electronic state, transitions occur typically in the UV ($\sim 200 - 400$ nm) and visible ($\sim 400 - 800$ nm) region. It follows that the electronic structure of molecules may be examined through UV- Vis Spectroscopy.
- Infrared absorption, again a photon excites a molecule to a higher vibronic level within a given electronic state, the energy absorbed during these transitions are in the infrared or far infrared ($\lambda = 3 - 100 \mu\text{m}$). Molecules' vibrational structure can be determined using infrared, IR, spectroscopy.

1.16 Optical Emission (Luminescence)

The mirror image of absorption, emission is a product of the relaxation of a molecule to a lower energy level from a higher energy state. Radiative emission occurs between vibrational states, however it is mainly observed during transitions between electronic states. Two major emission processes are possible in the presence of an incident beam,

- Stimulated emission, where incident photons interact with an excited molecule to give the emission of an identical photon.
- Spontaneous emission occurs in the absence of an incident photon and therefore may occur at any energy once the transitions are allowed.

Luminescence is not solely based on the simple mechanism of photon absorption by a molecule followed by its subsequent reemission; there are preceding and/or competing nonradiative processes which are also in effect.

When a molecule in the ground state absorbs a photon (to go from one electronic state to another), the time required to do so ($\approx 10^{-15}$ s) is relatively short compared to the time required for all other electronic processes and nuclear motion. It can be assumed that immediately after excitation a molecule has the same geometry and is in the same environment as it was prior to excitation. In this case the molecule can do one of two things depending on its environment:

- Emit a photon from the same vibrational level to which it was excited initially; this occurs in the gas phase, as the emission of an infrared photon is the molecule's only means to lose vibrational energy to return to the ground state.
- Undergo changes in vibrational levels prior to emission of radiation, (for molecules in solution). The excess vibrational energy of the excited state of the molecule may be lost through thermal relaxation from the solute molecule to the solvent. The process of thermal relaxation is so efficient (occurs within 10^{-13} to 10^{-11} s) that all the excess vibrational energy of the excited state is lost, so, before an excited molecule in a solution can emit a photon, it will undergo vibrational relaxation, and therefore photon emission will always occur from the lowest vibrational level of an excited state.

Once a molecule arrives at the lowest vibrational level of an excited singlet state, a number of processes can occur,

- Fluorescence, which consists of photon absorption by a molecule to go to an excited singlet state, relaxation from higher vibrational levels of that state to its lowest vibrational level and photon emission to the ground state. Fluorescence decay has the same lifetime as an excited singlet state and is approximately 10^{-9} to 10^{-7} s.
- Phosphorescence, similarly, consists of photon absorption by a molecule to go to an excited singlet state (population of triplet states by direct absorption from the ground state is insignificant), followed by intersystem crossing (a spin-dependent internal conversion process involving vibrational coupling between the excited singlet state and a triplet state), relaxation from higher vibrational levels of the triplet state to its lowest vibrational level and photon emission to the ground state. As phosphorescence originates from the lowest triplet state, it will have a decay time approximately equal to the lifetime of the triplet state: 10^{-4} to 10 s.

1.17 Elastic and inelastic scattering

Scattering process involve the simultaneous absorption of an incident photon and the emission of another 'scattered' photon, light scattering processes are divided into two distinct groups

- Elastic (Rayleigh) scattering, here incident and scattered electrons have the same energy; this process leaves the molecule at the same energy level, i.e. no transfer of energy occurs between the photon and molecule, and fails to excite the molecule's internal structure.
- Inelastic scattering, here the scattered photon has a different energy E_S to the incident E_L , this difference in energy corresponds to transitions between molecular states.

One of the most important forms of inelastic scattering is Raman scattering, involving vibrational and rotational transitions, which reveal much of the internal structure of a molecule.

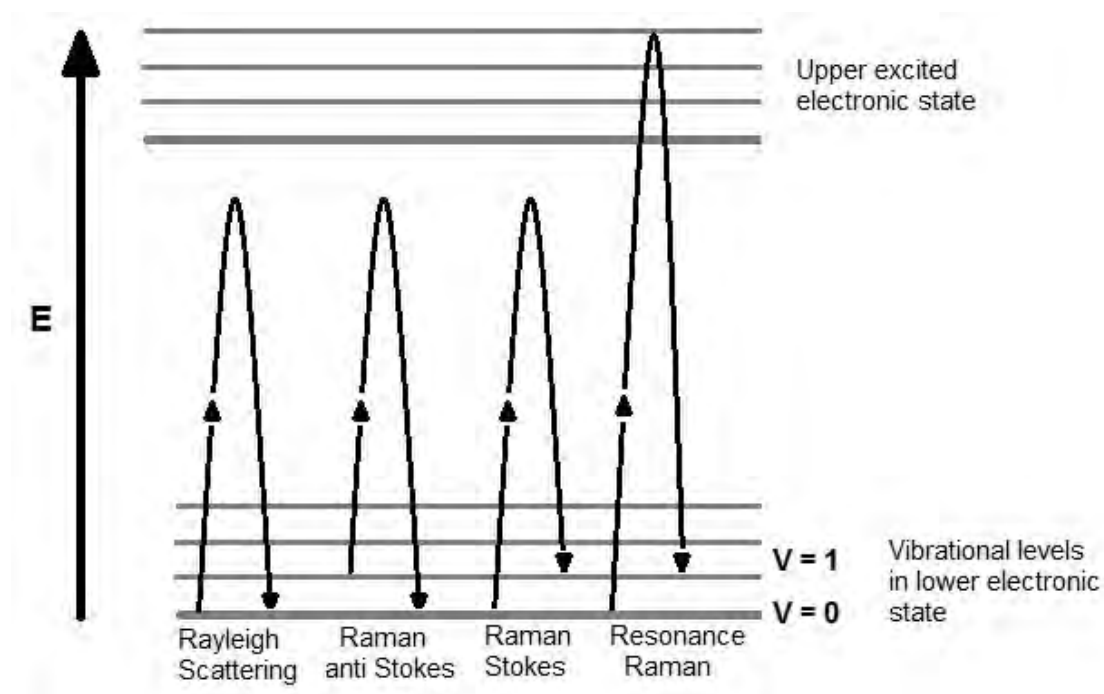


Figure 1.8: Different types of scatter

1.18 Raman scattering

Raman Spectroscopy utilises the light scattered by an analyte, if a molecule were excited by phonons with the energy $h\nu_0$ the majority of the scattered light would possess energy (frequency) identical to that of the incident light, designated as Rayleigh scattering (figure 1.8). A portion of the diffused photons, however, undergo a shift in frequency, (indicating a loss or gain in energy) this is Raman scattering^{73, 94}.

Stokes Raman scattering is a result of the incident photon transferring energy to the analyte, and causes the analyte to migrate to a higher energy state. Stokes Raman typically corresponds to the excitation of the analyte molecule from the vibrational ground state $\nu = 0$ to the first excited state $\nu = 1$. The energy of the vibration is given by the difference between the incident and scattered photon $h\omega_\nu = E_L - E_S$.

If energy is transferred from an excited molecule to the incident photon, thus reverting to the lower energy state the scattering is termed anti – Stokes Raman scattering. Here the analyte molecule has relaxed from an excited vibrational ($\nu = 1$) state to its ground state ($\nu = 0$) and the vibrational energy is determined by $-h\omega_\nu = E_S - E_L$.

Generally experimental Raman results can be described in the following terms, where individual molecules are treated as simple harmonic oscillators. The electric field of the incident light may be described as,

$$E = E_0 \cos(2\pi\nu_0 t) \quad 1.16$$

Where, E is the time – dependent field factor, E_0 is the maximum amplitude and ν_0 the frequency. This electric field generates in the target molecule a dipole μ defined as,

$$\mu = \alpha E = \alpha E_0 \cos(2\pi\nu_0 t) \quad 1.17$$

Where the proportional constant, α , is the polarisability. Equation (1.17) may be expressed in three dimensions in both Cartesian and matrix form⁹³. If α is independent of time, the radiation discharged by the induced dipole is Rayleigh scattering (the same frequency as the incident radiation). However, if the polarisability, α , is dependant on time, and hence vibrational frequencies of the

molecule, i.e. $\alpha = \alpha(t)$, then the incident energy will be altered and a portion of the radiation scattered at different frequencies. If the scattering molecule has vibrational modes, Q_k , they may be denoted as,

$$Q_k = Q_k^0 \cos(2\pi\nu_k t) \quad 1.18$$

Where Q_k^0 is the maximum amplitude and ν_k is the oscillation frequency. The polarisability of the dipole can be extended as follows in a Taylor series,

$$\alpha = \alpha_0 + \frac{\partial \alpha}{\partial Q_k^0} Q_k + \dots \quad 1.19$$

considering only the first order term and multiplying by E yields,

$$\alpha E = \mu = \alpha_0 E + \frac{\partial \alpha}{\partial Q_k^0} Q_k E \quad 1.20$$

or

$$\mu = \alpha_0 E_0 \cos(2\pi\nu_0 t) + \frac{1}{2} E_0 \frac{\partial \alpha}{\partial Q_k^0} Q_k^0 [\cos 2\pi(\nu_0 - \nu_k)t + \cos 2\pi(\nu_0 + \nu_k)t] \quad 1.21$$

Where $\alpha_0 E_0 \cos(2\pi\nu_0 t)$ denotes Rayleigh scattering, and the frequency terms with $(\nu_0 - \nu_k)$ and $(\nu_0 + \nu_k)$ describe Stokes and anti - Stokes Raman scattering, respectively. As the ground state is more populated than the excited state, it follows that Stokes scattering is the more intense of the two.

1.19 Raman spectroscopy

Raman spectroscopy is both non-destructive and non-invasive, which utilises the inelastic scattering of monochromatic light such as that obtained through laser excitation to study vibrational, rotational and other low-frequency modes of a molecule^{94 - 96}. Raman elucidates the molecular profiles of systems by measuring frequency shifts that adhere to a selection rule, whereby changes in polarisability of the analyte is required^{97 - 98}. However, the usefulness of Raman in practical applications is hindered by the very weak signal produced by Raman scattering as

typically only one in $10^6 - 10^8$ photons undergo inelastic (Raman) scattering when interacting with a sample^{99 - 101} This results in the need to use high power lasers or long sampling times to counteract the inefficient scatter for adequate spectral acquisition in real world applications¹⁰².

This lack of sensitivity has encouraged the development of the technique with emphasis on improving / augmenting the signal output. Resonance Raman discovered by Shorygin, has had a significant impact on Raman's usefulness. Shorygin found that although many substances, especially coloured ones, may absorb laser beam energy and generate strong fluorescence, which contaminates the Raman spectrum, under certain conditions some types of coloured molecules produce strong Raman scattering instead of fluorescence.

This resonance Raman effect takes place when the excitation laser frequency is chosen in a way that it resonates with the frequencies of the analyte's electronic excited states. The intensity of Raman bands, which originate from electronic transitions between those states are enhanced 3 – 5 orders of magnitude, improving the technique's sensitivity^{115 - 116}.

As explained above, resonance Raman scattering occurs when using a laser excitation wavelength that approaches or coincides with a sample's UV-visible absorption band, and the resonance effect can give a large increase in the scattering intensity enabling spectra to be recorded from samples at low concentrations. In addition this enhancement occurs only for the Raman bands of the species giving the UV-visible absorption band in resonance, such that an appropriate choice of laser wavelength can provide not only sensitivity but also selectivity.

However, a potential disadvantage of the technique is that a laser wavelength that coincides with a sample UV-visible absorption band can result in fluorescence emission that may be much stronger than the Raman scattering, and which, in some cases, may be so strong that a resonance Raman spectrum is effectively unobservable above the emission background.

Resonance Raman spectroscopy offers good potential for the analysis of coloured compounds such as dyes because a laser excitation wavelength in resonance with a dye absorption band may typically be expected to provide high sensitivity and selectivity for the dye, provided that fluorescence does not obscure the Raman signal¹¹⁷. Recently Raman spectroscopy as a technique is undergoing a nano evolution, with the emergence of SERS, Surface Enhanced Raman Spectroscopy.

1.20 Surface Enhanced Raman spectroscopy, SERS

Surface Enhanced Raman Scattering (SERS) is another technique used to amplify the weak Raman signal and involves a substrate, typically of the nanoscale. The substrates may be produced in a variety of ways (figure 1.9); including, metal colloids, electrode roughening, vapour deposition of metal particles onto a substrate, lithography produced metal spheroid assemblies and metal deposition over a deposition mask of polystyrene nanospheres¹⁰³ (figure 1.10).

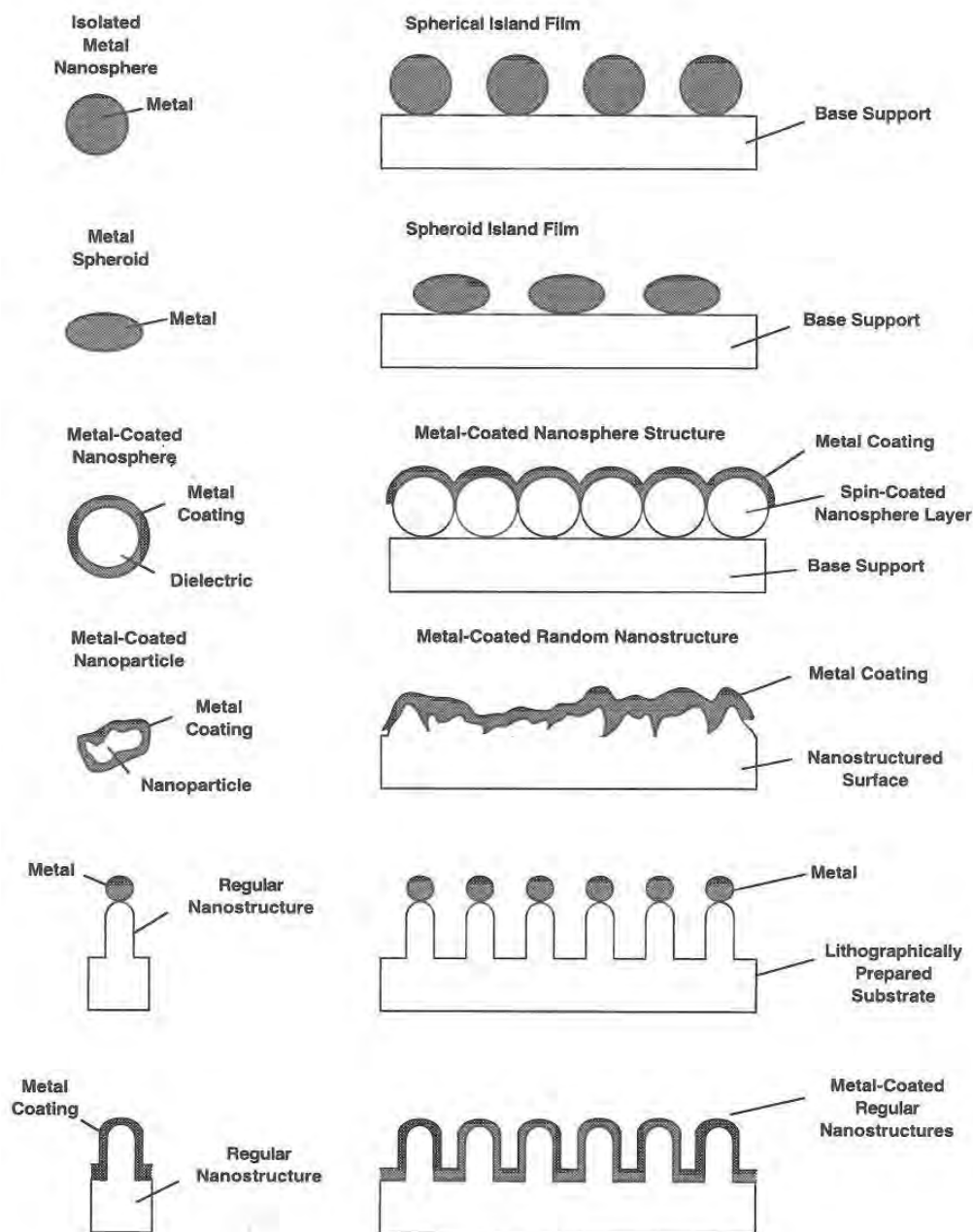


Figure 1.9: An assortment of SERS active nanostructures¹⁰⁴.

- Surface: SERS is a surface spectroscopy technique. Enhancement of an analyte's Raman signature is seen only if the compound is at (or close to) the metal's surface. Hence the frequent issue in practical application of the SERS technique is the transfer of analyte molecules from a volume to a surface.
- Enhanced: signal augmentation is produced by plasmon resonances in the metal substrate (note; the SERS substrate is generally in the form of metallic nanostructures).

Interest in the application of SERS as an effective analytical tool is increasing, with the potential of the development of highly selective and sensitive detection^{105 - 107}. Plasmons are at the heart of SERS enhancement therefore it's unsurprising that advances in plasmonics (section 1.13) hugely benefit SERS. It is necessary therefore to consider the origin of the plasmon activity. Due to the presence of free conduction electrons, silver, gold, copper and aluminium are known to display different optical properties from standard dielectrics.

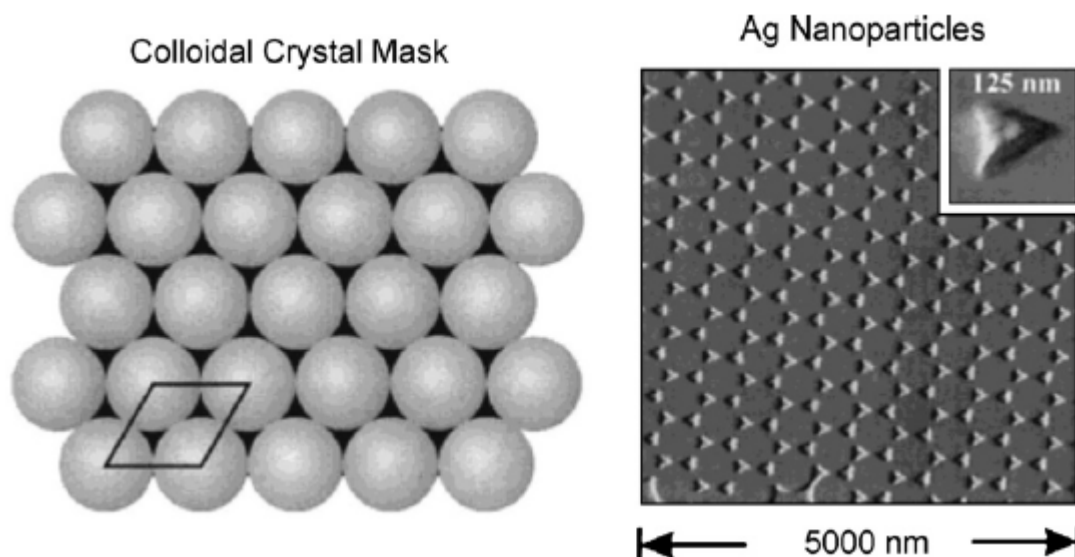


Figure 1.10: Silver nanostructures fabricated through metal deposition.⁸²

SERS can significantly amplify ($10^5 - 10^6$ ¹⁰⁸) the weak Raman signal. This coupled with improved methodologies; equipment and the possibility of tailor made substrates, gives SERS remarkable potential within many sensing fields^{103,105}.

Most materials exhibit a SERS spectrum that correlates well with the original Raman spectrum (under the same excitation conditions), particularly the distinctive Raman fingerprint peaks¹¹⁸. However, there are some considerations for interpreting SERS spectra, as it is not simply a case of obtaining an augmented Raman signal.

This is due to the complex origin of SERS spectra, the Raman spectrum of a molecule, in the gas phase, is determined by the molecule in question and the incident radiation.

Therefore its spectrum can be described by first determining the stationary vibrational energy levels of the molecule and second, defining the intensity, monochromaticity and polarisation of the incident radiation and finally establishing the interaction between the radiation field and the molecule, combining the resulting energy changes with the selection rules to constitute the molecule's spectrum¹⁰⁹.

In contrast, the basic components of the SERS spectrum also include the metallic nanostructure, thus introducing a greater level of complexity to the SERS experiment, mostly as a result of the interaction of the nanostructure with light and / or the analyte molecule itself¹⁰⁶.

As a result of this innate complexity of the SERS spectrum, the application of SERS within quantitative analytical applications has been hampered (considering its initial perception by Fleischmann *et. al.* in 1974¹¹⁰) due to the difficulty in producing reliably reproducible nanostructures¹⁰⁵. Recently research in the area has produced specifically fabricated substrates¹¹¹⁻¹¹² to eliminate this issue.

The development of simple models (spherical and spheroidal) based on the theory of an electromagnetic enhancement mechanism have also assisted with both spectral interpretation and experiment design. It should also be noted that the plasmon resonances (the major contributor to SERS enhancement) of the metallic nanoparticles are wavelength dependent, producing a non-uniform distribution of plasmon resonance, which can result in different levels of signal enhancement of the analyte's spectrum¹¹³.

1.21 SERS enhancement mechanisms

As described above Raman spectra are produced through the interaction of a photon with a polarisable analyte, and using SERS the Raman spectroscopy's sensitivity is significantly enhanced. The two enhancement mechanisms for SERS are

- Electromagnetic, which involves enhancements in the field intensity as a result of plasmon resonance excitation
- Chemical, where an enhancement in polarisability is observed due to chemical effects such as charge transfer excited states.

The intensity of Raman scattered radiation is proportional to the square of the magnitude of any electromagnetic fields incident on the analyte.

$$I_R \propto E^2 \quad 1.22$$

where I_R is the intensity of the Raman signal, and E is the total electromagnetic fields coupling with the analyte; and where

$$E = E_a + E_p \quad 1.23$$

E_a is the electromagnetic field on the analyte in the absence of any roughness features (normal Raman) and E_p is the electromagnetic field emitted from the metal nanostructure. Clearly the presence of the SERS substrate and its electromagnetic field contributes to the total magnitude of E and therefore the overall Intensity of the Raman signal.

However, as the surface electrons of the metal SERS substrate are confined to the particle, the particle's plasmon excitation is also confined to the metal nanostructure requiring that the analyte be in near proximity to the metal particle. It also follows that the analyte adsorbed between two SERS – active particles will be further enhanced than the analyte proximate to only one such particle.

Based on the proposed mechanism electromagnetic enhancements should be chemically non-selective; that is, providing the same enhancement for different analyte molecules adsorbed onto the same type of metal surface. However this is not the case, for example, N_2 and CO enhancements can differ by a factor of 200, despite possessing similar polarisabilities (adsorption orientation differences wouldn't account for the large difference in enhancement).

Therefore an additional enhancement mechanism must be in effect; chemical enhancement although less understood than the electromagnetic mechanism, this occurs as a consequence of the manner of the analyte molecule's interaction with the metal nanostructure, particularly if the molecule is adsorbed onto the substrate's surface.

The proximity of the metal adsorbate can allow electronic couplings, which produce charge – transfer intermediates that possess higher Raman scatter than the individual analyte or that the molecular orbital of the adsorbate (analyte) broaden into the conducting electrons of the metal (substrate), altering the analyte's chemistry and thus its Raman intensity ¹¹⁴.

1.22 Chemiresistor Sensors

One of the sensor disciplines in which nanotechnology is having a significant impact is in chemiresistor – based sensors, whose resistance changes in the presence of an analyte. Metal nanoparticles embedded in a matrix have proven highly effective, producing a nanocomposite that can utilise not only the nanoparticulates properties, but those of its base as well (e.g. polymers, sol gels etc.) ¹¹⁵. The use of resistive – type polymeric sensors is also of huge interest, as they are easy to prepare, inexpensive, have a fast response and also have good compatibility with modern circuit technology ¹⁰¹. *J. Riu et al* ⁶⁸, have described the development of multiple nanosensors highlighting their potential and current applications in environmental analysis. The authors describe a variety of sensor types, including localised surface plasmon resonance (LSPR) and luminescence biosensors based on monitoring how individual nanoparticle's and nanocluster's novel optical properties are affected by the surrounding environment.

Other sensing devices characterised in the work include highly sensitive, selective, and reversible electrochemical sensors established on nanocomposite materials. These sensors have the added advantage of inherent flexibility as their composition can be tailored for the analyst's needs. For example the authors describe simple resistance based sensors that incorporate nanostructures with different organic matrices for the detection of a diverse range of analytes, including ammonia and toluene.

As described above, chemiresistor sensors have many potential applications, particularly in environmental monitoring, ⁸ however the sensors can become unstable in extreme environments. The preparation of a nanocomposite can counteract the

existing weaknesses of conventional sensors by combining the strengths of nanoparticles with the composite material ¹¹⁷.

1.23 Humidity

Humidity Refers to the water vapour content in air or other gases. It can be measured in a variety of terms and units. The three more commonly used terms are

- Absolute humidity, the ratio of the mass of water vapour to the volume of air or gas, expressed in grams per cubic meter.
- Dew point, expressed in °C or °F, is the temperature and pressure at which a gas begins to condense into a liquid.
- Relative humidity (RH), expressed as a percentage, refers to the ratio of the moisture content of air compared to the saturated moisture level at the same temperature and pressure.

Relative humidity is the most useful and most often used in real world situations and therefore will be the focus of this discussion.

1.24 Commercial humidity sensors

Rapid advancements in semiconductor technology, such as thin film deposition, ion sputtering, and ceramic/silicon coatings, has resulted in the commercial production of highly accurate humidity sensors with resistance to chemicals and physical contaminants. No single sensor, however, can satisfy every application with environmental conditions dictating the choice of sensor. It is also the case that the majority of commercial RH sensors are either capacitive or resistive with each technology offering distinct advantages ¹¹⁸.

Capacitive RH sensors consist of a substrate (typically glass, ceramic, or silicon) on which a thin film of polymer or metal oxide is deposited between two conductive electrodes. The sensing surface is coated with a porous metal electrode to protect it from contamination and exposure to condensation.

The sensor's mechanism is based on the proportional changes to the dielectric constant of the sensing layer by the relative humidity of the surrounding environment. The capacitive RH sensors are widely used in industry as they are characterised by their low temperature coefficient, ability to function at elevated temperatures (up to 200 °C), full recovery from condensation, relatively short response times (30 to 60 s for a 63% RH step change), and reasonable resistance to chemical vapours

Modern capacitive sensors take advantage of semiconductor manufacturing methods to yield sensors with minimal long-term drift and hysteresis. However they can be limited by the location of the sensing element in the signal conditioning circuitry, this is due to the capacitive effect of the connecting cable with respect to the relatively small capacitance changes (0.2 – 0.5 pF per 1% RH change) of the sensor ^{119 - 121}. Resistive humidity sensors measure the change in electrical impedance (typically an inverse exponential relationship to humidity) of a hygroscopic medium such as a conductive polymer, salt, or treated substrate. Impedance is measured because the "resistive" sensor is not purely resistive, as in capacitive effects are present for resistances greater than 10 – 100 MΩ.

Resistive RH sensors consist of noble metal electrodes either deposited on a substrate, coated with a salt or conductive polymer, by either photoresist techniques or wire – wound electrodes on a plastic or glass cylinder. At elevated humidities the sensor absorbs water vapour and the ionic functional groups of the sensing coating are dissociated, resulting in an increase in its electrical conductivity.

Resistive RH sensors are also used throughout industry because of their small size, low cost, rapid response times (10 to 30 s for a 63% RH step change) and long-term stability (general life expectancy of over 5 years). Another desirable quality is that resistive humidity sensors are generally field replaceable, this is because of the sensor's interchangeability, within $\pm 2\%$ RH, which allows the electronic signal conditioning circuitry of the resistor to be calibrated at a fixed and known RH, eliminating the need for humidity calibration standards ^{122 - 124}.

Resistive RH sensors can be damaged by exposure to chemical vapours and other contaminants such as oil mist, which may lead to premature failure of the sensor. Other drawbacks of some resistive sensors are their tendency to shift values when exposed to condensation if a water-soluble coating is used and significant temperature

dependencies when installed in an environment with large ($> 10\text{ }^{\circ}\text{C}$) temperature fluctuations.

To counteract such limitations in environments where condensation occurs, resistive humidity sensors have been developed using a ceramic coating. The sensors consist of a ceramic substrate with noble metal electrodes deposited by a photoresist process and coated with a conductive polymer/ceramic binder mixture (a ceramic powder suspended in liquid form). After the surface is coated and dried, the sensors are heat treated resulting in a clear non-water-soluble thick film coating that fully recovers from exposure to condensation^{125–127}.

1.25 Humidity Sensing Materials

Humidity sensing materials can be grouped into two types; ceramics and polymers. Both possess good chemical and thermal stability, environmental adaptability and a wide range of working temperatures. Often the sensing mechanisms these materials employ are their surface electrical conductivity or the dielectric constant, which are affected by the adsorption of water vapour. Polymer-based humidity sensing materials possess some advantages in comparison to ceramics; including a higher sensitivity, decreased humidity hysteresis, low cost, flexibility and easy processability^{92–93}. For example, *J. Wang et al.*¹²⁸ describe the improved humidity sensing capability and stability seen by combining nano BaTiO_3 with acrylic resin as a nanocomposite humidity sensor. The authors determined that the electrical properties of the sensor, including resistance versus relative humidity, humidity hysteresis, response recovery time and long term stability of the composite sensor were better than that of a sensor composed just of the nano BaTiO_3 . Work by *P.G. Su and L.N. Huang*¹²⁹, comparing resistive type humidity sensors fabricated from pure polypyrrole and a TiO_2 polypyrrole nanocomposite came to the same conclusion, as sensors based on the nanocomposite showed higher sensitivity and better linearity, smaller hysteresis, faster response / recovery times and better long – term stability than the sensor without TiO_2 nanoparticles.

Similar research has led to multiple reports on chemical polymerisation and electrochemical techniques for the preparation of polymer nanocomposites for gas and humidity sensor applications^{130–132}.

1.26 Impedance Spectroscopy

Resistance is the ability of a circuit to resist the flow of current; this concept of electrical resistance is well known and is defined by Ohm's law

$$R = \frac{V}{I} \quad 1.24$$

where R is resistance in ohms, V is voltage in volts, and I is current in amperes. Ohm's law, however, is limited to one circuit element, the ideal resistor. This has several simplifying properties:

- It follows Ohm's Law at all current and voltage levels.
- Its resistance value is independent of frequency.
- AC current and voltage signals through the ideal resistor, are in phase with each other.

As many real world systems exhibit more complex behaviour it is necessary to develop the concept of impedance. Like resistance, impedance is a measure of the ability of a circuit to resist the flow of electrical current. Unlike resistance, impedance is not limited by the simplifying properties listed above^{133 - 136}.

$$Z = \frac{V_{ac}}{I_{ac}} \quad 1.25$$

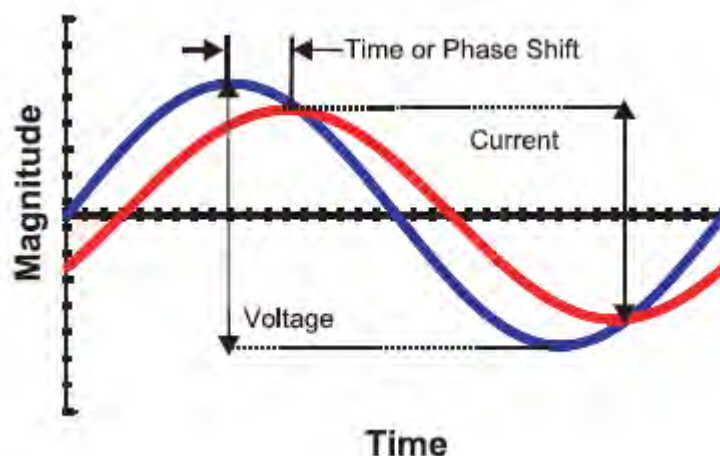


Figure 1.11. A sine wave voltage applied to an electrochemical cell and the current response as a function of time.

When a sine wave voltage applied to an electrochemical cell, for example, the current response is also a sine wave, but it is shifted in time due to the slow response of the system. This time shift can be expressed as an angle, Θ (figure 1.11).

The magnitude of the system's impedance, $|Z|$, can be determined from the ratio of the size of the voltage, and that of the current.

Impedance is expressed graphically using a Bode plot (often used to display Electrochemical Impedance Spectroscopy, EIS, data), where both the magnitude, $|Z|$, and phase, Θ , of the impedance as well as the frequency, f (in cycles per second, or Hertz), at which it was measured is reported (figure 1.12).

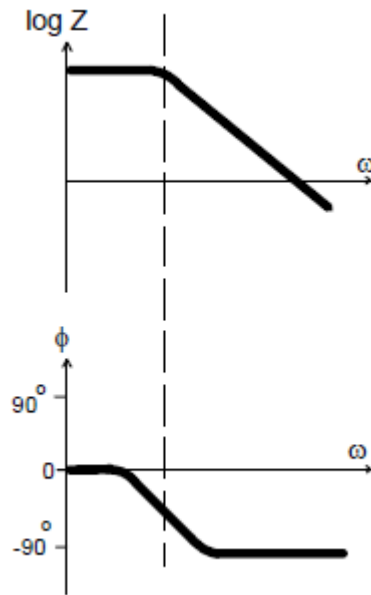


Figure 1.12: Bode Plot with One Time Constant

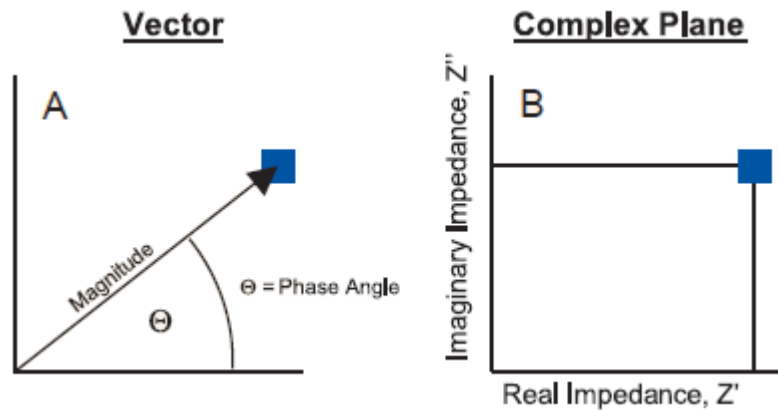


Figure 1.13: Vector representation, polar coordinates (A) and Complex Plane representation, Cartesian coordinates, (B) both specify the same point.

The $|Z|$ and Θ information from the Bode plot can also be displayed either in polar form as a vector, (figure 1.13A) the length of the vector is equal to $|Z|$ and the phase angle, Θ , is the rotation of the vector.

It is possible to express the end position of the vector in Cartesian coordinates as shown in Figure 1.13B. This means that point in the complex plane can be identified either as $(|Z|, \Theta)$ in the polar coordinates or as (X, Y) in the Cartesian coordinates.

Moreover by re – labelling the axes as Real (X axis) and Imaginary (Y axis), the point in the Complex Plane may also be expressed as a complex number (Real, Imaginary)

$$Z = X + jY \text{ where } j = \sqrt{-1} \quad 1.26$$

The “complex” or “imaginary” number (j) is a mathematical way of expressing and manipulating the impedance vector. The values of the “real” (X) and the “imaginary” parts of the impedance (Y) are as Z' and Z'' respectively. The magnitude of a complex number (or the magnitude of an impedance) can be easily calculated by

$$\sqrt{Z_{re}^2 + Z_{im}^2} = Z_{magnitude} = |Z| \quad 1.27$$

Plotting the impedance measured at a number of frequencies on the Cartesian axes, gives a Nyquist plot.

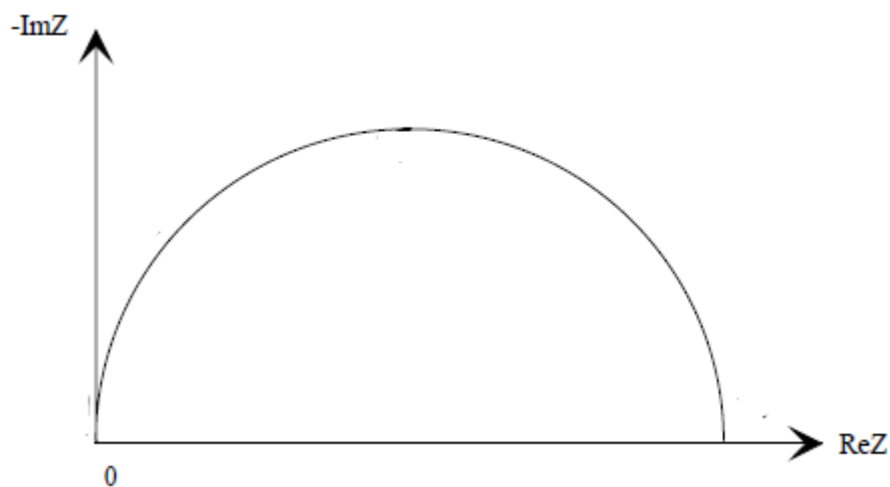


Figure 1.14. Nyquist plot magnitude and phase

Both plotting formats are used because each has its strengths and certain features that are difficult to identify in the Nyquist plot may be readily apparent in the Bode plot, and vice versa.

The Bode plot shows the frequency directly and small impedances are identifiable in the presence of large impedances. The Nyquist plot also allows individual impedances to be resolved, but the frequency is not explicitly shown. Small impedances in a Nyquist plot may be difficult to identify in the presence of large impedances.

Electrochemical Impedance Spectroscopy (EIS) is a useful technique for both the analysis and modelling of electrochemical systems, this is because electrochemical systems such as coated surfaces or corroding metals often behave like simple electronic circuits, using EIS a few simple circuit elements can be examined and modelled.

For example a simple resistor was discussed earlier in terms of Ohm's law when a sine wave voltage is applied across a resistor, the current will also be a sine wave, because the current through a resistor reacts instantaneously to any change in the potential applied across it.

The current sine wave would be in phase with the voltage sine wave meaning there would be no time lag so the phase angle of a resistor's impedance ($Z = V_{ac} / I_{ac}$) is 0° . Furthermore as the current sine wave is exactly in phase its amplitude depends only on the resistance R (in ohms) and the amplitude of the voltage sine wave. This means that the impedance of a resistor is easy to write as a complex number. Since the phase angle is always 0, the end of the "vector" always lies on the X , or real axis. The Y (imaginary) component is always zero.

$$\begin{aligned} Z_{resistor} &= Z_{re} + jZ_{im} & 1.28 \\ &= R + j0 \\ &= R \end{aligned}$$

Consequently the Bode plot for a resistor is quite simple as the impedance of a resistor is independent of frequency, the Bode magnitude plot is just a horizontal straight line.

Another simple yet useful, electronic circuit element is a capacitor; its impedance current would be out – of – phase with the voltage by 90° . As a result the sine wave voltage waveform applied results in a cosine current waveform with the current reaching a maximum when the voltage crosses through zero.

The magnitude of the current also depends on frequency. The higher the frequency, the more rapidly the voltage changes, and the higher is the voltage sine wave. Since $Z = V/I$, a larger current at higher frequencies leads to a smaller impedance therefore as the frequency approaches zero, the current also approaches zero and the

impedance, Z , becomes infinitely large. The impedance of a capacitor can be expressed as

$$\begin{aligned}Z_{capacitor} &= Z_{re} + jZ_{im} & 1.29 \\ &= 0 + j[-1/(2\pi fC)] \\ &= j[-1/(2\pi fC)]\end{aligned}$$

Because the impedance of a capacitor varies with the inverse of the frequency the Bode magnitude plot for a capacitor is a straight line with a slope of -1 and because the phase shift of a capacitor is always 90° , the Bode phase plot is a horizontal line at -90° .

Through the combination of these two simple circuit elements it is possible to model electric circuits using EIS.

1.27 Overview of Study

The development of nanotechnology has produced new opportunities for research, it is also clear that the unique properties of silver nanoparticles has resulted with them being one of the most commonly investigated in multiple scientific fields ²⁷. This work involved the synthesis of silver nanoparticles and the investigation of their usefulness in sensor based research.

Primarily the study involved chemiresistor sensors; through the preparation of a simple polymer (PVA) nanocomposite and its application as a chemiresistor gas sensor. The sensor showed promise as a humidity sensor, giving a rapid and reversible response at standard temperature and pressure, the response was selective and proportional to % RH with a range of 10% to 60% RH ¹³⁷.

The focus of the work then shifted to the inherent optical properties of silver nanoparticles, and the development of a rapid synthesis for tuneable silver colloids ¹³⁸, followed by their application in the SERS technique. Here the nanostructures displayed SERS activity whether as colloids or cast as films. This prompted further investigation of the film substrate's capabilities and the influence of external parameters on signal response. Finally, the effectiveness of the films for SERS as an analytical technique for a real world application was investigated.

1.28 References

1. Transcript available at <http://www.its.caltech.edu/~feynman/plenty.html> (May 2009)
2. Committee for the review of National Nanotechnology Initiative, Division on Engineering and Physical Sciences, National Research Council, *Small wonders, endless frontiers: A review of the National Nanotechnology Initiative*, National Academy Press, Washington DC, 2002
3. C. Drake, S. Deshpande, D. Bera, S. Seal, *International Materials Reviews*, 2007, 52, 289 – 317
4. J.H. Lee, *Sensors and Actuators, B*, 2009, 140, 319–336
5. R. Booker, E. Boysen, *Nanotechnology for Dummies*, Ch 1, pg. 11, Wiley Publishing, Inc, Indianapolis, Indiana, 2005
4. K.L. Kelly, E. Coronado, L.L. Zhao, G.C. Schatz, *Journal of Physical Chemistry B*, 2003, 107, 668 – 677
5. P.H. Buffat, J.P. Borel, *Physical Review A*, 1976, 13, 2287 – 2298
6. G. Stix, ‘Little Big Science’, *Scientific America*, Sept 2001, 32
7. S.A. Wilson, R. P.J. Jourdain, Q. Zhang, *et al. Materials Science and Engineering R: Reports*, 2007, 56, 1-129
8. I. Naydenova, R. Jallapuram, V. Toal, S. Martin, *Applied Physics Letters*, 2008, 92, DOI 031109
9. K.L. Kelly, E. Coronado, L.L. Zhao, G.C. Schatz, *Journal of Physical Chemistry B*, 2003, 107, 668 – 677
10. P.H. Buffat, J.P. Borel, *Physical Review A*, 1976, 13, 2287 – 2298
11. S. Link and M. A. El-Sayed, *Journal of physical chemistry, B*, 1999, 103, 4212
12. Q. Lu, K.J. Lee, K.B. Lee, H.T. Kim, J. Lee, N.V. Myung, Y.H. Choa, *Journal of Colloid and Interface Science*, 2010, 342, 8 – 17
13. A. Zielińska, E. Skwarek, A. Zaleska, M. Gazda, J. Hupka, *Procedia Chemistry*, 2009, 1, 1560 – 1566
14. S. Chairam, C. Poolperm, E. Somsook, *Carbohydrate Polymers*, 2009, 75, 694 – 704
15. J. Zou, Y. Xu, B. Hou, D. Wu, Y. Sun, *China Particuology*, 2007, 5, 206 – 212
16. M. Datta, *Electrochimica Acta*, 2003, 48, 2975 – 2985
17. M. Isaacson, A. Muray, M. Scheinfein, I. Adesida, E. Kratschmer, *Microelectronic Engineering*, 1984, 2, 58 – 64

18. B.H. Ryu, Y. Choi, H.S. Park, J.H. Byun, K. Kong, J.O. Lee, H. Chang, *Colloids and Surfaces A: Physicochemical and Engineering Aspects*, 2005 270-271, 345 – 351
19. R. Vaidyanathan, S. Gopalram, K. Kalishwaralal, V. Deepak, S.R.K. Pandian, S. Gurunathan, *Colloids and Surfaces B: Biointerfaces*, 2010, 75, 335 – 341
20. K. Zou, X.H. Zhang, X.F. Duan, X.M. Meng, S.K. Wu, *Journal of Crystal Growth*, 2004, 273, 285 – 291
21. Z. Yang, H. Qian, H. Chen, J.N. Anker, *Journal of Colloid and Interface Science*, 2010, 352, 285 – 291
22. X.K. Wang, L. Shao, W.L. Guo, J.G. Wang, Y.P. Zhu, C. Wang, *Ultrasonics Sonochemistry*, 2009, 16, 747 – 751
23. A.R. Shahverdi, S. Minaeian, H.R. Shahverdi, H. Jamalifar, A. Nohi, *Process Biochemistry*, 2007, 42, 919 – 923
24. K. Ni, L. Chen, G. Lu *Electrochemistry Communications*, 2008, 10, 1027 – 1030
25. L. Carbone, P. D. Cozzoli, *Nano Today*, 2010 5, 449 – 493
26. W. Zhang, X. Qiao, J. Chen, *Materials Science and Engineering: B*, 2007, 142, 1-15
27. T.M. Tolaymat, A.M. El Badawy, A. Genaidy, K.G. Scheckel, T.P. Luxton, M. Suidan, *Science of The Total Environment*, 2010, 408, 999 – 1006
28. D. H. Everett, *Basic principles of colloid science*, Cambridge, Royal Society of Chemistry, 1988
29. *Handbook of surface and colloid chemistry*, edited by K.S. Birdi, Boca Raton, Fla., CRC Press, 2003
30. R.M. Pashley, M.E. Karaman, *Applied colloid and surface chemistry*, Chichester, West Sussex, England, J. Wiley, 2004
31. K.Y. Kim, Y.T. Choi, D.J. Seo, S. B. Park, *Materials Chemistry and Physics*, 2004, 88, 377 – 382
32. C. Zhao, Q. Zhao, Q.g Zhao, J. Qiu, C. Zhu, S. Guo, *Journal of Photochemistry and Photobiology A: Chemistry*, 2007, 187, 146 – 151
33. V.R. Manikam, K.Y. Cheong, K.A. Razak, *Materials Science and Engineering: B*, 2011, doi:10.1016/j.mseb.2010.11.006
34. A.M. Schwartzberg, J.Z. Zhang, *Journal of Physical Chemistry, C*, 2008, 112, 10323 – 10337
35. W. Zhang, X. Qiao, J. Chen, *Materials Science and Engineering B*, 2007, 142, 1 – 15

36. T. Sato, R. Ruch, *stabilization of colloidal dispersion by polymer adsorption*. Marcel Dekker Inc., New York, 1980
37. M. Boström, V. Deniz, G.V. Franks, B.W. Ninham, *Advances in Colloid and Interface Science*, 2006, 123-126, 5 – 15
38. L. Boinovich, *Current Opinion in Colloid & Interface Science*, 2010, 15, 297 – 302
39. D.H. Napper, *Polymeric Stabilization of Colloidal Dispersions*. Academic Press, London, 1983
40. Y. Liang, N. Hilal, P. Langston, V. Starov, *Advances in Colloid and Interface Science*, 2007, 134-135, 151 – 166
41. P.K. Khanna, Narendra Singh, Shobhit Charan, V.V.V.S. Subbarao, R. Gokhale, U.P. Mulik, *Materials Chemistry and Physics*, 2005, 93, 117 – 121
42. S. Kundu, D. Huitink, K. Wang, H. Liang, *Journal of Colloid and Interface Science*, 2010, 344, 334 – 342
43. T. Abdul kareem, A. Anu kaliani, *Arabian Journal of Chemistry*, doi:10.1016/j.arabjc.2010.06.054
44. M. K. Temgire, S. S. Joshi, *Radiation Physics and Chemistry*, 2004, 71, 1039 – 1044
45. V.K. Sharma, R.A. Yngard, Y. Lin, *Advances in Colloid and Interface Science*, 2009, 145, 83 – 96
46. J.L. Clement and P.S. Jarrett, *Metal Based Drugs* 1994, 1, 467 – 482
47. S.L. Percival, P.G. Bowler, D. Russell, *Journal of Hospital Infection*, 2005, 60, 1 – 7
48. S. Blome-Eberwein, R.M. Johnson, S.F. Miller, D.M. Caruso, M.H. Jordan, S. Milner, E.E. Tredget, K.M. Sittig, L. Smith, *Burns*, 2010, 36, 665 – 672
49. N. Stobie, B. Duffy, J. Colreavy, P. McHale, S. J. Hinder, D. E. McCormack, *Journal of Colloid and Interface Science*, 2010, 345, 286 – 292
50. T. Pradeep, Anshup, *Thin Solid Films*, 2009, 517, 6441 – 6478
51. Y. Li, N. Koshizaki, W. Cai, *Coordination Chemistry Reviews*, 2011, 255, 357 – 373
52. J.Garcia-Torres, E. Gómez, E. Vallés, *Journal of Electroanalytical Chemistry*, 2009, 635, 63 – 68
53. M.P. Pileni, *Surface Science*, 2009, 603, 1498 – 1505

54. M. Tominaga, T. Shimazoe, M. Nagashima, I. Taniguchi, *Journal of Electroanalytical Chemistry*, 2008, 615, 51 – 61
55. A.G. Ryder, *Current Opinion in Chemical Biology*, 2005, 9, 489 – 493
56. D.G. Thompson, A. Enright, K. Faulds, W.E. Smith, D. Graham, *Analytical Chemistry*, 80, 2008, 2805 – 2810
57. S.T. Dubas, V. Pimpan, *Talanta*, 76, 2008, 29 – 33
58. S.T. Dubas, V. Pimpan, *Materials Letters*, 62, 2008, 2661 – 2663
59. T.L. Yeo, T. Sun, K.T.V. Grattan, *Sensors and Actuators A: Physical*, 2008, 144, 280 – 295
60. H. Gunzler & A. Williams, *Handbook of Analytical Techniques*, Volume 2, Chapter 28, *Chemical and Biochemical sensors*, Weinheim; Cambridge, Wiley-VCH, 2001
61. P. Hauptmann, *Sensors: principals and applications*, Munich, Carl Hanser, Hemel Hempstead, Prentice Hall, 1993
62. J. Janata, *Principles of Chemical Sensors*, Plenum Press, New York, 1989
63. I. Stanimirova, B. Walczak, D. L. Massart, V. Simeonov, C. A. Saby, E. Di Crescenzo, *Chemometrics and Intelligent Laboratory Systems*, 2004, 73, 219 – 233
64. B. Barshan, T. Aytac, C.Yuzbasioglu, *Pattern Recognition*, 2007, 40, 2607 – 2620
65. R. Huber, N. Singer, *Materials Today*, 2002, 5, 36 – 43
66. C. Gao, D. Yan, *Progress in Polymer Science*, 2004, 29, 183 – 275
67. P. Pallavicini, Y.A. Diaz-Fernandez, L. Pasotti, *Coordination Chemistry Reviews*, 2009, 253, 2226 – 2240
68. J. Riu, A. Maroto, F. Xavier Rius, *Talanta*, 2006, 69, 288 – 301
69. J. Li, J.Z. Zhang, *Coordination Chemistry Reviews*, 2009, 253, 3015 – 3041
70. H. Chik, J. M. Xu, *Materials Science and Engineering: R: Reports*, 2004, 43, 103 – 138
71. E.C. Le Ru, P.G. Etchegoin, *Principals of Surface – Enhanced Raman Spectroscopy and related plasmonic effects*, Chapter 2, Elsevier, Oxford, 2009
72. E.C. Le Ru, P.G. Etchegoin, *Principals of Surface – Enhanced Raman Spectroscopy and related plasmonic effects*, Chapter 3, Elsevier, Oxford, 2009
73. R.Aroca, *Surface-enhanced vibrational spectroscopy*, Wiley & Sons Ltd., Chichester, England, 2007, Ch. 1
74. D.M. Ledwith, A.M. Whelan and J.M. Kelly, *Journal of Materials Chemistry*, 2007, 17, 2459 – 2464

75. D. Aherne, D.M. Ledwith, M. Gara, and J.M. Kelly, *Advanced Functional Materials*, 2008, 18, 2005 – 2016
76. C.F. Bohren, D.R. Huffman, *Absorption and scattering of light by small particles*, New York; Chichester: Wiley, 1983
77. A. Slistan-Grijalva, R. Herrera-Urbina, J.F. Rivas-Silva, M. Avalos-Borja, F.F. Castillon-Barraza, A. Posada-Amarillas, *Physica E*, 2005, 27, 104 – 112
78. S. Link, M.A. El – Sayed, *International Reviews in Physical Chemistry*, 2000, 19, 409 – 453
79. X. He, X. Zhao, Y. Chen, J. Feng, *Materials Characterisation*, 2008, 59, 380 – 384
80. G. Si, W. Shi, K. Li, Z. Ma, *Colloids and Surfaces A*, 2011, 380, 257 – 260
81. Y. Deng, Y. Sun, P. Wang, D. Zhang, X. Jiao, H. Ming, Q. Zhang, Y. Jiao, X. Sun, *Current Applied Physics*, 2008, 8, 13 – 17
82. M.K. Fan, G.F.S. Andrade, A.G. Brolo, *Analytica Chimica Acta*, 2011, 693, 7 – 25
83. R. Picorel, G. Chumanov, T.M. Cotton, G. Montoya, S. Toon, M. Seibert, *Journal of Physical Chemistry*, 1994, 98, 6017
84. T. Vo-Dinh, K. Houck, D.L. Stokes, *Analytical Chemistry*, 1994, 66, 3379
85. N.R. Isola, D.L. Stokes, T. Vo-Dinh, *Analytical Chemistry*, 1998, 70, 1352
86. Vo-Dinh, D.L. Stokes, G.D. Griffin, M. Volkan, U.J. Kim, M.I. Simon, *Journal of Raman Spectroscopy*, 1999, 30, 785
87. J.D. Speed, R.P. Johnson, J.T. Hugall, N.N. Lal, P.N. Bartlett, J.J. Baumberg, A.E. Russell, *Chemical Communications*, 2011, 47, 6335
88. S. Mahajan, J. Richardson, T. Brown, P.N. Bartlett, *Journal of the American Chemical Society*, 2008, 130, 15589
89. Y.H. Lee, S. Farquharson, P. Rainey, *Chemical Microsensors and Applications II, Proceedings of the Society of Photo-Optical Instrumentation Engineers*, Spie, Ed. S. Buttgenbach, 1999, 76
90. D.L. Stokes, J.P. Alarie, V. Ananthanarayanan, T. Vo-Dinh, *Environmental Monitoring and Remediation Technologies, Proceedings of the Society of Photo-Optical Instrumentation Engineers*, Spie, Eds T. VoDinh, R.L. Spellicy, 1999, 647
91. L.G. Olson, Y.S. Lo, T.P. Beebe, J.M. Harris, *Analytical Chemistry*, 2001, 73, 4268

92. J. Shi, Y. Zhu, X. Zhang, W.R.G. Baeyens, A.M Garcia-Campana, *Trends in Analytical Chemistry*, 2004, 23, 351 – 360
93. http://www.shsu.edu/~chm_tgc/chemilumdir/JABLONSKI.html
94. B.J. Bulkin, *Analytical Raman Spectroscopy*, J.G. Grasselli, B.J. Bulkin (Eds.), New York, Wiley, 1991, Ch. 1
95. F.A. Miller, D.W. Mayo, R.W. Hannah, *Course notes on the interpretation of infrared and Raman spectra*, Hoboken, N.J., Wiley-Interscience, 2004.
96. I.R. Lewis, H.G.M. Edwards, *Handbook of Raman spectroscopy from the research laboratory to the process line*, New York, Marcel Dekker, 2001.
97. R. Sanci, M. Volkan, *Sensors and Actuators B*, 2009, 139, 150 – 155
98. A. Champion, P. Kambhampati, *Chemical Society Reviews*, 1998, 27, 241 – 250
99. D.L Stokes, T. Vo-Dinh, *Sensors and Actuators B*, 2000, 69, 28 – 36
100. C.J. Addison, A.G. Brolo, *Langmuir*, 2006, 22, 8696 – 8702
101. D.I. Ellis, R. Goodacre, *Analyst*, 2006, 131, 875 – 885
102. S. Feng, R. Chen, J. Lin, J. Pan, G. Chen, Y. Li, M. Cheng, Z. Huang, J. Chen, H. Zeng, *Biosensors and Bioelectronics*, 2010, 25, 2414 – 2419
103. M.E. Abdelsalam, S. Mahajan, P.N. Bartlett, J.J. Baumberg, A.E. Russell, *Journal of the American Chemical Society*, 2007, 129, 7399 – 7406
104. T. Vo-Dinh, *Trends in Analytical Chemistry*, 1998, 17, 557 – 582
105. W.E. Smith, *Chemical Society Reviews*, 2008, 37, 955 – 964
106. W.C. Lin, M.C. Yang, *Macromolecular Rapid Communications*, 2005, 26, 1942 – 1974
107. G.A. Ozin, A.C. Arsenault, L. Cademartiri, *Nanochemistry a chemical approach to nanomaterials*, Cambridge, UK, Royal Society of Chemistry, 2005, Ch. 5
108. M.G. Albrecht, J.A. Creighton *Journal of the American Chemical Society*, 1997, 99, 5215 – 5217
109. D.A. Long, *The Raman Effect*, New York, Chichester, Wiley, 2001
110. M. Fleischmann, P.J. Hendra, A.J. McQuillan, *Chemical Physics Letters*, 1974, 26, 163 – 166
111. A. Sánchez-Iglesias, P. Aldeanueva-Potel, W. Ni, J. Pérez-Juste, I. Pastoriza-Santos, R.A. Alvarez-Puebla, B.N. Mbenkum, L.M. Liz-Marzán, *Nano Today*, 2010, 5, 21 – 27
112. M.E. Abdelsalam, P.N. Bartlett, J.J. Baumberg, S. Cintra, T.A. Kelf, A.E. Russell, *Electrochemistry Communications*, 2005, 7, 740 – 744

113. E.C. Le Ru, P.G. Etchegoin, *Principals of Surface – Enhanced Raman Spectroscopy and related plasmonic effects*, Chapter 1, Elsevier, Oxford, 2009
114. A. Mathew, P. R. Sajanlal, T. Pradeep, *Journal of Crystal Growth*, 2010, 312, 587 – 594
115. V.K. Khanna, *Defence Science Journal*, 2008, 58, 608 – 616
116. Y. Li, L. Hong, Y. Chen, H. Wang, X. Lu, M. Yang, *Sensors and Actuators, B*, 2007, 123, 554 – 559
117. S.V. Ahir, Y.Y. Huang, E.M. Terentjev, *Polymer*, 2008, 49, 3841 – 3854
118. Z. Chen and C. Lu, *Sensor Letters* 3, 2005 274–295
119. B.M. Kulwicki, *Journal of the American Ceramic Society*, 1991, 74, 697 – 708
120. Z.M. Rittersma, *Sensors and Actuators A*, 2002, 92, 196 – 210
121. N. Yamazoe, Y. Shimizu, *Sensors and Actuators*, 1986, 10, 379 – 398
122. P.R. Story, D.W. Galipeau R.D. Mileham, *Sensors and Actuators, B*, 1995, 25, 681 – 685
123. Yoshiro Sakai, *Sensors and Actuators, B*, 1993, 13, 82 – 85
124. C.Y. Lee, G.B. Lee, *Sensor Letters*, 2005, 3, 1 – 15
125. Z. Yan, M.J. Sousa-Gallagher; F.A.R Oliveira, *Journal of Food Engineering*, 2008, 84, 359 – 367
126. Singh, R.P. Shelf life evaluation of foods, Man, C.M.D.; Jones, A.A. Ed.s, Blackie Academic & Professional, Glasgow, 1992, 3 – 24
127. E.L.J. Goossens, A.J.J. van der Zanden, W.H. van der Spoel, *Progress in Organic Coatings*, 2004, 49, 270 – 274
128. J. Wang, Q. Lin, R. Zhou, B. Xu, *Sensors and Actuators B*, 2002, 81, 248 – 253
129. P.G. Su, L.N. Huang, *Sensors and Actuators B*, 2007, 123, 501 – 507
130. B.M. Novak, *Advanced Materials*, 1993, 5, 422 – 433
131. F. Selampinar, L. Toppare, U. Akbulut, T. Yalcin and S. Süzer, *Synthetic Metals*, 1998, 68,109 – 116
132. K. Suri, S. Annapoorni, A.K. Sarkar and R.P. Tandon, *Sensors and Actuators B*, 2002, 81, 277 – 282
133. http://www.gamry.com/App_Notes/EchemImpedanceSpecs.htm
134. http://www.gamry.com/App_Notes/EIS_Primer/Basics_Of_%20EIS.pdf
135. A. Lasia, *Electrochemical Impedance Spectroscopy and Its Applications, Modern Aspects of Electrochemistry*, Kluwer Academic/Plenum Publishers, New York, 1999, 32, 143-248

- 136.** J.R. Macdonald, *Annals of Biomedical Engineering*, 1992, 20, 289 – 305
- 137.** A.C. Power, A.J. Betts, J.F. Cassidy, *Analyst*, 2010, 135, 1645 – 1652
- 138.** A.C. Power, A.J. Betts, J.F. Cassidy, *Analyst*, 2011, DOI: 10.1039/C1AN15250E

2. Synthesis and Characterisation of Silver Nanoparticles

2.1 Introduction

Metallic nanoparticles may be synthesised by a variety of methods, which can produce particles of multiple morphologies for a diverse range of applications ¹⁻⁵. The major route reported in the literature is by the production of colloidal dispersions using chemical – reduction methods. This method of metallic nano synthesis, long established ⁶, which classically involves the reduction of the metal by chemical means, is very popular due to the relative ease of production of nanomaterials. The process' advantages being, mild reaction conditions, low energy consumption, and simple separation procedures, coupled with high yields and relatively short reaction times ⁷.

General methods of colloid synthesis like the Lee – Meisel method ⁸ are uncomplicated and hence popular modes of producing silver colloids. In such processes, initially, solutes are formed to yield a supersaturated solution, leading to nucleation. The formed nuclei may further grow by a diffusive mechanism. The resulting primary particles aggregate to form secondary particles. This latter process is sometimes facilitated by changes in the chemical conditions in the system: the ionic strength may increase, or the pH may change, causing the surface potential to approach the isoelectric point. Formation of the final (secondary) particles, of narrow size distribution, is a diffusion-controlled aggregation process, proceeding via the addition-polymerization type growth by irreversible capture of primary particles by the aggregates.

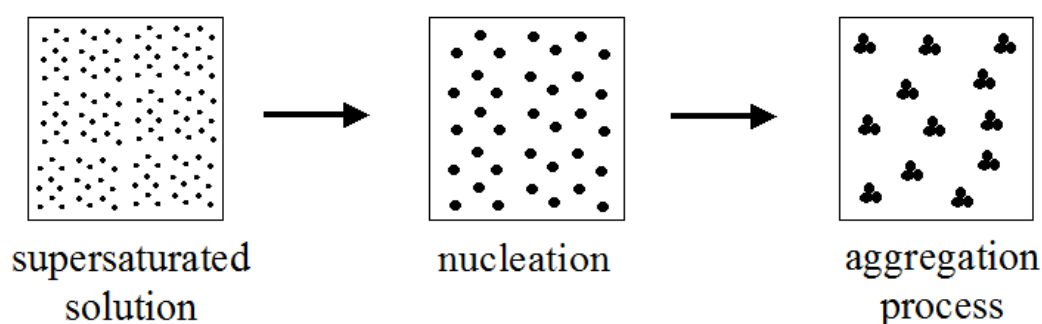


Figure 2.1: Chemical colloid synthesis

The final morphology of the nanoparticles is mostly determined by experimental conditions such as, the reducing and stabilising agents ⁷. It follows that adjustments to

the fabrication technique can give significant changes to the nanoparticles morphology, for example using citrate as the reducing agent requires additional energy (e.g. increased temperature) to produce a colloid whereas sodium borohydride readily reduces the silver ions in a solution; this is also true for the choice and concentration of stabilising agent used for instance, smaller particles are obtained by increasing the stabiliser concentration⁹⁻¹⁰.

Moreover as the potential applications of metallic nanoparticles continue to increase, current industry needs now demands quicker, simpler, greener, more cost effective, robust and reliable means of nanomaterial production. The demand for customised nanostructures is application driven; due to the novel features exhibited by silver nanomaterials that are dictated by the particle's structure.

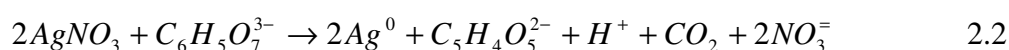
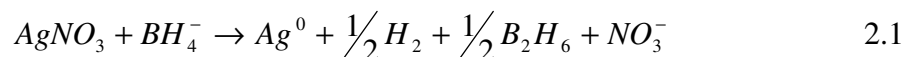
This is highlighted in the work of *J.M. Kelly et al.*¹¹⁻¹² where the colour and hence plasmonic properties of silver nanostructures are process directed. The authors outline a two step synthesis process where the basis from which the subsequent coloured colloids are grown. A seed solution is produced through; the chemical reduction of a silver salt (AgNO_3) by sodium borohydride while being stabilised by citrate in the presence of polymer (poly vinyl pyrrolidone, PVP or poly (sodium styrene sulphonate), PSSS) which further stabilises the nanostructures while simultaneously directing the particles morphologies. The growth process involves the addition of the seed solution to set volumes of the polymer and citrate stabilisers, silver salt and ascorbic acid. The colour change was controlled by the nanostructure's size which, in turn is determined by either the concentration of citrate¹¹ or the seed itself¹². The authors aim to capitalise on the unique and controlled optical properties of these silver nanostructures through their integration with spectrochemical analysis techniques such as surface enhanced Raman spectroscopy SERS (discussed later in chapters 4 – 6).

The development of composite materials is another area of interest as researchers attempt to exploit nanostructure's distinctive features by coupling them with other materials in nanocomposites. This is particularly evident with the development of nanoparticle – polymer composite sensing coatings, such as nanocomposite gas sensors (see chapter 3). These sensors are often resistance based and their mechanism of action is dependent on the conductivity of the composite coating. The composite is generally made up of polymer protected metallic nanostructures, with the organic compound in place to prevent aggregation. The particles presence alters the dielectric

constant of the polymer medium, as electric conduction between the metal particles is possible, thus establishing a set resistivity of the nanocomposite layer/coating. The introduction of a target analyte to the system may be monitored by a change in the property of the polymer, with the absorption of the vapour swelling the polymer and increasing the distance between the conducting metallic nanoparticles¹³⁻¹⁵. This and similar sensing nanocomposite mechanisms are dependent on the consistent fabrication of nanoparticles with uniform features and hence properties.

In this work silver nanoparticles were synthesised by a chemical reduction process in order to produce aqueous colloidal dispersions. The synthesis method was specific to the nanostructures intended application. Therefore two general methods were utilised, a one step/pot synthesis (nanocomposite with high Ag load and uniform particles) and a heterogeneous nucleation (nanoparticles with tuneable optical properties). In both cases the resulting colloids were then characterised by a combination of UV-Vis spectroscopy, dynamic light scattering, X-Ray diffraction and transmission electron microscopy.

Tolaymat² reported in an extensive review (section 1.8) that the most popular synthesis processes involved the chemical reduction of silver nitrate by either sodium borohydride or sodium citrate.



It should be noted however, that throughout the literature the ratio between Ag^+ and BH_4^- is not quantified. Rather it is stated that BH_4^- was added in excess, as BH_4^- is a strong reducing agent it often reduces water in a simultaneous competing reaction and thus its effectiveness is diminished. However excessive addition of BH_4^- can result in unwanted aggregation of the nanoparticles, and limit synthesis control. Therefore Job's method was conducted to confirm the stoichiometry of the reaction.

“Job's method or the method of continuous variation, is a simple and effective approach to the determination of chemical reaction stoichiometry and is based on the following principle: *if a series of solutions is prepared, each containing the same total*

number of moles of A and B, but a different ratio, R, of moles B to moles A, the maximum amount of product, D, is obtained in the solution in which R = k (the stoichiometric ratio)”⁵.

2.2 Experimental

2.2.1 Reagents

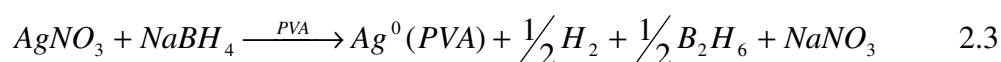
Silver nitrate (purum p.a. > 99.0%), sodium borohydride (reagent Plus 99%) polyvinyl alcohol (PVA), (99 + % hydrolyzed, typical M.W. 89000-98000 gmol⁻¹), tri-sodium citrate (TSC), (purum p.a., ≥ 99.0%) and hydrazine (reagent grade, N₂H₄) were all purchased from Sigma Aldrich and used as received without further purification.

2.2.2 Apparatus

Characterisation of the silver nanoparticles involved several techniques including UV-Vis absorption spectroscopy and dynamic light scattering (DLS), which were conducted using a Perkin Elmer Lambda 900 Spectrometer and a Malvern nano series Zetasizer, respectively. Transmission Electron Microscope (TEM or STEM) images were captured with a JEOL, 100CX Transmission Electron Microscope or a Hitachi SU 6600 FESEM and X-Ray diffraction (XRD) analysis was conducted using a Siemens Diffractometer, Model D500.

2.3 Silver nanocomposite / colloid synthesis

In the nanocomposite preparation, the silver nanoparticles were synthesised by chemical reduction of silver nitrate (AgNO₃) with sodium borohydride (NaBH₄) in an aqueous medium with PVA as the capping (stabilising) agent. The role of PVA as a capping agent is well-documented¹⁶, and it was observed that, in this case, without the presence of the PVA, the stability of the colloids was drastically reduced with metallic silver formed due to aggregation of nanoparticles. PVA has been widely used for polymer nanocomposites due to its water solubility allowing a simple ‘green’ water based synthesis¹⁷.



2.3.1 Silver nanocomposite / colloid recipe

The overall aim of this portion of the study is to utilise the prepared nanoparticles, within a composite coating for chemical (in the form of a gas) sensing – detailed in chapter 3. As explained previously optimisation of the colloidal recipe was necessary to ensure the nanoparticles are reasonably monodisperse and have a nanoparticle to monomer volume ratio of approximately 1:1, ^{14 - 15}. To do so the relative volume of the polymer to silver was determined using the simple “marbles in a box” model.

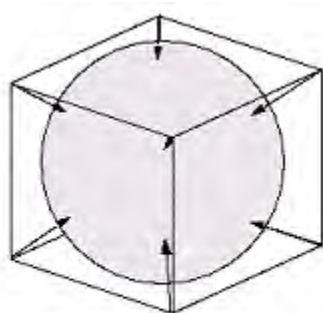


Figure 2.2: Marble in a box

$$\text{Volume of Cube: } L^3$$

$$\text{Volume of Sphere: } \frac{4}{3} \pi r^3$$

$$r = L/2$$

$$\Rightarrow \text{Volume of Sphere: } \frac{4}{3} \pi (L/2)^3$$

$$4.1762 (L^3/8)$$

$$0.52 L^3$$

\Rightarrow Sphere occupies ~ 52% of the cubes volume.

Basing this on a colloid of total volume 10 cm^3 ,

Volume of Ag in the colloid was determined as,

0.5 cm^3 of 1 M AgNO_3 was present in each colloid,

Atomic weight of AgNO_3 : 169.67 g/dm^3

Atomic weight of Ag: 107.90 g/dm^3

\Rightarrow In 0.5 cm^3 of 1 M AgNO_3 there is $53.92 \times 10^{-3} \text{ g}$ of Ag

Density of Ag: 10.50 g/cm^3

\Rightarrow Volume of silver in colloid and resulting film: $53.92 \times 10^{-3} / 10.5 = 5.14 \times 10^{-3} \text{ cm}^3$

= 52% of cubes volume.

\Rightarrow Volume of polymer (PVA) required = $(5.14 \times 10^{-3} / 52) \times 48 = 4.74 \times 10^{-3} \text{ cm}^3$

\Rightarrow Mass of PVA required = Volume x Density = $4.74 \times 10^{-3} \text{ cm}^3 \times 1.2690 \text{ g/cm}^3$

= $6.02 \times 10^{-3} \text{ g}$

Using 1% PVA solution $\Rightarrow 1 \text{ g} / 100 \text{ cm}^3 \Rightarrow 0.0100 \text{ g/cm}^3$

\Rightarrow Volume of 1% PVA required = $6.02 \times 10^{-3} \text{ g} / 0.0100 \text{ g/cm}^3 = 0.602 \text{ cm}^3$

This recipe ensured that colloids were of high Ag concentration (~ 5000 ppm). A 1 Ag : 1 PVA monomer was prepared. Experimentation proved that best results were observed where the reagents were kept at low temperatures ($\leq 4 \text{ }^\circ\text{C}$ – on ice) during

synthesis. Characterisation of the silver nanoparticles was then conducted to confirm their uniformity.

2.3.2 High load silver nanocomposite / colloid preparation

1 M AgNO_3 (0.5 cm^3) and 1% PVA (0.66 cm^3) were mixed together with deionised water (Millipore, 2.84 cm^3) in a beaker (50 cm^3) and placed in an ice bath with constant agitation. To this cold ($\leq 4 \text{ }^\circ\text{C}$) 0.001 M NaBH_4 (6 cm^3) was added dropwise, producing a dark brown colloid.

2.4 High load silver nanocomposite colloid characterisation

2.4.1 UV-Vis analysis – Perkin Elmer, Lambda 900 Spectrometer

The absorption spectrum of the colloid, shown in Figure 2.3, indicates the production of the nanoparticles where the presence of a plasmon absorption band at $\sim 400 \text{ nm}$ is characteristic of silver nanoparticles¹⁸.

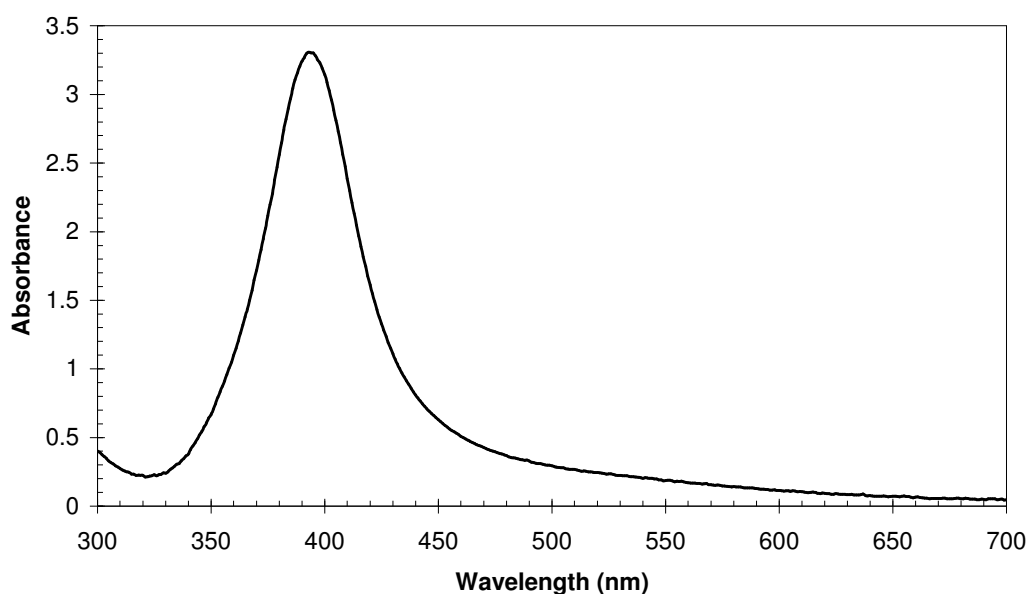


Figure 2.3: UV-Vis spectrum of stable aqueous colloidal Ag polymer mixture, with λ max of 391 nm. $[\text{Ag}^+] = 1\text{M}$ (0.5cm^3), $[\text{PVA}] = 1\%$ wt/wt (0.66 cm^3), $[\text{NaBH}_4] = 0.1\text{M}$ (6cm^3) diluted to 10cm^3 and maintained at a low temperature.

The spectrum illustrated in figure 2.3 displays the characteristic Surface Plasmon Resonance (SPR) of silver nanoparticles, commonly seen in the literature^{19–21}.

2.4.2 Job's Method

The stoichiometric ratio of Ag^+ to BH_4^- in the PVA stabilised colloids was determined using Jobs method²². A series of solutions was prepared, each containing the same total number of moles of Ag^+ and BH_4^- , but utilising different ratios. The solution with the maximum amount of product (nanoparticles) yields the stoichiometric ratio¹⁹. The maximum absorbance at 400nm for the range of solutions prepared was observed in the solution, which corresponded to a ratio of 1:1 for Ag^+ and BH_4^- as can be seen in figure 2.4.

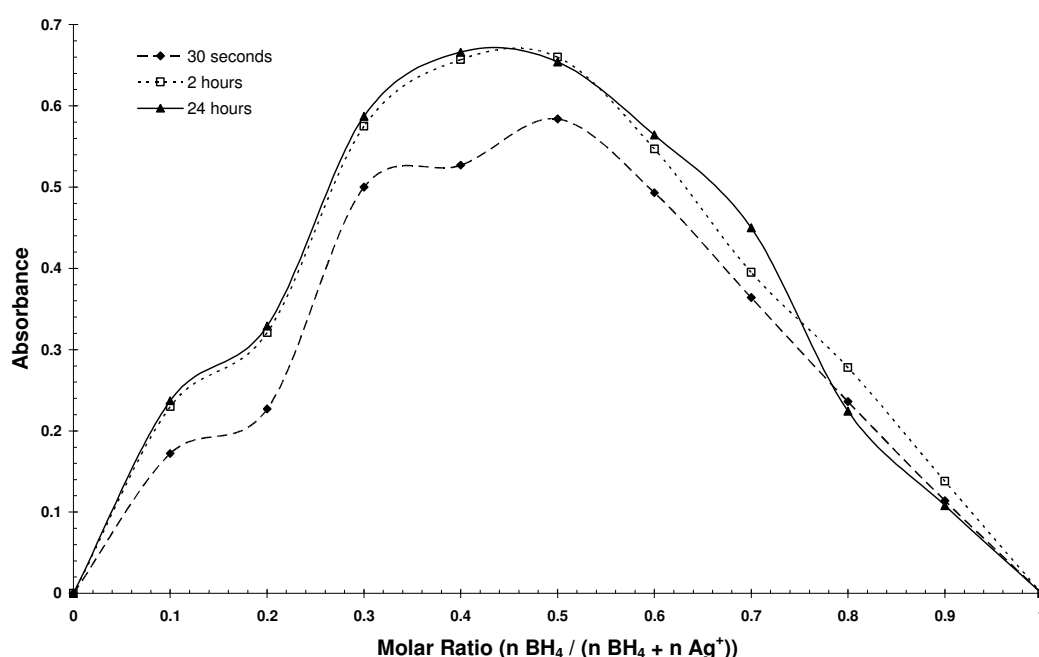


Figure 2.4: Graphical representation of the findings of Jobs method analysis, stoichiometry of AgNO_3 and NaBH_4 shown to be approximately 1:1

2.4.3 Dynamic light scattering, DLS – Malvern nano series Zetasizer

DLS, shown in Figure 2.5a, confirmed the production of particles ranging in size between about 8 nm – 38 nm, with an average diameter of 21 – 22 nm

Size analysis by DLS utilises the Brownian motion that particles, emulsions and molecules in suspension undergo as a result of bombardment by solvent molecules. If the particles are illuminated with a laser, the intensity of the scattered light fluctuates at a rate that is dependent upon the size of the particles as smaller particles are “hit” more frequently by the solvent molecules and move more rapidly. Analysis of these

intensity fluctuations yields the velocity of the Brownian motion and hence the particle size using the Stokes-Einstein relationship²³.

$$D = \frac{k_B T}{6\pi\eta r} \quad 2.4$$

Where D is the diffusion constant (m^2s^{-1}), k_B is Boltzmann's constant (JK^{-1}), T is the absolute temperature (K), η is the viscosity of the solvent ($\text{kgm}^{-1}\text{s}^{-1}$) and r is the particle radius (m). It should be noted that this technique does assume that the particles analysed are spherical.

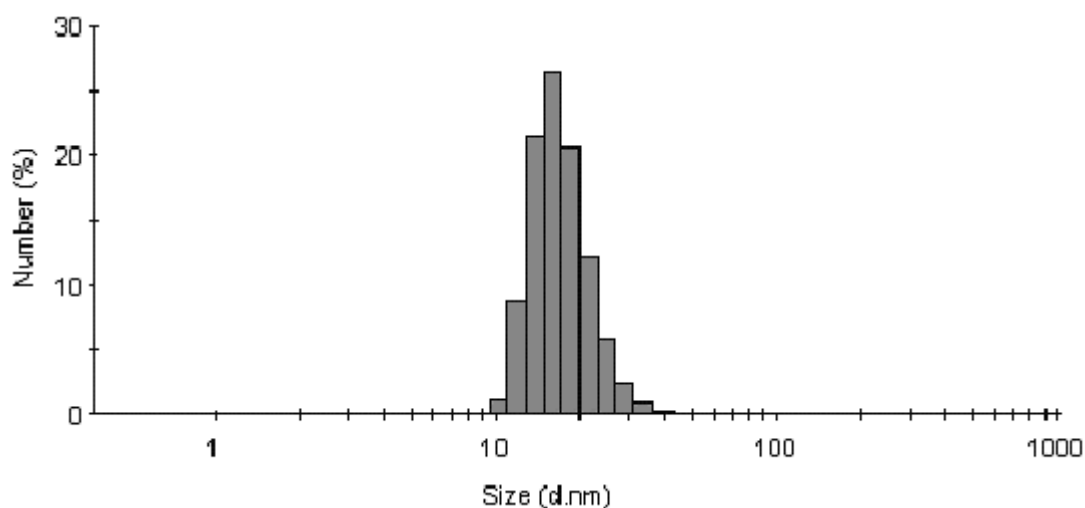


Figure 2.5a: Distribution of particle diameters within the Ag PVA colloid determined by DLS. This sample was prepared in an identical manner to that in figure 2.3.

2.4.3.1 Zeta potential

As described in section 1.6, zeta potential is a good indicator of colloidal stability. Figure 2.5b shows the zeta potential distribution for the aqueous colloid, with a zeta potential of - 43.4 mV the colloid can be considered sufficiently stable.

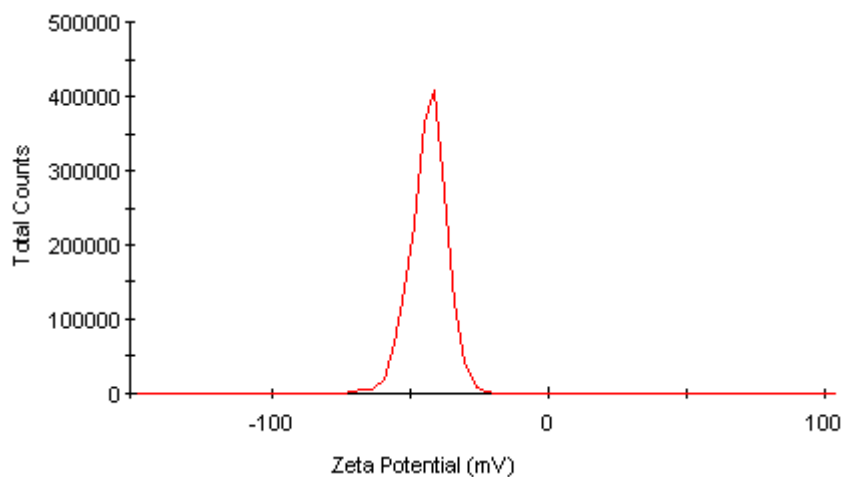


Figure 2.5b Zeta potential distribution of the aqueous based Ag PVA colloid. This sample was prepared in an identical manner to that in figure 2.3.

2.4.4 Transmission electron microscopy, TEM – JEOL, 100CX Transmission Electron Microscope

Using TEM, an image of the nanoparticles, (Figure 2.6a) was obtained arising from the interaction of the composite and the beam of electrons transmitted through it. Before analysis, the colloidal sample (prepared in the same manner as Figure 2.3) was diluted in methanol and sonicated for 30 mins, before being cast onto the TEM grid (Agar scientific, formvar/carbon 200 mesh (Cu)) by drop coating. The average diameter of the nanoparticles was determined to be in the range of 21 – 22 nm, using ImageJ software²⁴ which is in good agreement with the DLS result. Figure 2.6b gives a breakdown of the diameters determined from a sample group of 250 nanostructures.

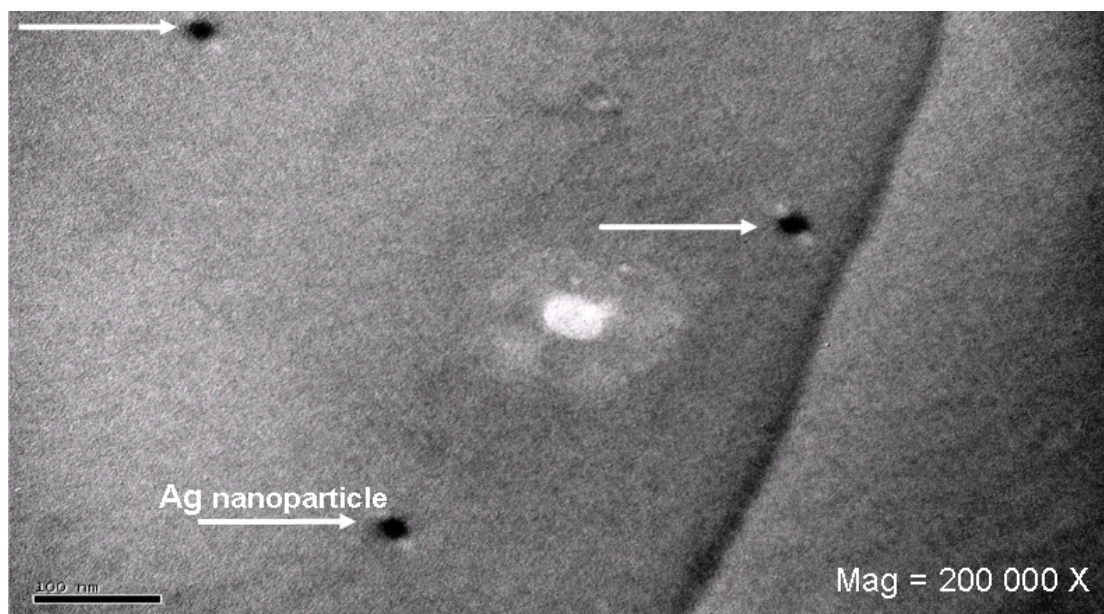


Figure 2.6a. TEM image of silver nanoparticles stabilised with PVA. Colloidal dispersion was prepared as in Figure 2.3 and then diluted by a factor of 10 with methanol. The average diameter of nanoparticles were 21 – 22 nm, was determined using Image J.

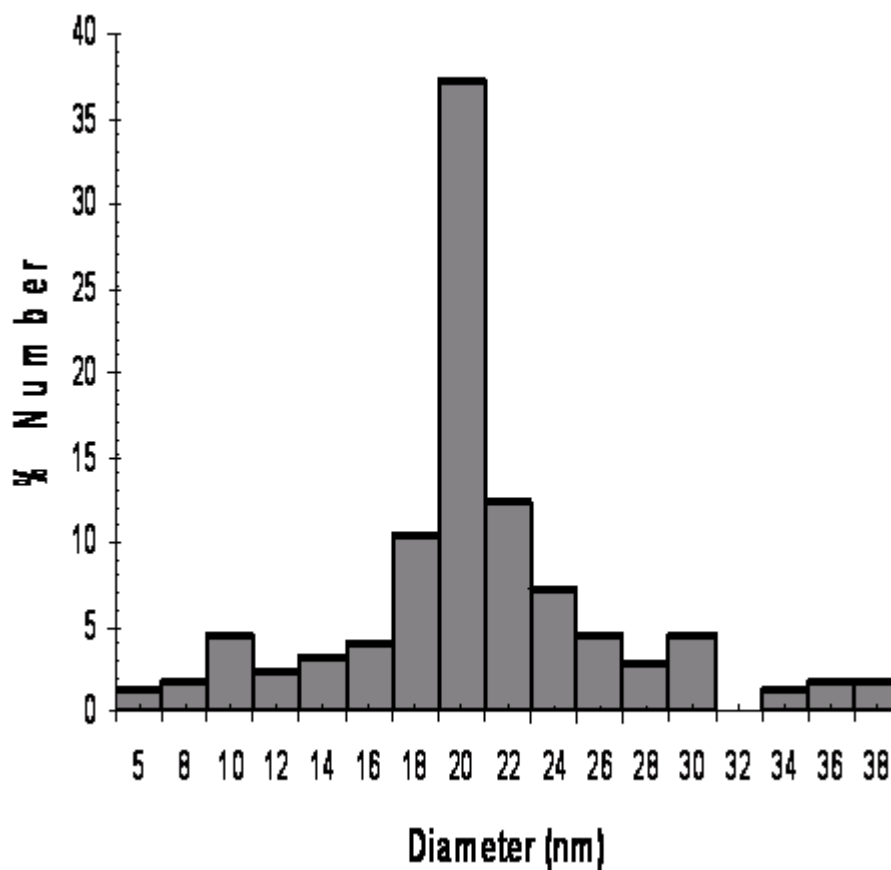


Figure 2.6b. Distribution of diameters of silver nanoparticles for 250 TEM measurements analysed with ImageJ.

2.4.5 X-Ray Diffraction, XRD – Siemens Diffractometer, Model D500

X-ray diffraction (XRD) analysis was conducted on the nanocomposite after it was cast onto a glass substrate. A number of strong Bragg reflections were observed which correspond to the (111 - $\sim 39^\circ$), (200 - $\sim 45^\circ$), (220 - $\sim 66^\circ$), (311 - $\sim 79^\circ$) reflections of face centred cubic silver^{25 - 28}, figure 2.7, indicating that the silver nanoparticles within the coating are crystalline. It should be noted that the peak at $\sim 48^\circ$ can be attributed to the presence of residual sodium²⁹ arising from the synthesis process.

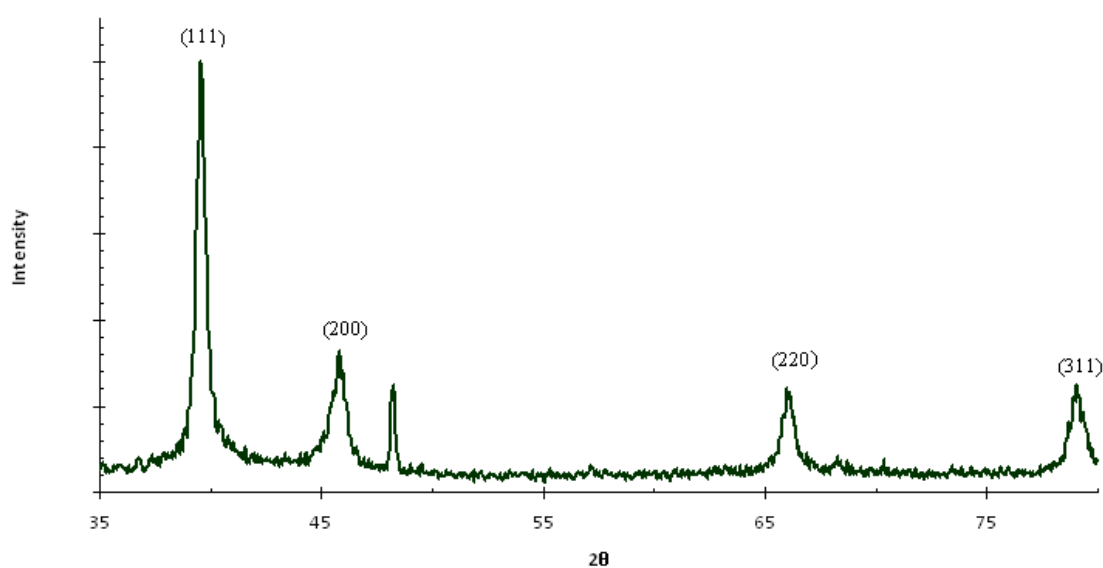


Figure 2.7: XRD pattern recorded from a drop-coated film of nanocomposite on glass substrate.

2.4.5.1 Scherrer equation

In XRD a perfect crystal would extend in all directions to infinity, therefore no crystal is perfect due to its limited size. Such a deviation from perfect crystallinity leads to the broadening of the diffraction peaks (Bragg reflections). This type of peak broadening is negligible when the crystallite sizes are larger than 200 nm, however it may be used to correlate the size of nanoparticles³⁰.

$$\tau = \frac{K\lambda}{\beta \cos \theta} \quad 2.5$$

where K is the shape factor a dimensionless shape factor has a typically about 0.9 (assumes that nanoparticles are spherical), λ is the x-ray wavelength, β is the line

broadening at half the maximum intensity (FWHM) in radians, θ is the Bragg angle and τ is the mean size of the ordered (crystalline) domains. In this case again with the assumption that the nanoparticles were spherical it was determined that the nanostructures had a diameter of the order of 21 – 22 nm.

2.5.1 Colloids with tuneable optical properties

Another series of silver colloids were prepared by heterogeneous nucleation^{19 – 20}. First a seed solution was prepared by the chemical reduction of AgNO_3 with NaBH_4 in the presence of a stabiliser and capping agent, polyvinyl alcohol (PVA)¹⁷. The seed solution was then added to a mixture of tri sodium citrate (TSC) and hydrazine (H_4N_2), and agitated to produce a homogeneous ‘growth’ solution. To this, set volumes of AgNO_3 were added, producing the different colloids by crystal growth. The different volumes of excess AgNO_3 that were added to the growth solution determined the morphology, and therefore the colour, of the nanoparticles in the solution.



Figure 2.8: Colloids of tuneable optical properties.

2.5.2.1 ‘Seed’ production

0.001 M AgNO_3 (2 cm^3) and 1% PVA (2 cm^3) were mixed together in a beaker (50 cm^3), to this **cold** ($\leq 4^\circ\text{C}$) 0.001 M NaBH_4 (2 cm^3) was added dropwise, producing the ‘seed’ solution, a golden yellow colloid.

2.5.2.2 Preparation of coloured colloids

In a beaker (250 cm^3) 1% PVA (1 cm^3), the ‘seed’ solution (1 cm^3), 0.1 M TSC (3 cm^3) and 0.1 M H_4N_2 (5 cm^3) were mixed producing a pale green solution. To this, set

volumes of 0.001M Silver Nitrate were added to produce the appropriate colloid, see table 2.1

0.001 m AgNO₃ (cm³)	Colour
0.40	Yellow
1.00	Orange
1.30	Red
2.50	Purple
6.00	Blue
20.00	Green

Table 2.1: Summary of volumes of 0.001 M AgNO₃ and the resulting colloids.

2.5.2.3 UV-Vis analysis – Perkin Elmer, Lambda 900 Spectrometer

The absorption spectrum of the ‘seed’ colloid, shown in Figure 2.9, again indicates the production of the nanoparticles with the presence of a characteristic plasmon absorption band¹⁸.

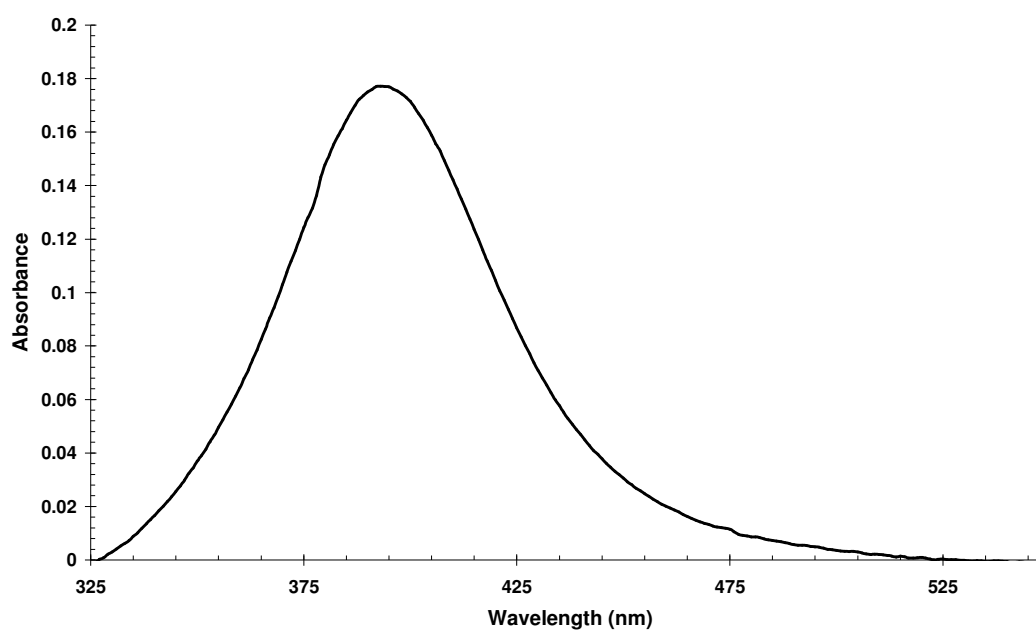


Figure 2.9: UV-Vis spectrum of stable aqueous colloidal Ag seed solution, with $\lambda_{\text{max}} = 393 \text{ nm}$. $[\text{Ag}^+] = 0.001\text{M}$ (2.0 cm^3), $[\text{PVA}] = 1\% \text{ wt/wt}$ (2.0 cm^3), $[\text{NaBH}_4] = 0.001\text{M}$ (2.0 cm^3), with a total volume of 6cm^3 .

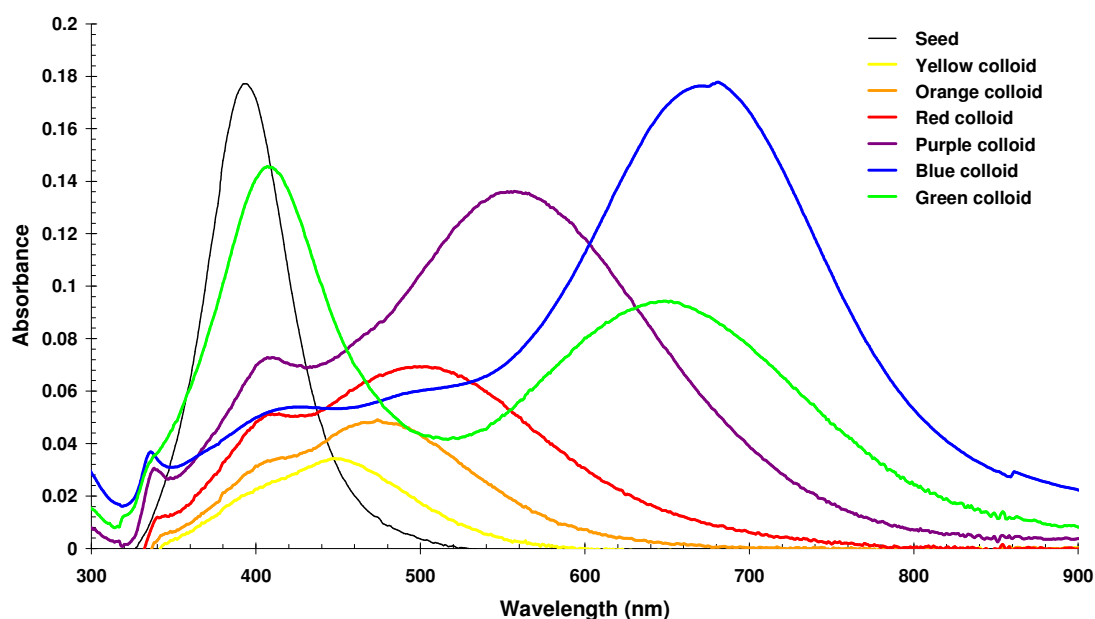


Figure 2.10: UV-Vis spectra of aqueous coloured Ag colloids. General make up of colloids [PVA] = 1% wt/wt (1.0 cm³), seed solution (1.0 cm³), [TSC] = 0.1M (3.0 cm³), [H₄N₂] = 0.001M (5.0 cm³) + [AgNO₃] = 0.001M (X cm³).

The absorbance spectra of the different coloured colloids in figure 2.10, clearly changes as the nature of the colloids themselves do. It should be noted that for smaller particle size ranges e.g. Yellow, a narrower/sharper absorbance band is observed while Blue with a wider particle size range clearly has broader peaks. The λ_{\max} shifts position with changes in the nanoparticles size and shape.

The different nature of each colloid is also highlighted in the UV-Vis spectra of the green colloid where two distinct absorbance peaks are observed as a result of the interaction of two species (types) of nanoparticles i.e. the larger blue nanoparticles and the smaller yellow nanoparticles, (these are the most likely species contributing to the green as the peaks are seen to have similar λ_{\max} 's – Yellow 445 nm, Blue 670nm, Green band 1, 405 nm, band 2, 648 nm) while the other colloids exhibit just one distinct band (which can however display a shoulder, but this could be attributed to band broadening due to the wider particle size range).

2.5.2.4 Dynamic light scattering, DLS – Malvern nano series Zetasizer

The DLS results for each colloid fit the expected trend indicated by the previous UV-Vis analysis. A breakdown of the UV-Vis, DLS results is supplied in table 2.2. It can

be seen that the λ_{\max} shifts with particle size as seen elsewhere in the literature^{11-12, 19-21, 28-33}. Note that although the methodologies of preparing the seed solution and the high load are quite similar, a single change in the relative concentration of the capping / stabilising agent (significant increase) drastically affects the size⁹⁻¹⁰ of the nanoparticles produced from ~ 20 nm to ~ 8 nm as can be seen in figure 2.11.

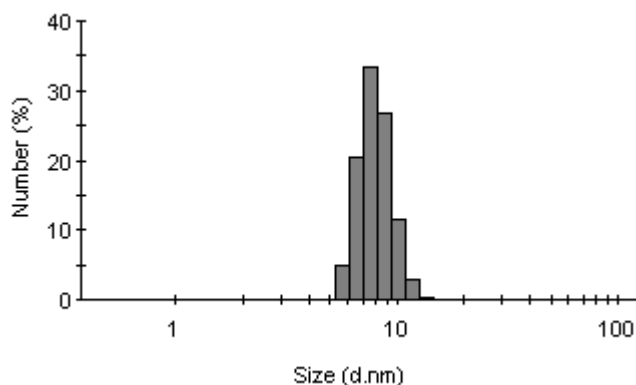


Figure 2.11 a: Distribution of particle diameters within the 'seed' Ag colloid.

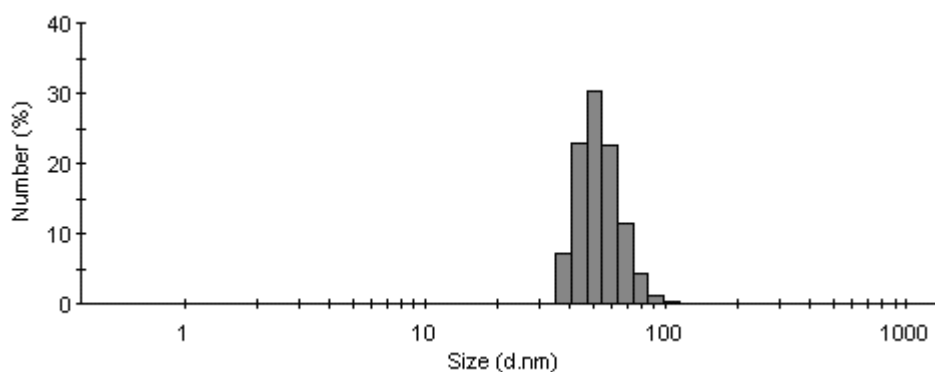


Figure 2.11 b: Distribution of particle diameters within the Blue Ag colloid.

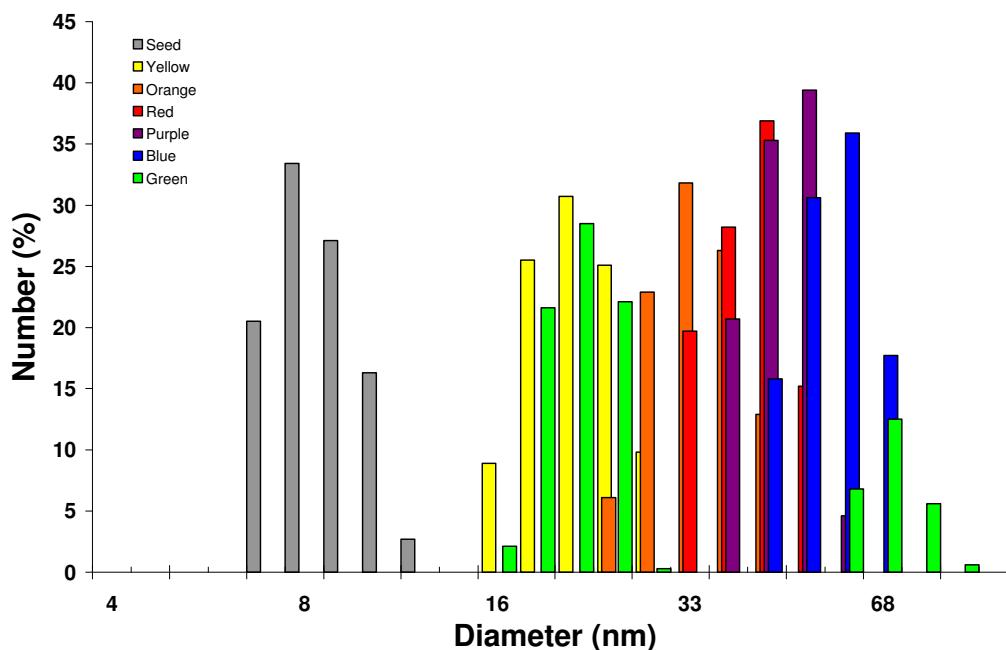


Figure 2.11 c: Combined graphical representation of the distribution of particle diameters of the nanoparticles in the coloured Ag colloids. Individual DLS graphs are included in appendix A.2.2.

Colour	UV-Vis λ max	DLS	
		Particle Size Range	Average Size Range
Seed	393 nm	5 – 14 nm	8 – 9 nm
Yellow	445 nm	6 – 28 nm	20 – 22 nm
Orange	473 nm	11 – 38 nm	30 – 33 nm
Red	495 nm	21 nm – 60 nm	40 – 42 nm
Purple	555 nm	35nm – 70 nm	51 – 54 nm
Blue	670 nm	57 nm – 105 nm	58 – 65 nm
Green	405 nm & 648 nm	11 – 250 nm	91.1 % 20- 21 nm & 8.9 % \geq 60 nm

Table 2.2: Summary of Colloids UV-Vis λ_{\max} 's and DLS results.

2.5.2.5 Electron microscopy – JEOL, 100CX Transmission Electron Microscope / Hitachi, SU 6600 FESEM

Images of the nanoparticles (figure 2.12) were obtained from the interaction of a beam of electrons transmitted through a dried film of the colloid. Before analysis, the colloidal samples (prepared in the same manner as outlined in Figure 2.9 and Table 2.2) were diluted in ethanol and sonicated for 30 mins, before being cast onto the TEM grid (Agar scientific, holey carbon 200 mesh (Cu)) by drop coating. The

average diameters of the nanoparticles were determined, using Zeiss axiovision software ³⁴ and correlated well with the DLS results. Note; additional TEM and STEM images appear in appendices A.2.3 and A.2.4 respectively.

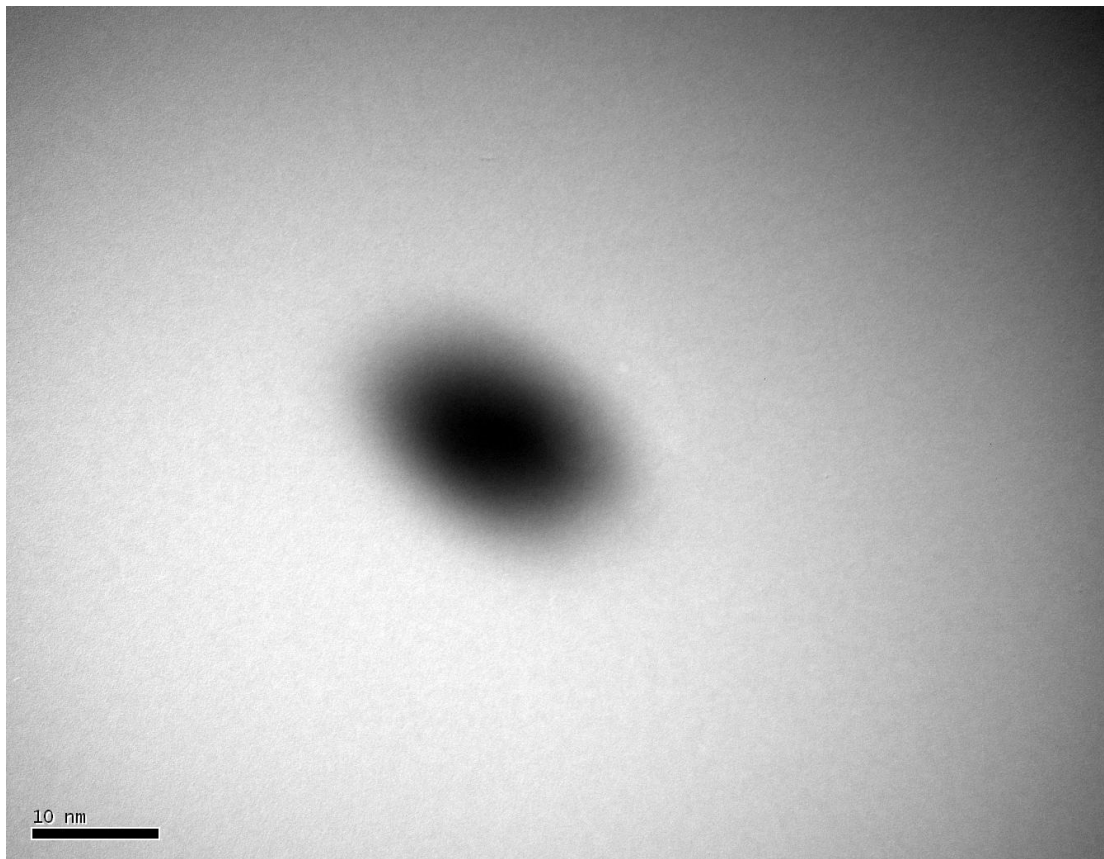


Figure 2.12a : A TEM image of silver nanoparticle (seed colloid) with an average diameter range of ~ 9 nm.

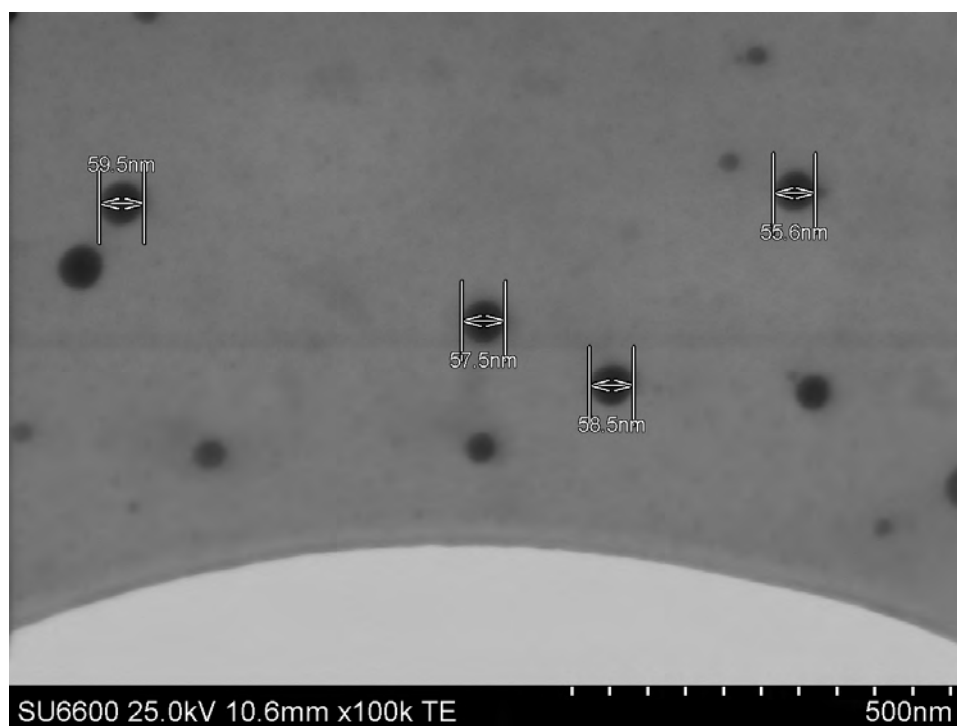


Figure 2.12b : A STEM image of silver nanoparticles (blue colloid) with an average diameter range of 58 - 60 nm. Image taken by Anne Shanahan MSc. - Instrumental Support – Focas Institute

2.5.2.5.1 Shape of silver nanostructures of tuneable colloids

Whereas the majority of silver nanostructures described in the literature are spherical (table 1.1, section 1.8), it would be incorrect to assume that this is always the case. A not insignificant percentage of silver nanoparticles may be prepared in a variety of shapes. Alternative shapes as expected, produce different properties for the nanostructures. For example against gram negative bacterium *Escherichia coli* triangular silver nanoparticles have a stronger biocidal action than spherical or rod shaped particles³⁵.

The different shapes of silver nanostructures may be readily observed in their absorption spectra, (sections 1.13 and 2.5.2.3). Figure 2.10 shows clear shifts in the colloid's λ_{\max} depending on the colloid's colour, these shifts when compared to others reported in the literature^{11 - 12, 36} and those available commercially³⁷ infer that the nanoparticles in the tuneable colloids are not spherical as the λ_{\max} shift is too great. The electromagnetic microscopy data however does indicate that the structures are rounded, this points to the nanostructures being disc or 'hockey puck' shaped.

2.5.2.6 Colloid Stability

The prepared colloids proved highly stable when stored appropriately (best results observed when stored in dark), with repeat spectroscopic (UV-Vis) analysis of the individual colloids over time (after a 6 month period) correlating well with initial analysis (figures 2.13 and 2.14).

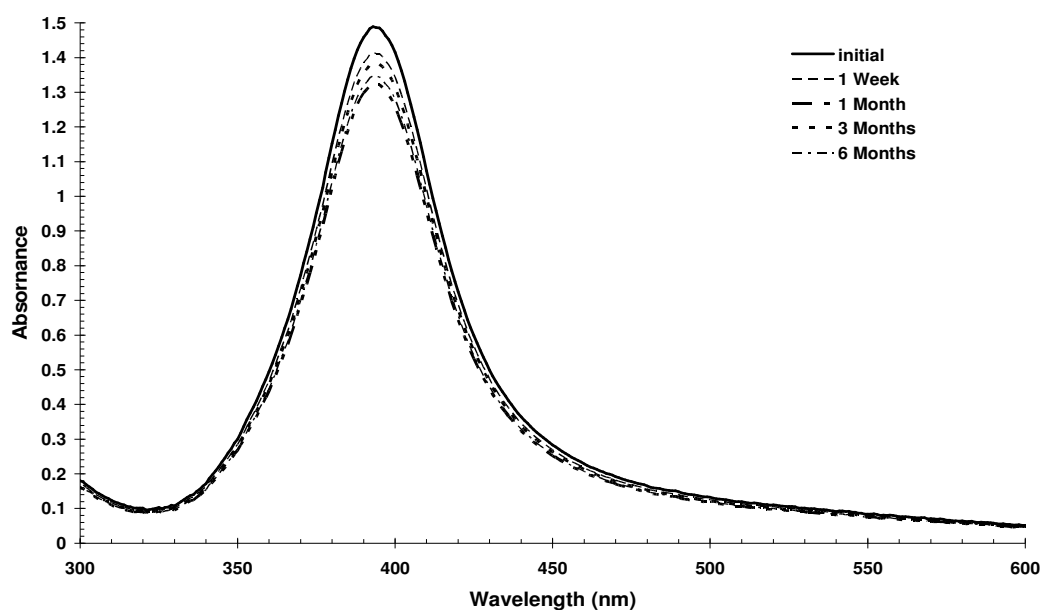


Figure 2.13: UV-Vis spectra of aqueous colloidal Ag polymer mixture over a 6 month period, colloid was stored at room temperature 18 ± 2 °C in the dark. With a total loss of absorbance after 6 months of $\sim 9.5\%$

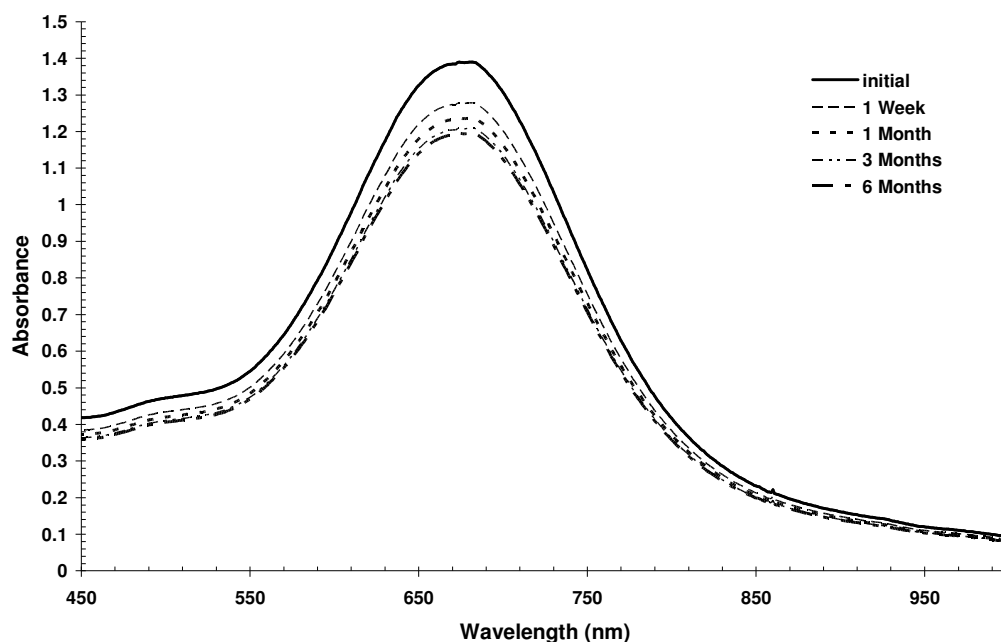


Figure 2.14: UV-Vis spectra of blue colloid over a 6 month period, colloid was stored at room temperature 18 ± 2 °C in the dark. A % decrease of $\sim 14\%$ was observed after 6 months.

2.6 Alternative high load colloid recipes

Following the successful application of PVA as a stabilising agent, the application of alternative solvent and stabilisers were investigated. Preliminary studies involved the use of methanol-based colloids as a means of speeding up the casting process of the nanocomposite films. However the use of these solvents had a detrimental affect on the colloid's stability, most likely as a result of a decrease in the electrostatic stabilisation of the colloid due to methanol being less polar than water (section 1.6); confirmed by a significant drop in the observed zeta potential (figure 2.15) from -43.4 mV for the aqueous based colloids to -22.9 mV for the methanol dispersed.

This resulted in greater concentrations of PVA being required to stabilise the system, negating the initial work to optimise the nanocomposite structure through defining the monomer to metal ratio.

This prompted the investigation of the effectiveness of different stabilising agents polyvinyl chloride and a surfactant, Triton 100x.

The surfactant (Triton 100x) was suitably effective as a stabilising agent, producing nanoparticles with a size distribution range of 6 – 20 nm and an average diameter of 8 – 10 nm (figure 2.16) and displaying reasonable stability over time (figure 2.17).

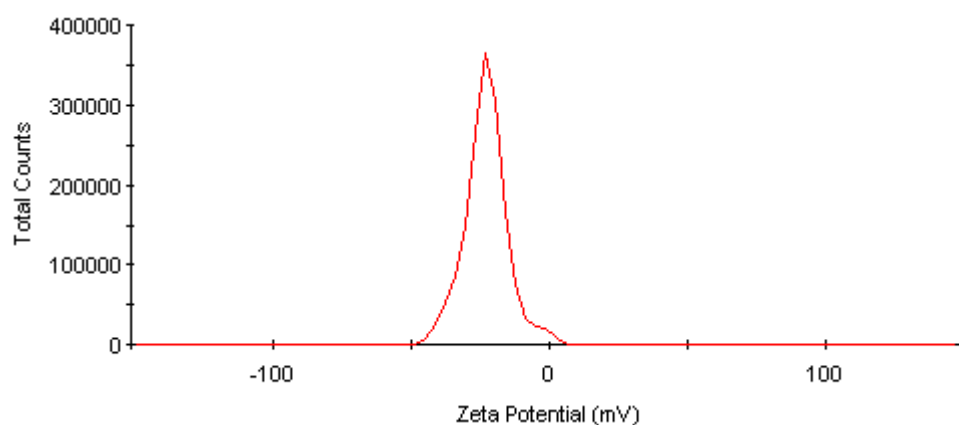


Figure 2.15: Zeta potential distribution of the methanol based Ag PVA colloid.

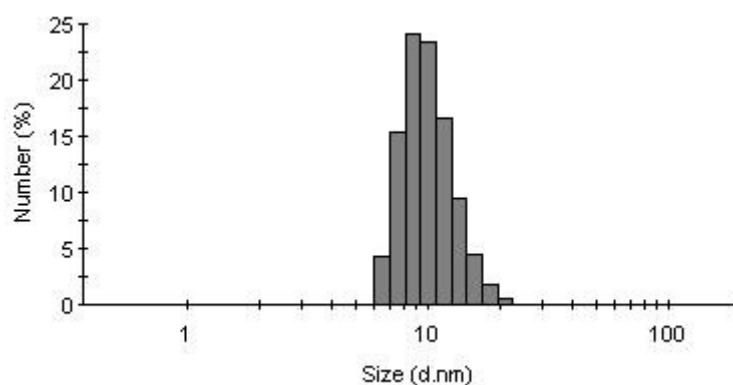


Figure 2.16: Distribution of particle diameters within the Triton stabilised Ag colloid

PVC demonstrated some effectiveness as a capping agent, however its size distribution range was wider, 28 – 70 nm with a larger average diameter (figure 2.18). This wider distribution range is clearly indicated by the broad plasmon band in its absorbance spectra (figure 2.18).

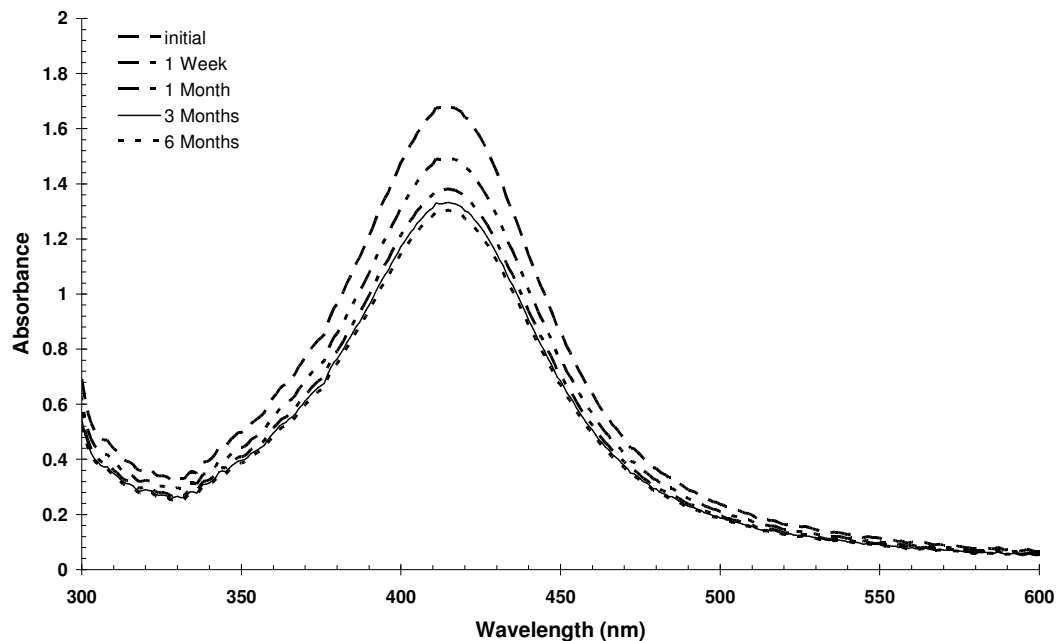


Figure 2.17: UV-Vis spectra of methanol dispersed colloidal Ag Triton stabilised mixture over a 6 month period, colloid was stored at room temperature $18 \pm 2^\circ\text{C}$ in the dark. With a total loss of absorbance after 6 months of $\sim 22.3\%$

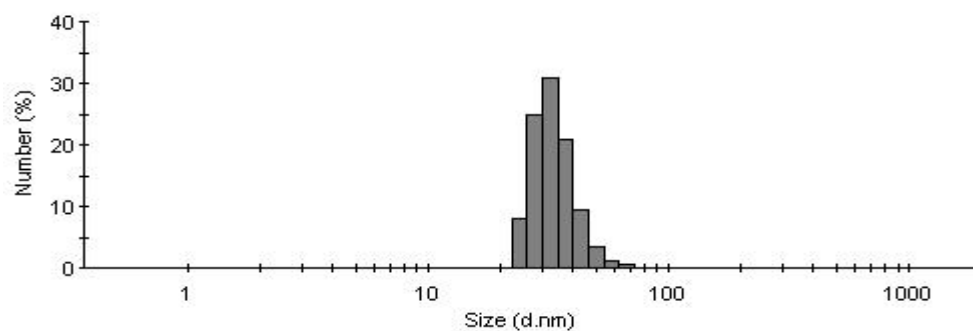


Figure 2.18: Distribution of particle diameters within the PVC stabilised Ag colloid

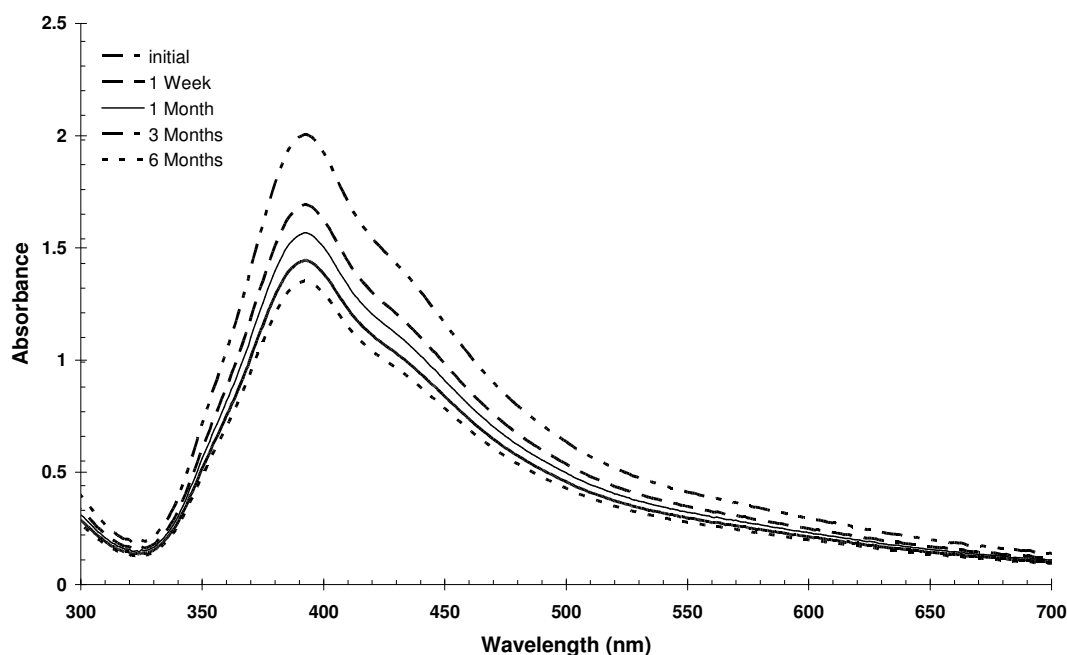


Figure 2.19: UV-Vis spectra of PVC stabilised methanol dispersed Ag colloid over a 6 month period, colloid was stored at room temperature 18 ± 2 °C in the dark. With a total loss of absorbance after 6 months of $\sim 33\%$

2.7 Conclusions

Silver-polyvinyl alcohol colloidal dispersions were successfully prepared by the reduction of aqueous AgNO_3 with NaBH_4 using PVA as a capping agent. The colloid's properties may be divided into two distinct sub groups; colloids with high silver loads, one step synthesis, or colloids with tuneable optical properties, heterogeneous nucleation. For the synthesis of both sets of colloids, the stoichiometric molar ratio of $\text{AgNO}_3:\text{NaBH}_4$ was determined as 1:1

The initial focus of the work was to prepare high load colloids for nanocomposite fabrication. Here the effect of experimental parameters was clearly evident with best results observed at lower temperatures ($< 4^\circ\text{C}$). Preparation of the colloids at low temperatures coupled with the use of the stabilising/capping agent, PVA, also had a positive effect on the uniformity of the prepared nanostructures, verified by UV-Vis spectroscopy and Dynamic Light Scattering measurements.

The absorbance spectra of the colloids, initially confirmed the presence of silver nanoparticles with the characteristic plasmon band, the narrow peak of the band indicating a narrow particle size range, DLS analysis determined the particle size range of the high load colloids to be 8nm – 38 nm (with an average of 21 – 22 nm) in

the colloids, which correlated well with the findings of TEM analysis where silver nanoparticles were observed to have an average size of 22 nm.

A simple heterogeneous nucleation (building block) process was used to produce silver colloids with tuneable λ_{\max} 's (where only the concentration of one reagent AgNO_3 , is changed). The synthesis was both rapid and repeatable at room temperature with the resulting colloids displaying good stability over time. The optical features of the resultant colloids were found to be dependent on the size of the particles. The synthesis method utilised here showed some advantages over other techniques reported in the literature, with a total synthesis time from seed to coloured colloids, of less than 5 minutes, with no need for specialised equipment, centrifugation, temperature control or 'ageing' of the seed or reagents required. The methodology is also 'greener' than other techniques using PVA, which is deemed "Not Hazardous" according to directive 67/548/EEC unlike other stabilising materials. The process proved sufficiently robust to be used as an introductory undergraduate practical (see appendix, A.2.1) in the institute, highlighting the novel optical properties of metallic nanoparticles through the demonstration and UV-Vis monitoring of their localised plasmon resonance and the Tyndall effect.

2.8 References

1. X.K. Meng, S.C. Tang, S. Vongehr, *Journal of Materials Science & Technology*, 2010, 26, 487 – 522
2. T.M. Tolaymat, A.M. El Badawy, A. Genaidy, K.G. Scheckel, T.P. Luxton, M. Suidan, *Science of The Total Environment*, 2010, 408, 999 – 1006
3. Y.C. Lu, K.S. Chou, *Journal of the Chinese Institute of Chemical Engineers*, 2008, 39, 673 – 678
4. K. Chaloupka, Y. Malam, A.M. Seifalian, *Trends in Biotechnology*, 2010, 28, 580 – 588
5. W. Likussar, D. F. Boltz, *Analytical Chemistry*, 1971, 43, 1265 – 1272
6. A.M. Schwartzberg, J.Z. Zhang, *Journal of Physical Chemistry, C*, 2008, 112, 10323 – 10337
7. W. Zhang, X. Qiao, J. Chen, *Materials Science and Engineering B*, 2007, 142, 1 – 15
8. P.C. Lee, D. Meisel, *Journal of Physical Chemistry*, 1982, 86, 3391 – 3395
9. A. Henglein, M. Giersig, *Journal of Physical Chemistry, B*, 1999, 103, 9533 – 9539
10. W. Wang, X. Chen, S. Efrima, *Journal of Physical Chemistry, B*, 1999, 103, 7238 – 7246
11. D.M. Ledwith, A.M. Whelan, J.M. Kelly, *Journal of Materials Chemistry*, 2007, 17, 2459 – 2464
12. D. Aherne, D.M. Ledwith, M. Gara, J.M. Kelly, *Advanced Functional Materials*, 2008, 18, 2005 – 2016
13. C. Drake, S. Deshpande, D. Bera, S. Seal *International Materials Reviews*, 2007, 52, 289 – 317
14. M.J. Hostetler, S.J. Green, J.J. Stokes, R.W. Murray, *Journal of the American Chemical Society*, 1996, 118, 4212 – 4213
15. M.J. Hostetler, A.C. Templeton, R.W. Murray, *Langmuir*, 1999, 15, 3782 – 3789
16. Q.F. Zhou, J.C. Bao, Z. Xu, *Journal of Materials Chemistry*, 2002, 12, 384 – 387
17. P.K. Khanna, N. Singh, S. Charan, V.V.V.S. Subbarao, R. Gokhale, U.P. Mulik, *Materials Chemistry and Physics*, 2005, 93, 117 – 121
18. T. Li, H.G. Park, S. Choi, *Materials Chemistry and Physics*, 2007, 105, 325 – 330
19. K.L. Kelly, E. Coronado, L.L. Zhao, G.C. Schatz, *Journal of Physical Chemistry B*, 2003, 107, 668 – 677

20. Y. Kunieda, K. Nagashima, N. Hasegawa, Y. Ochi, *Spectrochimica Acta Part B*, 2009, 64, 744 – 746
21. E. Filippo, A. Serra, D. Manno, *Sensors and Actuators B*, 2009, 138, 625 – 630
22. W. Likussar, D.F. Boltz, *Analytical Chemistry*, 1971, 43, 1265 – 1272
23. P. Atkins, J. de Paula, *Atkins' Physical Chemistry*, 7th ed., Oxford University Press, Oxford, New York, 2002, 845.
24. <http://rsb.info.nih.gov/ij/> (Downloaded May 2009)
25. A. Sinha, B. P. Sharma, *Bulletin of Materials Science*, 2005, 28, 3, 213 – 217
26. S. Mandal, S. K. Arumugam, R. Pasricha M. Sastry, *Bulletin of Materials Science*, 2005, 28, 503 – 510
27. D.G. Yu, W.C. Lin, C.H. Lin, L.M. Chang, M.C. Yang, *Materials Chemistry and Physics*, 2007, 101, 93 – 98
28. W.C. Lin, M.C. Yang, *Macromolecular Rapid Communications*, 2005, 26, 1942 – 1947
29. F. Guo, Z.G. Peng, J.Y. Dai, Z.L. Xiu, *Fuel Processing Technology*, 2010, 91, 322 – 328
30. C.C. Koch, I.A. Ovid'ko, S. Seal, S. Veprek, *Structural nanocrystalline materials: fundamentals and applications*, Cambridge University Press, 2007, Ch. 3.
31. C.F. Bohren, D.R. Huffman, *Absorption and scattering of light by small particles*, New York; Chichester: Wiley, 1983
32. A. Shkilnyy, M. Souce, P. Dubois, F. Warmont, M.L. Saboungi, I. Chourpa, *Analyst*, 134, 2009, 1868 – 1872
33. M.E. Abdelsalam, S. Mahajan, P.N. Bartlett, J.J. Baumberg, A.E. Russell, *Journal of the American Chemical Society*, 2007, 129, 7399 – 7406
34. <http://www.zeiss.com/c12567be0045acf1/ContentsFrame/cbe917247da02a1cc1256e0000491172> (down loaded December 2010)
35. S. Pal, Y.K. Tak, J.M Song, *Applied Environmental Microbiology*, 2007, 73, 1712 – 1720
36. S. Guoli, S. Wentao, L. Kai, M. Zhanfang, *Colloids and Surfaces, A*, 2011, 380, 257 – 260
37. <http://www.sigmaaldrich.com/materials-science/nanomaterials/silver-nanoparticles.html>

3. Humidity Sensor

3.1 Introduction

In the recent past, development of nanoscale science and technology has continued at a rapid pace, as demand for miniaturised devices increases. Due to the novel physiochemical properties metallic nanostructures often exhibit and the ease at which such properties may be tailored, this has resulted in a marked increase in the fabrication of 'smart' materials for applications in numerous fields, including biomedicine, electronics, optical and magnetic devices ¹.

Nanocomposites are multiphase solid materials where one of the phases has one, two or three dimensions on the nanoscale, or structures having nano-scale repeat distances between the different phases that make up the material. They usually combine a solid bulk matrix, (generally ceramic, metallic or polymer) and nanostructured 'filler' phase, the presence of which influences the mechanical, electrical, thermal, optical, electrochemical or catalytic properties of the nanocomposite leading to the nanocomposite exhibiting markedly different properties from those of the component materials. This is due to the exceptionally high surface area to volume ratio of the nano phase ², which can be readily exploited in sensor applications.

Previously, polymers have been widely utilized in a wide range of sensing devices with definite roles, either in the sensing mechanism or through immobilizing the species responsible for sensing of the analyte component. This is possible as polymers may be tailored for particular properties ^{3 - 5}, are easily processed, and may be selected to be inert in the environment containing the analyte; this flexibility and relative low cost also means they are appealing to industry. ⁶

Hence the coupling of specific polymers with select nanostructures ⁷ affords researchers the ability to further develop new and enhance existing sensing devices. This is illustrated best in the continued development of gas sensors, where the high surface area to volume ratio of nanomaterials greatly improves sensitivity as a greater interaction between the analyte and sensor is permitted ⁸⁻¹⁴.

Humidity is a major component of our environment, significantly impacting on not only human comfort but a broad range of technologies as well. Thus relative humidity (RH) detection and its control are important in a wide range of industrial applications (see figure 3.1) including the pharmaceutical, food and electronics industries. The close monitoring of RH during processes can help maintain product quality and can also be necessary during transport of materials ¹⁵⁻¹⁷.

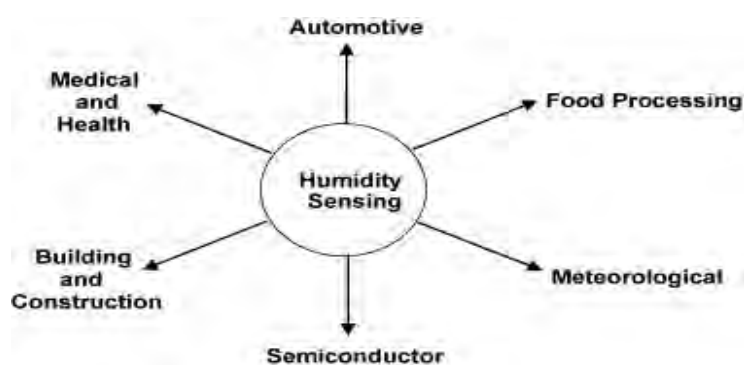


Figure 3.1: A range of the various applications of humidity sensors in industry ¹⁸

Existing humidity sensing methodologies rely upon optical, gravimetric, capacitive, resistive, piezoresistive and magnetoelastic properties of selected materials ¹⁹.

RH is generally measured and controlled by meters that detect change in a physical property of a thin film, such as capacitance, resistivity, or thermal conductivity (sections 1.24 – 1.26) ²⁰ In this work the sensor is based on a polyvinyl alcohol (PVA) silver nanoparticle composite cast on an interdigital electrode array. Gas sensing films containing nanoparticles (chains) have been used to sense multiple analytes. Previously in the literature it was observed that the inter particle conductivity of films was reduced when the gas (analyte) penetrated and interacted with the polymer aspect of the composite film, causing the polymer to swell and disrupt the nanoparticle chain, increasing the resistivity of the film ^{1, 6, 13 – 14, 21}. Based on this evidence the composite's makeup was optimised to ensure that the ratio of insulating polymer (PVA) and Ag nanoparticle was ~1:1, see chapter 2, section 2.3. The aim of this study was to determine the Ag – PVA composites suitability as a sensing film, in terms of sensitivity, selectivity and repeatability.

3.2 Experimental

Sensor coatings were produced by casting the colloid Ag/polymer composites onto platinum interdigital electrodes (CC2.W2), or graphite interdigital electrodes (CC1.W4), purchased from BVT Technologies and used as received (figure 3.2). 0.1 ml of the colloid was deposited by drop coating onto the surface of the electrodes and air drying over a period of 12 – 15 hours. Coating thickness was measured using a Reichert-Jung optical microscope.

The behaviour of the resulting coating as a humidity sensor was investigated as follows; a constant potential of 1V was applied across the interdigital electrode using a Thompson ministat potentiostat and the resulting response measured. The sensor's response is a voltage signal which develops across the $1k\Omega$ 'counting' resistor on the potentiostat. The sensing membrane's responses to selected vapours were collected using a high-resolution data logger (PICO ADC 16).

All experiments were conducted at room temperature ($20 \pm 2^\circ\text{C}$) and N_2 (oxygen free 99.998%, BOC Gases) was used as the reference gas. These vapour streams were produced by bubbling dry N_2 gas using a bubbler apparatus, as shown in Figure 3.4.

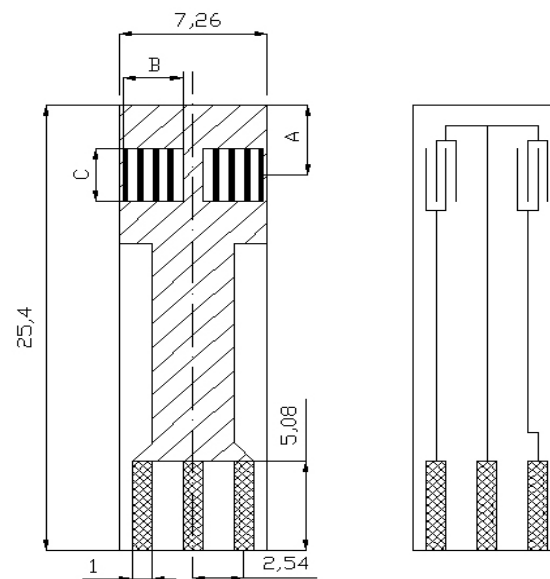


Figure 3.2: Schematic of BVT Technologies CC2.W* (*) conductometric sensor substrates, $A = 4.00 \pm 0.05$ mm, $B \text{ \& } C = 3.00 \pm 0.05$ mm²²

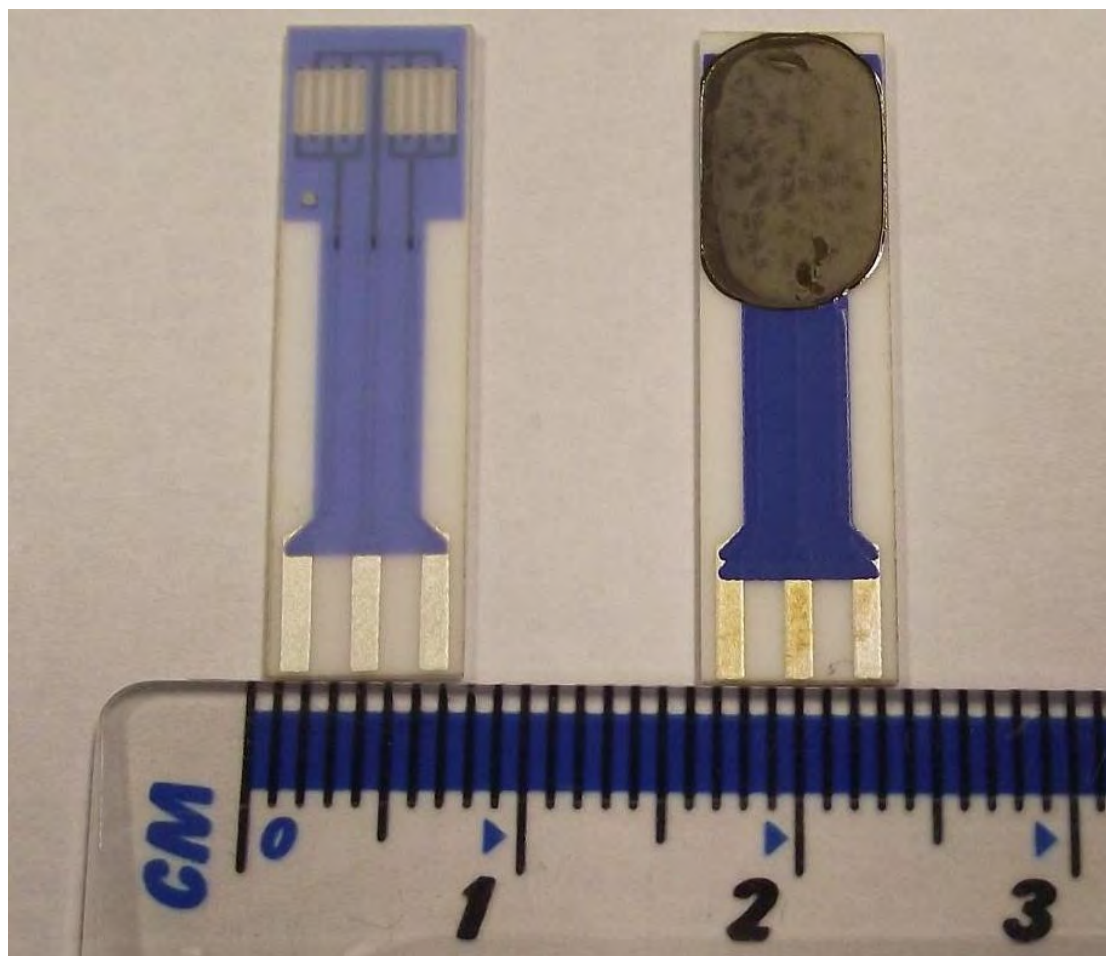


Figure 3.3: BVT Technologies interdigital electrodes, bare (left) and with nanocomposite sensing coating (right)

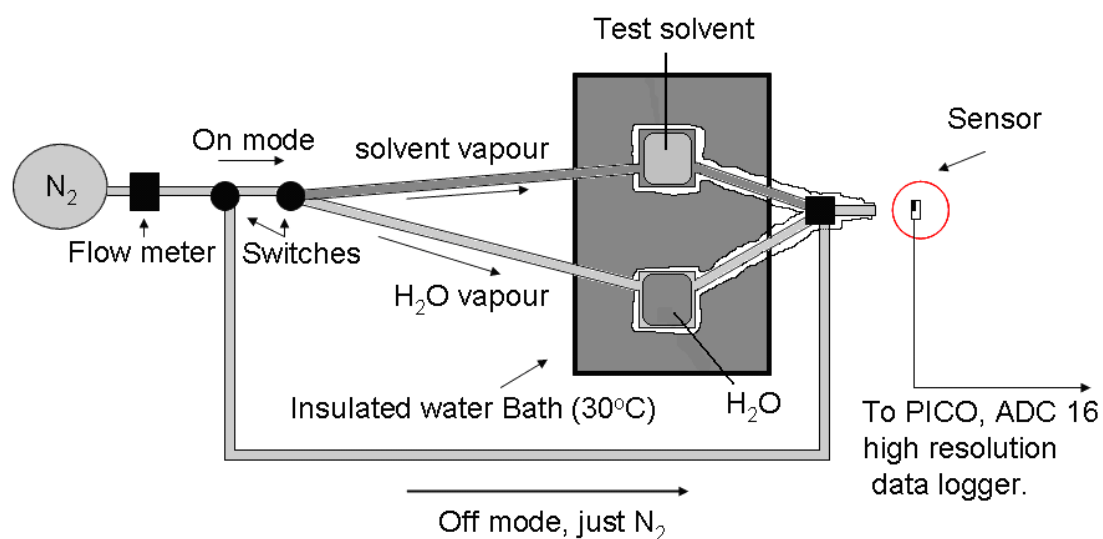


Figure 3.4: Bubbler apparatus schematic, the Dreschel flasks typically held a volume of 40 cm^3

The sensitivity of the film's response and suitability as a humidity sensor was further investigated by exposure of the sensor to a series of selected known humidity levels. A controlled environment chamber with a humidity control system (Electro-Tech systems model 503-20) was used to set each humidity level. The relative humidity within the chamber was maintained at a set level in the range of 10 - 100% RH \pm 1% RH. In addition the temperature of the environment was maintained at 21.3 ± 0.1 °C.

3.3 Humidity measurements

A clear response was observed when the coated substrates were exposed to water vapour. This response was found to be both rapid and repeatable over time. Figure 3.5 shows the sensor's response to repeated exposures at regular time intervals; the response is immediate, with a relatively consistent maximum peak height, with a total response time (despite a slight lag in the decay of the response signal) observed of 5 - 10 seconds.

Early results indicated that the coatings possessed a relatively good selectivity as a humidity detector. Vapour streams were produced by bubbling N₂ through the appropriate solvent contained in an insulated Dreschel flask, (Figure 3.4), in order to maintain a constant temperature and thus vapour pressure/concentration. A clear response for water vapour was observed with no obvious response for other non-polar vapours such as cyclohexane, as shown in Figures 3.6 and 3.7 and summarised in Table 3.1.

It can be seen from Figures 3.6 and 3.7 and Table 3.1 that there is a dramatic difference in response between water and a quite polar vapour, methanol. On magnification of the response (Figure 3.7) there is a small peak due to methanol and acetonitrile. However, these peaks are significantly smaller than those that would have been expected on the basis of their dielectric constants.

An investigation was conducted by placing the coated interdigital electrode in a precisely controlled environment chamber with a humidity control system. Here the sensor's response to increasing % RH at a constant temperature of 21.3 ± 0.1 °C was found to be constant and relatively linear over the 10-60% RH range. Before each measurement, the sensor was 'powered off' i.e. no voltage was applied across it and the environment set to the % RH of interest. Before each reading, the environment was allowed to equilibrate for 30 mins. Figure 3.8 shows the steady state response

obtained in this analysis. In this case, the humidity levels being measured were already constant before ‘sensing’ occurred, resulting in a response with none of the ramping up or down seen previously in Figures 3.5 and 3.6 where the amount of water vapour was altered during the measurement.

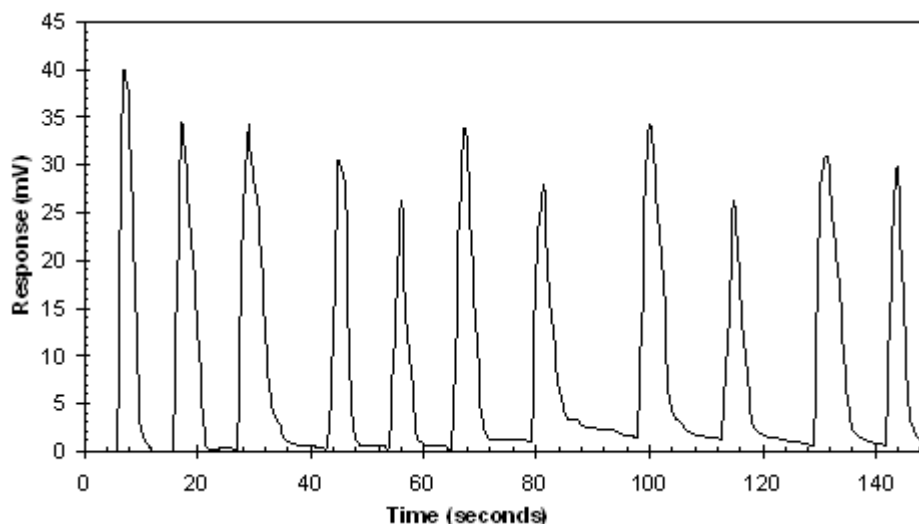


Figure 3.5: Representative plot of sensor's response to a change in environment. The sensing membrane was repeatedly exposed to water vapour at regular time intervals.

(1mV=1 μ A)

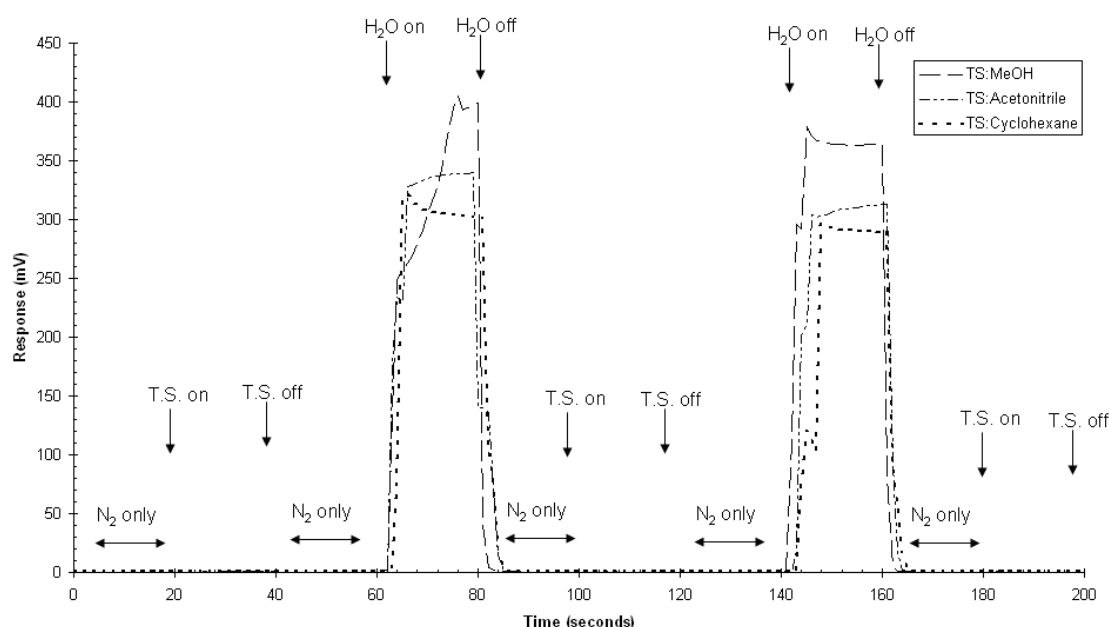


Figure 3.6: Sensor's response to exposure to various solvent vapours, summarised in Table 3.1. Exposure was conducted using the bubbler apparatus, where the streams passing over the sensing membrane were ‘switched’ from the reference gas to either the test solvent (T.S.) or water vapour as indicated.

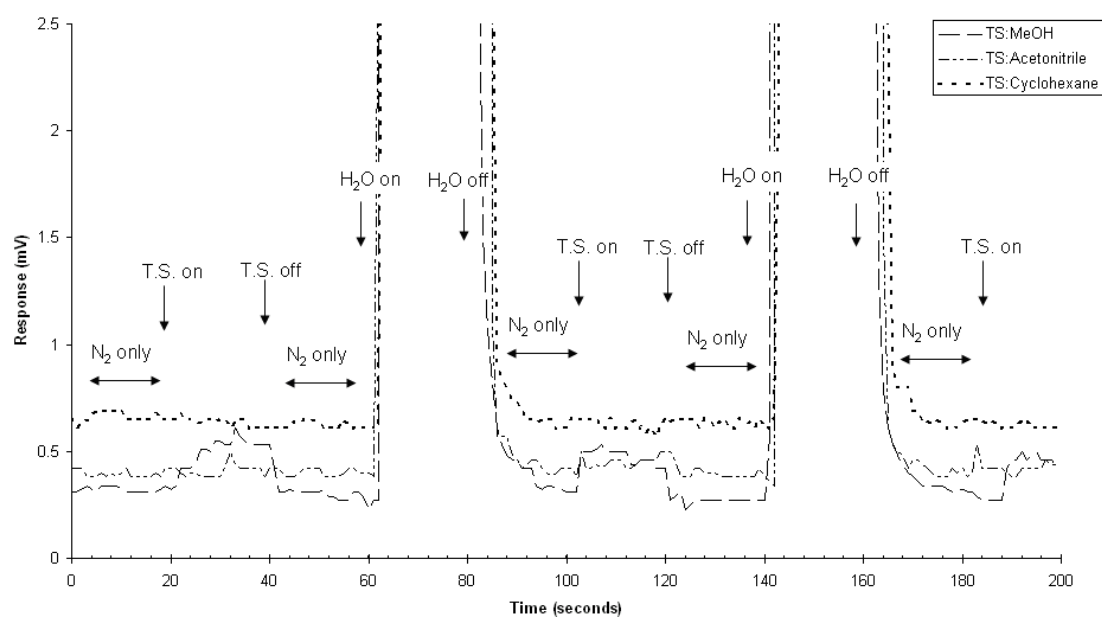


Figure 3.7: Magnification of the sensor's base line response of the results displayed in figure 3.5, illustrating the negligible response of certain test solvent (T.S.) vapours.

Vapour	B.P. at 1 Bar (°C)	Dielectric constant at 20°C	Response
Water	100	80.4 ^{23 a}	Yes
Acetonitrile	81	37.5 ^{23 b}	Negligible
Methanol	68	32.6 ^{23 c}	Negligible
Ethanol	78	24.3 ^{23 d}	Negligible
Cyclohexane	80.7	2 ^{23 e}	No

Table 3.1: Summary of sensor's response during exposure to different vapours. All vapour solvents were maintained at 30°C.

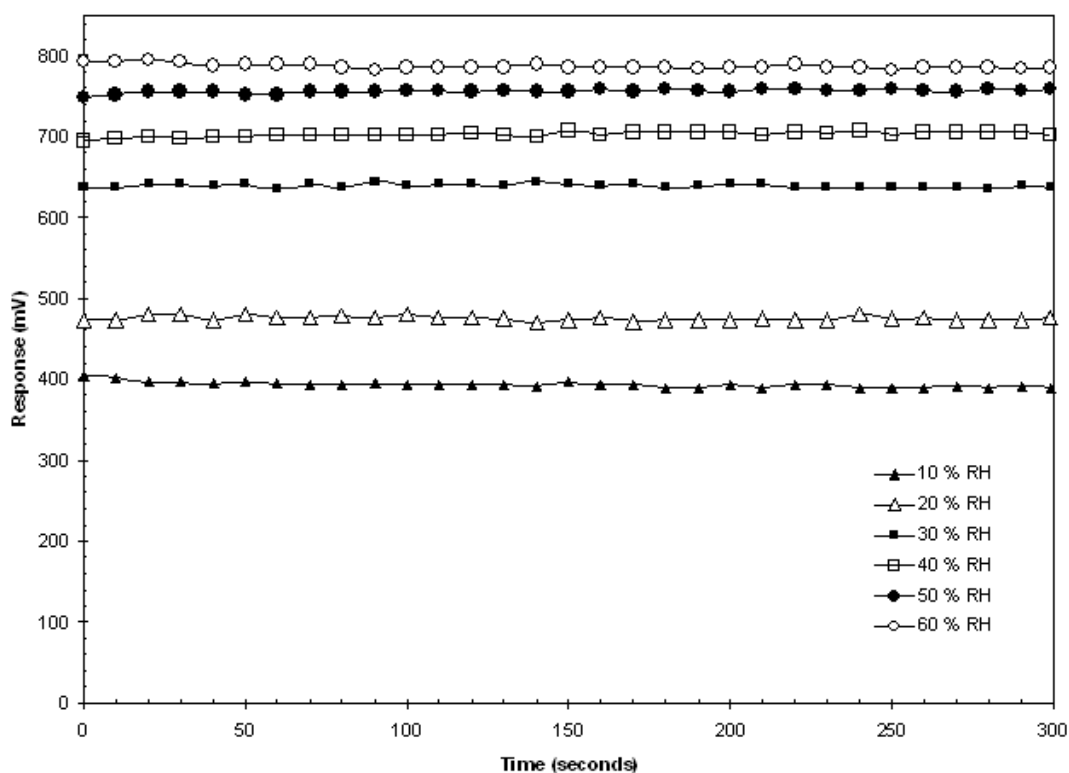


Figure 3.8: Graphical representation of sensor's response to increasing % RH over time at a constant temperature of 21.3 °C.

Typical results for repeated exposures of the same film (exposed repeatedly to set % RH humidities in the 10 – 60 % RH range) are summarised in Figure 3.9. It is thought that the mechanism of the sensing layer in this study may involve the presence of electrolyte remaining from the synthesis in the polymer. Introduction of water vapour allows hydration of the electrolyte, increasing its mobility, which allows an increase in current. It should be noted if the values of the responses for each % RH in Figure 3.9 were plotted; the resulting line would be relatively linear. However, it would produce a positive intercept. As prior analysis indicated that at 0 % RH, no response occurred, the sensor's response was modelled with a Langmuir adsorption equation²⁴, both first and second order, equations 3.1 and 3.2, respectively. The second order model was observed to be the best fit as indicated in Figure 3.9 by the broken lines.

$$S' = \frac{S}{S_s} \left(\frac{K_b C}{1 + K_b C} \right) \quad 3.1$$

$$S' = \frac{S}{S_s} \left(\frac{K_b \sqrt{C}}{1 + K_b \sqrt{C}} \right) \quad 3.2$$

The fit parameters K_b and S_s are the binding constant and the relative signal at saturation respectively and C is the relative the % RH²⁵. In Figure 3.10, the responses of four different sensing layers at incremental levels of humidity at the 100 second measurement time are compared graphically.

It should be noted that variations were observed for different sensors (same coating on similar substrates). This variation may be attributed to the composition of the sensing layer in each case, particularly in terms of the coatings thickness. Preliminary results with the Reichert – Jung optical microscope indicated that the coating's thickness ranged from 10 – 15 μm . As the sensing layer conductivity increases with greater analyte levels and since the film contains ions, the observed response was initially thought to be due to ionic movement. In order to determine the role of silver nanoparticles (if any), a similar composite of the same ionic strength was prepared (using NaNO_3 instead of AgNO_3) which yielded no response to any of the analytes investigated under the same experimental conditions. This suggests that the suspected

migration of anions in the composite on exposure to water vapour is not the sole sensing mechanism.

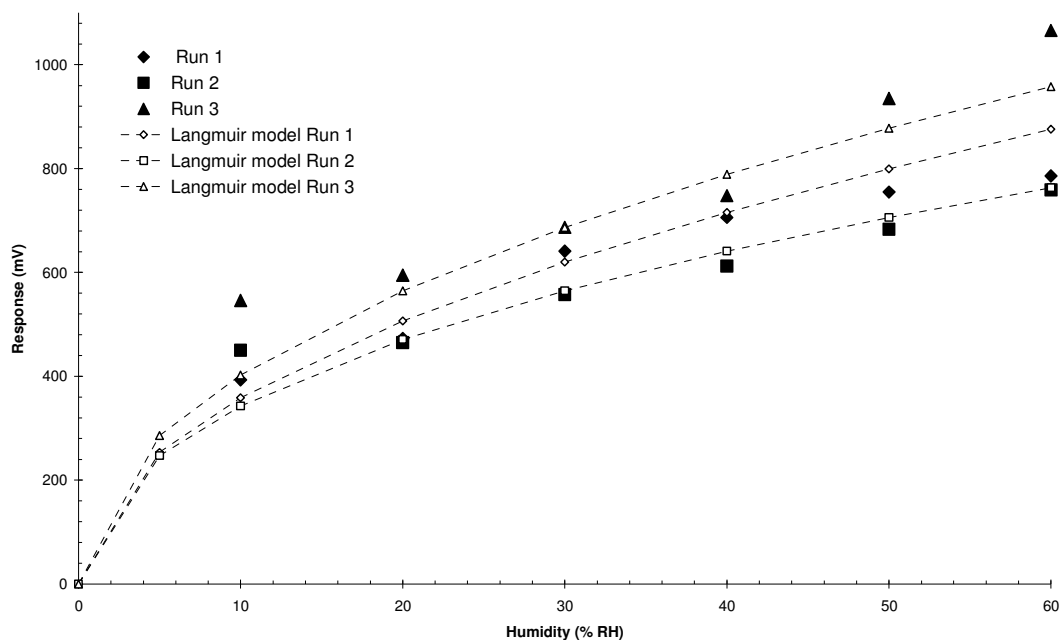


Figure 3.9: The sensor's response to repeated exposures to varying % RH at set time intervals. The dotted lines are the Langmuir model of the experimental data according to second order kinetics (equation 3.2).

However, layer thickness is not yet well defined using the drop casting process resulting in a significant variation in coating thickness which can be assumed to have an impact on the reproducibility of the sensitivity for each layer as seen in Figure 3.9, thus more work is required to optimise the thickness of the coating.

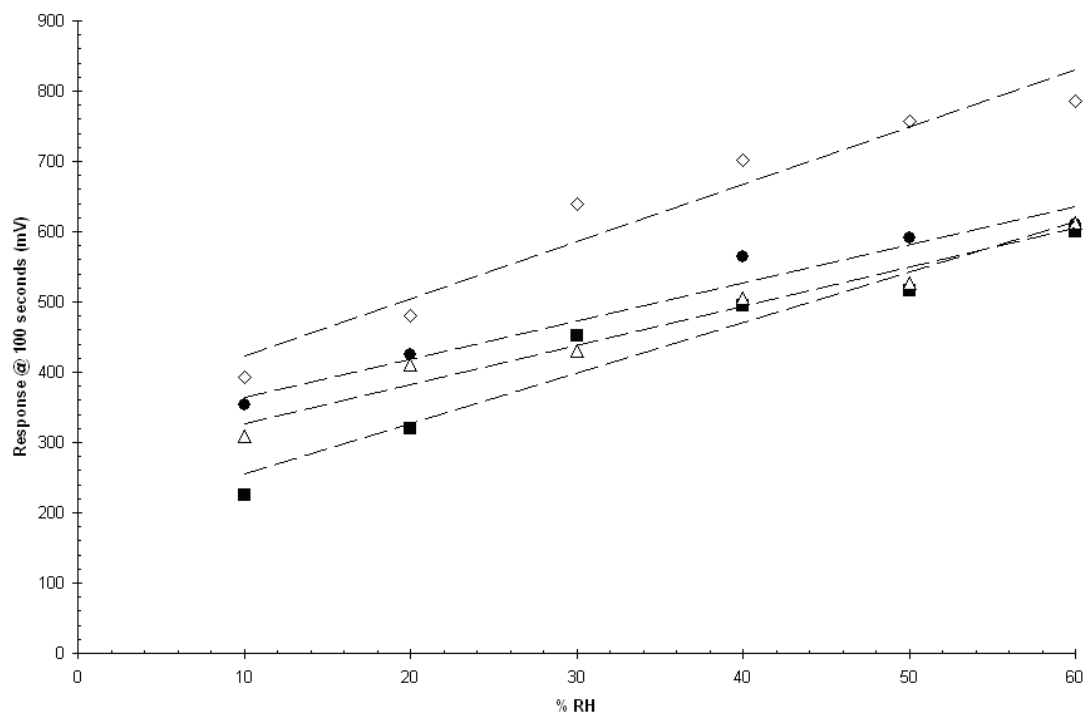


Figure 3.10: Responses of four different sensors prepared separately. The slopes for the lines are 5.4, 5.5, 7.2 and 8.2 ($mV/\%RH$).

3.4 Cyclic Voltammetry

The cyclic-voltammetry study of the cast film on the interdigits, (2 electrode system), indicated that the sensor coating appears to act as a background electrolyte in the presence of water vapour. No sensor response (i.e. current) was observed when the coating was exposed in the N_2 vapour stream. However, while the film displays a clear electrochemical response in a higher humidity environment, figure 3.11, (where there was an anodic peak that was attributed to Ag oxidation and a cathodic peak corresponding to Ag^+ reduction.) in the resulting voltammograms, both the silver nanoparticles and the ions within the coating appear to have an active role in the sensor's mechanism.

Analysis of a typical voltammogram indicated that approximately 6×10^{-10} mols of silver within the coating undergoes oxidation and reduction; a fraction ($\sim 1/10,000$) of the molar silver content of the cast nanocomposite coating. This may explain why, although the sensor's observed response appears to be migration controlled, no drop off of the steady state signal is observed during prolonged periods of exposure. In 'dry' conditions (N_2 stream) only a minute baseline current is observed as shown in figure 3.11.

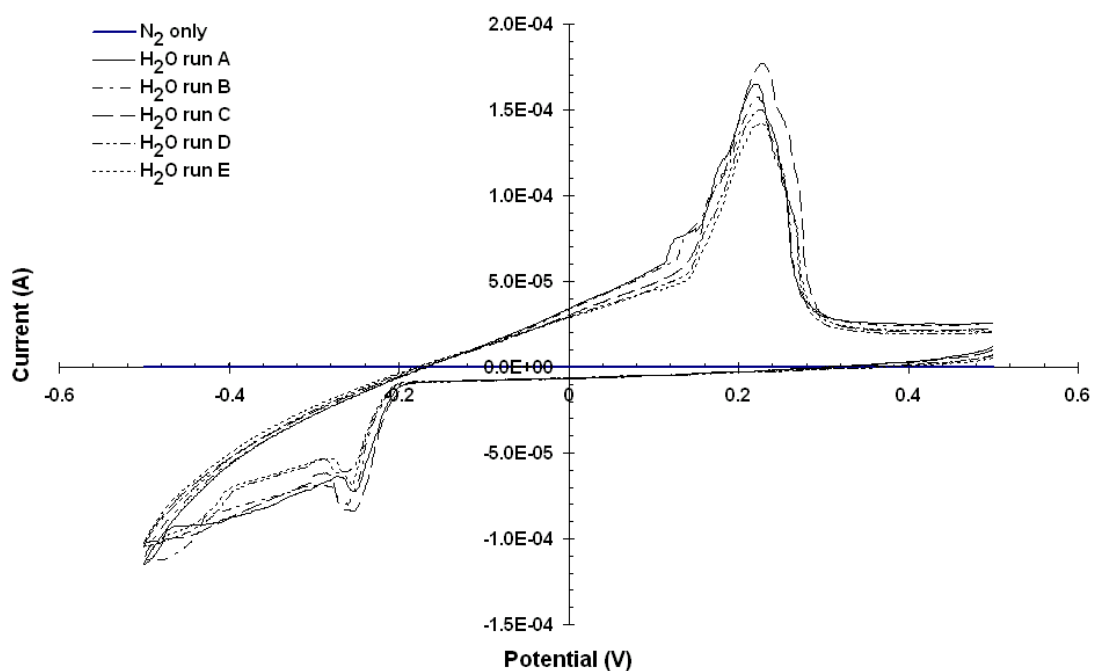


Figure 3.11: Cyclic voltammograms of sensing coating in both dry and humid conditions, initial $E = 0.5$ V, high $E = 0.5$ V, low $E = -0.5$ V with a scan rate of 0.1 V s^{-1} .

3.5 Electrochemical Impedance Spectroscopy, EIS

Impedance measurements were carried out over the frequency range of 1 Hz to 1 MHz using a Solartron Electrochemical interface, SI 1287 and a Solartron 1255B frequency response analyser. Humidity levels were established using closed vessel humidity saturated salt solutions, sodium hydroxide for 6%, potassium hydroxide for 9%, potassium acetate for 20%, calcium chloride for 35% and calcium nitrate for 55% RH²⁶. For each humidity level before the response was measured the sensor was placed in the relevant sealed container (figure 3.12) and left overnight to equilibrate. All measurements were carried out at a constant temperature of 20 ± 2 °C. Figures 3.13 and 3.14, show typical (multiple measurements were conducted) electrochemical impedance spectra of the sensing coating at different the humidity levels, Nyquist and Bode respectively.

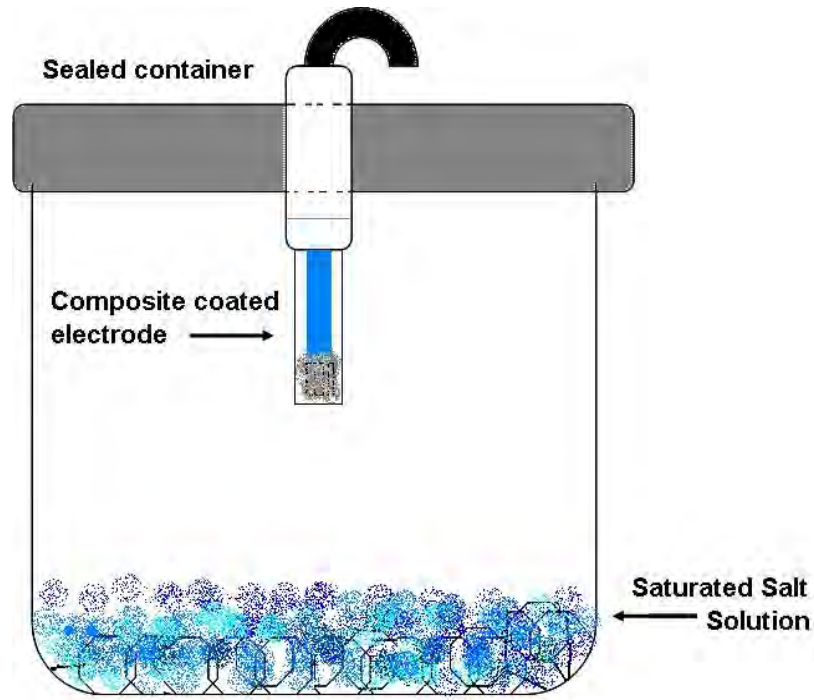


Figure 3.12: Schematic of EIS experimental set up

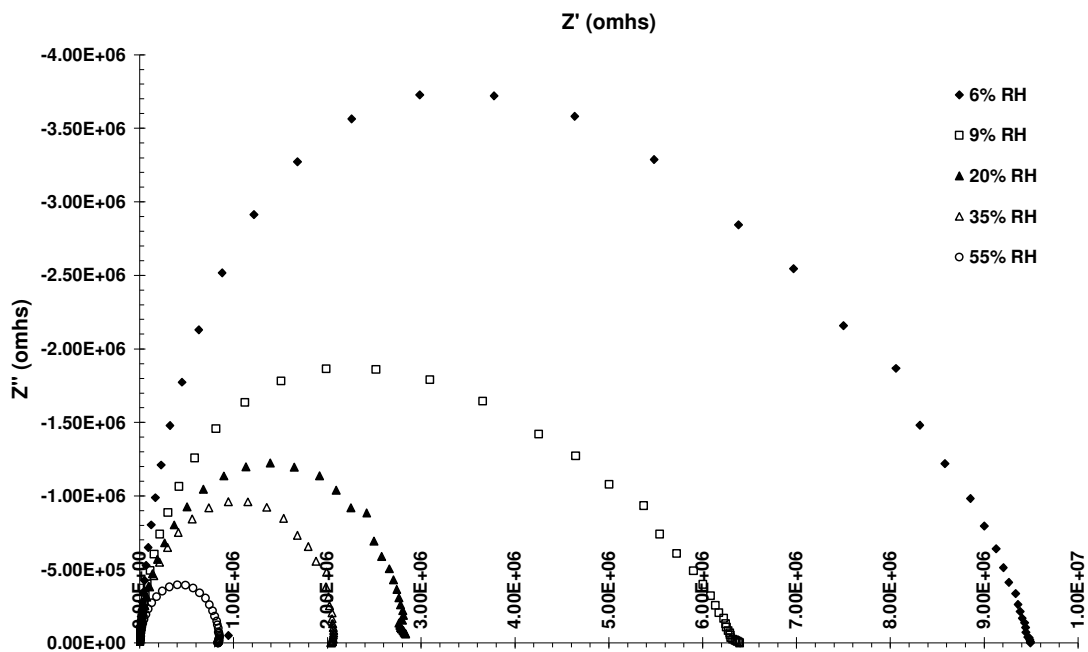


Figure 3.13: Nyquist plot of effect of humidity on the impedance of the sensing coating.

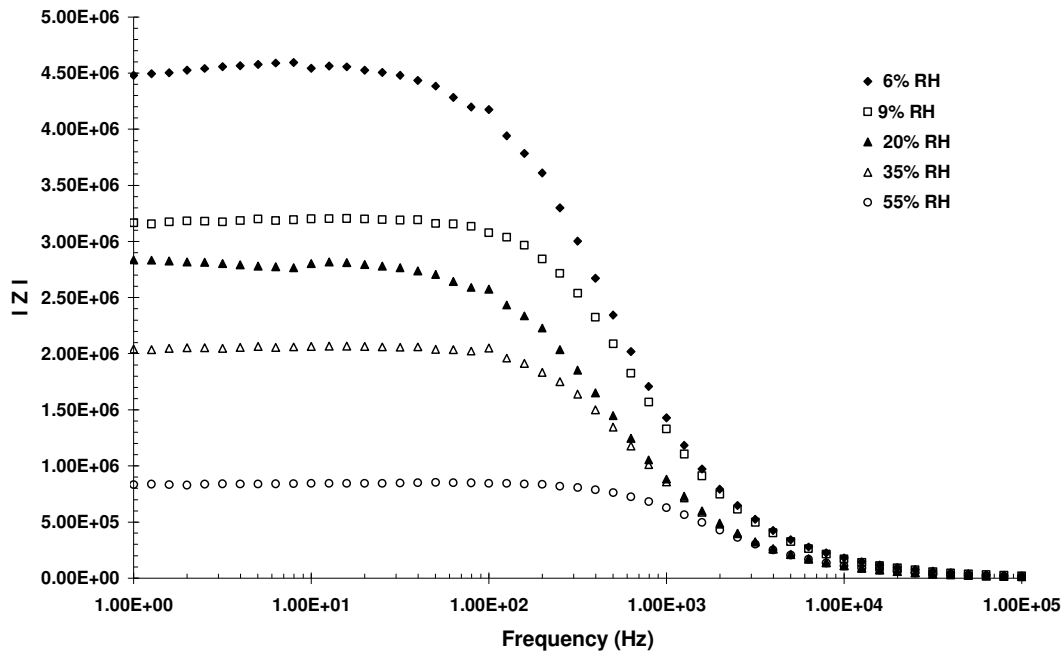


Figure 3.14: Bode plot of effect of humidity on the impedance of the sensing coating.

It can be seen that an increase in humidity results in a decrease of the sensing film's impedance. The EIS spectra of the coating at each humidity level can be fitted to a modified Randles circuit figure 3.15, the results of which are tabulated in table 3.2. Modelling was conducted using Z view 2 software, conductivity of the sensing film increases with humidity as illustrated in figure 3.16.

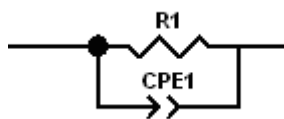


Figure 3.15: Modified Randles Circuit Model.

Element	Modelled Value	% Error
6% RH		
Resistor	$4.4924 \times 10^6 \Omega$	0.16
CPE-T	$3.245 \times 10^{-10} \text{ F}$	0.95
CPE-P	0.93466	0.11
9% RH		
Resistor	$3.1949 \times 10^6 \Omega$	0.21
CPE-T	$3.227 \times 10^{-10} \text{ F}$	0.84
CPE-P	0.94586	0.09
20% RH		
Resistor	$2.7979 \times 10^6 \Omega$	0.26
CPE-T	$2.944 \times 10^{-10} \text{ F}$	1.25
CPE-P	0.93466	0.12
35% RH		
Resistor	$2.076 \times 10^6 \Omega$	0.14
CPE-T	$2.608 \times 10^{-10} \text{ F}$	0.74
CPE-P	0.94586	0.07
55% RH		
Resistor	$0.85 \times 10^6 \Omega$	0.13
CPE-T	$2.495 \times 10^{-10} \text{ F}$	0.93
CPE-P	0.94877	0.08

Table 3.2: Summary of sensor's modelled response during EIS at different %RH levels.

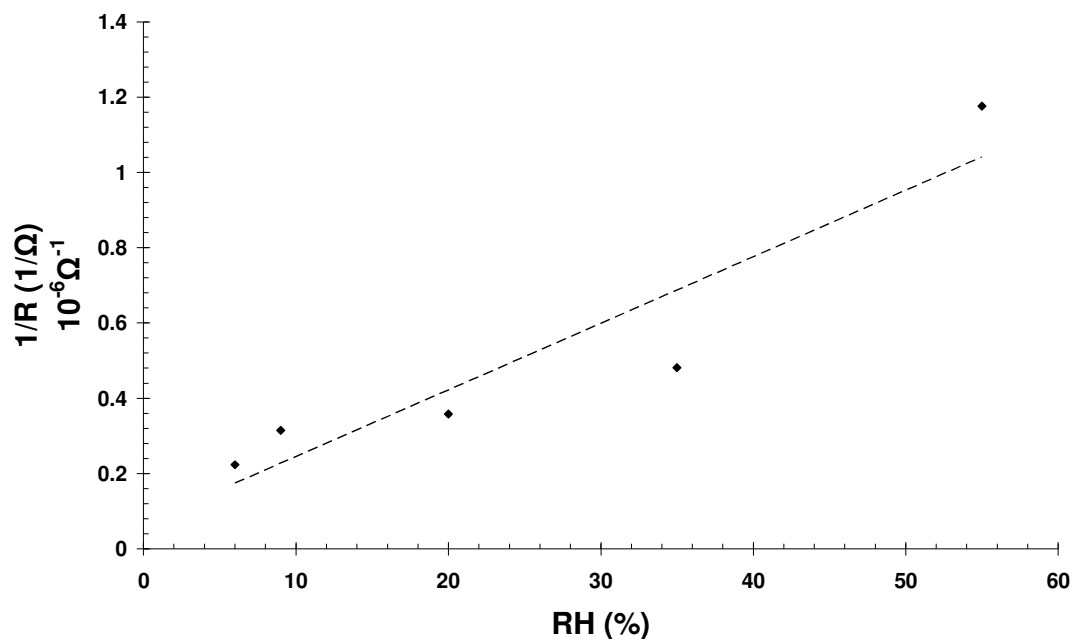


Figure 3.16: Calibration curve of sensor coatings impedance.

As described in section 1.27, electrochemical impedance spectroscopy can be used to analysis and model electrochemical systems. In this case EIS modelled the sensing coating as a modified Randles circuit (figure 3.15). A Randles circuit is an equivalent electrical circuit (a theoretical circuit that retains all of the electrical characteristics of a given circuit) commonly used in Electrochemical impedance spectroscopy (EIS) for interpretation of impedance spectra.

It consists of an active electrolyte resistance R_s in series with the parallel combination of the double-layer capacitance C_{dl} and an impedance of a faradaic reaction; often a constant phase element (CPE), is a non-intuitive circuit element that models the behaviour of a double layer, which is an imperfect capacitor, replaces the double layer capacity (C_{dl})²⁷⁻³⁰.

3.6 Sensing mechanism

The precise mechanism of the process is still unclear, although the necessity of silver nanoparticles within the sensor was confirmed by comparing the response of a coating no silver but of the same ionic strength this was achieved by the replacement of AgNO_3 with NaNO_3 in the coating synthesis. The coating containing no silver showed no response to changing humidity levels. One possible mechanism could be a form of

ionic migration with the introduction of water vapour during exposure hydrating the electrolyte (a result of synthesis process) and allowing the movement of the ions surrounding each nanoparticle, with the nanoparticles acting like a chain along which the current may flow. As the silver nanoparticles were found to have a negative zeta potential in solution, should they maintain a double layer in the cast film. Exposure of the film to water vapour could allow hydration of ions enhancing their mobility allowing the movement of ions from one nanoparticles double layer to the next.

3.7 Application of other composite films

The application of the Triton 100x stabilised layer (see section 2.6) was ineffectual as the casting of the film proved extremely difficult, with even curing at elevated temperatures 80°C producing a layer that remained tacky and viscous, this methodology of nanocomposite preparation was thus deemed unsuitable.

PVC stabilised coatings did cast well, and due to the methanol base, dispersed at a faster rate than the aqueous colloids, (2 – 3 hours rather than 18 +). The subsequent coating did show water sensing capabilities. However, their selectivity was poor, showing signal responses for several analytes listed in table 3.1, see figure 3.17.

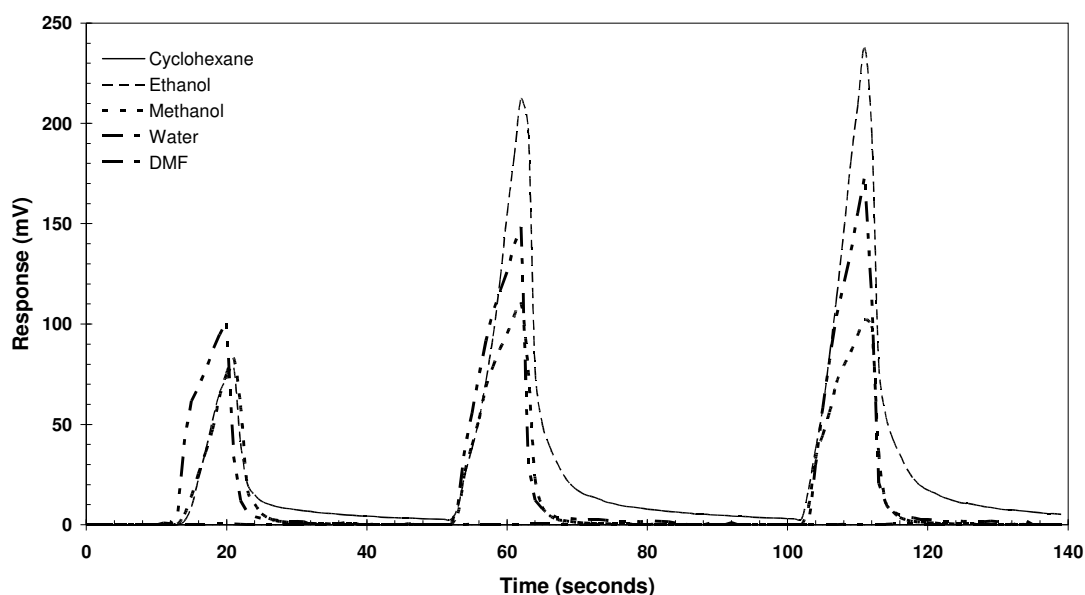


Figure 3.17: PVC stabilised sensor coating's response to exposure to various solvent vapours. Exposure was conducted using the bubbler apparatus, where the streams passing over the sensing membrane were 'switched' from the reference gas to either the test solvent (T.S.) or water vapour at 20 second intervals.

The PVC coating's response was instantaneous with preferential response seen for ethanol and methanol, no response was seen for cyclohexane so the sensor was deemed to be sensitive to polar vapours, however, this was the limit of its sensitivity.

3.8 Conclusions

The PVA stabilised aqueous based nanoparticle composite colloid when cast on an interdigital electrode array and on application of a constant potential was observed to produce a current, which was proportional to levels of humidity from 10% RH to 60% RH. The sensor gave a reversible rapid response at standard temperature and pressure. The steady state response was selective and increased with increasing levels of humidity.

The manner in which the layer is cast remains an issue, as a lack of uniformity in layer thickness impacts on the producing reproducible sensors. Work by groups such as *M.R Smyth's* in DCU have reported successful methods of inkjet printing nanocomposite based films^{31 - 32} of defined and controllable thickness for sensing applications, which supply a possible route for further investigation.

A PVC stabilised nanocomposite did respond to polar vapours, however its selectivity was low in comparison to the PVA based coating. Further investigation of the use of alternative stabilisers / composite matrices could produce similar sensors with selectivity for different analytes; however it is more likely that they would exhibit a sensing mechanism similar to those described in the literature as compared to the one illustrated above.

3.8 References

1. C. Drake, S. Deshpande, D. Bera, S. Seal, *International Materials Reviews*, 2007, 52, 289 – 317
2. P.M. Ajayan, L.S. Schadler, P.V. Braun, *Nanocomposite science and technology*, Wiley – CCH, Verlog, 2003, Ch. 1.
3. J.H. Lee, *Sensors and Actuators, B*, 2009, 140, 319 – 336
4. U. Lange, N.V. Roznyatovskaya, V.M. Mirsky, *Analytica Chimica Acta*, 2008, 614, 1 – 26
5. A. Pron, P. Rannou, *Progress in Polymer Science*, 2002, 27, 135 – 190
6. P.G Su, L.N. Huang, *Sensors and Actuators, B*, 2007, 123, 501 – 507.
7. L.J. Lee, C. Zeng, X. Cao, X. Han, J. Shen, G. Xu, *Composites Science and Technology*, 2005, 65, 2344 – 2363
8. Y. Li, M.J. Yang, Y. She, *Talanta*, 2004, 62, 707 – 712
9. A. Walcarius, D. Mandler, J.A. Cox, M. Collinson, O.J. Lev, *Journal of Materials Chemistry*, 2005, 15, 3663 – 3689
10. B. Adhikari, S. Majumdar, *Progress in Polymer Science*, 2004, 29, 699 – 766
11. R. Tarushee Ahuja, D. Kumar, *Sensors and Actuators, B*, 2009, 136, 275 – 286
12. H. Bai, G.Q. Shi, *Sensors*, 2007, 7, 267 – 307
13. M.J. Hostetler, S.J. Green, J.J. Stokes, R.W. Murray, *Journal of the American Chemical Society*, 1996, 118, 4212 – 4213
14. M.J. Hostetler, A.C. Templeton, R.W. Murray, *Langmuir*, 1999, 15, 3782 – 3789
15. Z. Yan, M.J. Sousa-Gallagher; F.A.R Oliveira, *Journal of Food Engineering*, 2008, 84, 359 – 367
16. R.P. Singh, *Shelf life evaluation of foods*, C.M.D. Man, A.A. Jones, Eds, Blackie Academic & Professional, Glasgow, 1992, 3 – 24
17. E.L.J. Goossens, A.J.J. van der Zanden, W.H. van der Spoel, *Progress in Organic Coatings*, 2004, 49, 270 – 274
18. T.L. Yeo, T. Sun and K.T.V. Grattan, *Sensors and Actuators, A*, 2008, 144, 280 – 295
19. C.Y. Lee, G.B. Lee, *Sensor Letters*, 2005, 3, 1 – 15
20. Z. M. Rittersma, *Sensors and Actuators, A*, 2002, 96, 196 – 210
21. G. Jimenez – Cadena, J. Riu, F. Xavier Rius, *Analyst*, 2007, 132, 1083 – 1099
22. www.bvt.cz/_files/438/cc2.pdf (last accessed February 2011)

- 23.** CRC Handbook of Chemistry and Physics, D.R. Lide, Editor in chief, 89th ed., Boca Raton, Fla, CRC; London, Taylor & Francis, (2008)
- a.** pp 6 – 163
 - b.** pp 8 – 138
 - c.** pp 8 – 140
 - d.** pp 8 – 139
 - e.** pp 6 – 4
- 24.** A. Sinha, B. P. Sharma, *Bulletin of Materials Science*, 2005, 28, 3, 213 – 217
- 25.** Y. Joseph, B. Guse, A. Yasuda, T. Vossmeier, *Sensors and Actuators, B*, 2004, 98, 188 – 195
- 26.** CRC Handbook of Chemistry and Physics, D.R. Lide, Editor in chief, 89th ed., Boca Raton, Fla, CRC; London, Taylor & Francis, 2008, 15 – 33 – 15 – 34
- 27.** http://www.gamry.com/App_Notes/EchemImpedanceSpecs.htm
- 28.** http://www.gamry.com/App_Notes/EIS_Primer/Basics_Of_%20EIS.pdf
- 29.** A. Lasia, *Electrochemical Impedance Spectroscopy and Its Applications, Modern Aspects of Electrochemistry*, Kluwer Academic/Plenum Publishers, New York, 1999, 32, 143-248
- 30.** J.R. Macdonald, *Annals of Biomedical Engineering*, 1992, 20, 289 – 305
- 31.** N. Lenhart, K. Crowley, A.J. Killard, M.R. Smyth, A. Morrin, *Thin Solid Films*, 2011, 519, 4351 – 4356
- 32.** K. Crowley, A. Morrin, R.L. Shepherd, M. Panhuis, G.G. Wallace, M.R. Smyth, A.J. Killard, *IEEE SENSORS JOURNAL*, 2010, 10, 1419 – 1426.

4. Surface enhanced resonance Raman spectroscopy with tuneable silver colloids

4.1 Introduction

Chemical sensing is an area where the novel physiochemical properties metallic nanostructures often exhibit can make a significant impact on both innovative and existing devices and techniques. This is possibly best illustrated by the impact of coinage nanoparticles on Raman spectroscopy. Silver nanoparticles have proved to be good candidates for use in Surface Enhanced Raman Spectroscopy (SERS), exhibiting the dual roles of both substrate and signal enhancers¹⁻².

SERS amplifies an inherently weak Raman signal using a catalyst, typically of the nanoscale. Nanoparticles (NPs) of noble metals have been found particularly useful as they exhibit surface plasmon resonance (SPR)³⁻⁴. This SPR involves a collective oscillation of the conduction electrons in resonance with certain frequencies of incident light, where the plasmon resonance of the metallic nanoparticles (colloids) provides the intense optical frequency fields responsible for the electromagnetic contribution to SERS signal⁵⁻⁹. It follows that by coupling these two means of signal enhancement, resonance Raman and SERS, the sensitivity of Raman as an analytical is further enhanced.

As described in section 1.20 SERS is a surface technique, with amplification of analyte signal a consequence of plasmon resonances at the substrate's surface, it follows that the choice of substrate used with the technique is very important.

Throughout the literature the significant majority of SERS substrates are nano metallic (predominately gold or silver) as the two metals exhibit the 'right' optical properties to support plasmons in the visible / near infrared range. These substrates are generally divided into three classes¹⁰.

- Metallic electrodes; SERS very discovery was through Fleischmann's work with silver electrodes in 1974. Recently the use of electrodes in the technique has reduced as the development of other substrates has advanced.
- Metallic particles (generally nano) in solutions – colloids; silver and gold colloids are ubiquitous in the literature as SERS substrates, having the advantage of stability in water coupled with the ability to maintain the necessary plasmonic energy to provide SERS enhancement. Additionally these

colloids may be used to fabricate simple planar metallic structures, by attachment to a suitable surface or simple drying/casting.

- ‘Planar’ metallic structures, the development of ordered planar nano metal surfaces has advanced rapidly in the last decade and continues to be a field of extensive research as specific applications, reliability, reproducibility and further optimisation/ enhancement of signal drives research.

The application of SER(R)S, (surface enhanced (resonance) Raman spectroscopy), as an analytical tool is increasing, with the potential to elevate the sensitivity of an already highly selective detection technique^{11 - 12}. The key to SERS is the surface plasmon resonances (SPR) of the SERS substrates. The literature shows that the high local electromagnetic fields associated with nanostructures due to their uniform electron oscillations, are major contributors to the signal enhancement¹³.

As described in section 1.21, many studies have determined that the SPR behaviour of a SERS substrate is dependent not merely on the interaction of the analyte and a single nanoparticle but the interaction between multiple nanostructures, leading to extensive research into the pairing of nanoparticles with the aim of producing ‘hot spots’ or areas of massive SERS enhancement^{6, 14 - 15}.

Classically these hot spots are produced in colloids by the creation of inter – particle junctions via the deliberate addition of aggregation agents such as potassium chloride, sodium chloride and hydrochloric acid.

However, these destabilised NPs aggregate in a non uniform manner and are prone to coagulate and precipitate, which increases the difficulty of use and ultimately results in SERS signals that are difficult to reproduce^{3, 5, 11 - 12, 16 - 17}. Because of this a deliberate decision was made to examine the effectiveness of the tuneable silver colloids, produced in chapter 2, as SERS substrates without the deliberate addition of an aggregating agent.

4.2 Experimental

The maximum SERS enhancement is expected to take place when the λ_{max} of the localised SPR of the nanoparticles is close to that of the excitation (laser) wavelength, both the Raman scattered photon and the incident photon are strongly enhanced^{9, 18 -}

¹⁹. The blue colloid (λ_{max} , 670 nm) was used to enhance measurements excited by the 660 nm laser.

SERS active measurements were conducted on three model analytes, crystal violet (Cr.V.), malachite green (MG) and Rhodamine 6G (R6G), and were performed with a Horiba Jobin Yvon LabRAM HR 800. SERS excitation was provided by solid state Diode laser with a maximum power of 100 mW. For conventional operation, the light is imaged to a diffraction limited spot (1 μm) via the Olympus m – plan 10 x objective, focal length 10.6 mm. The scattered light is collected by the objective in a confocal geometry, and is dispersed onto a Peltier cooled CCD array by 600 lines/mm grating, allowing the range from 150 cm^{-1} to 4000 cm^{-1} . The confocal, microscopic system allowed direct measurement of liquids and solutions and all measurements were performed with the laser at 1% strength. The spectral region of investigation was dependent on the analyte, 700 – 1200 cm^{-1} for Cr.V., 1000 – 1800 cm^{-1} for MG and 200 – 2000 cm^{-1} for R6G. Emphasis was placed on the use of the technique as an analytical tool, and as short sampling times are the ideal, in each case the exposure time was 5 seconds with the accumulation set to 20, ensuring that the total sampling time was never greater than 5 minutes.

4.2.1 SERS measurements

The performances of the colloids as SERS active agents were evaluated by their SERS activity using Cr.V., MG, and R6G as model compounds (figure 4.1.a). These dyes are commonly used as probe molecules for Raman specifically because they display intense Raman scatter due to the similarity of their electronic energies to the incident radiation, figure 4.1b.

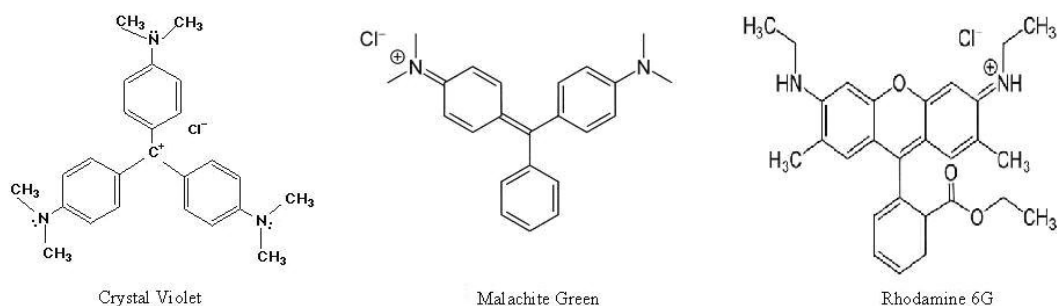


Figure 4.1a: Molecular structures of Crystal Violet, Malachite Green and Rhodamine 6G.

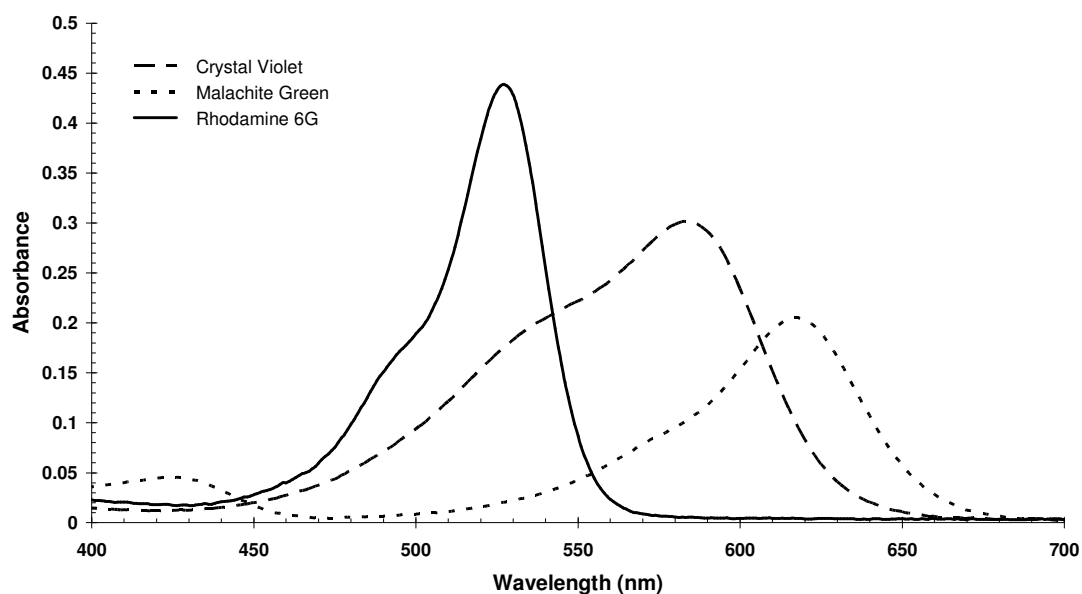
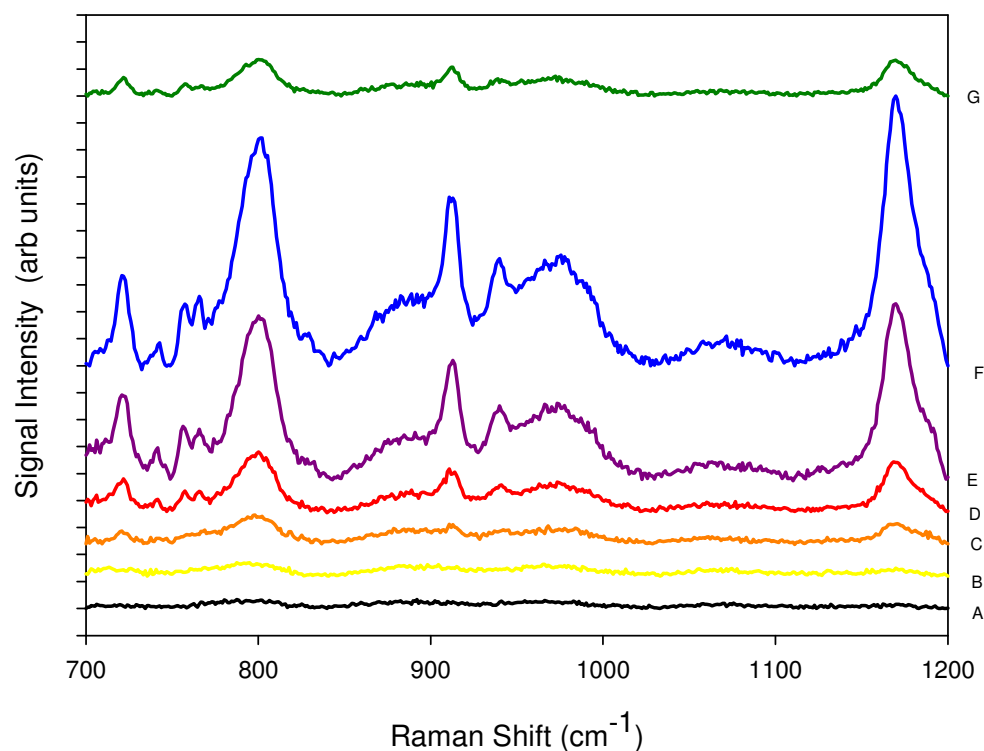


Figure 4.1b: Absorption spectra of probe dyes, Crystal Violet, Malachite Green and Rhodamine 6G.

All dyes were made up to 10^{-4} M aqueous solutions; further dilution occurred during the sampling process, producing samples with a final concentration of 3.33×10^{-5} M. (All volumes were maintained at 3cm^3 ensuring consistent concentrations.) Water molecules give very weak Raman scatter allowing analytes in aqueous solutions to be readily detected and identified in situ without separation at low concentrations.

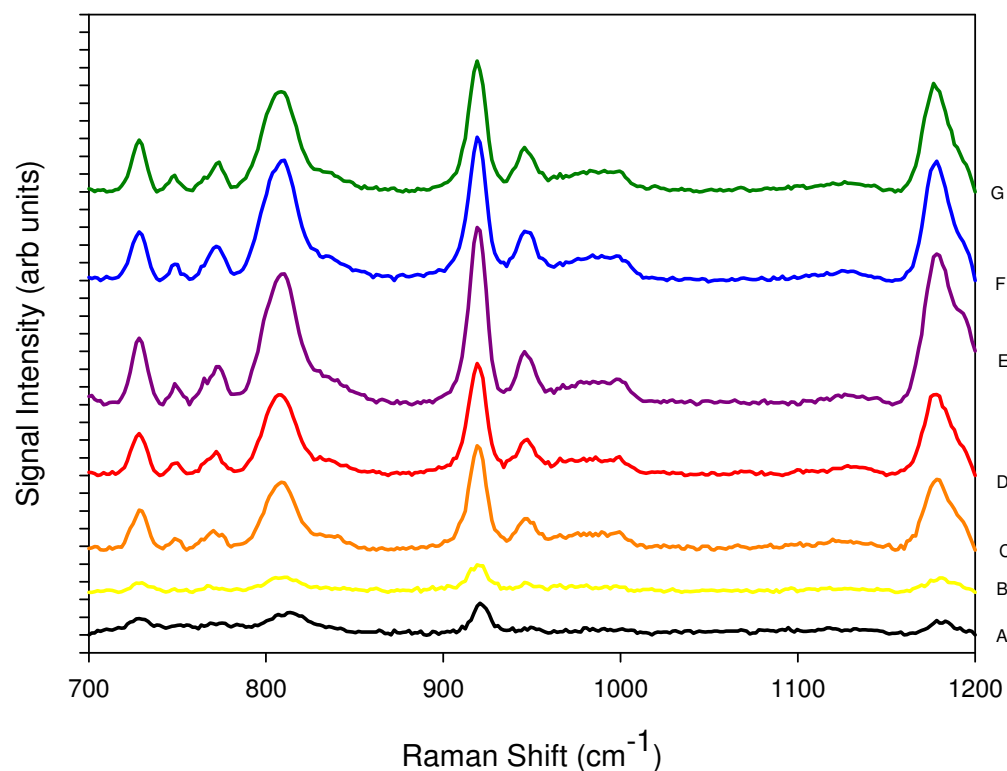
Liquid samples and SERS catalysts also enabled reproducible sampling where the constant disorder/movement (Brownian motion) of both the analyte and colloid produce a stable and reproducible system. This, coupled with the use of the confocal microscope on the Horiba Jobin Yvon LabRAM HR 800, had the advantage of creating a high power density in a small volume with a relatively weak laser, where the particles readily move in and out of the analysis volume during the measurement. This reduces problems with photodegradation that can be seen with other SERS substrates ¹¹.



- A: 3.3×10^{-5} Cr.V only
- B: 3.3×10^{-5} Cr.V + yellow colloid
- C: 3.3×10^{-5} Cr.V + orange colloid
- D: 3.3×10^{-5} Cr.V + red colloid
- E: 3.3×10^{-5} Cr.V + purple colloid
- F: 3.3×10^{-5} Cr.V + blue colloid
- G: 3.3×10^{-5} Cr.V + green colloid

Figure 4.2a: Raman Spectra of 3.33×10^{-5} M Cr.V. mixed with each colloid with excitation by the 660 nm laser. $[\text{Ag}] = 11 \times 10^{-5}$ M, for colours makeup please refer to Table 2.1 chapter 2.

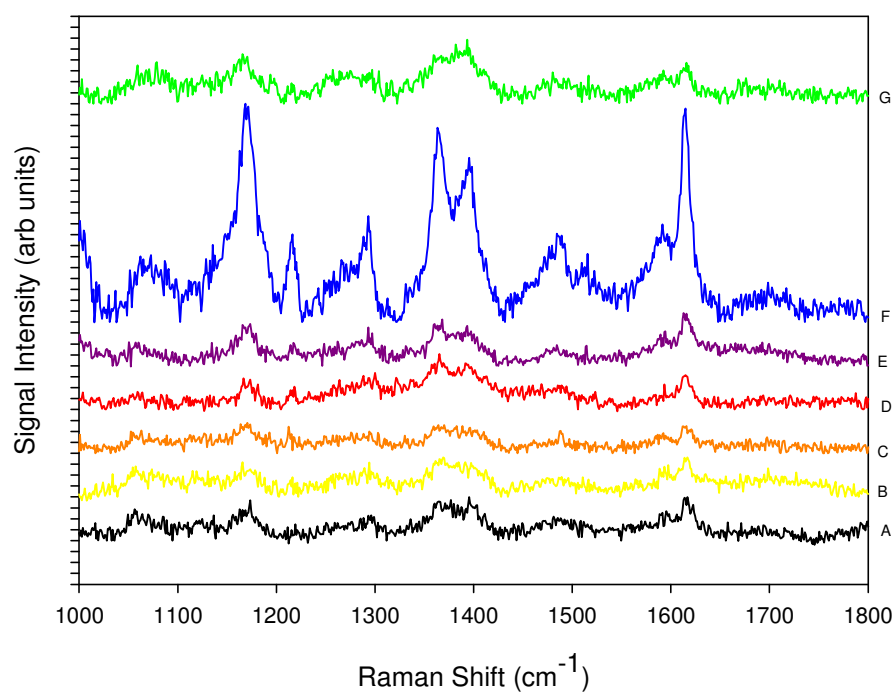
Figure 4.2a shows the SERS spectra of sample, where the Cr.V. concentration was 3.33×10^{-5} M and the silver concentration was 11×10^{-5} M in each case. As expected, based on the literature^{9, 20 - 21}, initial analysis of Cr.V with the 660 nm laser shown in figure 4.2a indicated that the blue colloid was the most effective SERS catalyst because it's nanoparticle's LSPR (localised SPR) was slightly longer than that of the excitation wavelength. Similarly the purple colloid was found to be the most effective (figure 4.2b) with excitation by the 532 nm laser for enhancing the signal.



- A: 3.3×10^{-5} Cr.V only
- B: 3.3×10^{-5} Cr.V + yellow colloid
- C: 3.3×10^{-5} Cr.V + orange colloid
- D: 3.3×10^{-5} Cr.V + red colloid
- E: 3.3×10^{-5} Cr.V + purple colloid
- F: 3.3×10^{-5} Cr.V + blue colloid
- G: 3.3×10^{-5} Cr.V + green colloid

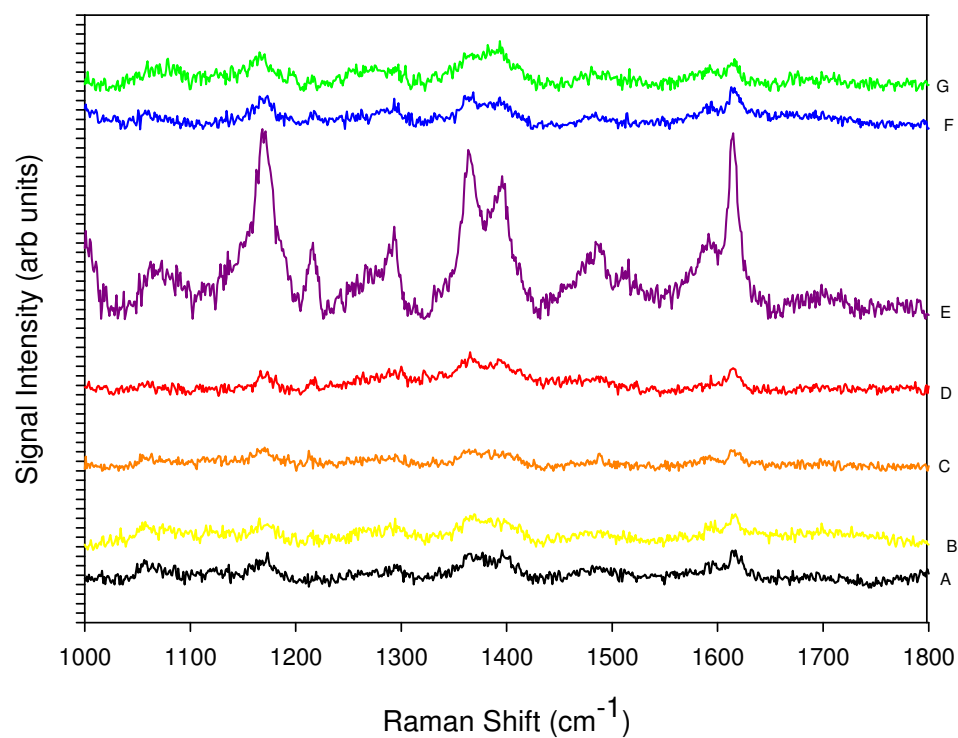
Figure 4.2b: Raman Spectra of 3.33×10^{-5} M Cr.V. mixed with each colloid with excitation by the 532 nm laser. $[\text{Ag}] = 11 \times 10^{-5}$ M.

Similar results were observed for MG and R6G, figures 4.3a to 4.3c (note R6G measurements were only conducted at the 660 nm excitation wavelength as the dye fluoresces when excited at 532 nm.) Therefore, for all measurements at the 660 nm excitation, the blue colloid's nanoparticles were used as the SERS substrate and the purple colloid's nanoparticles used for measurements excited by the 532 nm laser. It should be noted that as the overall silver concentration of each coloured colloid varied, it was necessary to dilute each sample to a set volume (3 cm^3) after addition of the nanoparticles to maintain consistent experimental conditions throughout the study.



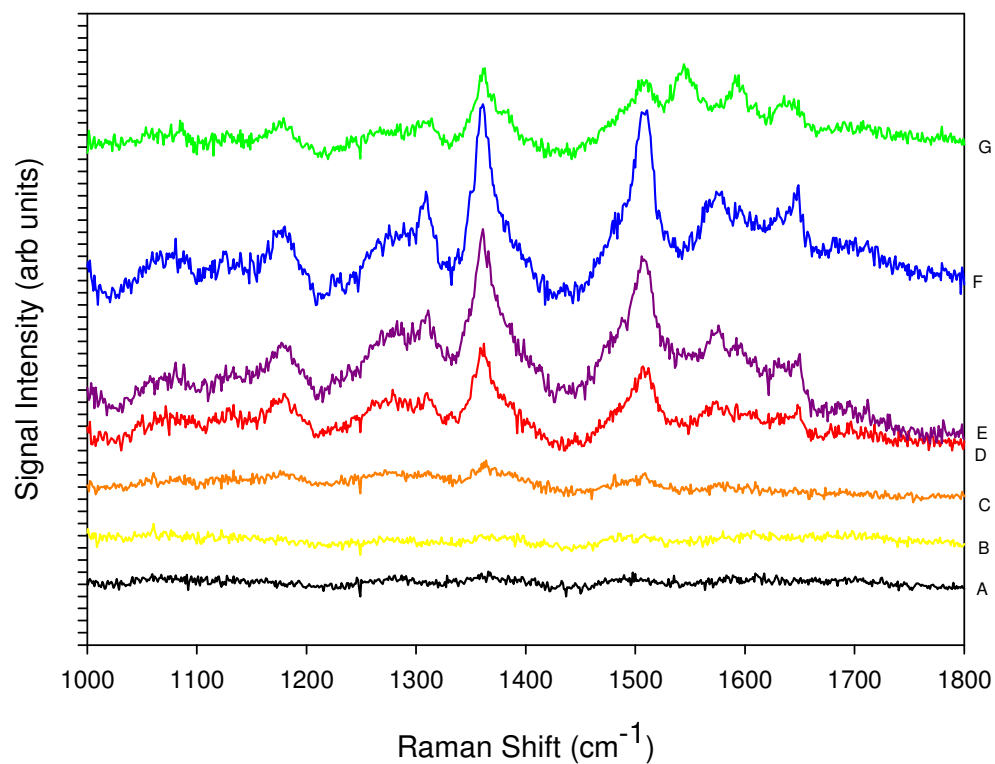
- A: 3.3×10^{-5} M.G. only
- B: 3.3×10^{-5} M.G. + yellow colloid
- C: 3.3×10^{-5} M.G. + orange colloid
- D: 3.3×10^{-5} M.G. + red colloid
- E: 3.3×10^{-5} M.G. + purple colloid
- F: 3.3×10^{-5} M.G. + blue colloid
- G: 3.3×10^{-5} M.G. + green colloid

Figure 4.3a: Raman Spectra of M.G. 3.33×10^{-5} M mixed with each colloid with excitation by the 660 nm laser. $[Ag] = 11 \times 10^{-5}$ M.



- A: 3.3×10^{-5} M.G. only
- B: 3.3×10^{-5} M.G. + yellow colloid
- C: 3.3×10^{-5} M.G. + orange colloid
- D: 3.3×10^{-5} M.G. + red colloid
- E: 3.3×10^{-5} M.G. + purple colloid
- F: 3.3×10^{-5} M.G. + blue colloid
- G: 3.3×10^{-5} M.G. + green colloid

Figure 4.3b: Raman Spectra of M.G. 3.33×10^{-5} M mixed with each colloid with excitation by the 532 nm laser. $[\text{Ag}] = 11 \times 10^{-5}$ M.



- A: 3.3×10^{-5} R6G only
- B: 3.3×10^{-5} R6G. + yellow colloid
- C: 3.3×10^{-5} R6G + orange colloid
- D: 3.3×10^{-5} R6G + red colloid
- E: 3.3×10^{-5} R6G + purple colloid
- F: 3.3×10^{-5} R6G + blue colloid
- G: 3.3×10^{-5} R6G + green colloid

Figure 4.3c: Raman Spectra of R6G 3.33×10^{-5} M mixed with each colloid with excitation by the 660 nm laser. $[Ag] = 11 \times 10^{-5}$ M.

Comparison of the enhancement observed at both excitation wavelengths pointed to a greater enhancement being observed when the experimental conditions were set to a laser excitation wavelength of 660 nm, using the blue colloid.

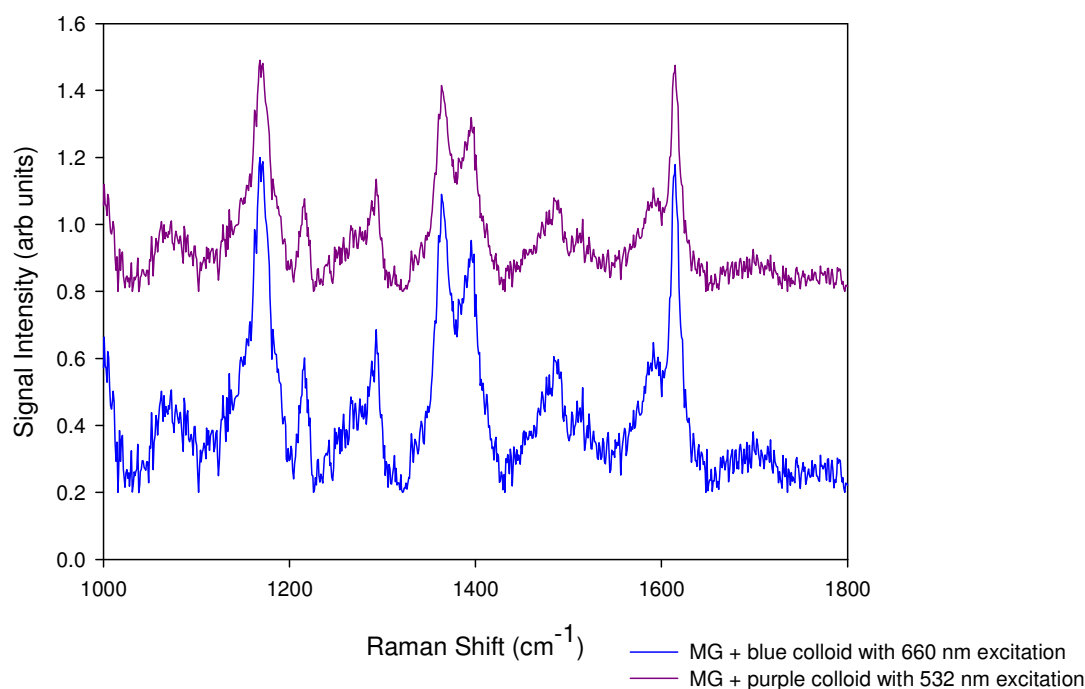


Figure 4.3d: Comparison of MG spectra (with best colloid enhancement) at the different excitation wavelengths with $[Ag] = 11 \times 10^{-5}M$.

4.2.2 Dye and colloid interaction

It is necessary to determine the effect of the analyte (if any) on the colloids as unwanted aggregation of nanoparticles despite the use of PVA as a stabiliser^{22 - 25} remains a concern. DLS was used to monitor the particles with increasing concentrations of dye.

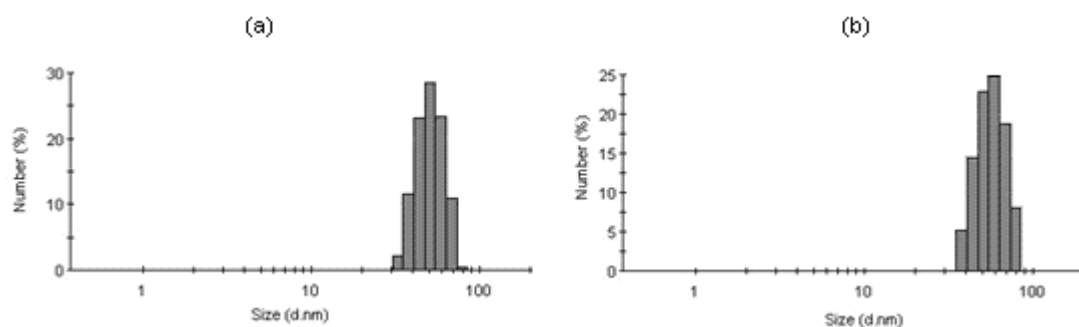


Figure 4.4. Effect of the Dye on the particle size range of the colloidal nanoparticles, (a) silver colloid (blue) $[Ag] = 1 \times 10^{-5}M$, (b) silver colloid (blue) $[Ag] = 1 \times 10^{-5}M$ with excess crystal violet $[Cr.V.] = 5 \times 10^{-5}M$.

Some aggregation occurs when the analyte is present, although the extent of aggregation is limited the bulk of the nanoparticles maintained an average diameter range of 58 – 60 nm.

This aggregation can have a significant impact on the SERS mechanism, as it is generally accepted that the greatest SERS enhancement is produced by electromagnetic hotspots that are produced during the interaction of coinage nanoparticles, with dimers or small clusters of colloidal coinage particles producing the strongest localised fields and hence Raman enhancement^{26–28}

4.3 Sensing Trend

The relevant colloids were then added incrementally to a set volume of the model compounds, and their Raman spectra recorded with each increase of the blue colloid's NPs. In doing so, the following trends were observed (figures 4.5 – 4.10). Figure 4.5 shows the SERS spectra of 3.33×10^{-5} M Cr.V. with the blue colloid's NPs prepared as described in section 2.5. Figure 4.6 shows the peak emissions observed with increasing concentrations of silver at certain wavelengths taken from figure 4.5. Similarly figure 4.8 comes from figure 4.7 where the SERS spectra of 3.33×10^{-5} M MG with the blue colloid's NPs is displayed and figure 4.10 comes from figure 4.9 where the SERS spectra of 3.33×10^{-5} M R6G with the blue colloid's NPs is illustrated. The bands of the Raman spectra of each analyte were assigned (table 4.1).

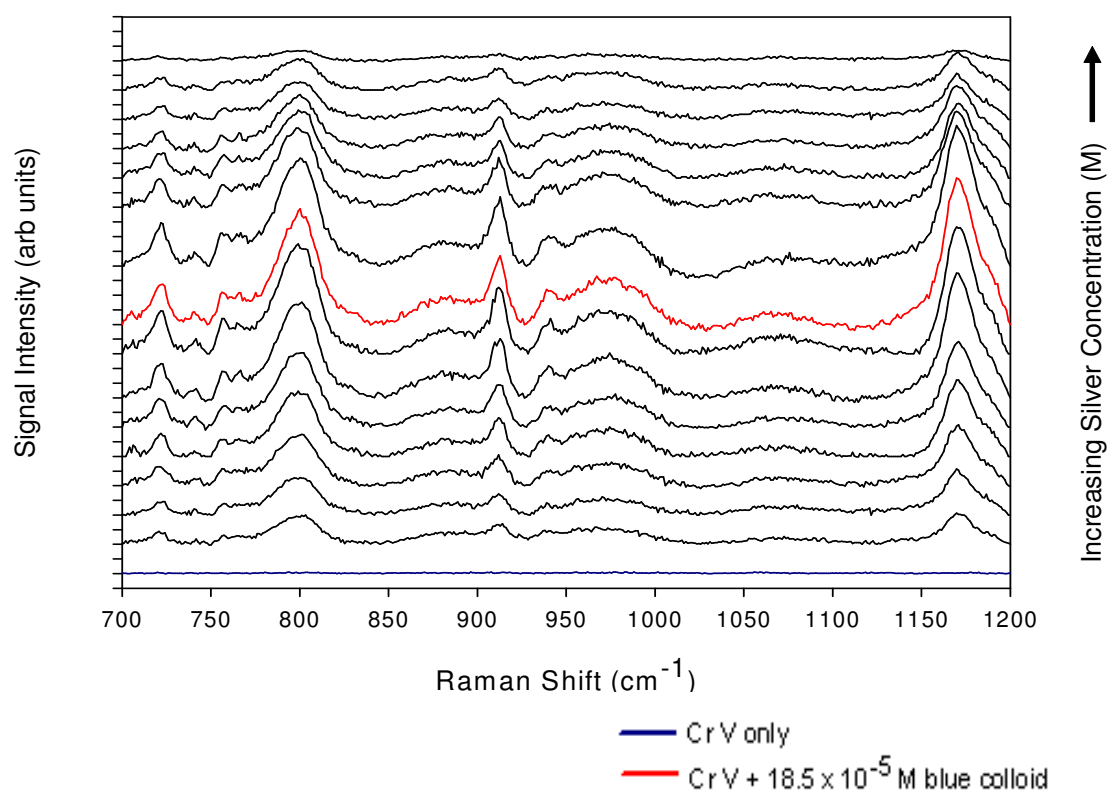


Figure 4.5: Raman Spectra of 3.33×10^{-5} M Cr.V. with increasing concentrations of the blue colloid's NPs with excitation by the 660 nm laser.

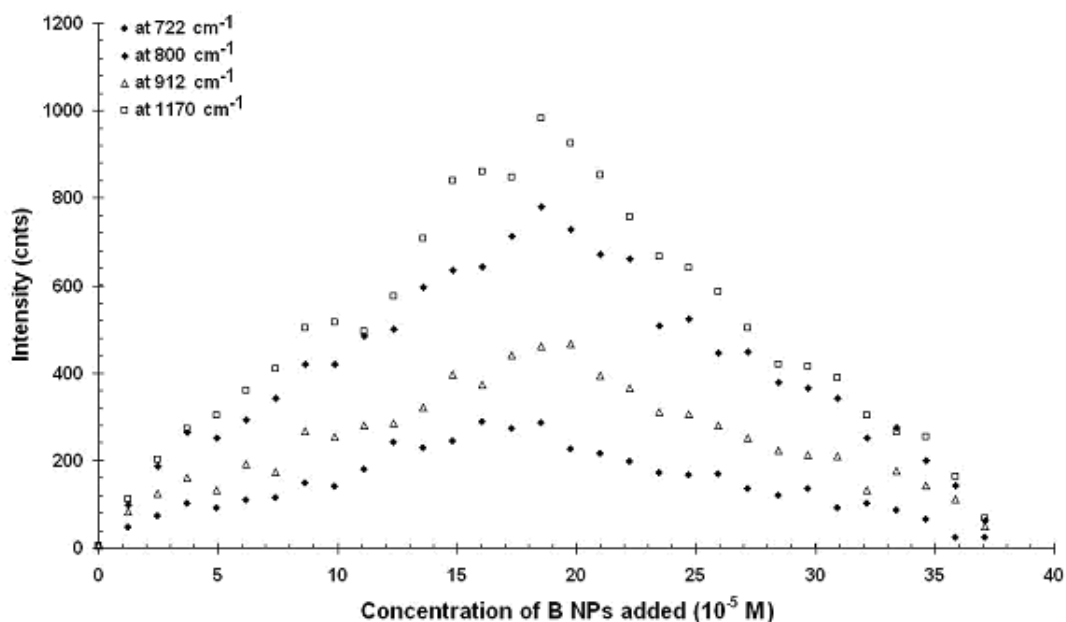
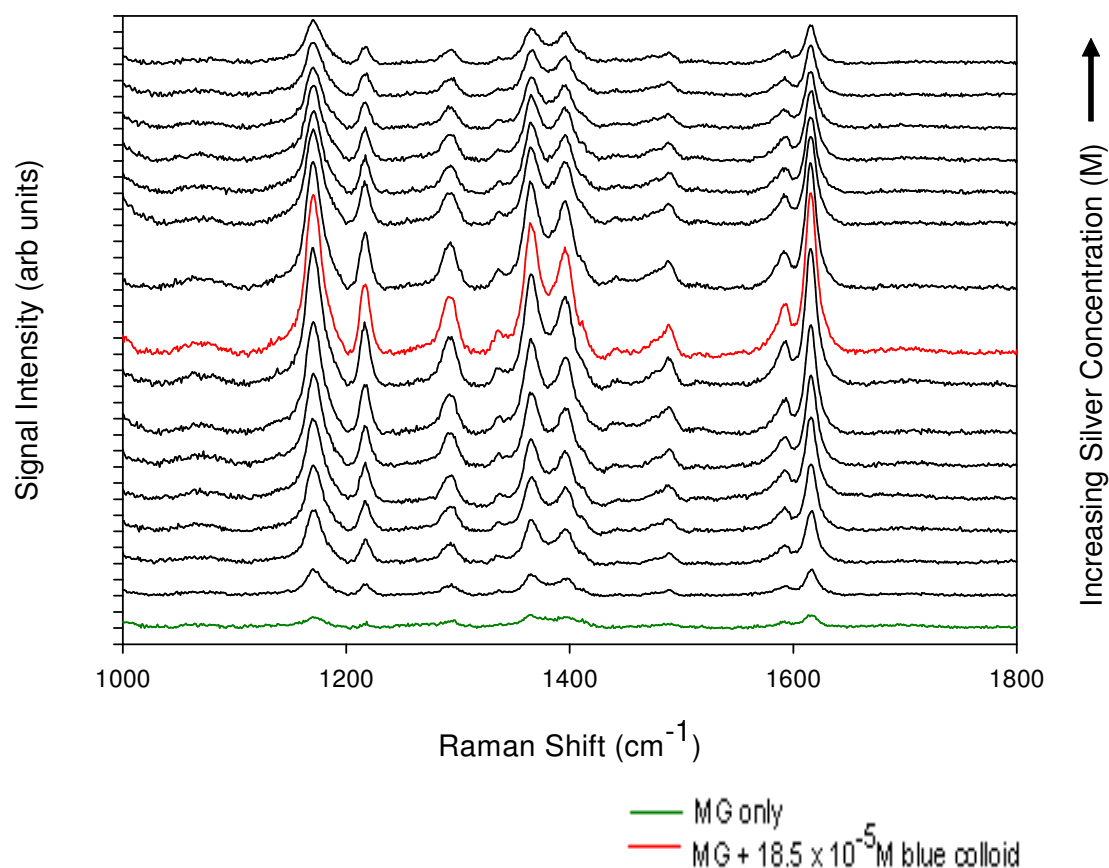


Figure 4.6: Observed Raman spectra emission trend of 3.33×10^{-5} M Cr.V. with increasing concentrations of the blue colloid's NPs with excitation by the 660 nm laser.

Compound	Peak Assignment ²⁹⁻³¹
Crystal Violet	<ul style="list-style-type: none"> • $\sim 722\text{cm}^{-1}$, In plane benzene ring bend, stretch • $\sim 800\text{cm}^{-1}$, out of plane aromatic C-H 'breathing' • $\sim 914\text{cm}^{-1}$, ring skeletal radial vibration • $\sim 1170\text{cm}^{-1}$, in plane aromatic C-H bending vibration
Malachite Green	<ul style="list-style-type: none"> • $\sim 1170\text{cm}^{-1}$, in plane aromatic C-H bending vibration • $\sim 1365\text{cm}^{-1}$, N-C stretch • $\sim 1395\text{cm}^{-1}$, C-C and C-H in plane motion (aromatic) • $\sim 1615\text{cm}^{-1}$, N-C (ϕ bond) and C-C stretch
Rhodamine 6G	<ul style="list-style-type: none"> • $\sim 610\text{cm}^{-1}$, C-C-C in plane aromatic vibration • $\sim 769\text{cm}^{-1}$, C-H out of plane bending • $\sim 1181\text{cm}^{-1}$, C-H in plane bending • $\sim 1316\text{cm}^{-1}$ and $\sim 1573\text{cm}^{-1}$ in plane bending • $\sim 1361\text{cm}^{-1}$, $\sim 1508\text{cm}^{-1}$ and 1648cm^{-1}, aromatic C-C stretching

Table 4.1: Probe molecules Raman spectra peak assignment.

Figure 4.7: Raman Spectra of 3.33×10^{-5} M MG with increasing concentrations of the blue colloid's NPs with excitation by the 660 nm laser.

In all cases, a clear build up of signal intensity is observed, until the optimum ratio is achieved, followed by a decline in signal intensity as the volume of NPs is further increased as seen in figures 4.6, 4.8 and 4.10.

Several explanations for this observed response are possible. For example an orientation change. That is at low concentrations, the analyte molecules could lie flat on the silver surface. However as the concentration increases, it is possible that the analyte 'stands-up' so although it is still adsorbed to the nanostructures surface it does so in a different way. Therefore the analyte is less able to benefit from the effect of the plasmons on the polarisation³².

Where the amount of NPs relative to the analyte increases, a decrease in signal is observed as the NPs block the incident light from accessing the entire analyte sample in the cuvette. It is also possible that there is not enough analyte compared to the volume of NPs, and thus despite the production of the plasmons from the silver NPs, the analyte itself is diluted by sheer numbers.

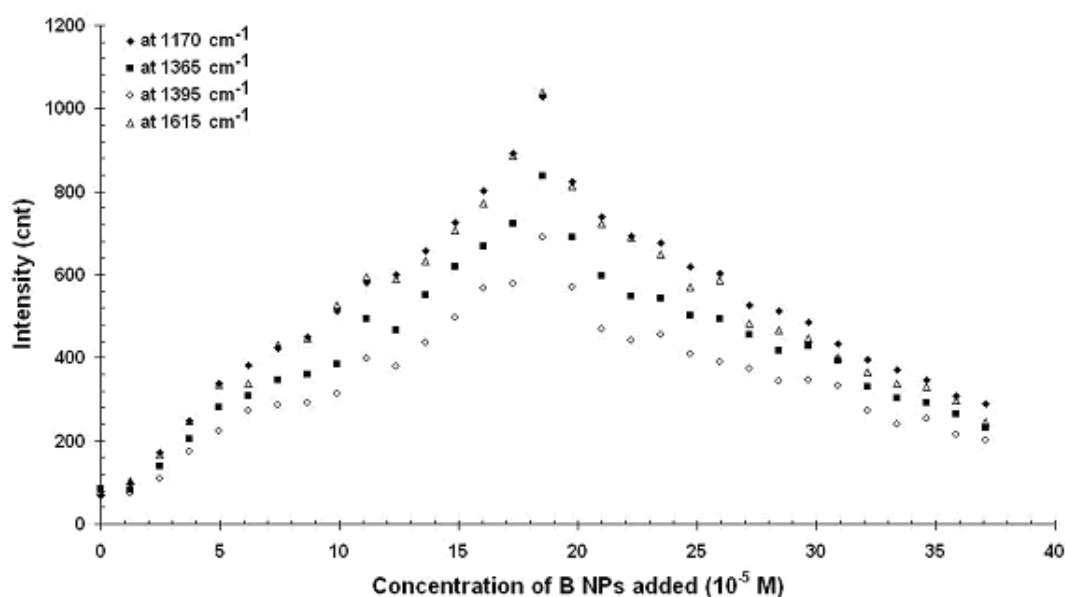


Figure 4.8: Observed Raman spectra emission trend of 3.33×10^{-5} M MG with increasing concentrations of the blue colloid's NPs with excitation by the 660 nm laser.

This is suggested by the observation that as the concentration of analyte is increased or decreased; the concentration of silver NPs is also observed to shift in order to

maintain the ratio observed at other concentrations, as illustrated in figures 4.11 and 4.12 by the SERS spectra of 10^{-7} M Cr.V with increasing nanoparticle concentrations. This seems unlikely however as a dropping off of signal is observed at higher concentrations of silver, since no change in the spectra was observed (whereas a 'levelling' of signal would be the expected result, correlating with better known adsorption models like Langmuir).

An alternative explanation could be due to the nature of the nanoparticles themselves. Because coinage metals support plasmons, the interactions of nanoparticles within the colloid system can generate intense electric fields when illuminated producing high SERS enhancement^{30,32}. Therefore, the continued addition of nanoparticles increases the interaction of nanoparticles with each other resulting in a large 'background' of plasmonic activity, which could mask or shield the very analyte signal that the SERS technique aims to enhance.

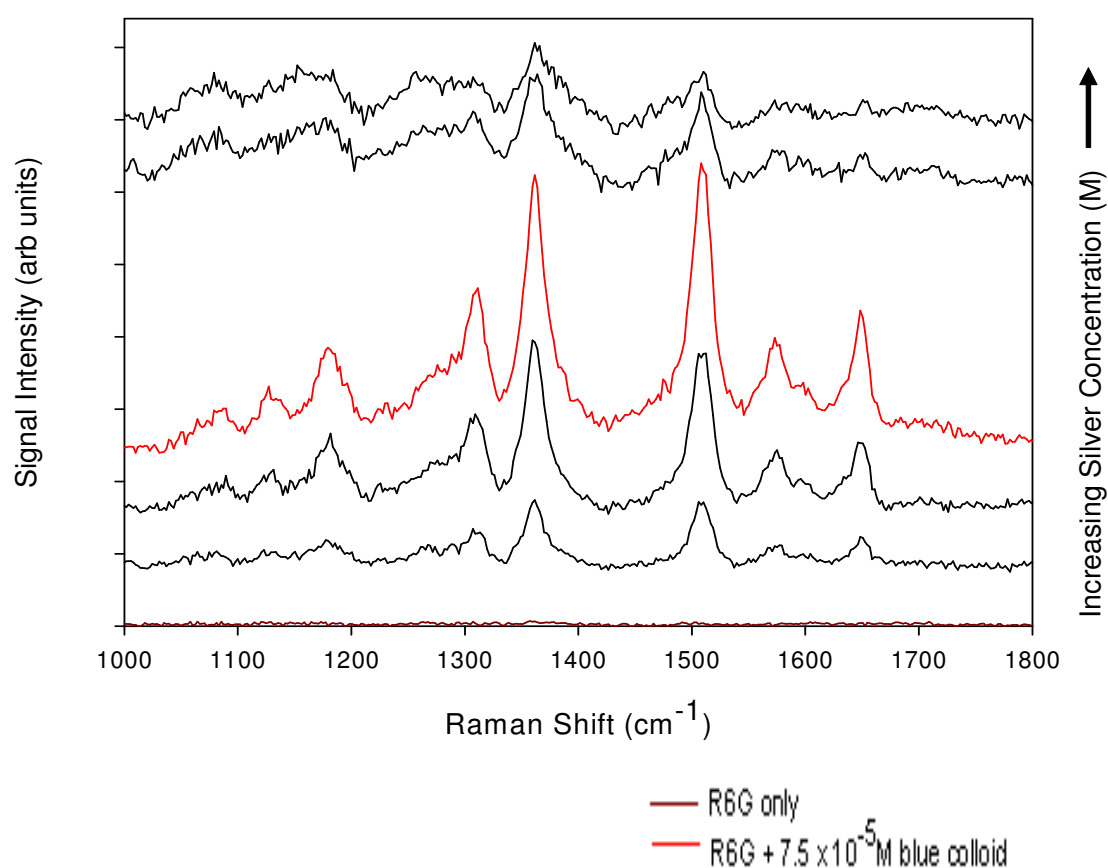


Figure 4.9: Raman Spectra of 3.33×10^{-5} M R6G with increasing concentrations of the blue colloid's NPs with excitation by the 660 nm laser.

It also must be noted that in each case the maximum SERS effect is seen for bands associated with the aromatic activity of each dye, bands $\sim 800\text{ cm}^{-1}$ and $\sim 1170\text{ cm}^{-1}$ for Cr.V. (figures 4.5 & 4.6), bands $\sim 1170\text{ cm}^{-1}$ and $\sim 1615\text{ cm}^{-1}$ for MG (figures 4.7 & 4.8) and bands $\sim 1361\text{ cm}^{-1}$ and $\sim 1508\text{ cm}^{-1}$ for R6G²⁹⁻³¹ (figures 4.9 & 4.10), implying that the structure of the analyte too has a role in the sensing mechanism. Thus it is unsurprising that Cr.V. and MG show similar sensing trends as structurally they share common attributes, in contrast to R6G which is markedly different in structure, (figure 6), from the other model dyes.

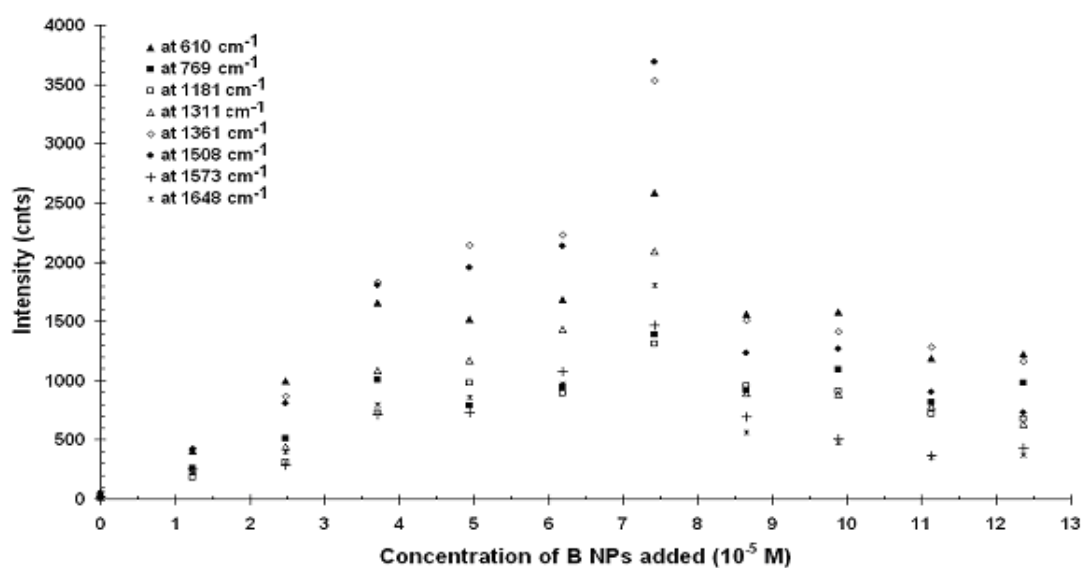


Figure 4.10: Observed Raman spectra emission trend of $3.33 \times 10^{-5}\text{ M}$ R6G with increasing concentrations of the blue colloid's NPs with excitation by the 660 nm laser.

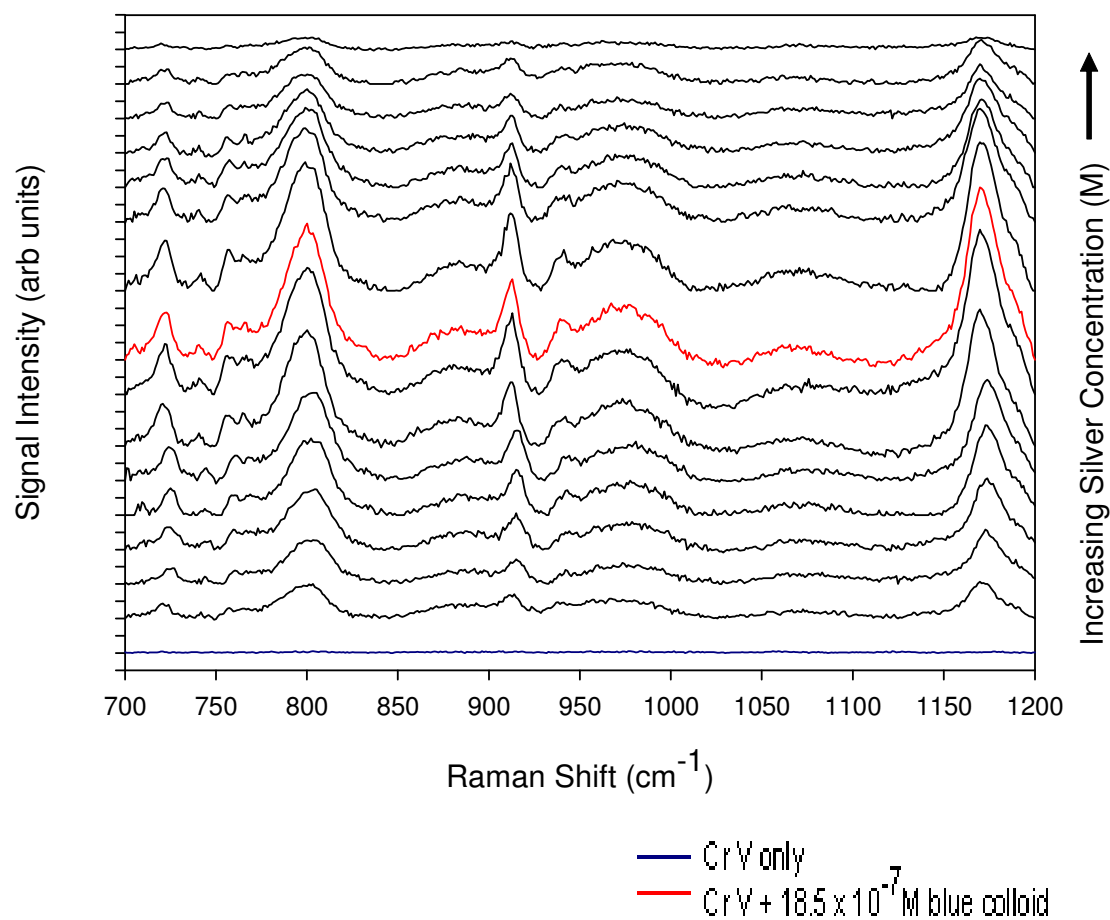


Figure 4.11: Raman Spectra of 3.33×10^{-7} M Cr.V. with increasing concentrations of the blue colloid's NPs with excitation by the 660 nm laser.

The role of the analyte's structure is also emphasised when looking at figures 4.6 and 4.8, where the dyes Cr.V. and MG both show a maximum signal at $\sim 18.5 \times 10^{-5}$ M Ag nanoparticles, a maximum signal enhancement at 1170 cm^{-1} and a maximum enhancement with the Ag : analyte molar ratio of $\sim 5.56 : 1$. Whereas R6G (figure 4.10) shows a maximum signal at $\sim 7.5 \times 10^{-5}$ M Ag nanoparticles, a maximum signal enhancement at 1508 cm^{-1} and a maximum enhancement with the Ag : analyte molar ratio of $\sim 2.25 : 1$. The Ag : dye ratio for R6G is approximately 40% of that of the other two dyes (Cr.V. and MG) which may indicate a different mode of adsorption, and further illustrates the importance of the analyte's structure.

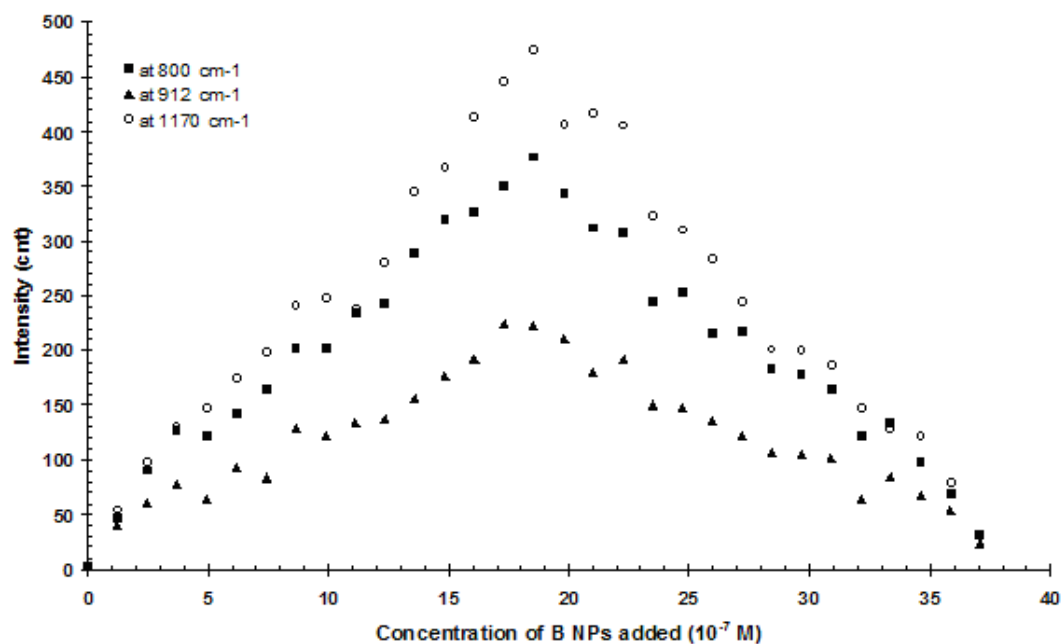


Figure 4.12: Observed Raman spectra emission trend of 3.33×10^{-7} M Cr.V. with increasing concentrations of the blue colloid's NPs with excitation by the 660 nm laser.

The focal length of the objective is also relatively long, and as a result there was an increase in signal noise due to stray scatter; however the large working distance allowed greater flexibility in the experimental setup, particularly in later studies (chapters 5 and 6).

Another issue is the determination of the limit of detection as it is dependent on the instrument's own parameters, adjustment of laser intensity and increasing sample acquisition times can have a drastic effect on the intensity of signal obtained. However this too can increase total sampling times and costs, which impact negatively upon the application of SERS as an analytical technique.

As Raman is non destructive and highly selective (providing a spectral fingerprint of the analyte), this enhancement, coupled with the short sampling time clearly demonstrates the potential of SERS as a rapid and highly sensitive sensing technique, within analytical chemistry.

However it is clear that further investigation is necessary regarding the manner in which the silver NPs are introduced to the system. Although the colloids clearly demonstrated signal enhancement, the level of method optimisation necessary for each individual analyte limits the technique, consequently driving significant research of the fabrication of reproducible SERS active substrates.

4.4 Conclusions

Silver colloids with tuneable λ_{max} 's; produced by a simple rapid and repeatable synthesis as outlined in chapter 2, were shown to be useful in the SERS technique, as synthesised, without the addition of aggregation agents.

Significant enhancement of the Raman signal for each dye occurred even with a relatively short sampling time. For each model analyte a clear trend was observed where with increasing volume of colloid, there resulted an enhancement of signal until an optimum ratio of analyte to colloid was established. This optimum ratio was found to be consistent for each analyte over a range of concentrations and so can be used to further improve sampling times.

A supplementary study of the nanoparticle's SERS activity as cast substrates could counteract the drop off in signal at elevated silver concentrations, and result in a more familiar adsorption model response (investigated in chapter 5).

4.5 References

1. C. Drake, S. Deshpande, D. Bera, S. Seal, *International Materials Reviews*, 2007, 52, 289-317
2. J.H. Lee, *Sensors and Actuators, B*, 2009, 140, 319–336
3. A. Shkilnyy, M. Souce, P. Dubois, F. Warmont, M.L. Saboungi, I. Chourpa, *Analyst*, 2009, 134, 1868 – 1872
4. M.E. Abdelsalam, S. Mahajan, P.N. Bartlett, J.J. Baumberg, A.E. Russell, *Journal of the American Chemical Society*, 2007, 129, 7399 – 7406
5. D.G. Yu, W.C. Lin, C.H. Lin, L.M. Chang, M.C. Yang, *Materials Chemistry and Physics*, 2007, 101, 93 – 98
6. C.E. Talley, J.B. Jackson, C. Oubre, N.K. Grady, C.W. Hollars, S.M. Lane, T.R. Huser, P. Nordlander, N.J. Halas, *Nano Letters*, 2005, 5, 1569.
7. L.L. Bao, S.M. Mahurin, C.D. Liang, S. Dai, *Journal of Raman Spectroscopy*, 2003, 34, 394
8. S. Kundu, M. Mandal, S.K. Ghosh, T. Pal, *Journal of Colloid and Interface Science*, 2004, 272, 134
9. A.D. McFarland, M.A. Young, J.A. Dieringer, R.P. Van Duyne, *Journal of Physical Chemistry B*, 2005, 109, 11279 – 11285
10. E.C. Le Ru, P.G. Etchegoin, *Principals of Surface – Enhanced Raman Spectroscopy and related plasmonic effects*, Chapter 1, Elsevier, Oxford, 2009
11. W.E. Smith, *Chemical Society Reviews*, 2008, 37, 955 – 964
12. W.C. Lin, M.C. Yang, *Macromolecular Rapid Communications*, 2005, 26, 1942 – 1974
13. G.A. Ozin, A.C. Arsenault, L. Cademartiri, *Nanochemistry, a chemical approach to nanomaterials*, Cambridge, UK, Royal Society of Chemistry, 2005, Ch. 5, 5.7, 226
14. P. Hildebrandt, M. Stockburger, *Journal of Physical Chemistry*, 1984, 88, 5935
15. A. Otto, A. Bruckbauer, Y.X. Chen, *Journal of Molecular Structure*, 2003, 661, 501
16. H.S. Shin, H.J. Yang, S.B. Kim, M.S. Lee, *Journal of Colloid and Interface Science*, 2004, 274, 89
17. T. Sugimoto, F. Shib, T. Sekiguchi, H. Itoh, *Colloids Surface A*, 2000, 164, 183
18. D.L Stokes, T. Vo-Dinh, *Sensors and Actuators, B*, 2000, 69, 28 - 36
19. C.J. Addison, A.G. Brolo, *Langmuir*, 2006, 22, 8696 – 8702
20. R. Sanci, M. Volkan, *Sensors and Actuators, B*, 2009, 139, 150-155

21. A. Champion, P. Kambhampati, *Chemical Society Reviews*, 1998, 27, 241 – 250
22. Q.F. Zhou, J.C. Bao, J. Xu, *Journal of Materials Chemistry*, 2002, 12, 384 – 387.
23. Y.J. Yang, *Materials Science and Engineering: B*, 2006, 131, 200 – 202.
24. V.K. Sharma, R.A. Yngard, Y. Lin, *Advances in Colloid and Interface Science*, 2009, 145, 83 – 96
25. Z.H. Mbhele, M.G. Salemane, C.G.C.E. van Sittert, J.M. Nedeljkovic, V. Djokovic, A.S. Luyt, *Journal of Chemistry Materials*, 2003, 15, 5019 – 5024
26. A. M. Michaels, M. Nirmal, L. E. Brus, *Journal of the American Chemical Society*, 1999, 121, 9932
27. J. T. Krug, G. D. Wang, S. R. Emory, S. M. Nie: *Journal of the American Chemical Society*, 1999, 121, 9208
28. S.E.J. Bell, N.M.S. Sirimuthu, *Chemical Society Reviews*, 2008, 37, 1012 – 1024
29. H.B. Lueck, D.C. Daniel, J.L. McHale, *Journal of Raman Spectroscopy*, 1993, 24, 363 – 370
30. M.M. Islam, K. Ueno, H. Misawa, *Analytical Sciences*, 2010, 26, 19 – 24
31. X.Z. Sun, L.H. Lin, Z.C. Li, Z.J. Zhang, J.Y. Feng, *Applied Surface Science*, 2009, 256, 916 – 920
32. W. Plieth, *Electrochemistry for Materials Sciences*, Elsevier, Amsterdam, 2008, 223 – 228

5. Effect of potential modulation of chemically synthesised Ag nanoparticles on SERS

5.1 Introduction

As the development of SERS continues, a large portion of research is focused on its application as an analytical technique. However reproducibility of output is still the major obstacle, and this has prompted a lot of work in the development of SERS substrates, with a large portion of recent literature describing advances in the production of reproducible, uniform SERS substrates ¹.

There is a large variety of SERS active substrates in existence (detailed in figure 1.10, section 1.20) and development of novel fabrication processes is ongoing. For example *P.N. Bartlett et al.* have developed an electrodeposition technique, which prepares reproducible nano 'void' substrates, these uniform surfaces offering tuneable optical properties that allow the tailoring of substrates for specific analysis.

SERS was first observed during spectroelectrochemical experiments carried out by Fleischmann in 1974. These initial experiments were all conducted using modified (roughened) silver electrodes ² Subsequent studies found that coinage metals were most appropriate for the SERS effect, as they provide strong localised surface plasmons key to the electromagnetic enhancement of the Raman signal ^{3 - 5}. As described in section 1.13, this plasmon resonance of the silver nanoparticles is a product of the uniform oscillation of the particle's conductance electrons due to irradiation by monochromatic light. It follows that any form of electromagnetic field applied would also influence the nanoparticle's electrons and similarly impact on the observed SERS spectra.

An investigation as to whether other outside factors could influence the degree of electromagnetic enhancement previously observed was conducted; Electrochemical methods were deemed the most suitable means of conducting the investigation, their effects controllable, and reproducible.

Initial investigations proved that running an electrical current through the colloids resulted in aggregation of the nanostructures. Therefore it was determined that casting the colloids, as films would be the most appropriate method for investigating the outside influence.

5.2 Experimental

The experimental process in this study comprised of a number of distinct steps. First the preparation SERS substrates, followed by an examination of the effect of varied experimental conditions on their suitability.

5.2.1 Materials

Crystal violet, (ACS reagent, $\geq 90.0\%$ anhydrous basis), was purchased from Sigma Aldrich, and used as received without further purification.

5.2.2 Preparation of SERS substrates

The different substrates utilised in this study may be placed in two subgroups based on their support, silver (metal) or carbon. The silver SERS structure was prepared by electrochemical roughening in aqueous 0.1M KCl, and involved three successive positive to negative cycles from - 0.3 to 0.3 to - 0.3Vs. With a sweep rate of 5 mVs^{-1} finishing at - 0.3 V, and then maintaining a - 0.4 V for five minutes before removing the silver from the circuit and washing with deionised water as described by Kudelski⁶. The silver plate (1cm^2 area) was polished with Al_2O_3 and placed in a three electrode cell with a 0.1M KCl Ag|AgCl reference electrode and a platinum counter electrode. AFM analysis of both the polished and roughened surface is shown in figures 5.2.a and 5.2.b. A clear difference in the morphology is evident when comparing the two surfaces 'roughened' surface exhibiting a significantly coarser surface than the polished electrode.

The carbon ink support was prepared coating acetate sheets (XEROX, Premium Transparencies, type CR) with carbon ink (Electrodag 423SS, graphite – based PTF ink), and drying overnight. Colloidal silver (prepared as described in chapter 2) was then drop cast onto the inert carbon surface (0.1 cm^3 per 1cm^2 portions) and after an additional drying period (eighteen + hours) the modified carbon substrates were ready for use.

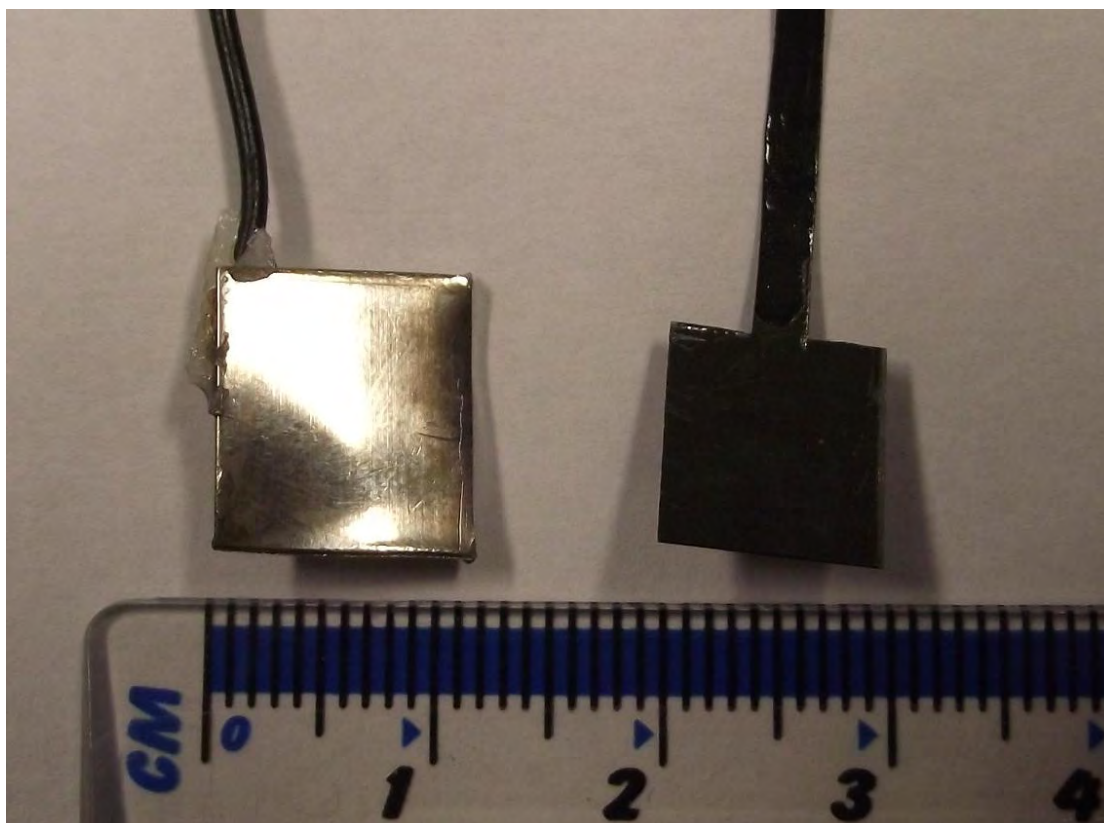


Figure 5.1: Silver (left) and carbon (right) SERS electrodes, scale in cm.

5.2.2.1 Atomic Force Microscope analysis – MFP – 3D BIO AFM

AFM analysis was performed using a MFP-3D BIO AFM (Asylum Research). Olympus silicon AC 240 cantilevers were used. Tips had a typical resonant frequency of 70 kHz. The AFM operated in AC mode (alternate contact) in order to minimise tip sample interaction. Typical free air amplitudes were approx 700 mV and a high amplitude set point relative to the free air amplitude was maintained to minimise sample/tip damage. All samples were imaged in air at ambient humidity. ARgyleT software rendered the images below in 3D and the images obtained contain 512 pixels per scan line.

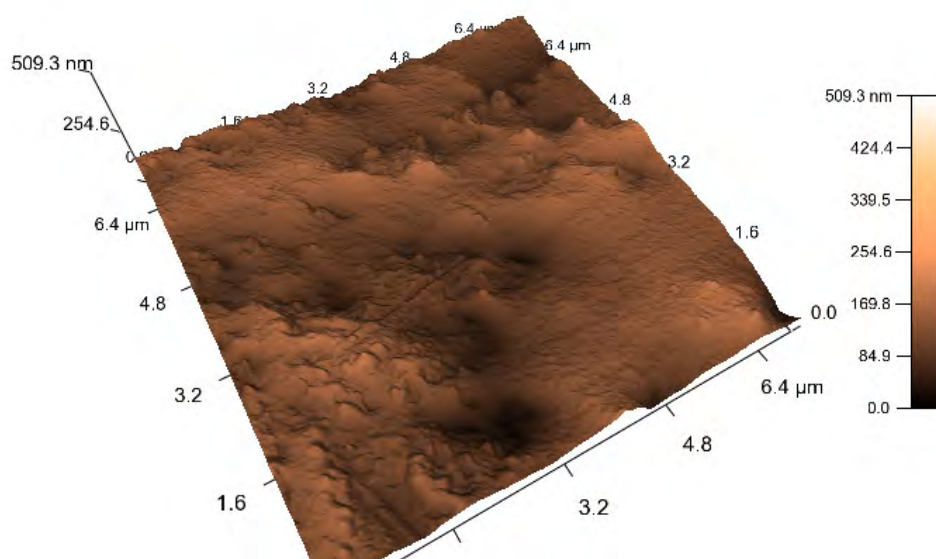


Figure 5.2.a: Morphology of polished silver SERS substrate. – Image taken by Dr. Luke O’Neill - Instrumental Support – Focas Institute

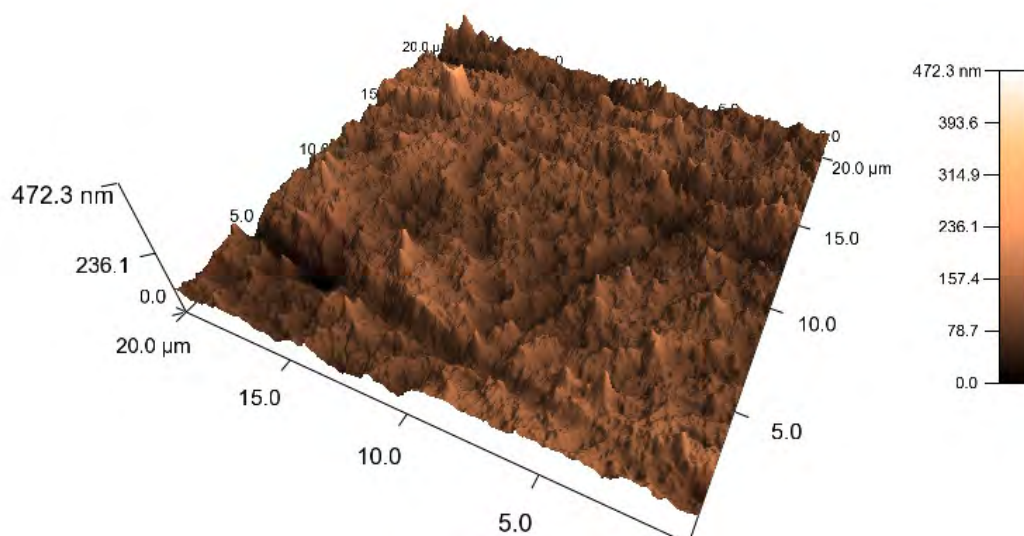


Figure 5.2.b: Morphology of roughened silver SERS substrate. – Image taken by Dr. Luke O’Neill - Instrumental Support – Focas Institute

5.2.3 SERS measurements

SERS active measurements were conducted using Crystal Violet (Cr.V.) as the model analyte and were performed with a Horiba Jobin Yvon LabRAM HR 800. SERS excitation was provided by Solid State Diode laser with a maximum power of

100mW. The spectrograph was equipped with a 600 grooves/mm grating, and all measurements were performed with a 1 μm entrance slit with the laser at 1% strength. The spectral region of investigation was dependent on the analyte, 700 – 2000 cm^{-1} for Cr.V. SERS has the potential to appreciably impact on the effectiveness of Raman spectroscopy as an analytical technique. Once more, emphasis was placed on short sampling times, therefore in each case the exposure time was five seconds with the accumulation set to twenty, ensuring that the total sampling time was never greater than five minutes.

5.2.3.1 SERS measurements experimental setup

A three electrode, one compartment cell, with the SERS surface acting as the working electrode, an Ag|AgCl reference and a platinum counter electrode was used, figure 5.3. A dilute aqueous solution of the probe molecule, crystal violet, was contained in the cell, and potentials applied between the working and reference electrodes using a Thompson ministat potentiostat. The system was left 'open' to aid SERS analysis, and hence all analytes were exposed to the environment, and therefore were not degassed.

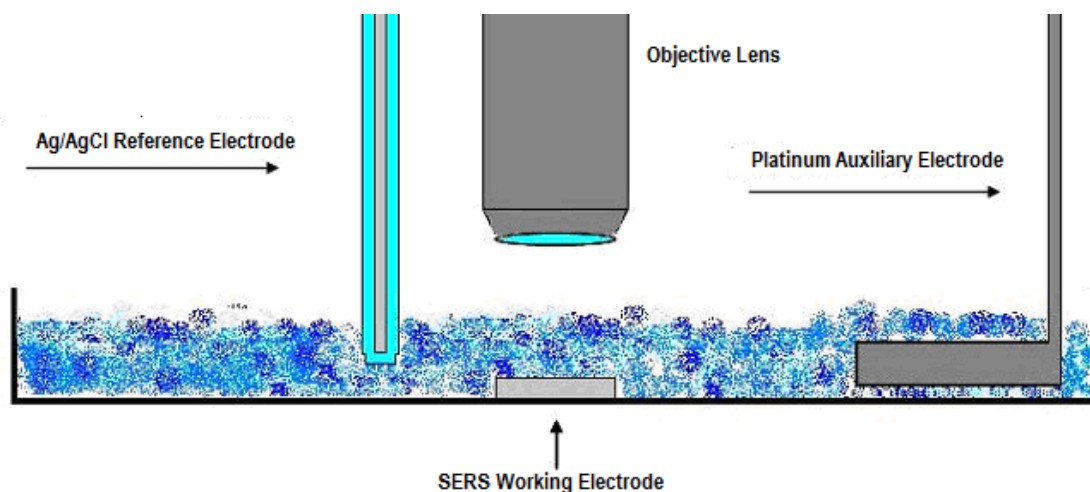


Figure 5.3: Schematic of spectrochemical cell employed for Raman Spectroscopy

5.3 Effectiveness of 'roughened' silver as SERS substrate

The objective of this study was to determine not only the SERS surfaces (both solid silver and nano silver coated carbon) efficiency, but to also determine the influence of an outside factor upon it (applied voltage). Initial experiments with the silver substrate showed a clear enhancement of the Raman signal (displaying a similar level of

enhancement as the colloids in the previous chapter), which was further augmented when a potential is applied (as can be seen in figure 5.4). This preliminary work shows that the spectral signal is enhanced in the presence of the roughened silver with a further enhancement occurring when a potential (- 0.4 V) is applied.

Subsequent studies with the silver substrate confirmed that the application of a potential did impact the observed Raman signal (shown in figure 5.5). The bands of the Raman spectra may be assigned as follows; $\sim 722\text{ cm}^{-1}$, in plane benzene ring bend, stretch; $\sim 800\text{ cm}^{-1}$, out of plane aromatic C – H ‘breathing’; $\sim 914\text{ cm}^{-1}$, ring skeletal radial vibration; $\sim 1170\text{ cm}^{-1}$, in plane aromatic C – H bending vibration in plane aromatic C – H bending vibration; $\sim 1365\text{ cm}^{-1}$, N – C stretch; $\sim 1395\text{ cm}^{-1}$, C – C and C – H in plane motion (aromatic); $\sim 1615\text{ cm}^{-1}$, N – C (ϕ bond) and C – C stretch.⁷⁻⁹

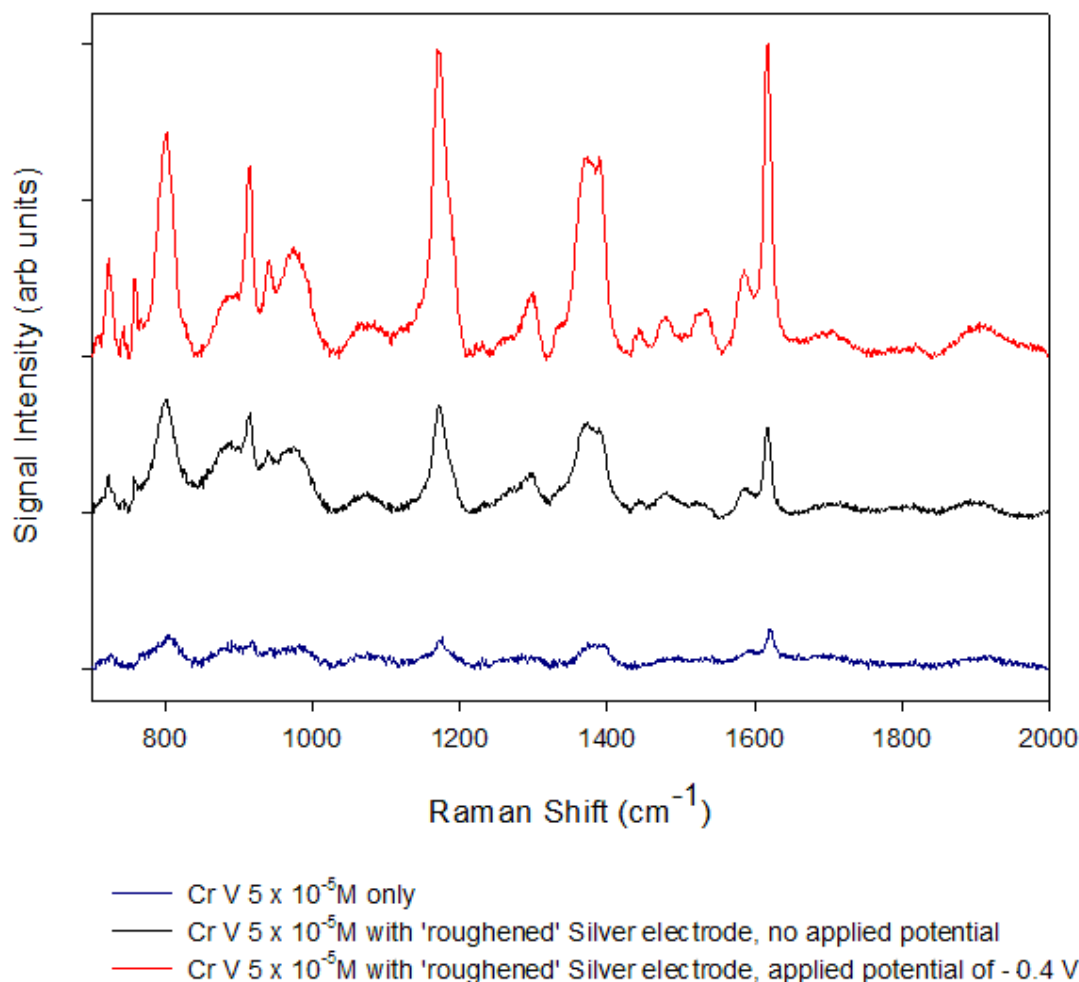


Figure 5.4: Spectra of 5×10^{-5} M Crystal Violet, 1% laser strength, 5 s exposure time and accumulation of 20, silver SERS substrate. Note the applied potential was - 0.4 V.

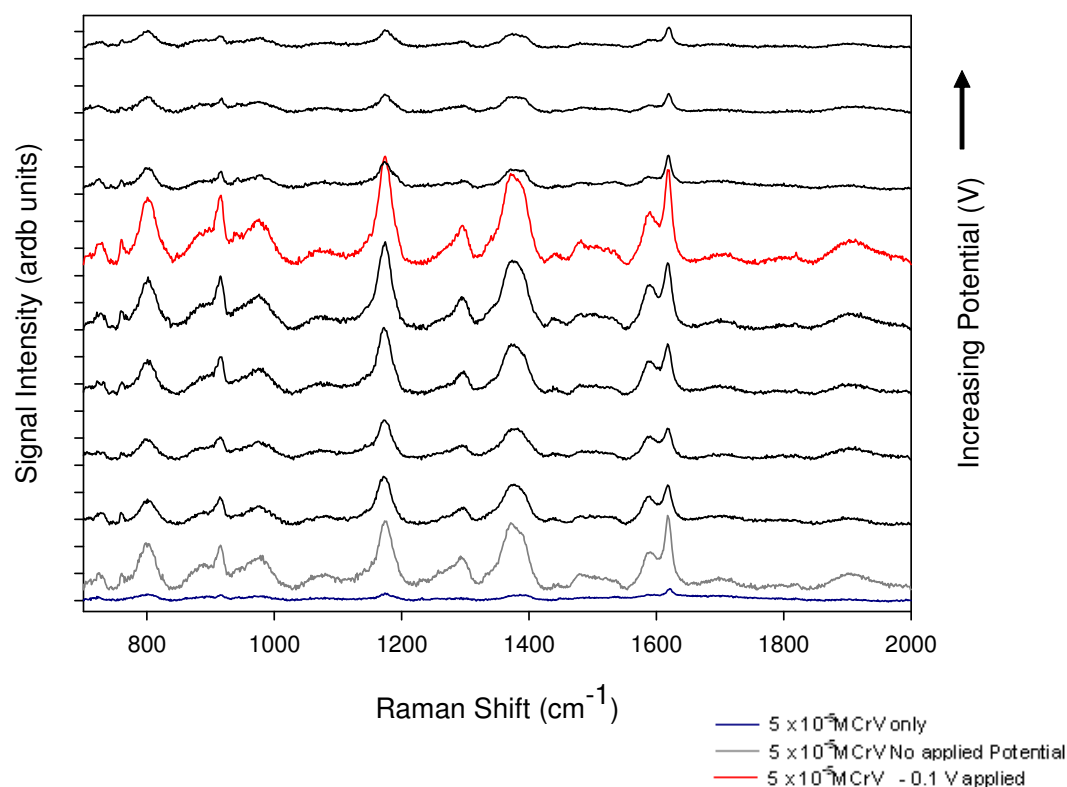


Figure 5.5: Spectra of 5×10^{-5} M Crystal Violet, 1% laser strength, 5 s exposure time and accumulation of 20, silver SERS substrate, with different applied potentials.

The effect of the systematic application of potential over the silver substrate is clearly illustrated in figure 5.5, the resulting intensity of signal at the optimum potential (- 0.1 V applied highlighted in red) more than double that of the substrate where no potential is applied and the colloids of the previous chapter. It was also found that repeat analysis was possible if a potential within the range of - 0.4 – 0.1 V was applied.

However if a potential outside this range in signal was applied, a rapid drop off in spectra intensity was observed with subsequent studies requiring the nanosurface to be re-established via the roughening technique outlined above. This was most likely a result of changes the surface undergoes beyond this potential window where potentials above 0.1 V result in the oxidation of the silver surface, whereas at potentials below - 0.4 V it is possible that the cation dye forms a double layer that disrupts the surface's nanostructures SERS effectiveness.

5.3.1 Impact of added electrolyte

An investigation was carried out where an electrolyte (0.1 M KNO_3) was added to the experimental system (figure 5.6). Again a clear signal enhancement was seen. The presence of an electrolyte also shifted the applied potential necessary to give the greatest increase in signal (- 0.7 V highlighted in red figure 5.6), requiring greater energy to produce an overall signal enhancement that was approximately half of that observed without the added electrolyte. Thus further investigations were carried out without adding an electrolyte. The presence of the electrolyte also had a negative impact on the repeatability with a 'fresh' nano surface needed for each set of analysis.

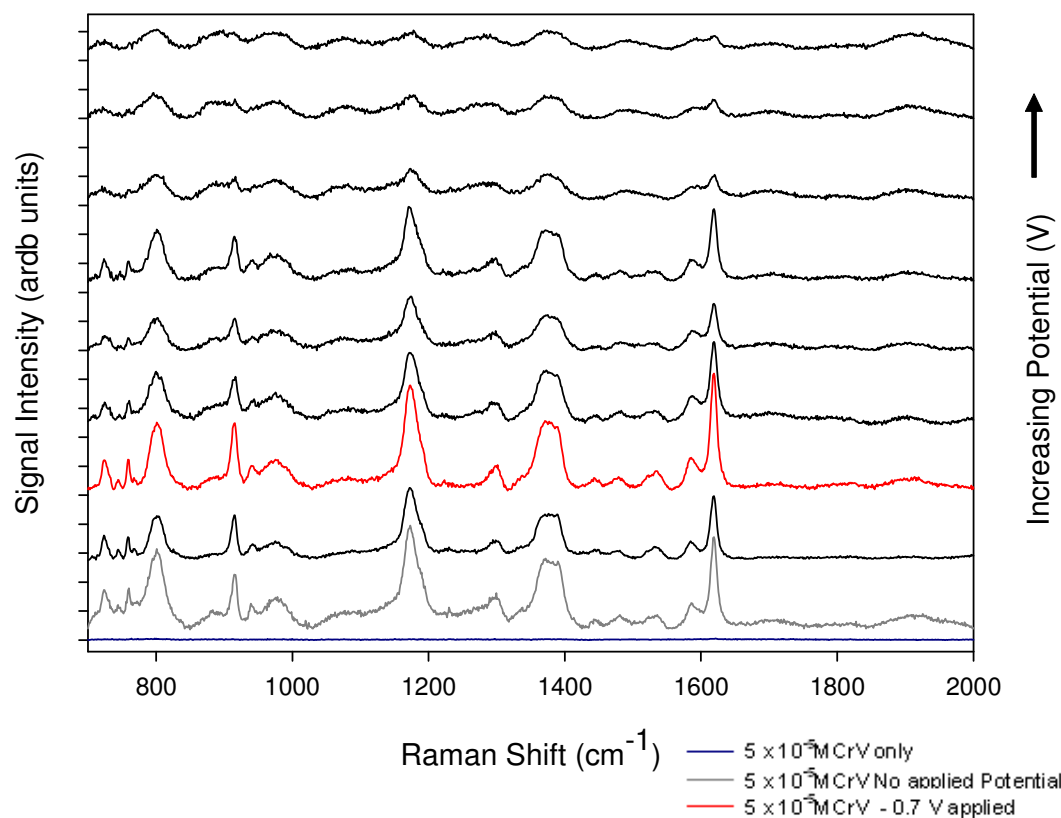


Figure 5.6: Spectra of $5 \times 10^{-5} \text{ M}$ Crystal Violet, 1% laser strength, 5 s exposure time and accumulation of 20, silver SERS substrate with different applied potentials in the presence of an electrolyte (0.1M KNO_3).

The roughened silver surface clearly displayed its utility as a SERS active surface. However it should be noted that the surface was produced by electrochemical roughening (as described above) and although it gives a nano plane, the substrate does

not have a uniform façade, leading to issues regarding uniformity of the SERS active surface and reproducibility of spectra.

5.4 Carbon – silver nanoparticles SERS surfaces

Once again the experimental set up was a three electrode system, with the carbon – silver nanoparticle (C – AgNP) surface acting as the working electrode. In the previous chapter colloidal nanostructures tuned to exhibit localised surface plasmons of λ_{\max} close to the wavelength of the incident radiation (laser), showed the maximum signal enhancement. As a result the nanostructures present in the blue colloid (prepared as described in chapter 2) were cast on the carbon substrate. The cast SERS coating clearly demonstrates SERS activity with a clear jump in signal intensity when ~ -0.1 V is applied (highlighted in red, figure 5.8). This correlates well with the previous study with the silver electrode, suggesting excellent electrical contact between the cast silver nanoparticles (of average 60 nm diameter) and the carbon electrode. The coating was also found to be stable for the timescale of the experiment ($\sim \geq 5$ hours) despite its use of PVA as the support matrix)

Also the possibility of the production of disposable devices exists as the total surface silver coverage of the carbon supported SERS substrate, $[\text{Ag}] = 6.875 \times 10^{-6}$ moles cm^{-2} , is significantly lower than that of the solid silver plate electrode once a methodology for producing a consistent coating is proven.

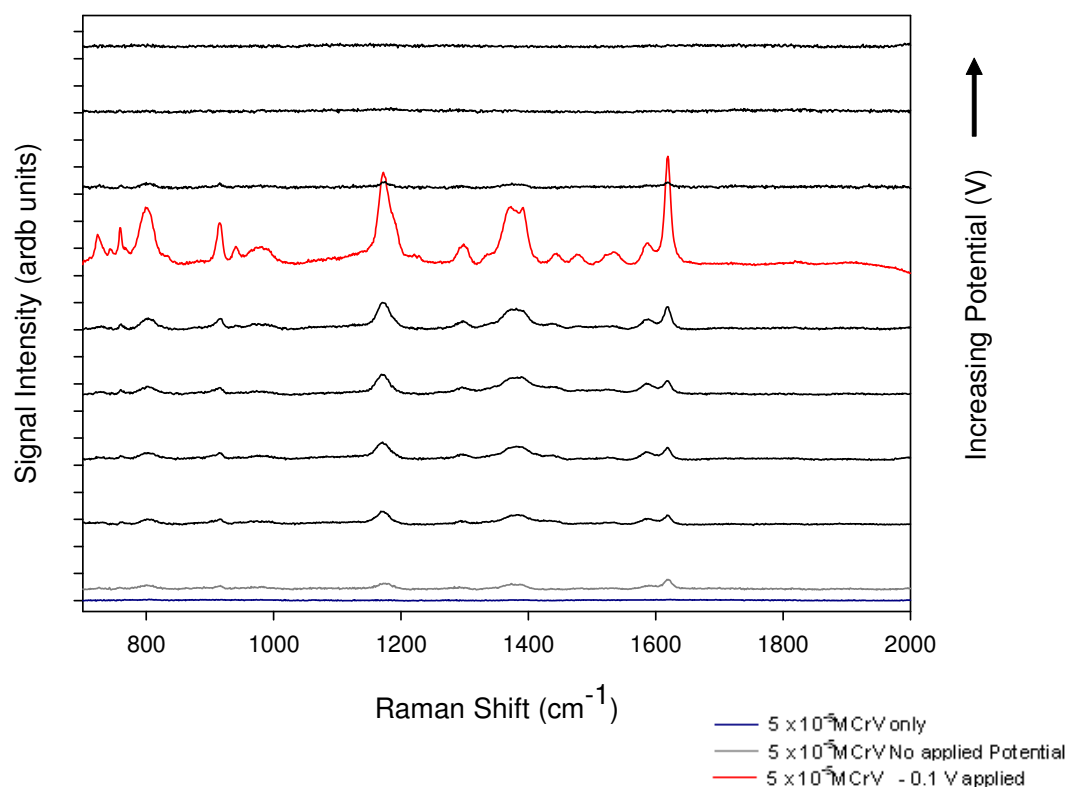


Figure 5.7: Spectra of 5×10^{-5} M Crystal Violet, 1% laser strength, 5 s exposure time and accumulation of 20, with C – AgNP (blue colloid) SERS surface and different applied potentials.

The potential's effect varies over the applied range with the spectral intensity increasing with applied potentials between - 0.7 V and through to - 0.1 V, and whereas the spectra at the lower end of this range correlate with the augmentation seen for the corresponding colloid in the previous chapter, it should be emphasised that the signal boost at the higher end of the range is over twice the gain that the colloid alone provides. The C – AgNP mirrored the silver SERS substrate with the greatest signal enhancement at - 0.1 V, this was also true in terms of repeatability where the process gave consistent enhancement if all analysis was conducted in a narrow potential range of - 0.3 – 0.0 V. The C – AgNP using the blue colloid supplied a viable alternative to the solid silver substrate, with the advantage of using particles of a defined size. This prompted an additional investigation with the aim of further developing the C – AgNP substrate.

5.4.1 Development of the Carbon – silver nanoparticles SERS surfaces

The literature surrounding SERS consistently attributes the fundamental element of the phenomenon to the interaction of not only a single nanoparticle but multiple nanostructures with the analyte. Greatest signal enhancement is often reported where multiple nanostructures engage to produce ‘hotspots’ of SERS activity. To achieve this ideal state a colloid with a high silver load (nanospheres of average 20 nm diameter) was used, (preparation described in chapter 2) in the primary investigation (figure 5.8).

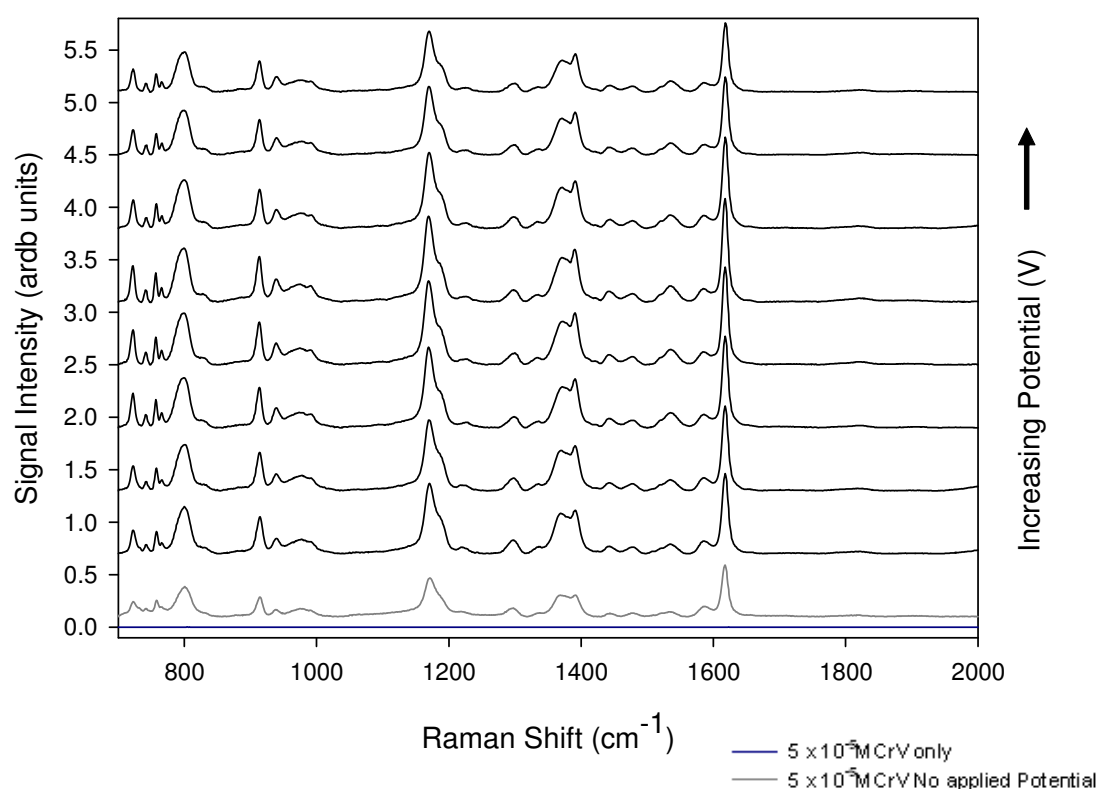


Figure 5.8: Spectra of 5×10^{-5} M Crystal Violet, 1% laser strength, 5 s exposure time and accumulation of 20, with C – AgNP (100% high load colloid – 20nm diameter nanostructures) SERS surface and different applied potentials. Note: Raman spectra of control 5×10^{-5} M Crystal Violet, highlighted in blue.

A drastic increase in signal is immediately evident; a signal enhancement greater than the best seen using either the tuneable colloids, roughened silver electrode or the blue colloid C – AgNP substrate. The level of enhancement however does not appear to be

influenced by the various potentials applied. This is most likely due to the substrate's construction, where unlike the roughened silver electrode is not part of the working electrode but coated upon it as a nanocomposite too far away from the electrode for contact to be made. Coupled with the insulating nature of the composites other component (PVA) the surface particles of the composite at which the SERS effect occurs are likely outside the applied potentials range of influence.

To counteract this, but also maintain the nanostructures interaction, the colloid was diluted to 10 % of its original concentration, and a new series of SERS active surfaces prepared.

5.4.2 C – AgNP SERS surfaces – colloid dilution

The subsequent analysis again showed the massive signal boost however there was no potential effect (figure 5.9).

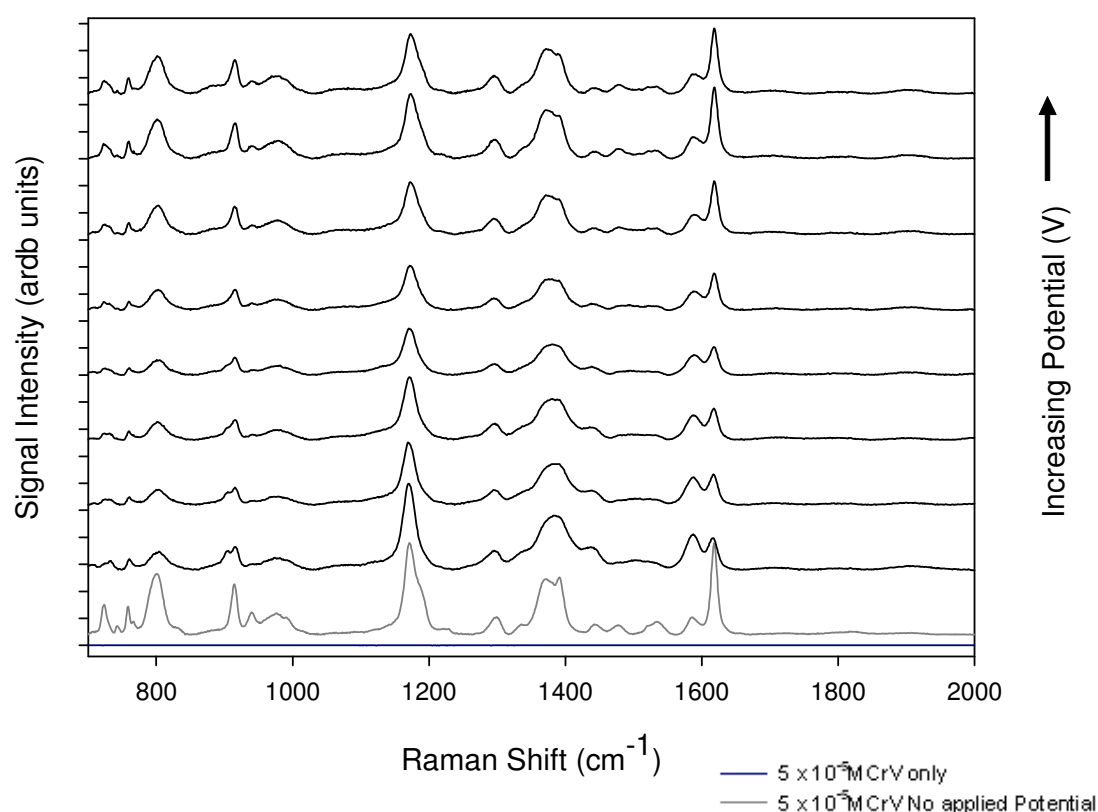


Figure 5.9: Spectra of 5×10^{-5} M Crystal Violet, 1% laser strength, 5 s exposure time and accumulation of 20, with C – AgNP (10% high load colloid - 20nm diameter nanostructures) SERS surface and different applied potentials.

This prompted a further dilution of the colloid, to 1 % of its primary concentration before the preparation of more C – AgNPs SERS surface.

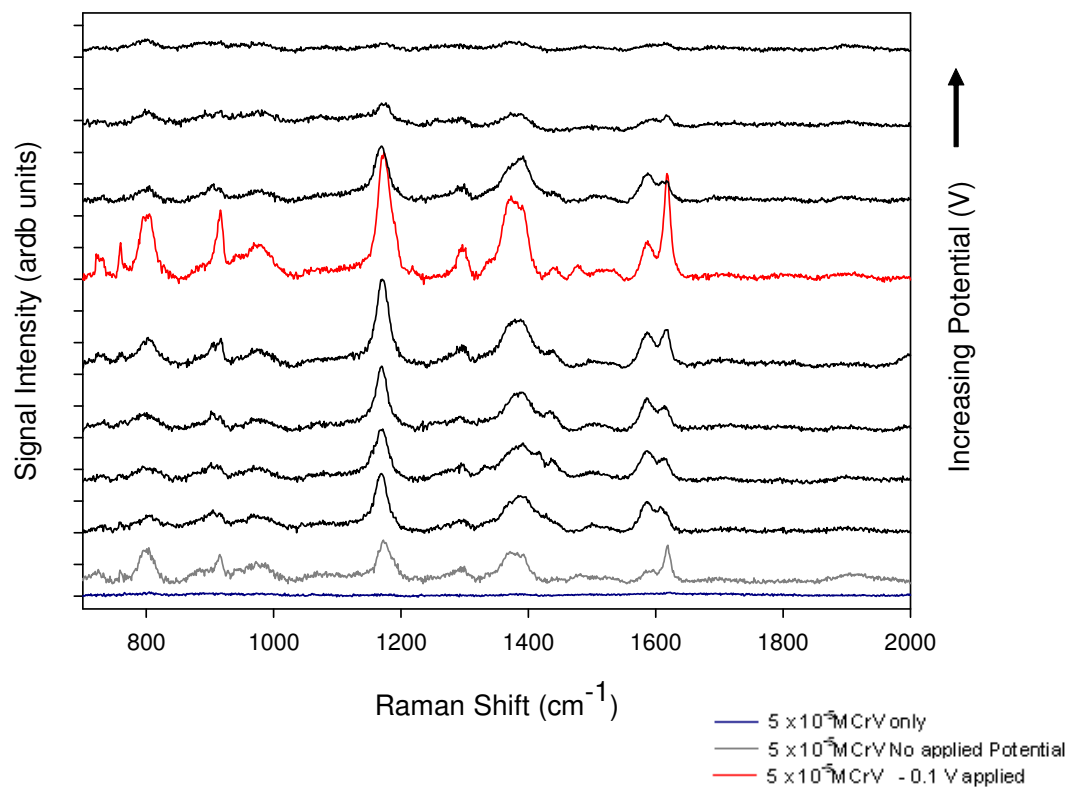


Figure 5.10: Spectra of 5×10^{-5} M Crystal Violet, 1% laser strength, 5 s exposure time and accumulation of 20, with C – AgNP (1% high load colloid) SERS surface and different applied potentials.

The resulting investigation showed both SERS activity (figure 5.10) and the influence of an applied potential, with the greatest intensity enhancement was again at ~ -0.1 V, highlighted in red. Confirming that the manner in which the composite was cast (and its resultant thickness) had an effect on the extent of the applied potential's influence. However the level of enhancement was a fraction of that observed for the previous C – AgNP surfaces, and less than that seen for both the silver SERS surface and the individual colloids in previous studies. This negated the colloid dilution approach as the overall aim of signal augmentation was best seen with a SERS surface with high nano loads and hence interaction. However, the aim of this study was to show that as well as size modification of the nanostructures the surface potential 'hotspots'

influence the extent of SERS enhancement. Therefore a further attempt to combine this enhancement with the observed potential gain was devised.

5.4.3 C – AgNP SERS surfaces – spin coated

An excess volume of the 20 nm high load colloid was deposited on to the carbon and allowed to stand for five minutes to ensure complete coverage. The substrate was then rotated at a high velocity spreading the fluid further by centrifugal force. The resulting coating was left to stand on the bench overnight (approximately 18 hours) before analysis.

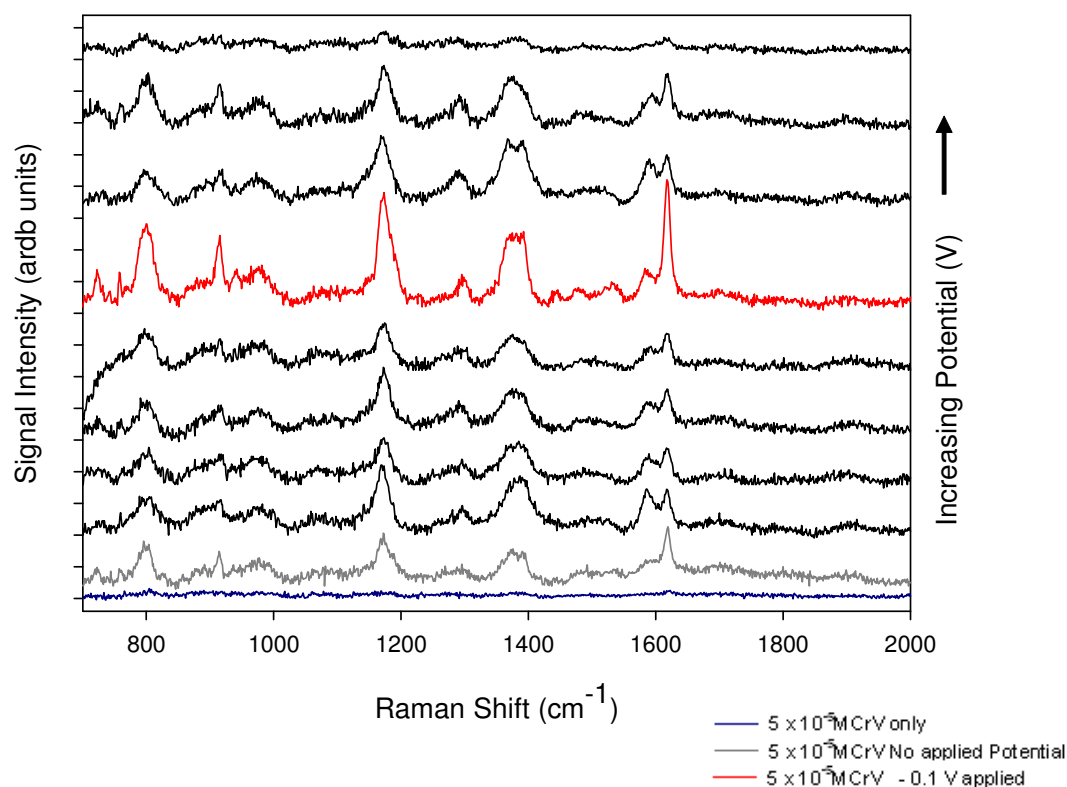
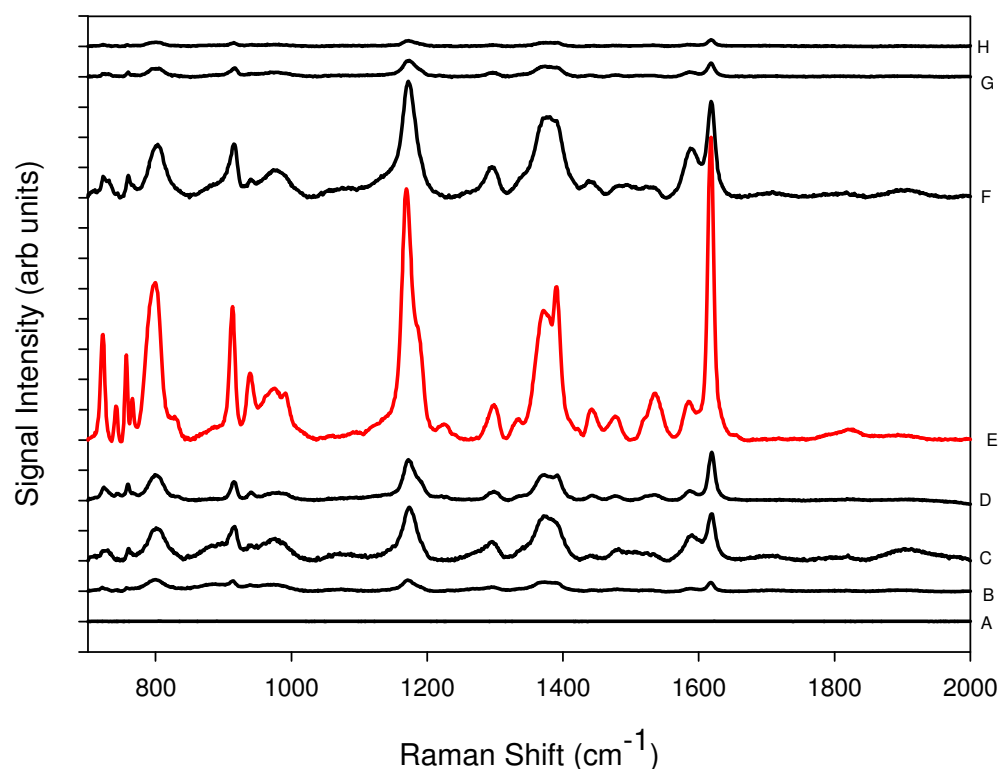


Figure 5.11: Spectra of 5×10^{-5} M Crystal Violet, 1% laser strength, 5 s exposure time and accumulation of 20, with C – AgNP (100% high load colloid - 20nm diameter nanostructures – spin coated) SERS surface and different applied potentials.

This method's intensity enhancement levels however was significantly lower than those of the previous methods. So despite showing SERS activity and the clear influence of an externally applied potential this method too displayed little enhancement due to inefficient casting of the silver.



- A: 5×10^{-5} Cr.V only
 B: Enhancement of 5×10^{-5} Cr.V by colloid (~ 60 nm)
 C: Enhancement of 5×10^{-5} Cr.V by roughened silver electrode
 D: Enhancement of 5×10^{-5} Cr.V by C – AgNP electrode (~ 60 nm)
 E: Enhancement of 5×10^{-5} Cr.V by C – AgNP electrode (~ 20 nm, 100%)
 F: Enhancement of 5×10^{-5} Cr.V by C – AgNP electrode (~ 20 nm, 10%)
 G: Enhancement of 5×10^{-5} Cr.V by C – AgNP electrode (~ 20 nm, 1%)
 H: Enhancement of 5×10^{-5} Cr.V by spin coated C – AgNP electrode (~ 20 nm, 100%)

Figure 5.12: Comparison of enhancement by different substrate/techniques

In figure 5.12 the effectiveness of each method of SERS signal enhancement used in the study is compared, note that in each case the optimum conditions for each technique were taken, i.e. for the roughened electrode the enhancement at - 0.1 V was used. It is clear that the greatest enhancement is achieved using the C – AgNP (~ 20 nm 100%) electrode.

5.5 Conclusions

Both full silver and silver nanocomposite coated carbon SERS surfaces demonstrated clear signal enhancement. Initial studies showed that when an external potential was applied the resulting spectra could be further enhanced within a limited window of applied voltage, greater than 0.1 V and oxidation of the silver particles occurred fouling the SERS surface and ultimately changing the morphology of the SERS electrode thereby inhibiting its effectiveness. Whereas at potentials below ~ -0.2 V it's possible that the cation dye forms a double layer which clouds and thus disrupts the surface nanostructure's SERS effectiveness. The addition of an electrolyte was also found to be detrimental to the nanosurface and thus was discontinued. Subsequent studies where emphasis was placed on the interaction of the coating nanostructures displayed the greatest boost to the signal intensity. However efforts to couple this with the amplification of signal due to the applied potential proved difficult as the overall enhancement in signal diminished with each attempt.

The effectiveness of the cast nanostructures (with diameters of ~ 20 nm) as SERS substrate was clearly illustrated (figure 5.12) prompting analysis of their utility for real world applications, described in chapter 6.

5.6 References

1. E.C. Le Ru, P.G. Etchegoin, *Principals of Surface – Enhanced Raman Spectroscopy and related plasmonic effects*, Chapter 8, Elsevier, Oxford, 2009
2. M. Fleischmann, P.J. Hendra, A.J. McQuillian, *Chemical Physics Letters*, 1974, 26, 163 – 166
3. S. Mahajan, M. Abdelsalam, Y. Suguwara, S. Cintra, A. Russell, J. Baumberg, P. Bartlett, *Physical Chemistry Chemical Physics*, 2007, 9, 6016 – 6020
4. J.J. Baumberg, T.A. Kelf, Y. Suguwara, S. Cintra, M. Abdelsalam, P.N. Bartlett, A.E. Russell, *Nano Letters*, 2005, 5, 2262 – 2267
5. S. Cintra, M. Abdelsalam, P.N. Bartlett, J.J. Baumberg, T. Kelf, Y. Suguwara, A.E. Russell, *Faraday Discussions*, 2006, 132, 191 – 199
6. A. Kudelski, *Chemical Physics Letters*, 2005, 414, 271 – 275
7. M.M. Islam, K. Ueno, H. Misawa, *Analytical Sciences*, 2010, 26, 19 – 24
8. X.Z. Sun, L.H. Lin, Z.C. Li, Z.J. Zhang, J.Y. Feng, *Applied Surface Science*, 2009, 256, 916-920
9. G. Socrates, *Infrared and Raman Characteristic group Frequencies: Tables and Charts*, 3rd ed., Chichester, J. Wiley, 2001

6. A study of Volatile Corrosion Inhibitor release using SERS

6.1 Introduction

Oxygen and moisture in the air are the major contributors to the atmospheric corrosion of metals. The presence of pollutants, dust, acidic compounds or corrosive gases can promote the corrosive effect of moisture and oxygen on metals.

There are multiple routes available to protect metal surfaces against corrosion during storage or transit including, the use of inert atmospheres, drying agents and protective coatings, all of which have their own strengths and weaknesses¹. Ideally the preferred protection method would be a technique that does not alter the surface of the metal and hence is non – permanent, and readily removed from the metal's surface before the item is used. In this regard 'permanent' protective coatings such as paints and greases are unsuitable. A common technique used to prevent corrosion such as rusting is the use of desiccants such as zeolites and silica gel, which reduce the relative humidity (RH) of the surrounding environment. This offers good protection, as below a certain humidity level (typically 40 – 50% RH for most common metals) corrosion rates drop to very low levels. However, desiccants can quickly saturate with water vapour and thus have limited life spans².

Volatile corrosion inhibitors (VCIs) are compounds with the ability to vaporise and then protect a metal surface from corrosion by condensing on it and forming a temporary surface coating. They are generally intended as a secondary defence against corrosion in an enclosed space where moisture may penetrate the container. The fundamental advantages of VCIs are that the corrosion inhibitor is rapidly applied in a 'once only' low dosage via gas phase transport. They may be used to protect items that cannot be coated (e.g. electronics) and the humidity level does not need to be controlled. They may be administered to inaccessible regions on the metal surface where conventional coatings cannot be used and as the protective coatings are temporary, they are readily removed and, moreover, do not interfere with the subsequent use or treatment of the protected surface. As a result, VCIs are one of the most cost effective methods of protecting surfaces against corrosion¹⁻⁵.

VCIs work by evaporating or subliming to the vapour phase, and rapidly dispersing within the sealed container to form an equilibrium concentration. The corrosion inhibitor then condenses upon the metal surface (which has the capacity to penetrate into crevices, slots and other hard to access areas) forming a protective barrier layer that prevents corrosion.

The effectiveness of a VCI depends principally on its vapour pressure (or more precisely its ability to sublime), being high enough under atmospheric conditions to allow meaningful vapour phase transport of the inhibitor within the container, and the VCI's ability to be adsorbed directly onto the metal's surface ⁷.

Here the mechanisms of dissociation of several components of a commercially available VCI (kindly supplied by MetPro, MetPro Group, Ballinorig Business Park, Tralee, Co. Kerry, Ireland) from an inert surface (carbon) were studied using surface enhanced Raman spectroscopy, SERS.

In this study, Raman spectra were first obtained directly from the neat VCI components. Modified carbon surfaces (silver nanoparticles, in colloidal dispersions prepared as described in chapter 2, had been drop cast upon the carbon surface) were then briefly 'wetted' with the VCI components and the resulting spectra measured at set time intervals to determine the rate of dissociation of the VCI components from the substrate's surface. A subsequent investigation determined the rate at which the commonly used inhibitor Benzotriazole, adsorbed onto a 'clean' SERS surface over time.

6.2 Experimental

6.2.1 Materials

The VCI components were received from MetPro, benzotriazole (M.W; 119.124 g/mol, mp; 100 °C, bp; 204 °C), monoethanolamine 90% (M.W; 61.083 g/mol, mp; 10.5 °C, bp; 171 °C), diethanolamine 88% (M.W; 105.136 g/mol, mp; 28 °C, bp; 268.8 °C), triethanolamine 90% (M.W; 149.188 g/mol, mp; 20.5 °C, bp; 335.4 °C), morpholine (M.W; 87.120 g/mol, mp; -4.8 °C, bp; 128 °C) and octanoic acid (M.W; 144.212 g/mol, mp; 16.5 °C, bp; 239 °C) ¹⁷. These were first analysed by FTIR and ¹H NMR to ensure their high level of purity before being used as received without further purification.

6.2.2 Apparatus

The experimental process in this study comprised of a number of distinct steps. Firstly the characterisations of the VCI components supplied by MetPro, was conducted by Fourier transform infrared and nuclear magnetic resonance spectroscopy. A Perkin Elmer spectrum 100 FTIR was utilised along with a Perkin Elmer Universal ATR sampling accessory with Perkin Elmer spectrum10 software and a Bruker 400 MHz

Ultra Shield with Bruker TopSpin software. It was necessary to dissolve the VCI components in deuterated chloroform (~ 1mg/ml in CDCl₃) for NMR investigation. This was followed by SERS active measurements on the VCI components, performed as described in the previous chapter with a Horiba Jobin Yvon LabRAM HR 800. The spectral region of investigation was 400– 4000 cm⁻¹. Again total sampling times were kept at a maximum of 5 minutes, with exposure times set to 20 seconds and accumulation of 5.

6.3.1 FTIR Analysis – Perkin Elmer spectrum 100 FTIR with Universal ATR sampling accessory

When an analyte interacts with electromagnetic radiation its molecules absorb radiation of frequencies, which exactly match the frequencies of vibrations within the molecule. This is the basis of infrared (I.R.) spectroscopy. The energies associated with the vibrations of a molecule may be quantised as absorption of electromagnetic radiation in the infrared region for different vibrational states, elucidating the rotational and vibrational energies of the molecules, and permitting the determination of bond strengths. So through the measurement of an I.R. absorption spectrum over a range of energies a series of absorptions corresponding to characteristic vibrations of particular bonds is obtained. Analysis of the location of the frequencies of these absorptions can assist the identification of the molecules and hence determine the analyte¹⁸.

6.3.2 NMR Analysis – Bruker 400 MHz Ultra Shield

Nuclear magnetic resonance spectroscopy is based on the resonance an analyte's nuclei undergo in a magnetic field. The nuclei absorb and re-emit electromagnetic energy, which is at a specific resonance frequency that is dependent on the strength of the magnetic field and allows the observation of specific quantum mechanical magnetic properties of an atomic nucleus¹⁸. Proton NMR, H¹NMR, analysis of the MetPro compounds confirmed their structure and attested to their high purity.

6.3.3 Characterisation of MetPro Samples

The quality of the samples provided was very high, with no significant contaminants found in any of the sample. The IR and H¹NMR spectra of each component and tables assigning the peaks observed in each case are detailed in appendices A.3.1 and A.3.2.

6.4 Preparation of SERS surfaces

Inert carbon surfaces were prepared by coating acetate sheets (XEROX, Premium Transparencies, type CR) with carbon ink (Electrodag 423SS, graphite – based PTF ink), and then allowed to dry overnight. High load colloidal silver, with an average diameter of ~ 20 nm (prepared as described in chapter 2), was then drop cast onto the inert carbon surface (1cm² portions) and after an additional drying period (18 + hours) the modified carbon substrates were ready for use.

6.5 Raman spectra of neat compounds

Spectra of the neat compounds are shown in figure 6.1. In this instance the spectrometer settings were: 10% laser strength, with an exposure time of 20 seconds, an accumulation of 5 and an excitation wavelength of 660 nm.

It was not possible to obtain a spectrum of morpholine even when it was deposited on the modified carbon substrate. Therefore it did not undergo further study. The peaks of the Raman spectra for the other components were assigned as reported in table 6.1.

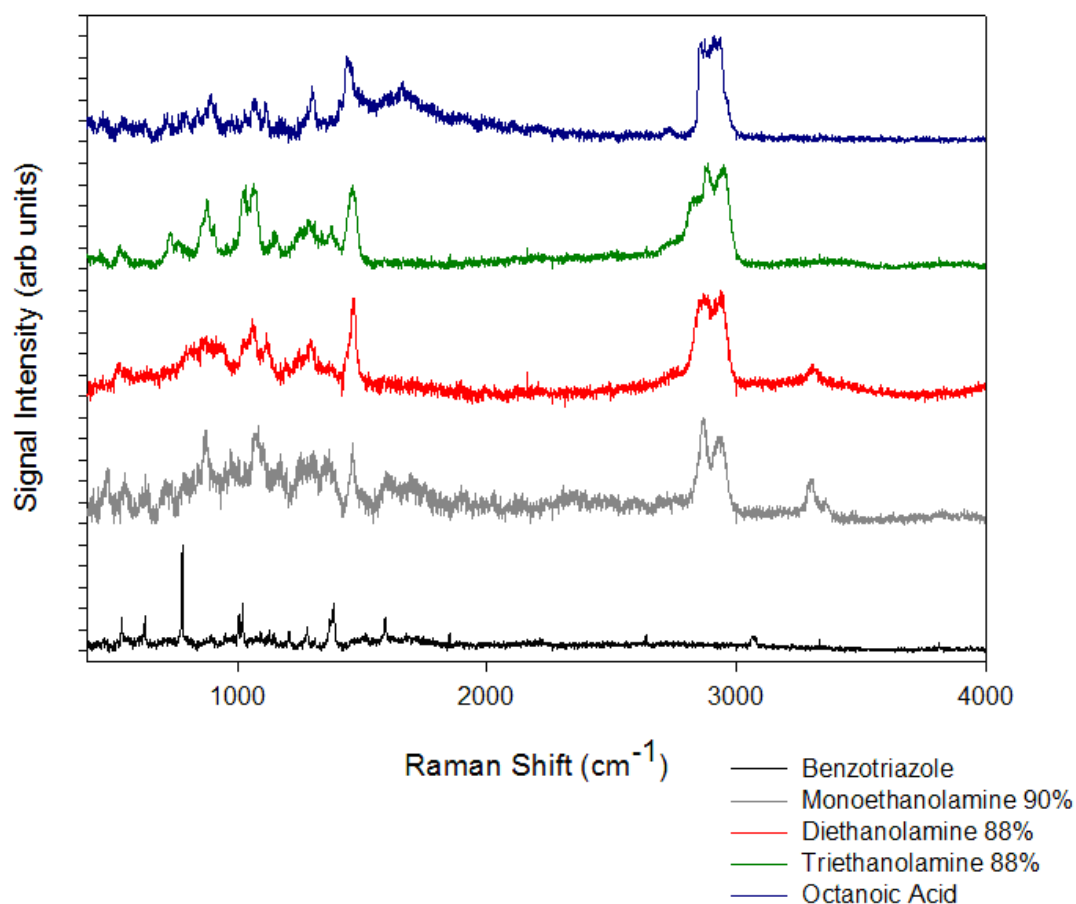


Figure 6.1: Raman spectra of neat MetPro compounds, laser strength 10 %, exposure time 20 s, accumulation 5 and excitation wavelength 660 nm.

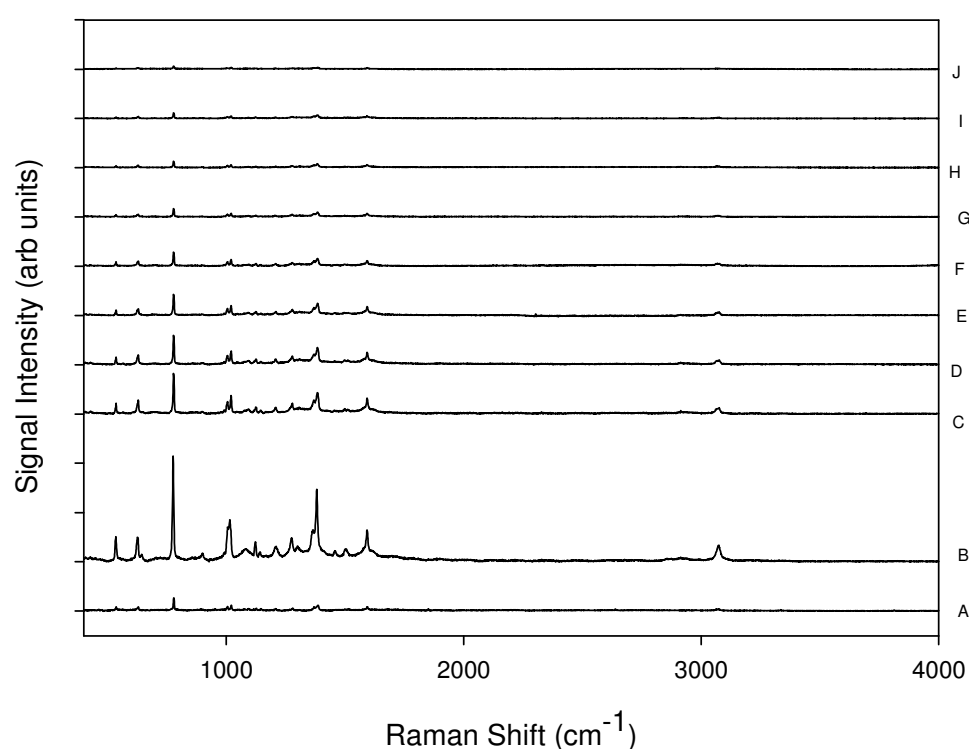
Compound	Peak Assignment ¹⁹
Benzotriazole	<ul style="list-style-type: none"> • ~ 537 cm⁻¹ (in plane ring deformation vibration) • ~ 629 cm⁻¹ (in plane ring deformation vibration) • ~ 779 cm⁻¹ (out of plane ring deformation vibration) • ~ 1022 cm⁻¹ (Aromatic – NH stretch) • ~ 1386 cm⁻¹ (N – CH, CH deformation vibration) • ~ 1592 cm⁻¹ (Aromatic ring vibrations) • ~ 3075 cm⁻¹ (C – H stretching vibration of heterocyclic aromatic compounds)
Octanoic acid	<ul style="list-style-type: none"> • ~ 893 cm⁻¹ (O – H --- O out of plane deformation vibration) • ~ 1301 cm⁻¹ (C – O stretch) • ~ 1438 cm⁻¹ (combination band due to C – O stretch and O – H vibration) • ~ 1663 cm⁻¹ (C = O symmetric stretch) • ~ 2732 cm⁻¹ (– OH stretching vibrations) • ~ 2874 cm⁻¹ (– CH₂ stretching vibrations) • ~ 2936 cm⁻¹ (– CH₂ stretching vibrations)
Monoethanolamine	<ul style="list-style-type: none"> • ~ 477 cm⁻¹ (CH₂ – OH, C – O deformation vibration) • ~ 868 cm⁻¹ (N – H, out of plane bending vibration) • ~ 1076 cm⁻¹ (straight chain C – C stretch) • ~ 1461 cm⁻¹ (alcohols in plane OH deformation vibration) • ~ 2874 cm⁻¹ (CH₂NH₂, CH₂ symmetric stretch) • ~ 2943 cm⁻¹ (CH₂NH₂, CH₂ asymmetric stretch) • ~ 3304 cm⁻¹ (NH₂ symmetric stretch)
Diethanolamine	<ul style="list-style-type: none"> • ~ 526 cm⁻¹ (CH₂ – OH, C – O deformation vibration) • ~ 863 cm⁻¹ (N – H, out of plane bending vibration) • ~ 1065 cm⁻¹ (CH₂ – OH, C – C – O characteristic stretch) • ~ 1300 cm⁻¹ (CH₂ – OH, CH₂ twisting vibration) • ~ 1465 cm⁻¹ (alcohols in plane OH deformation vibration) • ~ 1582 cm⁻¹ (N – H wagging vibration) • ~ 2881 cm⁻¹ (CH₂ – OH, CH₂ asymmetric stretch) • ~ 3314 cm⁻¹ (NH stretch)
Triethanolamine	<ul style="list-style-type: none"> • ~ 879 cm⁻¹ (N – H, out of plane bending vibration) • ~ 1027 cm⁻¹ (CH₂ – OH, C – C – O characteristic stretch) • ~ 1073 cm⁻¹ (CH₂ – OH, C – C – O characteristic stretch) • ~ 1459 cm⁻¹ (alcohols in plane OH deformation vibration) • ~ 1592 cm⁻¹ (N – H wagging vibration) • ~ 2889 cm⁻¹ (CH₂ – OH, symmetric O – H stretch) • ~ 2946 cm⁻¹ (CH₂ – OH, asymmetric O – H stretch) • ~ 3405 cm⁻¹ (NH stretch)

Table 6.1: VCI components Raman spectra peak assignment

6.6 SERS analysis of compounds

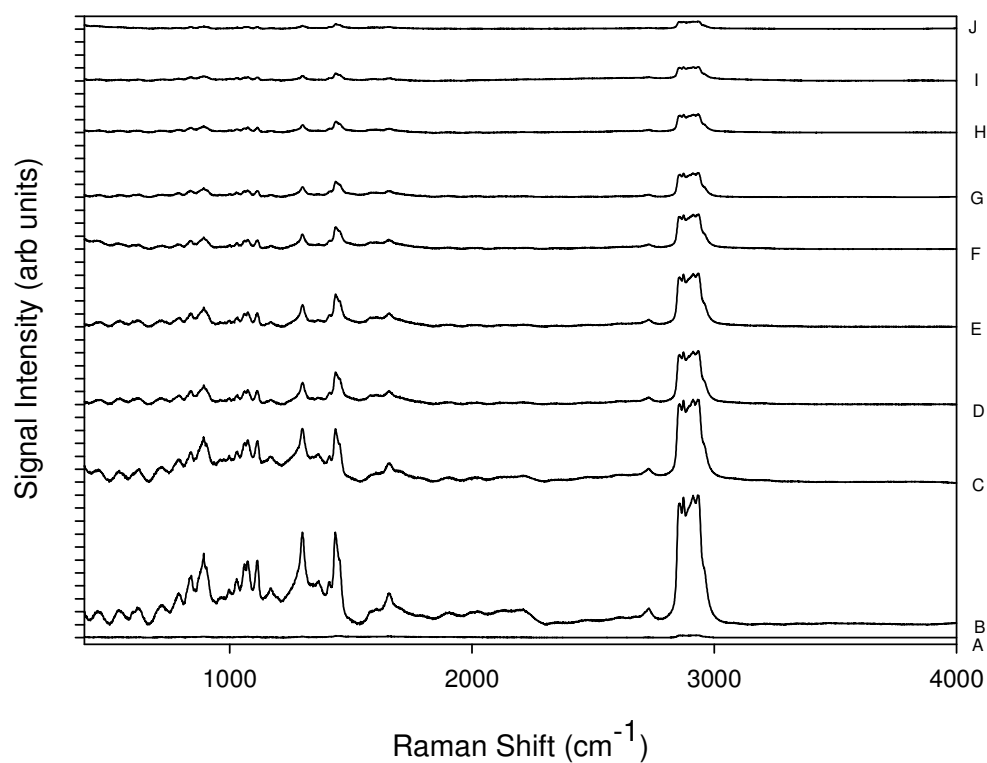
6.6.1 Dissociation rate of compounds

The Raman spectra of each compound were obtained by ‘wetting’ the surface of the modified carbon substrate (0.1 cm^3 of each sample, **note:** it was necessary to dissolve the benzotriazole compound, a 50% w/v solution in CDCl_3 was used for SERS analysis) the spectra were obtained at set time intervals (hourly) over a period of eight hours before a final spectrum was obtained after a period of eighteen hours, figures 6.2 – 6.6.



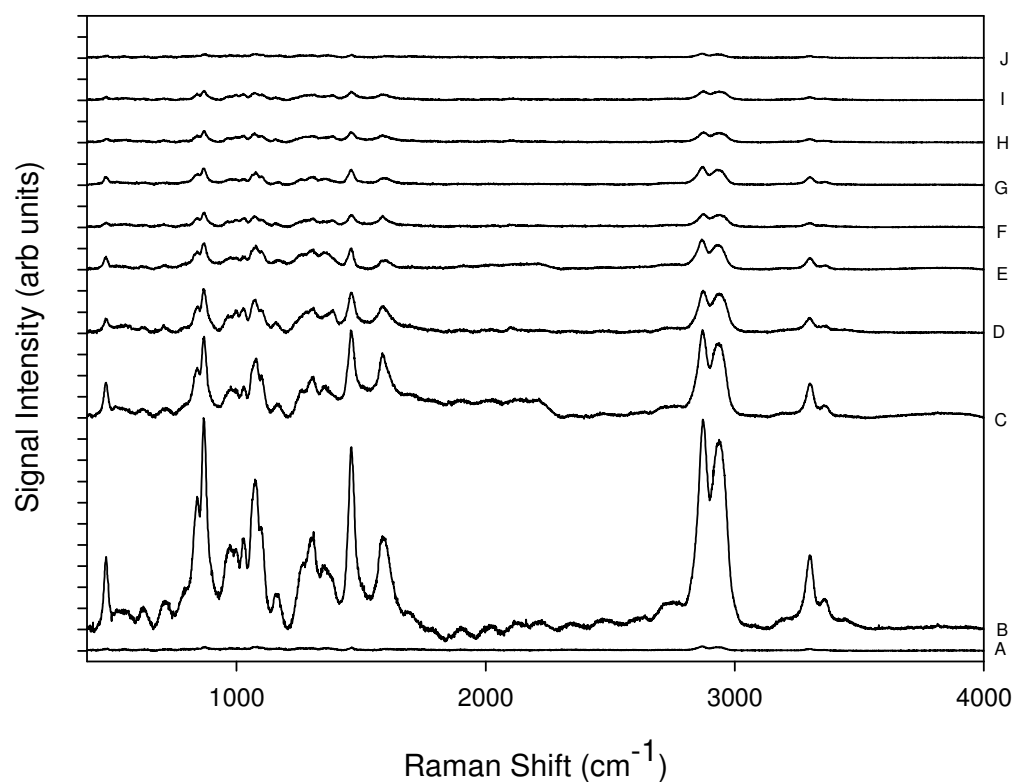
- A: Benzotriazole (10% laser)
- B: Benzotriazole T = 0 hrs
- C: Benzotriazole T = 1 hrs
- D: Benzotriazole T = 2 hrs
- E: Benzotriazole T = 3 hrs
- F: Benzotriazole T = 4 hrs
- G: Benzotriazole T = 5 hrs
- H: Benzotriazole T = 6 hrs
- I: Benzotriazole T = 7 hrs
- J: Benzotriazole T = 8 hrs

Figure 6.2: Graphical representation of changes in intensity of the SERS spectra of 50 % w/v benzotriazole in CDCl_3 over time, laser strength 1 %, exposure time 20 s, accumulation 5 and excitation wavelength 660 nm.



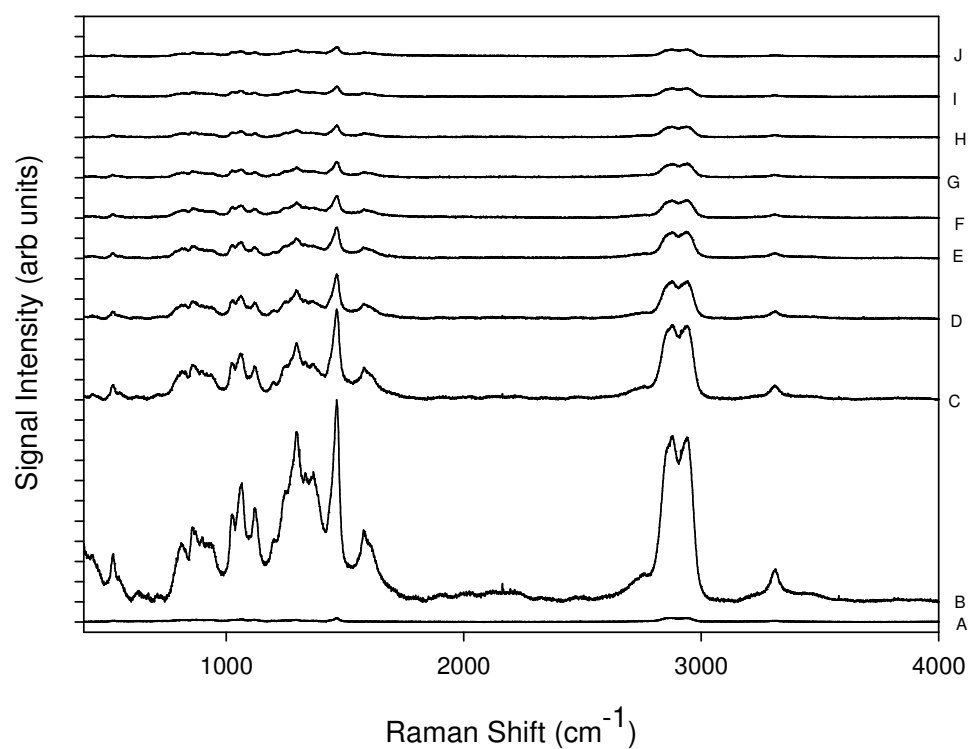
- A: Octanoic Acid (10% laser)
- B: Octanoic Acid T = 0 hrs
- C: Octanoic Acid T = 1 hrs
- D: Octanoic Acid T = 2 hrs
- E: Octanoic Acid T = 3 hrs
- F: Octanoic Acid T = 4 hrs
- G: Octanoic Acid T = 5 hrs
- H: Octanoic Acid T = 6 hrs
- I: Octanoic Acid T = 7 hrs
- J: Octanoic Acid T = 8 hrs

Figure 6.3: Graphical representation of changes in intensity of the SERS spectra of octanoic acid over a set time period, laser strength 1 %, exposure time 20 s, accumulation 5 and excitation wavelength 660 nm.



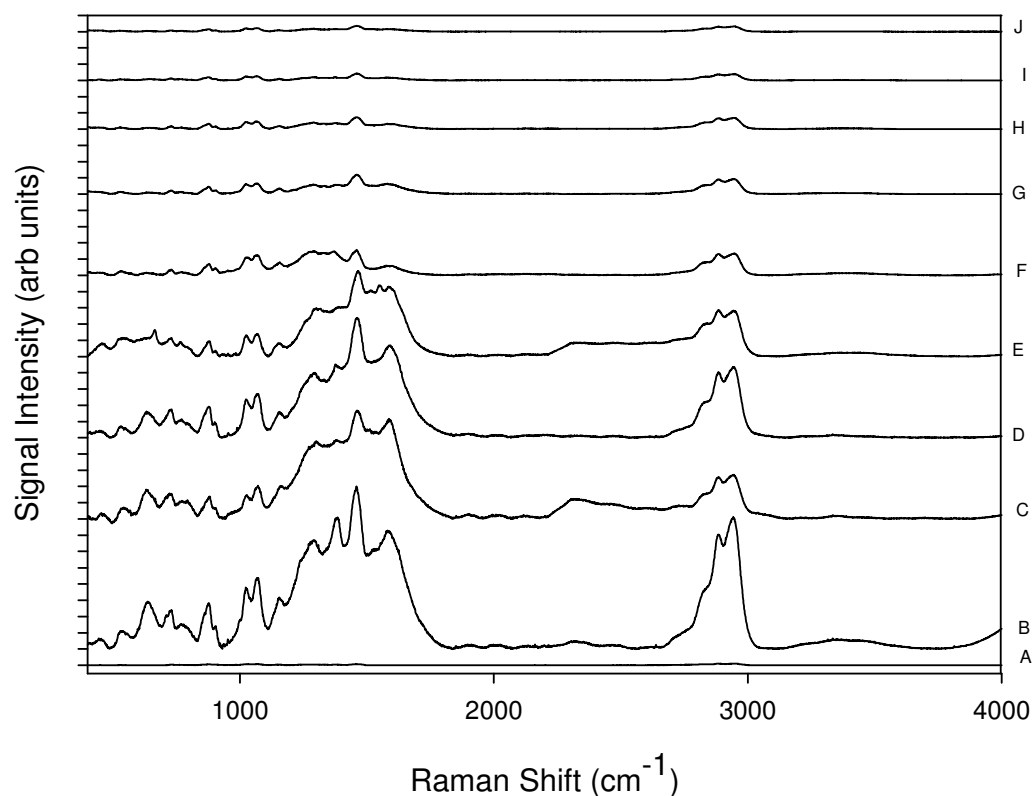
- A: Monoethanolamine 90% (10% laser)
- B: Monoethanolamine 90% T = 0 hrs
- C: Monoethanolamine 90% T = 1 hrs
- D: Monoethanolamine 90% T = 2 hrs
- E: Monoethanolamine 90% T = 3 hrs
- F: Monoethanolamine 90% T = 4 hrs
- G: Monoethanolamine 90% T = 5 hrs
- H: Monoethanolamine 90% T = 6 hrs
- I: Monoethanolamine 90% T = 7 hrs
- J: Monoethanolamine 90% T = 8 hrs

Figure 6.4: Graphical representation of changes in intensity of the SERS spectra of monoethanolamine 90 % over a set time period, laser strength 1 %, exposure time 20 s, accumulation 5 and excitation wavelength 660 nm.



- A: Diethanolamine 88% (10% laser)
- B: Diethanolamine 88% T = 0 hrs
- C: Diethanolamine 88% T = 1 hrs
- D: Diethanolamine 88% T = 2 hrs
- E: Diethanolamine 88% T = 3 hrs
- F: Diethanolamine 88% T = 4 hrs
- G: Diethanolamine 88% T = 5 hrs
- H: Diethanolamine 88% T = 6 hrs
- I: Diethanolamine 88% T = 7 hrs
- J: Diethanolamine 88% T = 8 hrs

Figure 6.5: Graphical representation of changes in intensity of the SERS spectra of diethanolamine 88 % over a set time period, laser strength 1 %, exposure time 20 s, accumulation 5 and excitation wavelength 660 nm.



- A: Triethanolamine 90% (10% laser)
- B: Triethanolamine 90% T = 0 hrs
- C: Triethanolamine 90% T = 1 hrs
- D: Triethanolamine 90% T = 2 hrs
- E: Triethanolamine 90% T = 3 hrs
- F: Triethanolamine 90% T = 4 hrs
- G: Triethanolamine 90% T = 5 hrs
- H: Triethanolamine 90% T = 6 hrs
- I: Triethanolamine 90% T = 7 hrs
- J: Triethanolamine 90% T = 8 hrs

Figure 6.6: Graphical representation of changes in intensity of the SERS spectra of triethanolamine 90 % over a set time period, laser strength 1 %, exposure time 20 s, accumulation 5 and excitation wavelength 660 nm.

The Raman peaks observed in these SERS spectra correlate well with the VCI compounds characterised by FTIR and NMR. Hence the combination of SERS and other analytical methods appear to provide useful information on the rate at which each VCI compounds disassociate from the SERS substrate. However it was seen that the not all the VCI components (morpholine) were Raman active, and thus the

absence of Raman peaks for a VCI component is not compelling evidence that the VCI is present or inactive.

6.6.2 Dissociation kinetics

The dissociation of each compound was modelled as diffusion controlled (figures 6.7 – 6.16).

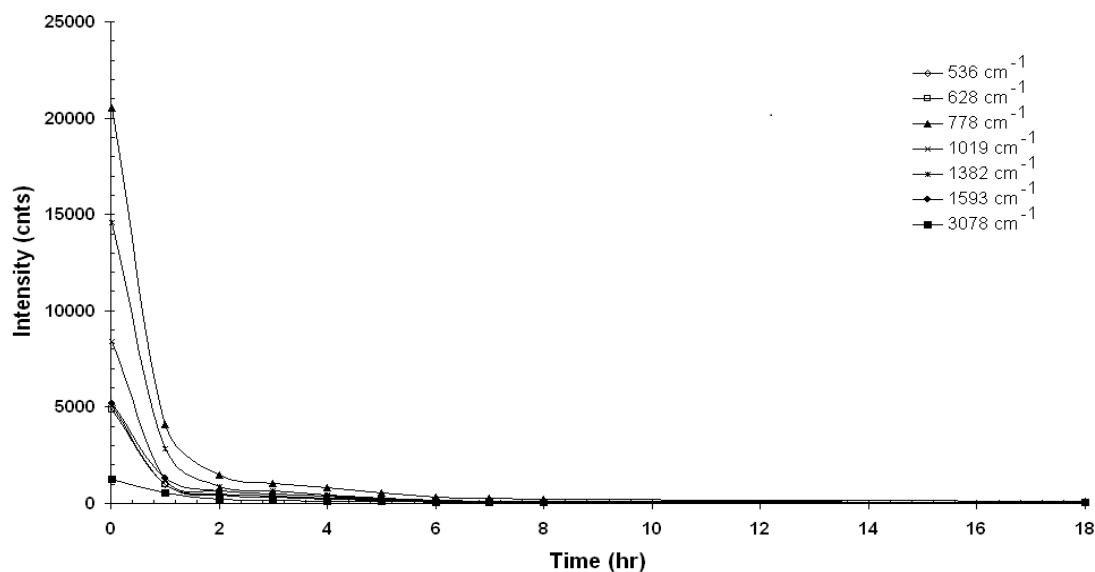


Figure 6.7: Dissociation of 50 % w/v Benzotriazole in CDCl_3 over a set time period.

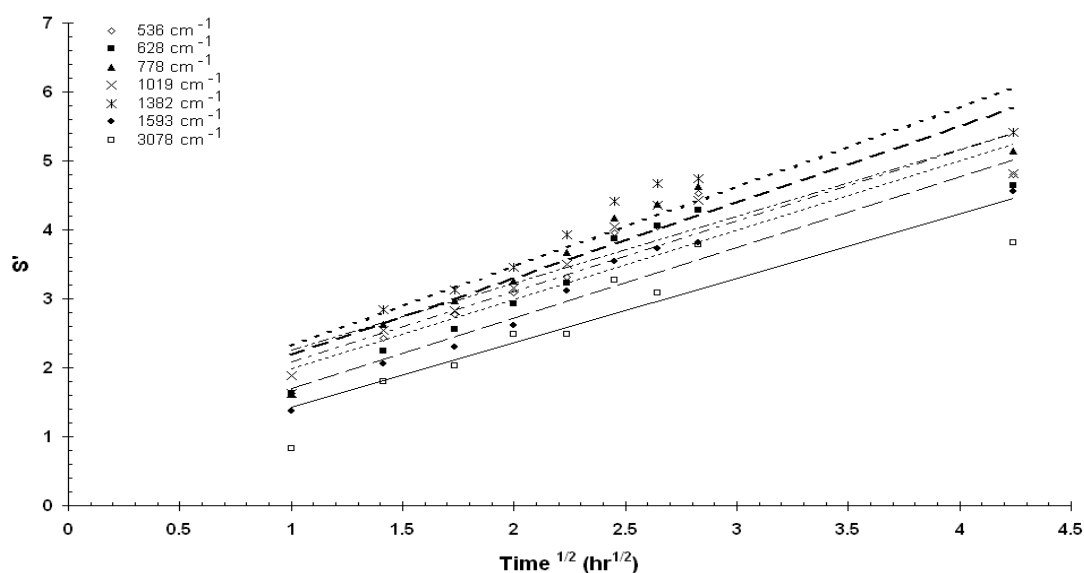


Figure 6.8: Modelling of dissociation of 50 % w/v Benzotriazole in CDCl_3 over a set time period.

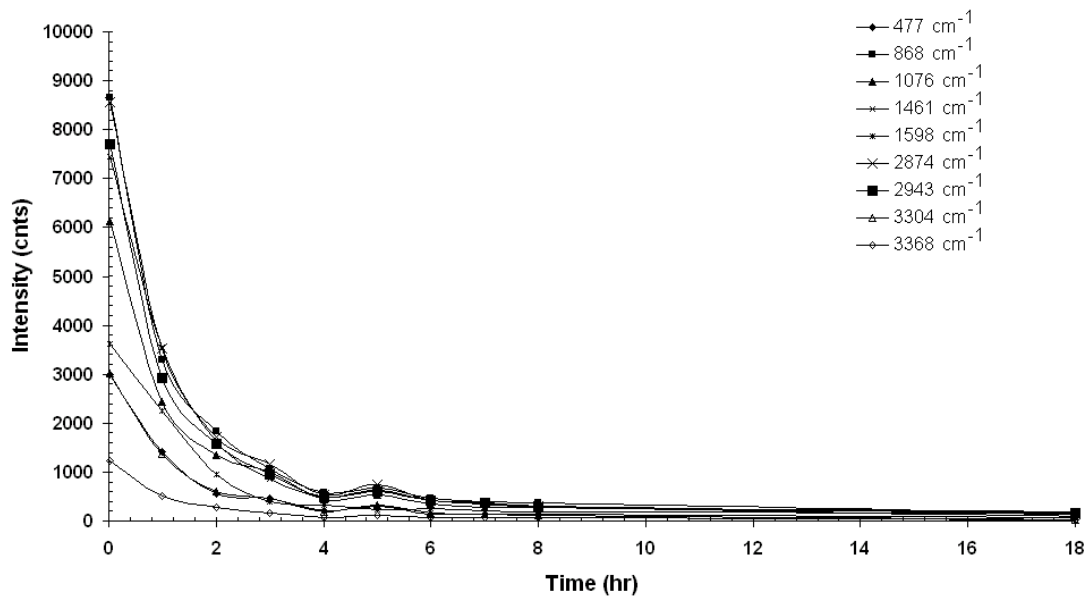


Figure 6.9: Dissociation of Monoethanolamine 90% over a set time period.

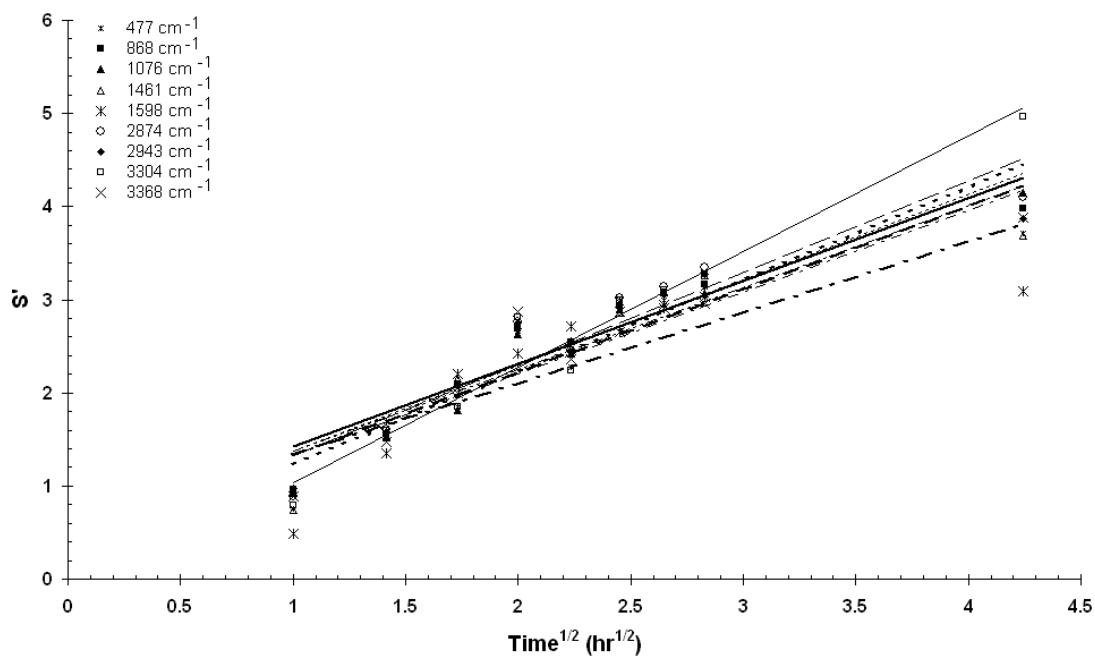


Figure 6.10: Modelling of dissociation of Monoethanolamine 90 % over a set time period.

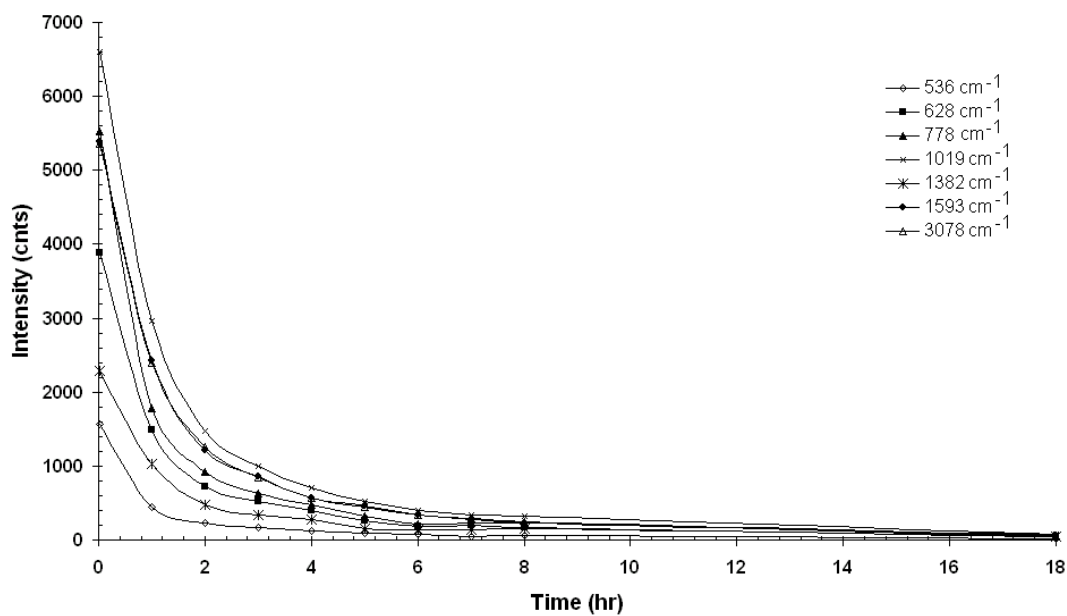


Figure 6.11: Dissociation of Diethanolamine 88 % over a set time period.

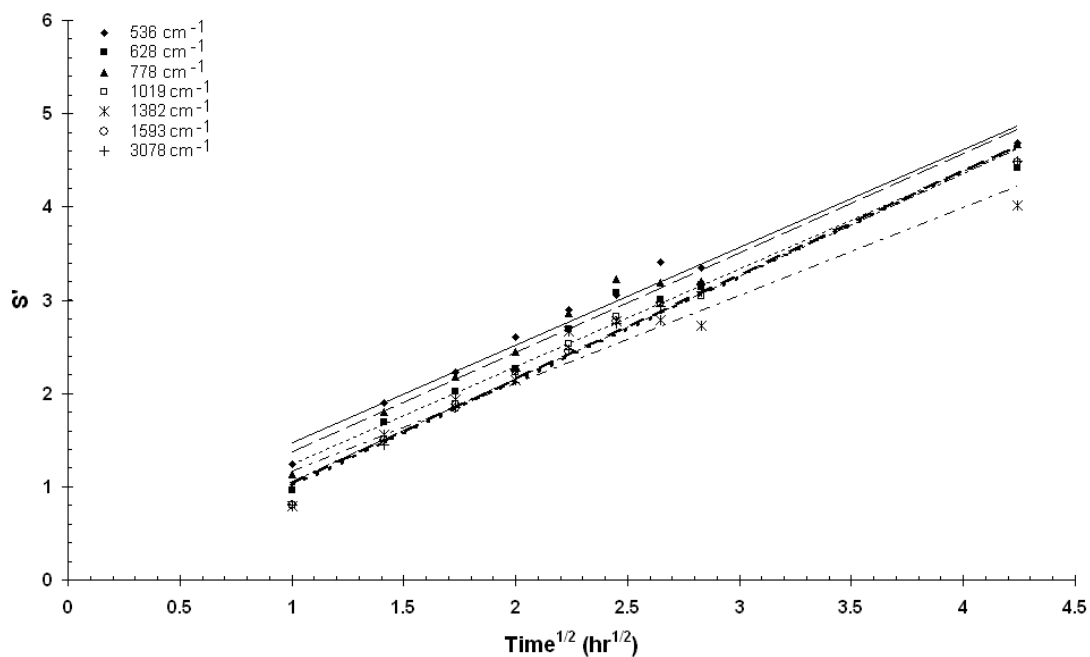


Figure 6.12: Modelling of desorption of Diethanolamine 88 % over a set time period.

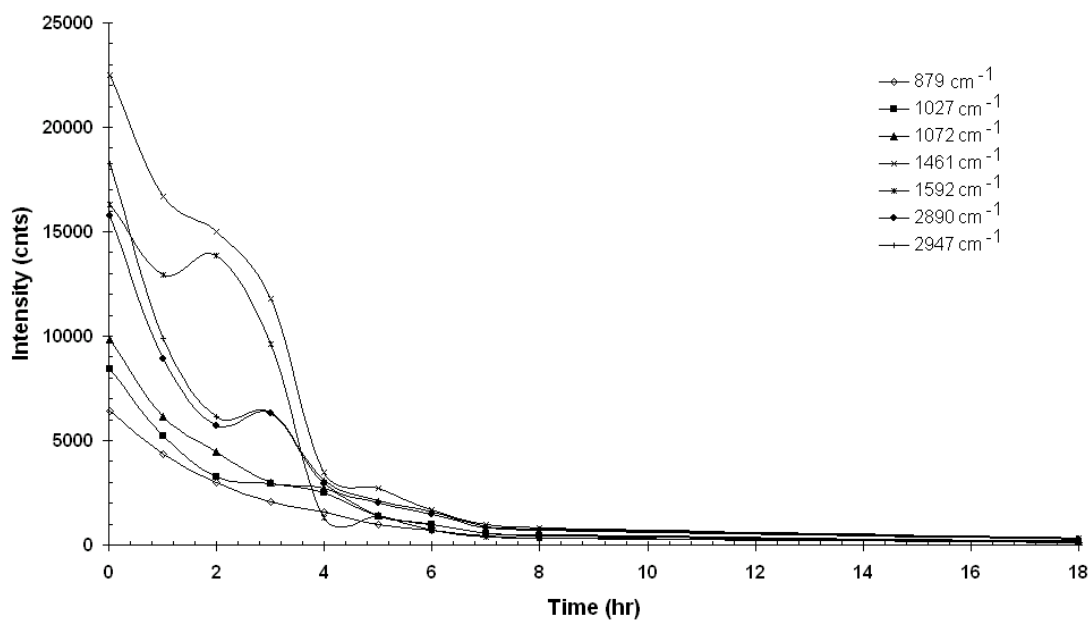


Figure 6.13: Dissociation of Triethanolamine 90 % over a set time period.

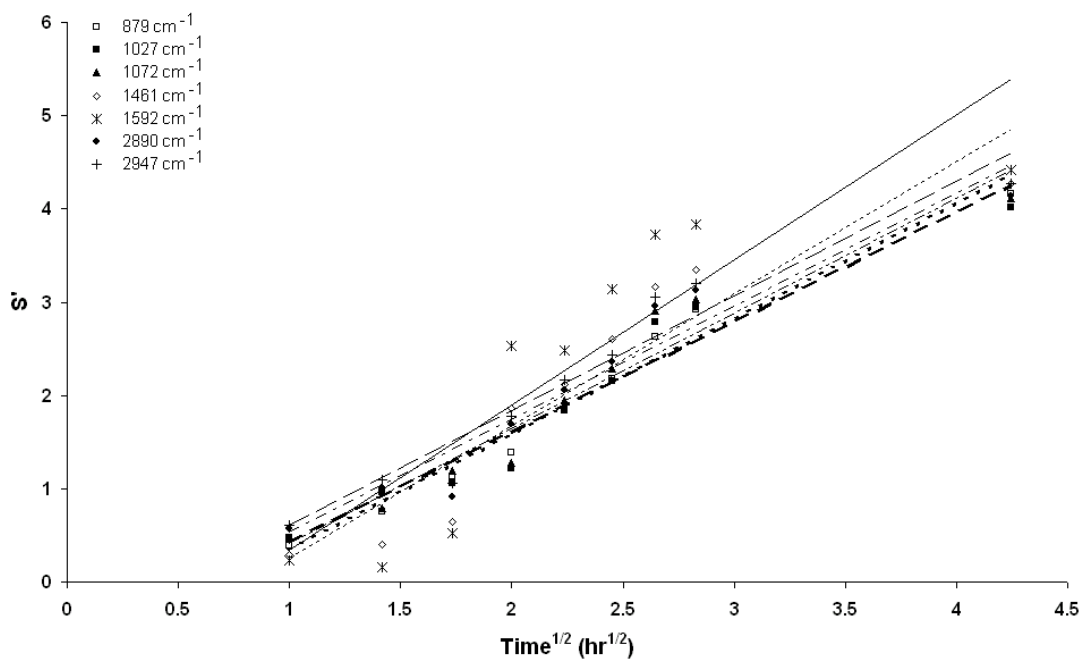


Figure 6.14: Modelling of dissociation of Triethanolamine 90 % over a set time period.

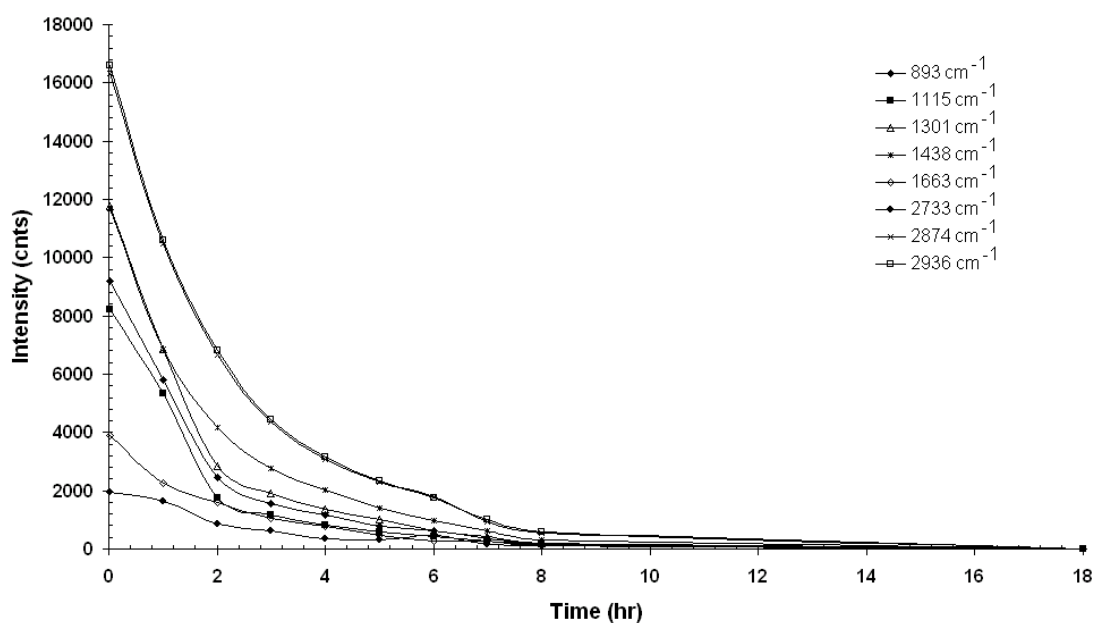


Figure 6.15: Dissociation of Octanoic Acid over a set time period.

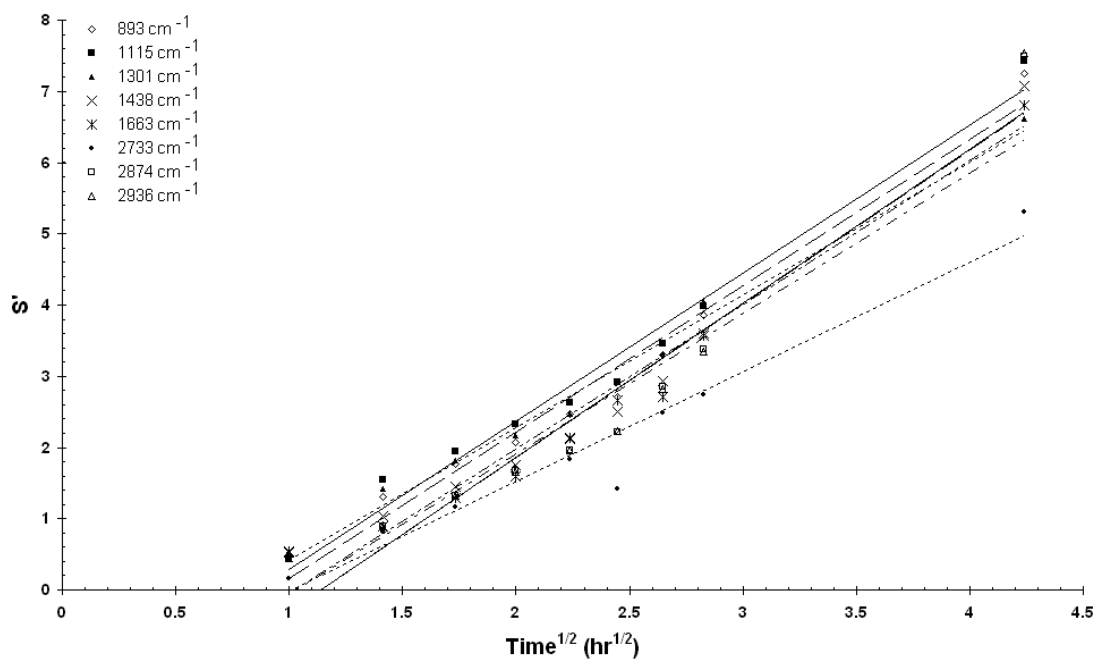


Figure 6.16: Modelling of dissociation of Octanoic Acid over a set time period.

6.6.3 Diffusion Model

A clear trend is observed for the dissociation of each VCI component, which may be modelled as diffusion controlled, indicating a rapid volatilisation of each component, essential to their suitability as vapour phase inhibitors.

In electrochemistry signal occurs at the electrode interface and so is reliant on the rate of flux into the electrode.

$$i = k \left. \frac{\partial C}{\partial x} \right|_{x=0} \approx k \frac{(C^\infty - C_e)}{\delta} \quad \mathbf{6.1}$$

Equation 6.1 is the Cottrell equation, where i is current / the signal, C is concentration, k is a constant, C^∞ is the bulk concentration, C_e is the concentration at the electrode and δ is the diffusion layer. As,

$$\delta = \sqrt{\pi D t} \quad \mathbf{6.2}$$

the system is diffusion controlled and

$$\int i dt = \int \left(\frac{k C^\infty}{\sqrt{\pi D}} \right) t^{-\frac{1}{2}} dt \quad \mathbf{6.3}$$

$$Q = \left(\frac{k C^\infty}{\sqrt{\pi D}} \right) \sqrt{t} \quad \mathbf{6.4}$$

Q is the charge / flux within the system. In the VCI SERS monitoring system the signal observed is due to surface interaction. Therefore if it is assumed that because the system is based on the VCIs action of evaporating to produce an equilibrium environment, the systems total flux in should equal the flux out, and so if the initial signal observed at $t \approx 0$, is taken as the limiting concentration signal, S_{lim} , and the signal of desorption after any time is taken as S_t . The inward signal may be calculated as S' . Where,

$$S' = S_{\text{lim}} - S_t \quad \mathbf{6.5}$$

or

$$S' = k \left(\frac{C^\infty - C_e}{\delta} \right) = \left(\frac{k C^\infty}{\sqrt{\pi D}} \right) \sqrt{t} \quad \mathbf{6.6}$$

however there is an accumulation over time, and hence,

$$\int S' \partial t = \int \left(\frac{kC^\infty}{\sqrt{\pi D}} \right) t^{-\frac{1}{2}} \partial t \quad 6.7$$

$$S' = \frac{kC^\infty \sqrt{t}}{\sqrt{\pi D t}} = S_{\text{lim}} - S_t \quad 6.8$$

indicating a diffusion controlled system if a straight line is the product of plotting $S_{\text{lim}} - S_t$ against $t^{-\frac{1}{2}}$.

6.6.4 Adsorption of benzotriazole onto SERS surface

The overall mechanism of VCIs as explained above is to rapidly evaporate and disperse within a container forming an equilibrium environment; a component of the corrosion inhibitor then condenses upon the metal surface to form a protective barrier layer preventing the onset of corrosion. Benzotriazole is a VCI component that has been observed to condense onto a metal surface³, and was the component on which a subsequent study was focused.

First it was necessary to prepare a sealable container, which would allow SERS measurement; this was achieved by the fabrication of a Petri dish with sample stage and quartz window in the lid, figure 6.17. The quartz window is necessary as the polystyrene that the dish is made of has a particularly intense Raman signal that overlaps that of the benzotriazole.

Benzotriazole was placed in the well of the container, a SERS substrate placed on the container's stage, as illustrated in figure 6.17 and the container sealed. Measurements were taken at set time intervals (figure 6.18). The condensation of benzotriazole over time is illustrated in figure 6.19 where after a period of evaporating the condensation of benzotriazole is observed; the protective layer appears to 'build up' rapidly before levelling off to a constant level. The maximum signal at ~ 7 hours could be classed as the saturation coverage of the substrate, with the subsequent lower SERS signal be due to the system maintaining an desorption/adsorption equilibrium.

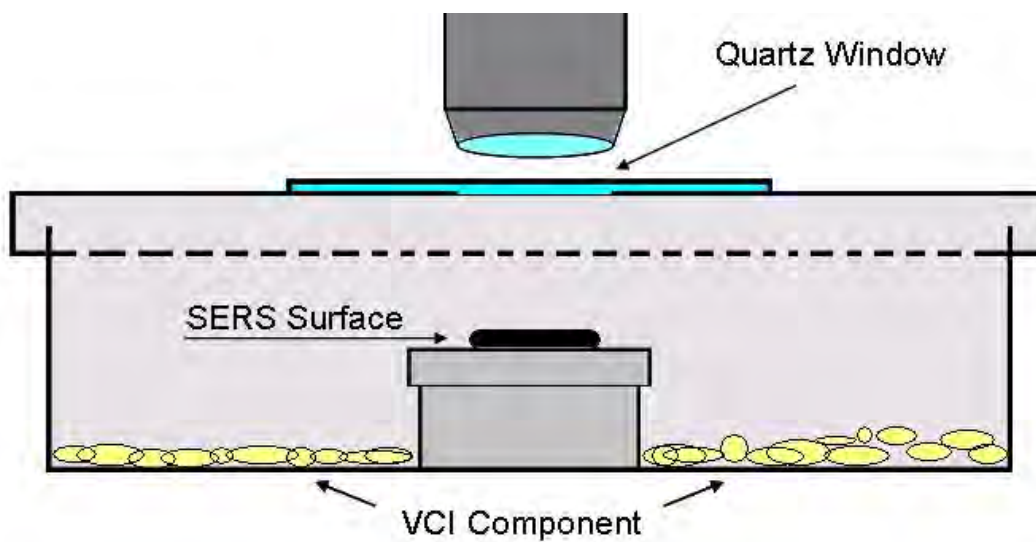
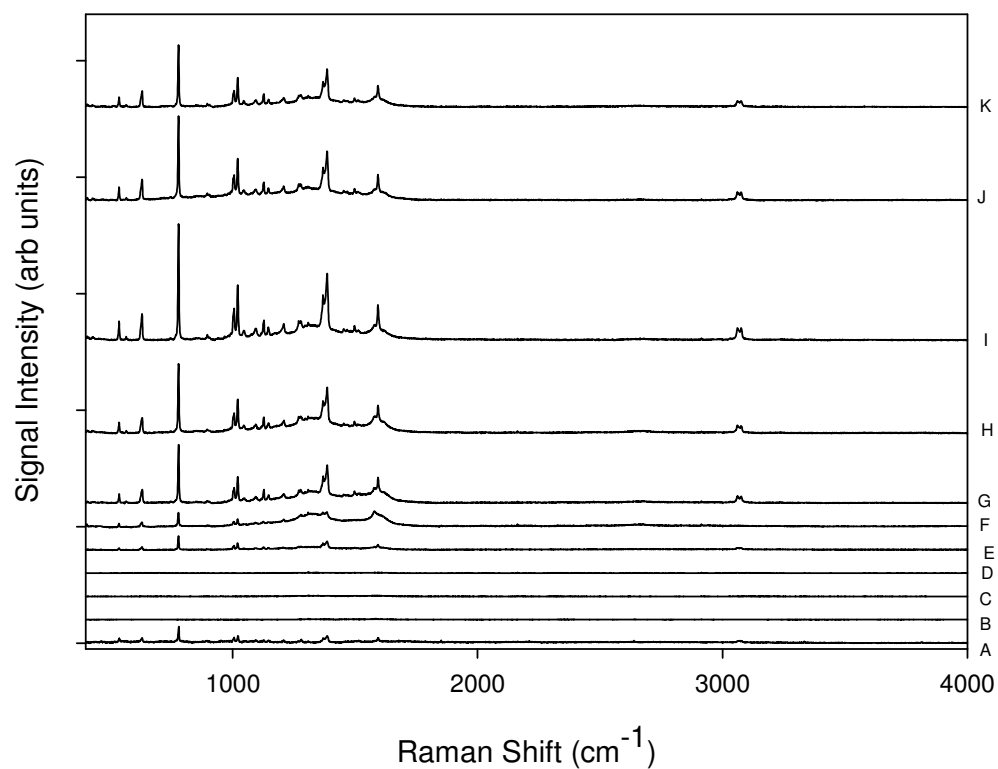


Figure 6.17: Schematic of sealed diffusion/condensation container with quartz window.



- A: Benzotriazole (10% laser)
- B: Benzotriazole T = 0 hrs
- C: Benzotriazole T = 1 hrs
- D: Benzotriazole T = 2 hrs
- E: Benzotriazole T = 3 hrs
- F: Benzotriazole T = 4 hrs
- G: Benzotriazole T = 5 hrs
- H: Benzotriazole T = 6 hrs
- I: Benzotriazole T = 7 hrs
- J: Benzotriazole T = 8 hrs
- K: Benzotriazole T = 18 hrs

Figure 6.18: Graphical representation of changes in intensity of the SERS spectra of Benzotriazole over a set time period, laser strength 1 %, exposure time 20 s, accumulation 5 and excitation wavelength 660 nm.

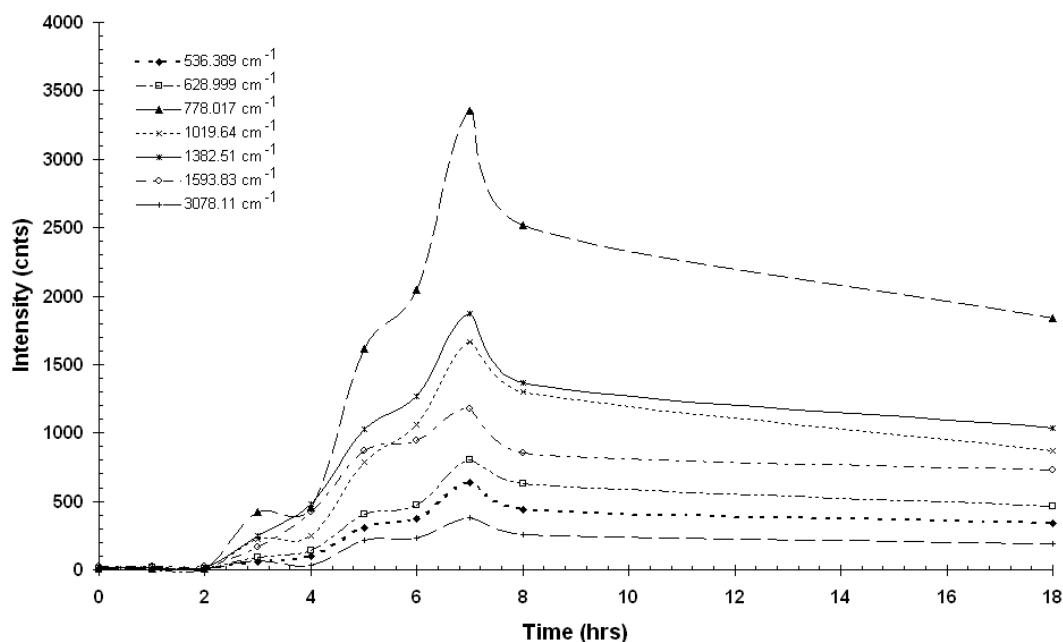


Figure 6.19: Condensation of benzotriazole over a set time period.

The condensation of other components was investigated however they proved to operate in an alternative fashion, merely saturating the containers environment rather than condensing upon the SERS surface, confirming descriptions of their mechanism in the literature²⁰.

6.7 Conclusions

Silver nanostructured SERS substrates with an inert (carbon) support were shown to significantly enhance the Raman spectra of multiple VCI components. SERS was found to be suitable for monitoring the volatilisation / desorption of VCI components and their subsequent adsorption to a surface within a sealed environment over time. The volatilisation was determined to be diffusion controlled.

Also Raman spectroscopy clearly showed that adsorption of benzotriazole occurs. However, the mechanism of adsorption to a surface was less clear as the action of the components came in to play, hence only the adsorption of Benzotriazole was monitored, the initial evaporation of which appears to be slow suggesting that the presence of the other components in the complete VCI 'catalyse' the process' mechanism. This confirms SERS potential as a means of monitoring VCI compounds in real time, but suggests that analysis of a complete / commercial VCI is still necessary.

6.8 References

1. N. Pieterse, W.W. Focke, E. Vuorinen, I. Rácz, *Corrosion Science*, 2006, 48, 1986 – 1995
2. L.R.M. Estevao, R.S.V. Nascimento, *Corrosion Science*, 2001, 43, 1133 – 1153
3. G. Tormoen, J. Burket, J.F. Dante, N. Sridhar, *Corrosion*, 2006, 62, 1082 – 1091
4. D.M. Bastidas, E. Cano, E.M. Mora, *Anti -Corrosion Methods and Materials*, 2005, 52, 71 – 77
5. D.Q. Zhang, L.X. Gao, G.D. Zhou, *Surface & Coatings Technology*, 2010, 204, 1646 – 1650
6. U.Rammelt, S. Koehler, G. Reinhard, *Corrosion Science*, 2009, 51, 921 – 925
7. R. Sanci, M. Volkan, *Sensors and Actuators, B*, 2009, 139, 150-155
8. A. Champion, P. Kambhampati, *Chemical Society Reviews*, 1998, 27, 241 – 250
9. D.L Stokes, T. Vo-Dinh, *Sensors and Actuators B*, 2000, 69, 28 - 36
10. C.J. Addison, A.G. Brolo, *Langmuir*, 2006, 22, 8696 – 8702.
11. D.I. Ellis, R. Goodacre, *Analyst*, 2006, 131, 875 – 885
12. C.E. Talley, J.B. Jackson, C. Oubre, N.K Grady, C.W. Hollars, S.M. Lane, T.R. Huser, P. Nordlander, N.J. Halas, *Nano Letters*, 2005, 5, 1569
13. W.E. Smith, *Chemical Society Reviews*, 2008, 37, 955 – 964
14. W.C. Lin, M.C. Yang, *Macromolecular Rapid Communications*, 2005, 26, 1942 – 1974
15. P. Hildebrandt, M. Stockburger, *Journal of Physical Chemistry*, 1984, 88, 5935
16. A. Otto, A. Bruckbauer, Y.X. Chen, *Journal of Molecular Structure*, 2003, 661, 501
17. CRC Handbook of Chemistry and Physics, D.R. Lide, Editor in chief, 89th ed., Boca Raton, Fla, CRC; London, Taylor & Francis, 2008, 3 – 40, 3 – 162, 3 – 232, 3 – 380, 3 – 404, 3 – 496
18. S. Duckett, B. Gilbert, *Foundations of Spectroscopy*, Oxford, Oxford University Press, 2000
19. G. Socrates, *Infrared and Raman Characteristic group Frequencies: Tables and Charts*, 3rd ed., Chichester, J. Wiley, 2001
20. B.A. Miksic, R.H. Miller, *Fundamental principles of corrosion protection with vapour phase inhibitors*, 5th European Symposium on Corrosion Inhibitors, 1980

7. General Conclusion & Future Work

The current and potential future impact nanotechnology could have is most clearly evident in the field of sensor research, where it combines with the three realms of science, physics, biology and chemistry. The use of nanoparticles in sensors and sensing techniques coupled with ongoing research for simple controlled (morphology) synthesis of nanoparticles continues to be an active and expanding research field.

In chapter 2 a simple ‘bottom up’ preparation of silver nanoparticles as PVA stabilised colloids with both high loads and tuneable optical properties was developed where the nanostructure’s morphology was controlled and optimised.

In both cases the synthesis was rapid and repeatable producing nanoparticles of distinct size and morphology. Best results were obtained when the high load colloids were prepared at lower temperatures ($\leq 4^{\circ}\text{C}$). The resulting colloids displayed good stability over time when stored appropriately (in the dark).

The synthesis process for the ‘coloured’ colloids could be carried out at room temperature on the bench and so was deemed sufficiently robust that it was adapted as an undergraduate laboratory practical, to demonstrate the unique optical properties of nanostructures and infer the potential of nanotechnology. The laboratory practical has been run for both first and second year students as part of an inorganic module for the last two academic years. Whereas previously the classic Turkevich method had been used to prepare gold colloids, the silver colloids prepared more prominently displayed (through colour change) the impact of particle morphology on the physiochemical properties of nanomaterials.

The application of the high load silver colloid as a nanocomposite chemiresistor sensor was investigated in chapter 3. The nanoparticle composite sensor gave a selective, reversible, and rapid response that was proportional to increasing humidity levels at room temperature and pressure. This was surprising as work throughout the literature on nanocomposite sensor coatings suggest that increasing analyte should result in a decrease in signal as the overall resistance of the coating increases as the composite material (generally polymers) swell with increasing analyte concentration¹
-4.

Although the precise mechanism of the sensing process remained unresolved, it is suggested that the ‘scaffold’ proposal⁵ for the sensing action remains the most likely, where a form of ionic migration occurs with the introduction of water vapour

hydrating residual electrolyte (a remnant of the synthesis process) in the composite's makeup and allowing the movement of the ions surrounding the silver nanoparticles, which in essence act as a scaffold along which the current flows. The primary obstacle in the application of the composite coating is the difficulty in depositing uniform films. Printing methods such as screen and inkjet printing could solve this issue. *M.R Smyth et al.* have recently reported successful methods of printing of thin films, an adaptation of which could be highly useful⁶⁻⁷.

There still exists a lot of scope for the application of similar nanocomposites in other sensing applications; a possible route of investigation would be the development of non polar composites for VOC (volatile organic compound) detection, using compounds like PTFE (polytetrafluoroethylene) as the composite matrix.

A shift of focus occurred as the optical properties of the nanoparticles were utilised; through their application as surface enhanced Raman (resonance) spectroscopy substrates in both their colloidal (metal nanoparticles) form and as cast planar nanoparticle films. The study and application of the SER(R)S technique underwent a marked increase in recent decades, primarily because of advances in the 'nano' field, which has contributed to a significant development of the technique specifically in terms of the design and fabrication of novel and improved SERS substrates.

Advances in Raman instrumentation has also benefited the technique, resulting in a greater exposure to the wider scientific community. At present the major contributors to SERS research are illustrated in figure 7.1.

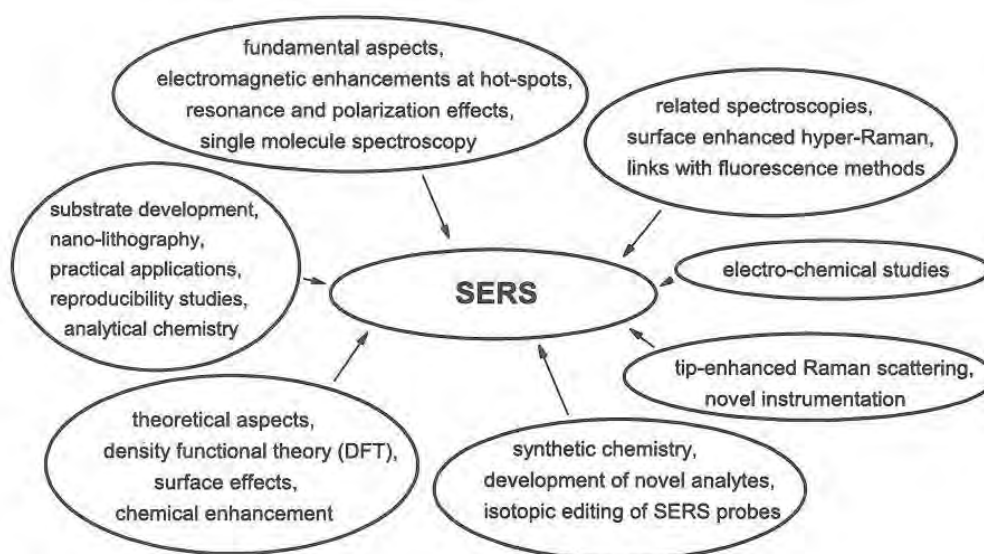


Figure 7.1: Some of the major contributors to current SERS research⁸

Significant enhancement of the Raman signal for probe molecules was observed; chapter 4 showed a clear trend where with increasing concentration of colloid, there resulted an enhancement of signal, until an optimum ratio of analyte to colloid was established. This optimum ratio was found to be consistent for each analyte over a range of concentrations.

A supplementary study of the nanoparticle's SERS activity as cast substrates was conducted in chapter 5. Here both full silver and silver nanocomposite coated carbon SERS surfaces demonstrated clear signal enhancement. Initial studies showed that when an external potential was applied the resulting spectra could be further enhanced within a limited window of applied voltage.

Emphasis was then placed on the interaction of the coating nanostructures in subsequent displayed a greater boost to signal intensity, however attempts to apply potentials to films of high loaded silver composites failed because the layer was too thick. Screen printing methods could alleviate this problem.

The effectiveness of the cast nanostructures as SERS substrate was clearly illustrated prompting investigation into their application in real world situations in chapter 6, namely the real time monitoring of volatile corrosion inhibitors. SERS was found to be suitable for monitoring the dissociation of VCI components (supplied to us by MetPro) from the silver metal nanostructures and their subsequent adsorption to a surface within a sealed environment over time. The dissociation was determined to be diffusion controlled; the mechanism of adsorption to a surface was less clear as the competitive action of the components came in to play. Hence only the adsorption of Benzotriazole was monitored. The initial evaporation and dispersion of the Benzotriazole appeared to be slow suggesting that the presence of the other components in the complete VCI 'catalyse' the process' mechanism. This provides an avenue for future work as ideally a follow up analysis of a complete / commercial VCI is necessary to fully illuminate the mechanisms involved.

Finally in conclusion this body of work establishes that nanostructured sensors and techniques provide great potential for selective and sensitive analyses through careful control of structure and interface interaction properties, coupled with novel physical and chemical features, nano – based sensors will undoubtedly be more widespread and instrumental in future sensing applications offering multiple advantages over traditional analysis.

7.1 References

1. C. Drake, S. Deshpande, D. Bera, S. Seal, *International Materials Reviews*, 2007, 52, 289 – 317
2. P.G Su, L.N. Huang, *Sensors and Actuators, B*, 2007, 123, 501 – 507
3. M.J. Hostetler, S.J. Green, J.J. Stokes, R.W. Murray, *Journal of the American Chemical Society*, 1996, 118, 4212 – 4213
4. M.J. Hostetler, A.C. Templeton, R.W. Murray, *Langmuir*, 1999, 15, 3782 – 3789
5. G. Jimenez – Cadena, J. Riu, F. Xavier Rius, *Analyst*, 2007, 132, 1083 – 1099
6. A.C. Power, A.J. Betts, J.F. Cassidy, *Analyst*, 2010, 135, 1645 – 1652
7. N. Lenhart, K. Crowley, A.J. Killard, M.R. Smyth, A. Morrin, *Thin Solid Films*, 2011, 519, 4351 – 4356
8. K. Crowley, A. Morrin, R.L. Shepherd, M. Panhuis, G.G. Wallace, M.R. Smyth, A.J. Killard, *IEEE SENSORS JOURNAL*, 2010, 10, 1419 – 1426.
9. E.C. Le Ru, P.G. Etchegoin, *Principals of Surface – Enhanced Raman Spectroscopy and related plasmonic effects*, Chapter 1, Elsevier, Oxford, 2009

Appendix

A.1. Publications

A.1.1 Journal Articles

A.C. Power, A.J. Betts, J.F. Cassidy, Silver Nanoparticle Polymer Composite Based Humidity Sensor, *Analyst*, 2010, 135, 1645 – 1652

A.C. Power, A.J. Betts, J.F. Cassidy, Non Aggregated Colloidal Silver Nanoparticles for Surface Enhanced Resonance Raman Spectroscopy, *Analyst*, 2011, DOI: 10.1039/C1AN15250E

A.1.1.2 Conference Papers

A.C. Power, A.J. Betts, J.F. Cassidy, Development of a Novel Humidity Sensor Based on a Polymer Silver Nanoparticle Composite, ECS transactions, 2009, 19, 181-190

A.1.2 Conferences

A.1.2.1 Oral Presentations

Development of a Novel Humidity Sensor Based on a Polymer Silver Nanoparticle Composite, 215th ECS Meeting – Symposium J2 - 35 Years of Chemical Sensors - Honorary Symposium for Professor Jiri Janata, San Francisco, CA, May 2009

Silver Polymer Nanocomposite Based Humidity Sensor, 62nd Irish Universities Chemistry Research Colloquium, School of Chemistry & Chemical Engineering, Queen's University Belfast, July 2010

Silver Polymer Nanocomposite Based Humidity Sensor, INSPIRE BioNano Workshop, Conway Research Institute, University College Dublin, October 2010

The Application of a Silver Nanocomposite as a Humidity Sensor, 3rd Annual Materials Ireland Conference, Dublin Institute of Technology, Kevin St., December 2010

Nanosilver and Sensing, 1st Annual Postgraduate Research Symposium, Dublin Institute of Technology, Kevin St., January 2011

Non Aggregated Colloidal Silver Nanoparticles for Surface Enhanced Raman Spectroscopy, 6th CASi conference, The Helix, Dublin City University, February 2011-06-06

A.1.2.2 Poster Presentations

Development of a Nano-Silver based gas Sensor, Analytical Sciences Conference, Waterford Institute of Technology, May 2008

Silver Polymer Nanocomposite based Humidity Sensor, Symposium 11, 61st Annual Meeting of the International Society of Electrochemistry, Nice, France, September 2010

Colloidal Silver Nanoparticles Analogues for Surface Enhanced Raman Spectroscopy (SERS), Symposium 11, 61st Annual Meeting of the International Society of Electrochemistry, Nice, France, September 2010

Colloidal Silver Nanoparticles Analogues for Surface Enhanced Raman Spectroscopy (SERS), INSPIRE BioNano Workshop, Conway Research Institute, University College Dublin, October 2010

Colloidal Silver Nanoparticles Analogues for Surface Enhanced Raman Spectroscopy (SERS), 3rd Annual Materials Ireland Conference, Dublin Institute of Technology, Kevin St., December 2010 – Prize – Best Poster

Appendix

Application of Silver Nanoparticles (Colloids/Films) in Surface Enhanced Raman Spectroscopy, Eirelec 2011: Electrochemistry the Future?, Dunraven Arms Hotel, Adare, May 2011

A.1.2.3 Related Courses

Bath Electrochemistry Winter School 2010, University of Bath, January 2010

A.2.1 Undergraduate Laboratory Practical

Silver Colloids and Colour

Introduction

Nanoparticles (particles of the nanoscale 1-100nm or 0.000000001 – 0.0000001 metres) can be prepared by either Physical or Chemical means.

The physical method involves the breaking down of a material. This can be difficult and problems with the repeatability, uniformity, and consistency can often arise.

The chemical method involves preparing the nanoparticles chemically. This method is much simpler and generally gives much better results. (There are numerous chemical techniques but we'll be focusing on the reduction of the metal salt.) When preparing nanoparticles in this manner, it is often useful to do so by preparing the colloid, which can be manipulated later to produce the desired effect.

A colloid is a type of mixture that appears to be a solution but is actually a mechanical mixture. A colloidal system consists of two separate phases: a dispersed phase (internal phase), and a continuous phase (dispersion medium).

In a colloid, the dispersed phase is made of tiny particles or droplets that are distributed evenly throughout the continuous phase. The dispersed-phase particles are sized between 1 nm and 100 nm in at least one dimension.

Many familiar substances including butter, milk, cream, aerosols (fog, smog, smoke), asphalt, inks, paints, glues, and sea foam, are colloids.

A major advantage of colloids is their stability. In fact colloids made by Faraday over 100 years ago are still in existence today.

Colloidal Stability

What causes this stability?

Steric stabilization and electrostatic stabilization are the two main mechanisms for colloid stabilization.

In the case of silver colloids, electrostatic stabilisation occurs. This is based on the mutual repulsion of like electrical charges. Different phases generally have different charge affinities, so that a charge double-layer forms at any

interface. Small particle sizes lead to enormous surface areas, and results in this effect being greatly amplified in colloids. This can be better explained by the DLVO theory.

The Deryagin-Landau-Verwey-Overbeek (DLVO) theory suggests that the stability of a particle in solution is dependent upon its total potential energy function V_T . This theory recognizes that V_T is the balance of several competing contributions:

$$V_T = V_A + V_R + V_S$$

V_S (the potential energy due to the solvent) usually only makes a marginal contribution to the total potential energy over the last few nanometers of separation. More important is the balance between V_A and V_R ; these are the attractive and repulsive contributions.

DLVO theory suggests that the stability of a colloidal system is determined by the sum of these Van der Waals attractive (V_A) and electrical double layer repulsive (V_R) forces that exist between particles as they approach each other due to the Brownian motion they are undergoing. This theory proposes that an energy barrier resulting from the repulsive force prevents two particles approaching one another and adhering together. Therefore, if the particles have a sufficiently high repulsion, the dispersion will resist flocculation and the colloidal system will be stable. However, if a repulsion mechanism does not exist then flocculation or coagulation will eventually take place. To maintain the stability of the colloidal system, DLVO theory states that the repulsive forces between the particles must be dominant.

The stability of many colloids of both natural and man-made origin can be improved by the presence of macromolecules or polymers, e.g. fatty acids in milk are stabilised by the presence of casein. Polymers increase viscosity in the colloids, altering the sedimentation behaviour. This coupled with their high molecular weights results in only a small concentration being necessary to achieve this.

PVA is a well known and commonly used random block copolymer stabiliser. Only part of the macromolecule adsorbs to the particle allowing the rest to solvate and to expand away from the interface, preventing other particles from

approaching. PVA is widely used for polymer nanocomposites, and due to its water solubility the nanoparticles can be produced in an aqueous medium making the preparation process non-toxic.

Colloids and Colour

Nanoparticles of noble metals in colloidal form often display characteristic colours (Silver – spherical – yellow to red/gold, Gold – spherical – Ruby Red) These colours are a result of the unique physical properties of the nanoparticles themselves.



Figure 1. A sample set of the different coloured colloids produced in the practical, and their λ max.

How does it work?

When an external electro-magnetic field such as light is applied to a metal, the conduction electrons of the metal move collectively so as to screen the perturbed charge distribution in what is known as 'plasma oscillation'. The surface plasmon resonance (SPR) is therefore, a collective excitation mode of the plasma localised near the metal surface. This produces the shine associated with a metal.

In the case of a metal nanoparticle, the surface plasmon mode is 'restricted' due to the small dimensions to which the electrons are confined, i.e. the surface plasmon mode must conform to the boundaries of the dimensions of the nanoparticle.

Therefore, the resonance frequency of the surface plasmon oscillation of the metal nanoparticle is different from the plasma frequency of the bulk metal. Surface interactions can alter the optical properties and influence the spectral profile of the light scattered by the SPR of the metal nanoparticles. Among the metal nanoparticles known to exhibit SPR, silver nanoparticles have an especially strong SPR. Using UV-Vis and Mie theory, which solves Maxwell's

equations and in turn describe the extinction spectra (extinction = scattering + absorption), the size of spherical particles may be determined.

Factors affecting a colloids colour include the source metal (in this case Silver), the size range, and the shape of the nanoparticles within.

The Tyndall effect

The Tyndall effect, also known as Tyndall scattering, is the scattering of light by colloidal particles or particles in suspension, and may be demonstrated using a laser pointer. Shine the laser through a cuvette of DI water and the point where it hits the surface and passes through is evident, but the path the laser travels through the media is absent. If you shine the laser through a cuvette containing a colloid the path of the laser is clearly illuminated.

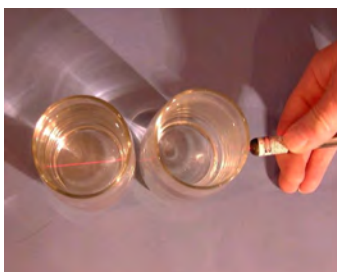


Figure 2. The glass on right contains only DI water, while glass on left contains silver colloid.

Characterisation of Nanoparticles

Characterisation of nanoparticles in colloids can be conducted using UV-Vis spectroscopy, Dynamic Light Scattering (D.L.S) and Transmission Electron Microscopy (T.E.M).

Size analysis by DLS utilises the Brownian motion that particles, emulsions, and molecules in suspension undergo as a result of bombardment by solvent molecules. If the particles are illuminated with a laser, the intensity of the scattered light fluctuates at a rate that is dependent upon the size of the particles, as smaller particles are 'hit' further by the solvent molecules and move more rapidly. Analysis of these intensity fluctuations yields the velocity of the Brownian motion and hence the particle size using the Stokes-Einstein relationship.

$$D = k_B T / 6\pi\eta r$$

Where D is the diffusion constant, k_B is Boltzmann's constant, T is the absolute temperature, η is the viscosity of the solvent and r is the particle radius.

DLS works on the principal that the nanoparticles in the dispersion are in constant Brownian motion; the larger a particle in the dispersion the slower it moves. A laser beam is applied to the colloid solution. Depending on the size of the particles, the light will be scattered differently and thus the intensity of the scattered light changes. This change is related to the size of the nanoparticles. Images of the nanoparticles can be obtained using TEM where an image is produced from the interaction of a beam of electrons transmitted through a thin layer of the colloid.

Experimental

Substance	Hazardous properties including physical hazards	Risk phrase	Target organs
Silver Nitrate	Skin Contact: May cause skin irritation or burns. Skin Absorption: May be harmful if absorbed through the skin. Eye Contact: May cause eye irritation. Inhalation: May be harmful if inhaled. Material may be extremely destructive to mucous membranes and upper respiratory tract. Ingestion: May be corrosive if swallowed. Poison	H272/314/410 P220/273/280/305/351/338/310/501 R8/34/50/53 S26/36/37/39/45/60/61	various
Sodium Borohydride	Skin Contact: Causes burns. Eye Contact: Causes burns. Inhalation: May be harmful if inhaled. Material is extremely destructive to the tissue of the mucous membranes and upper respiratory tract. Ingestion: Toxic if swallowed.	R15/24/25/34 S22/26/36/37/39/43/45	various
tri Sodium Citrate	Skin Contact: may cause skin irritation. Eye Contact: may cause irritation. Inhalation: May be harmful if inhaled. Material may be irritating to the tissue of the	Not Hazardous according to Directive 67/548/EEC	various

	mucous membranes and upper respiratory tract. May be harmful if inhaled. Ingestion: may be harmful if swallowed.		
Poly Vinyl Alcohol	Skin Contact: may cause skin irritation. Eye Contact: may cause irritation. Inhalation: May be harmful if inhaled. Material may be irritating to the upper respiratory tract. May be harmful if inhaled. Ingestion: may be harmful if swallowed.	Not Hazardous according to Directive 67/548/EEC	N/A
Hydrazine	Skin contact: Toxic if absorbed through skin. Causes skin burns. Eye contact: Causes eye burns. Inhalation: Toxic if inhaled. Material extremely destructive to the tissue mucous membranes and upper respiratory tract. Ingestion: Toxic if swallowed. Causes burns.	H226/301/314/317/331/350/410 P20/273/280/305/310/338/351/501 R10/23/24/25/34/43/45/50/53 S53/45/60/61	various
Rhodamine 6G	Skin contact: May be harmful if absorbed through skin. May cause skin irritation. Eye contact: May cause eye irritation. Inhalation: May be harmful if inhaled. May cause respiratory tract irritation. Ingestion: Harmful if swallowed.	H302 P none R22 S none	various
Malachite Green	Skin contact: May be harmful if absorbed through skin. May cause skin irritation. Eye contact: May cause eye irritation. Inhalation: May be harmful if inhaled. May cause respiratory tract irritation. Ingestion: Harmful if swallowed.	R22/41/50/53/63 S26/36/37/39/46/60/61	Kidney
Crystal Violet	Skin contact: May be harmful if absorbed through skin. May cause skin irritation. Eye contact: Causes eye burns. Inhalation: May be harmful if inhaled. May cause respiratory tract irritation. Ingestion: Harmful if swallowed.	H318/410 P273/280/305/338/351/501 R22/40/41/50/53 S26/36/37/39/46/60/61	various

Hydrochloric Acid	Inhalation May be harmful if inhaled. Material is extremely destructive to the tissue of the mucous membranes and upper respiratory tract. Ingestion May be harmful if swallowed. Causes burns. Skin May be harmful if absorbed through skin. Causes skin burns. Eyes Causes eye burns.	H314/335 P261/280/305/310/351/338 R34/37 S26/45	various
Sodium Hydroxide	Inhalation May be harmful if inhaled. Material is extremely destructive to the tissue of the mucous membranes and upper respiratory tract. Skin May be harmful if absorbed through skin. Causes severe skin burns. Eyes Causes severe eye burns. Ingestion May be harmful if swallowed. Causes severe burns.	H314 P280/305/351/310/338 R35 S26/37/39/45	various

Seed production method:

Put 2 cm³ 0.001 M Silver Nitrate and 2 cm³ 1% PVA in a clean dry beaker and stir, to this add **drop wise** 2 cm³ 0.001 M sodium borohydride, producing a yellow colloid or seed solution.

Colour Solution preparation:

1 cm³ 1% PVA

1 cm³ seed solution

3 cm³ 0.1M Tri Sodium Citrate

5 cm³ 0.1M (note conc. Hydrazine ~ 15.5M)

+ X cm³ 0.001M Silver Nitrate

X (cm³)	Colour	λ max	Observations
~ 0.40	Yellow		
~ 1.00	Orange		
~ 1.30	Red		
~ 2.50	Purple		
~ 6.00	Blue		
~ 20.00	Green		

1. Make up the seed solution using the method stipulated by your laboratory instructor.
2. Using this seed solution make up a series of colloids following the recipe above. (Note: Add reagents as ordered above, and manner of addition of 0.001M silver nitrate is important)
3. Using the laser pointer supplied, check for the presence of nano particles, indicated by the Tyndall effect, described in the pre lab talk.
4. Analysis resulting colloids using UV-Vis.
5. Tabulate results as above.
6. TEM images and DLS results of a series of previously prepared colloids will be provided, incorporate the information they provide in to your assessment of the colloids prepared in this practical.

Further Reading

A rapid, straight-forward method for controlling the morphology of stable silver nanoparticles

Deirdre M. Ledwith, Aine M. Whelan and John M. Kelly
Journal of Material Chemistry, 2007, 17, 2459–2464

Optical Properties and Growth Aspects of Silver Nanoprisms Produced by a Highly Reproducible and Rapid Synthesis at Room Temperature

Damian Aherne, Deirdre M. Ledwith, Matthew Gara, and John M. Kelly
Advanced Functional Materials, 2008,18, 2005–2016

The Optical Properties of Metal Nanoparticles: The Influence of Size, Shape, and Dielectric Environment.

K. Lance Kelly, Eduardo Coronado, Lin Lin Zhao, and George C. Schatz
Journal of Physical Chemistry B., 2003, 107, 668-677

Synthesis of silver nanoprisms with variable size and investigation of their optical properties

Andrew J. Frank, Nicole Cathcart, Kenneth E. Maly and Vladimir Kitaev

Journal of Chemical Education, 2010, 87, 1098-1101

Synthesis and study of silver nanoparticles

Sally D. Solomon, Mozghan Bahadory, Aravindan V. Jeyarajasingam, Susan A. Rutkowsky and Charles Boritz

Journal of Chemical Education, 2007, 84, 322-325

Silver Voyage from Macro- to Nanoworld

Jana Soukupova, Libor Kvitek, Martina Kratochvilova, Ales Panacek, Robert Prucek

Journal of Chemical Education, 2010, 87, 1094-1097

Non aggregated colloidal silver nanoparticles for Surface Enhanced Raman Spectroscopy

A.C. Power, A.J. Betts, J.F.

The Analyst, 2011, 136, 2794-2802

A.2.2 DLS for Individual 'Coloured' Colloids - Malvern nano series Zetasizer

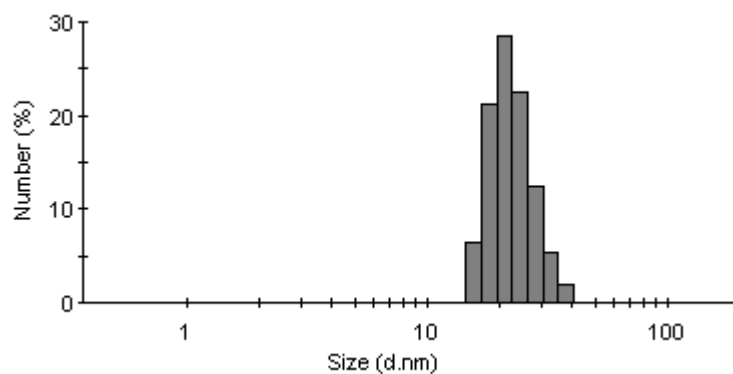


Figure A.2.2.1: DLS 'Yellow' Colloid

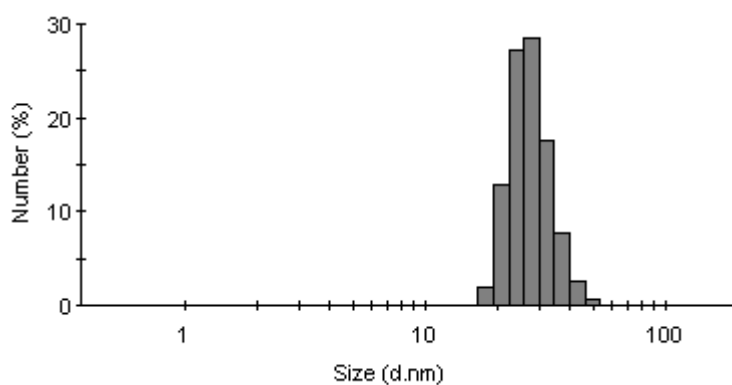


Figure A.2.2.2: DLS 'Orange' Colloid

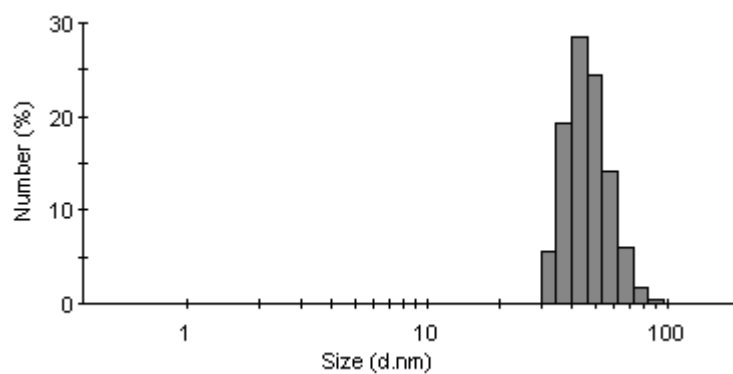


Figure A.2.2.3: DLS 'Red' Colloid

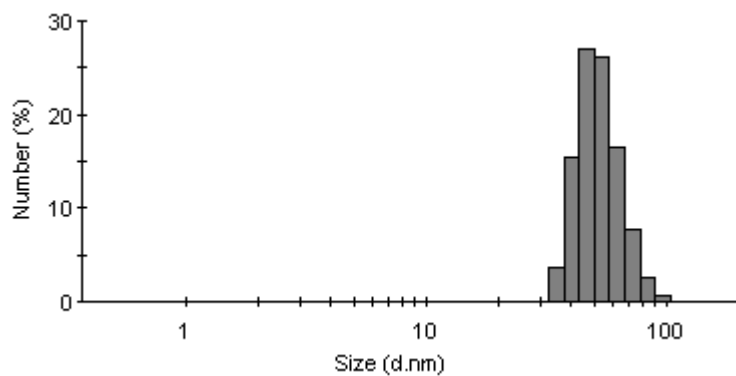


Figure A.2.2.4: DLS 'Purple' Colloid

A.2.3 TEM Images of 'Coloured' Colloids - JEOL, 100CX Transmission Electron Microscope

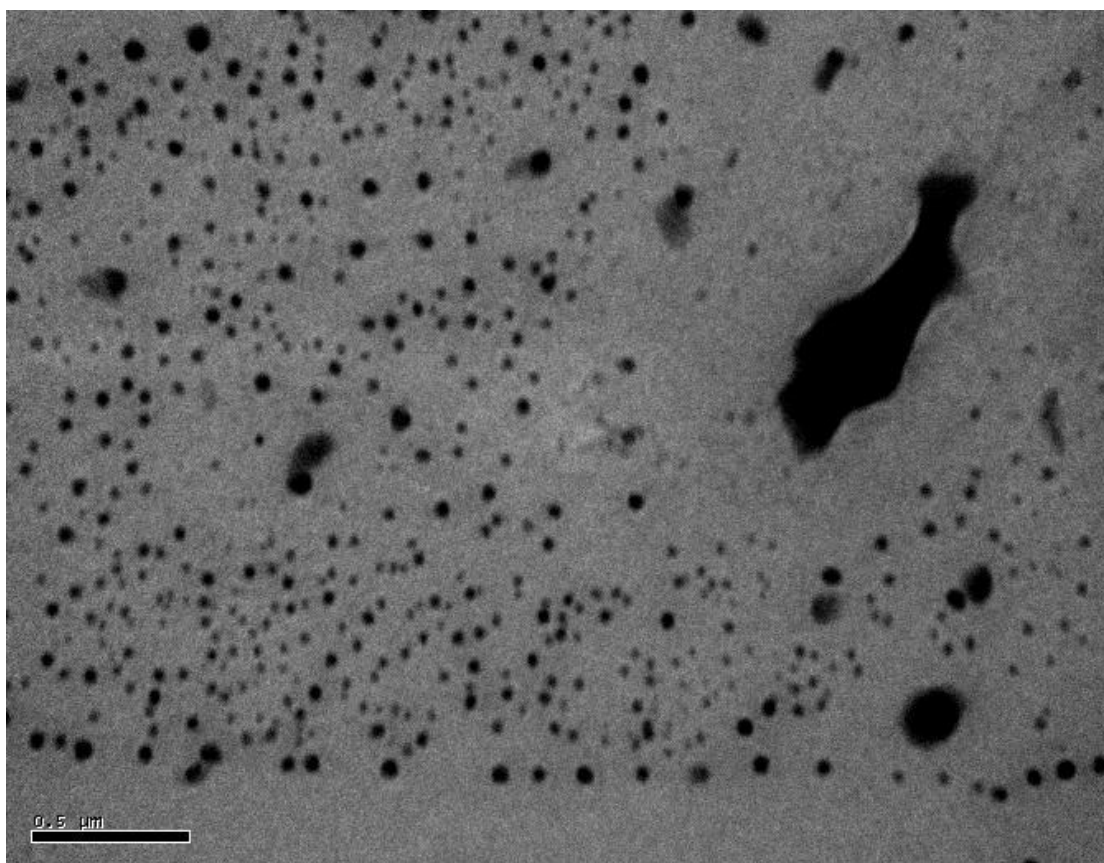


Figure A.2.3.1: Yellow colloid ~ 22nm average diameter – 67K Magnification

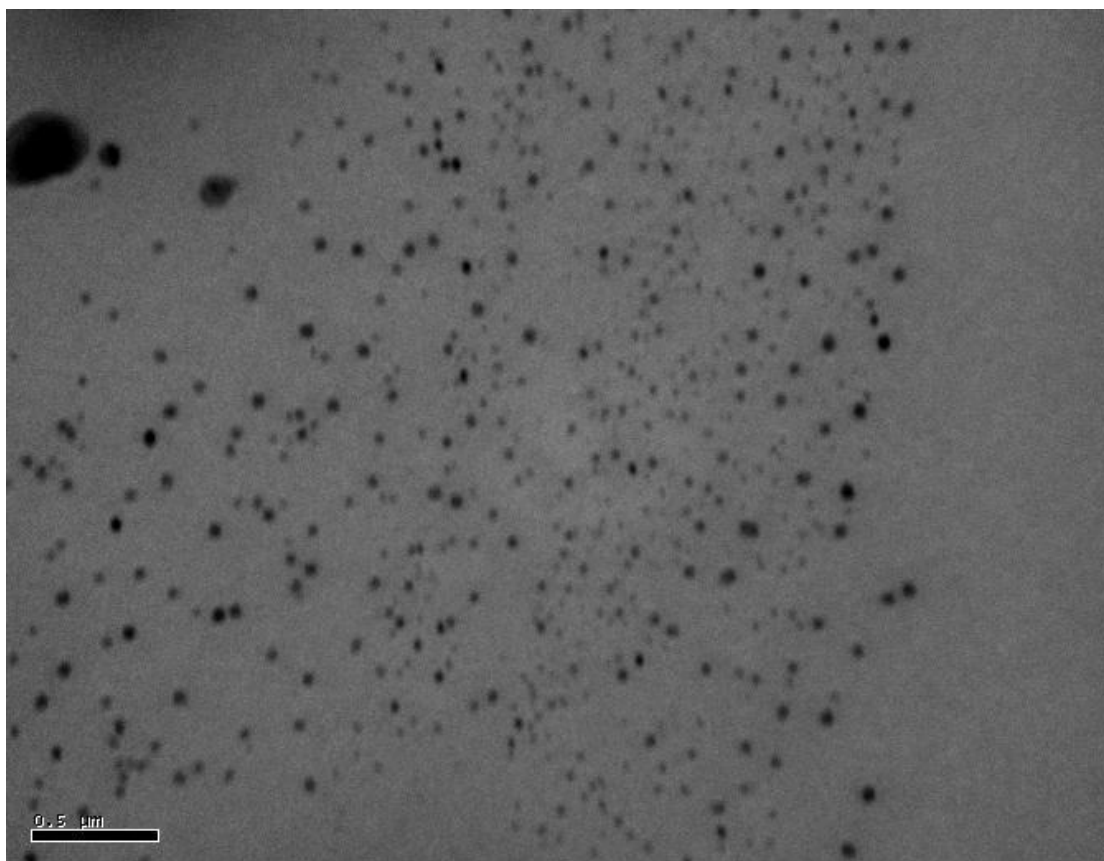


Figure A.2.3.2: Orange colloid ~ 35 nm average diameter – 40K Magnification

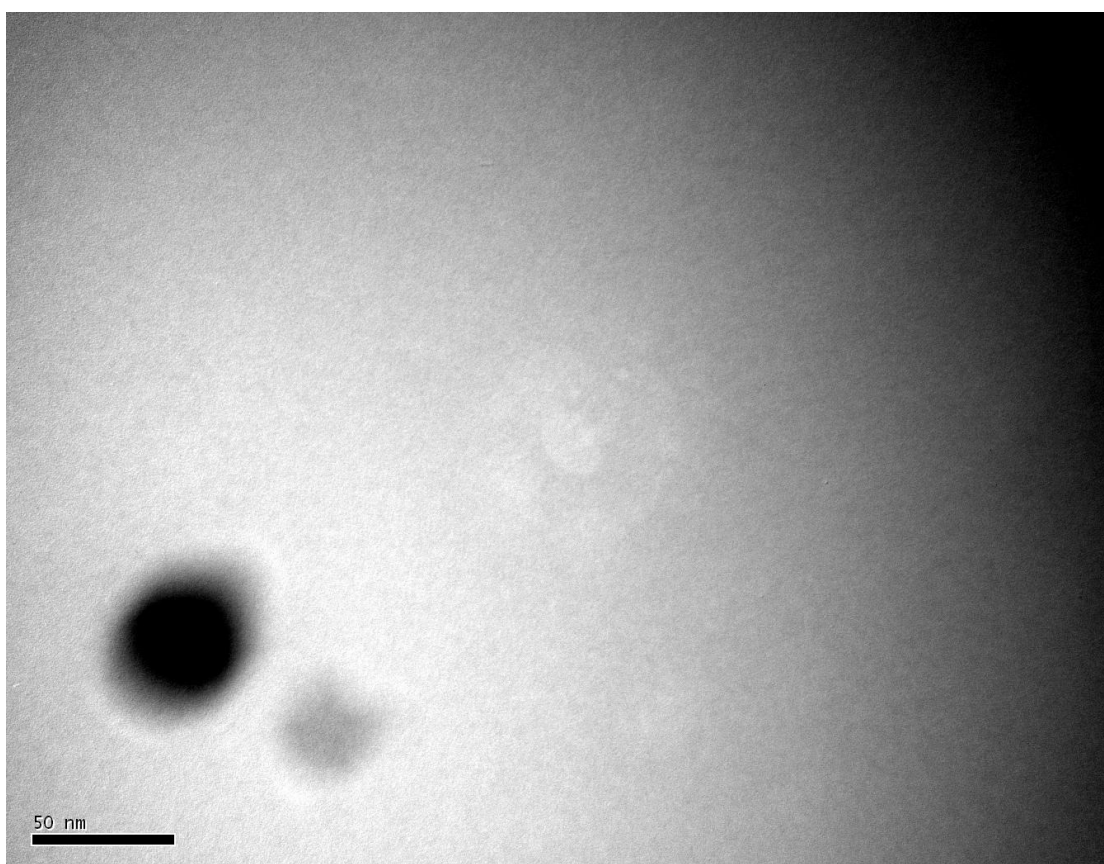


Figure A.2.3.3: Red colloid ~ 40 nm diameter – 450K Magnification

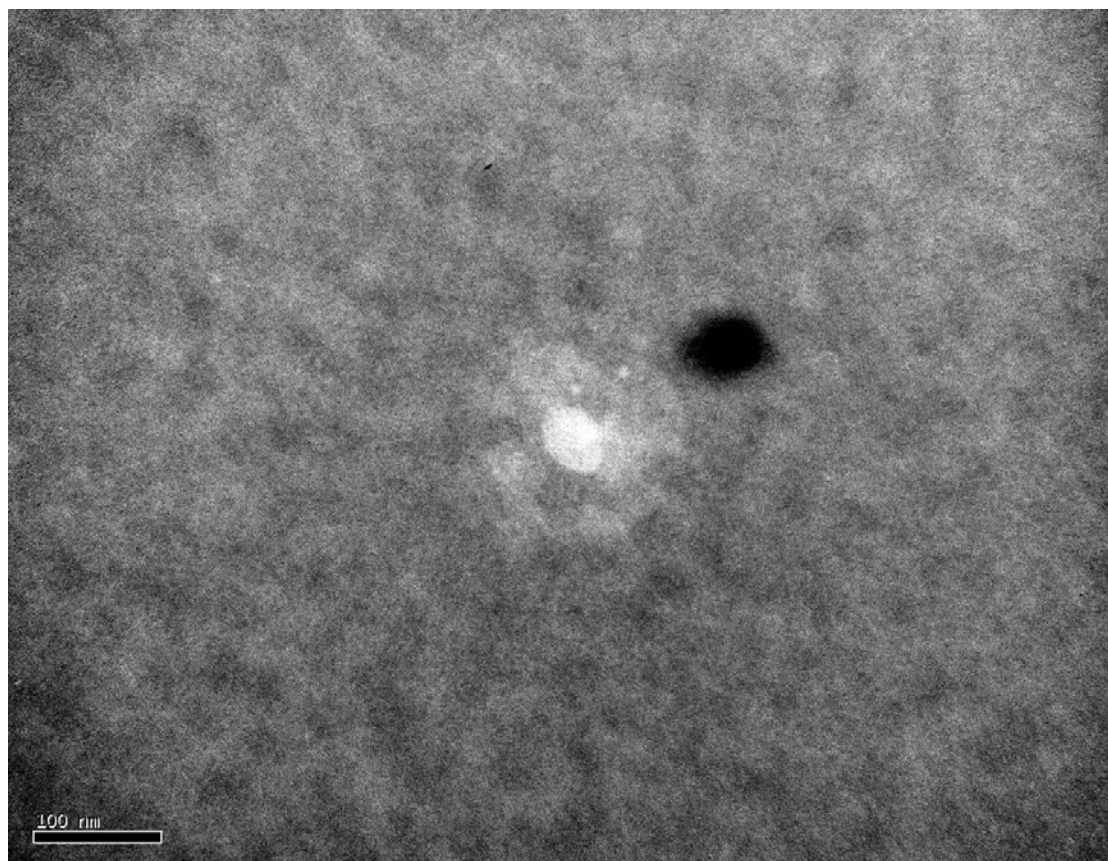


Figure A.2.3.4: Purple colloid ~ 55 nm diameter – 100K Magnification

A.2.4 STEM Images of ‘Coloured’ Colloids - Hitachi SU 6600 FESEM – Images taken by Anne Shanahan BSc. - Instrumental Support – Focas Institute

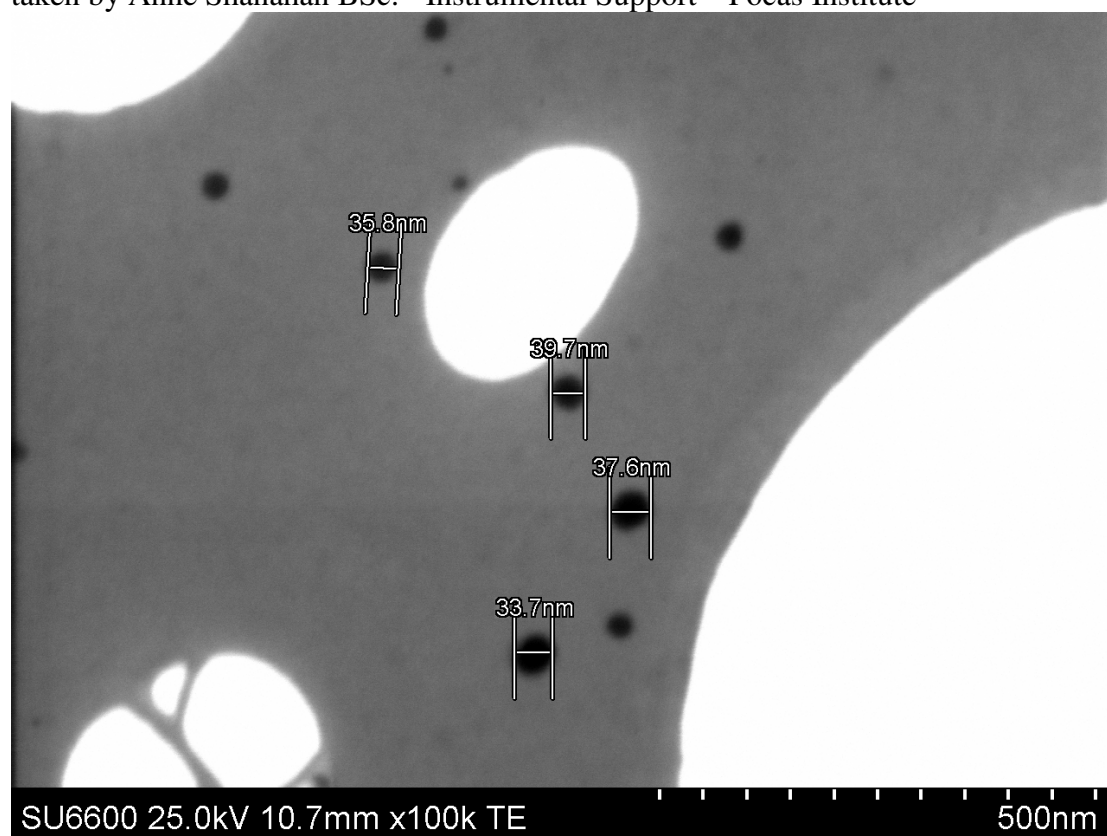


Figure A.2.4.1: Orange colloid ~ 36 nm average diameter – 100K Magnification

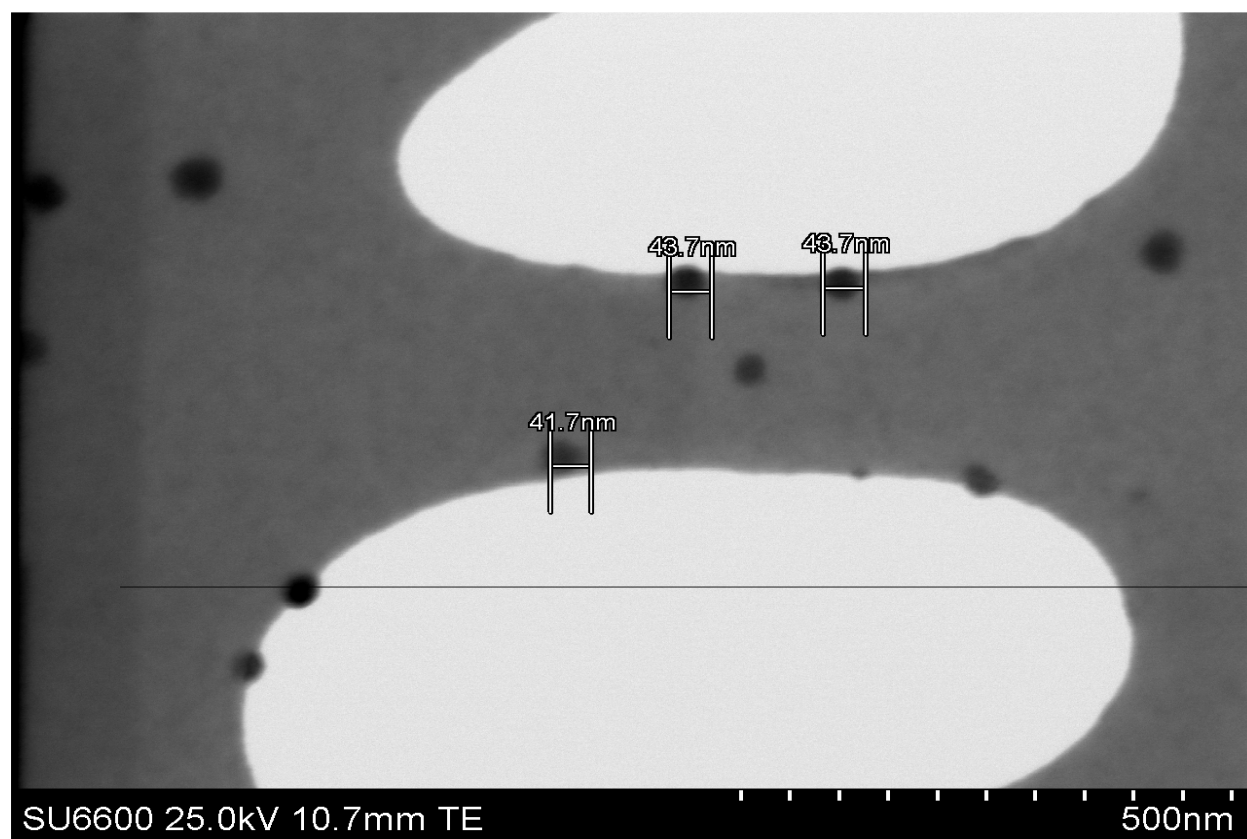


Figure A.2.4.2: Red colloid ~ 43 nm average diameter – 100K Magnification

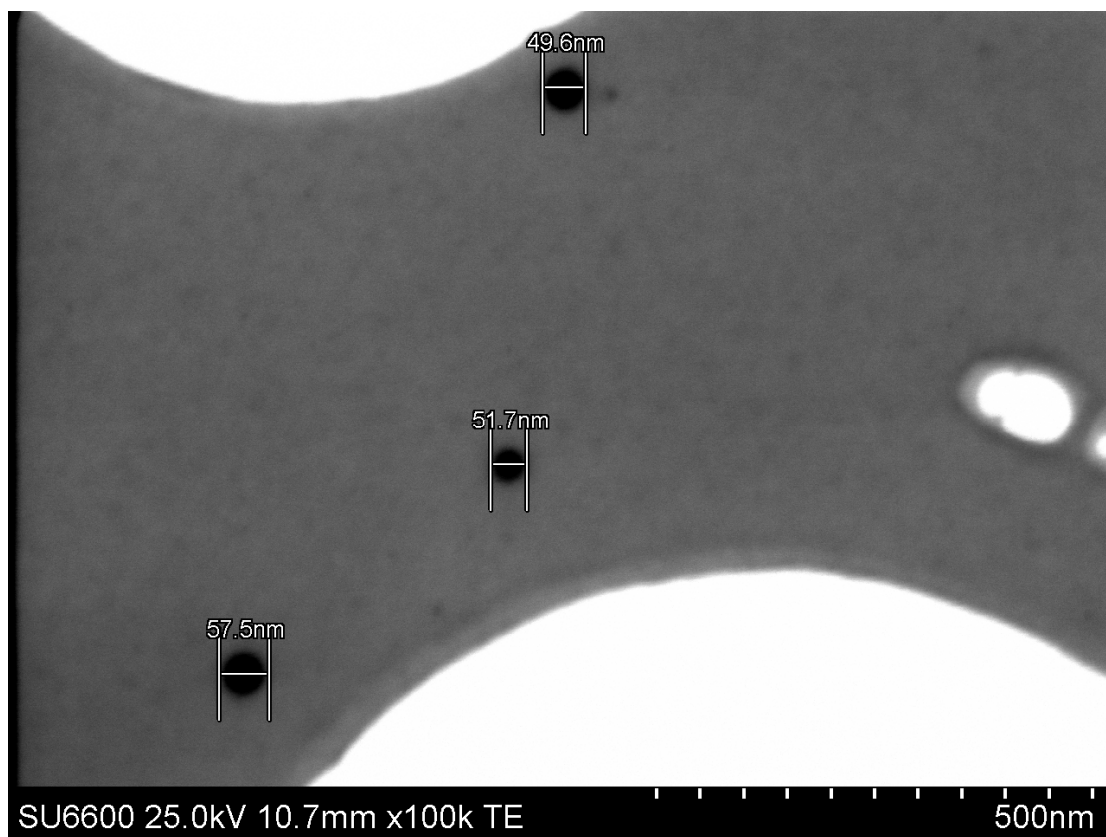


Figure A.2.4.3: Purple colloid ~ 53 nm average diameter – 100K Magnification

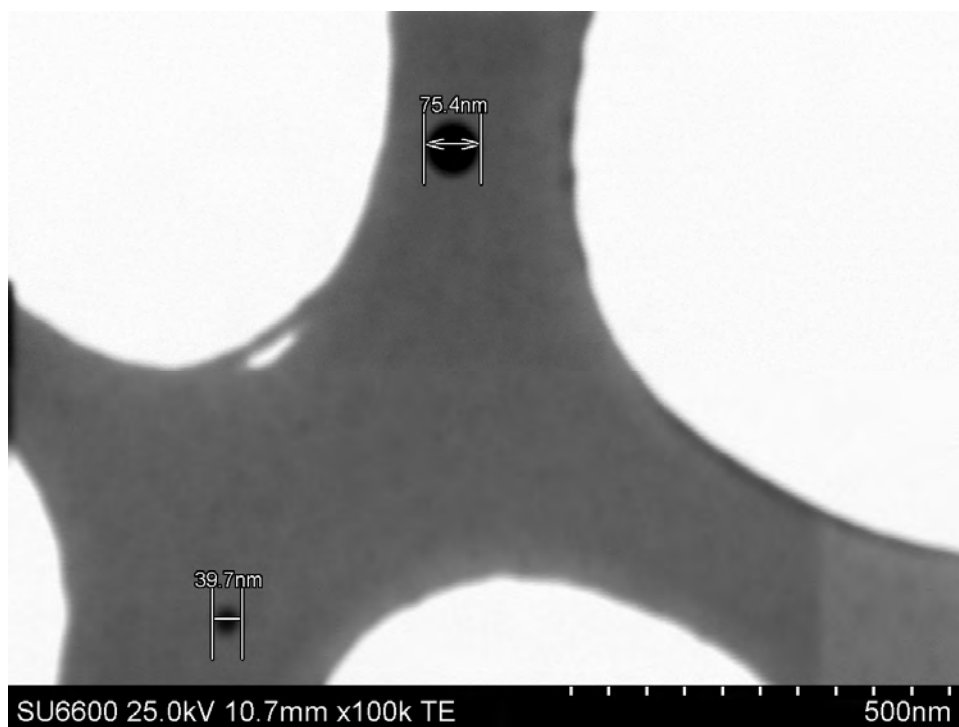


Figure A.2.4.3: Green colloid – 100K Magnification – two separate size ranges.

A.3.1 Characterisation of MetPro Samples - FTIR Analysis

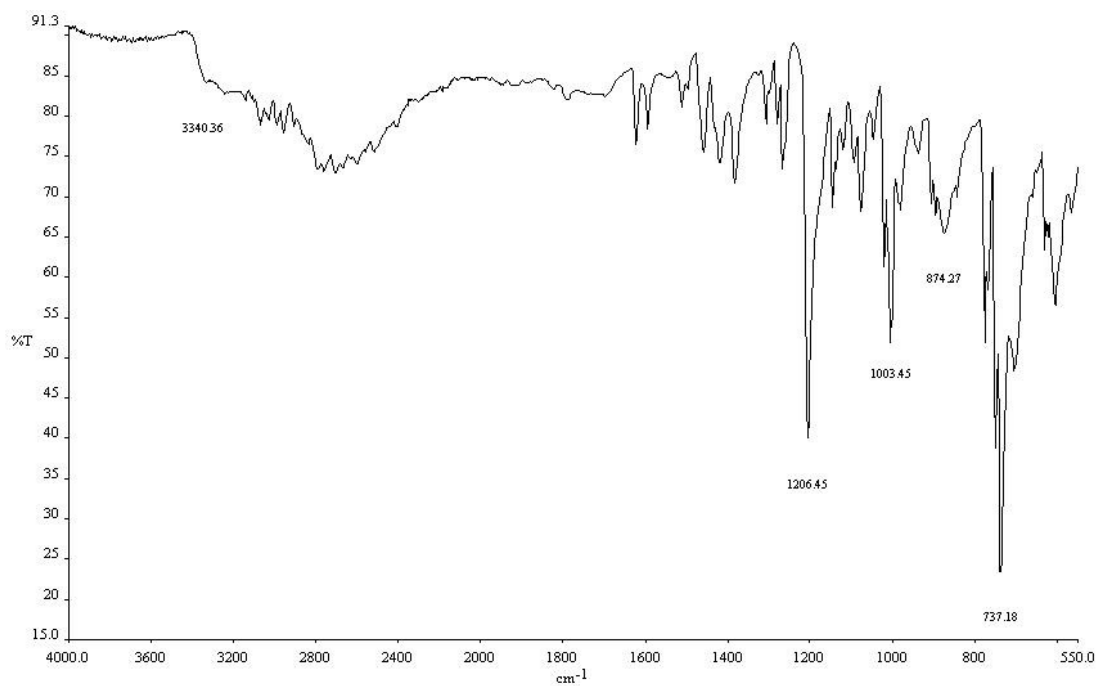


Figure A.3.1.1: FTIR spectrum of benzotriazole

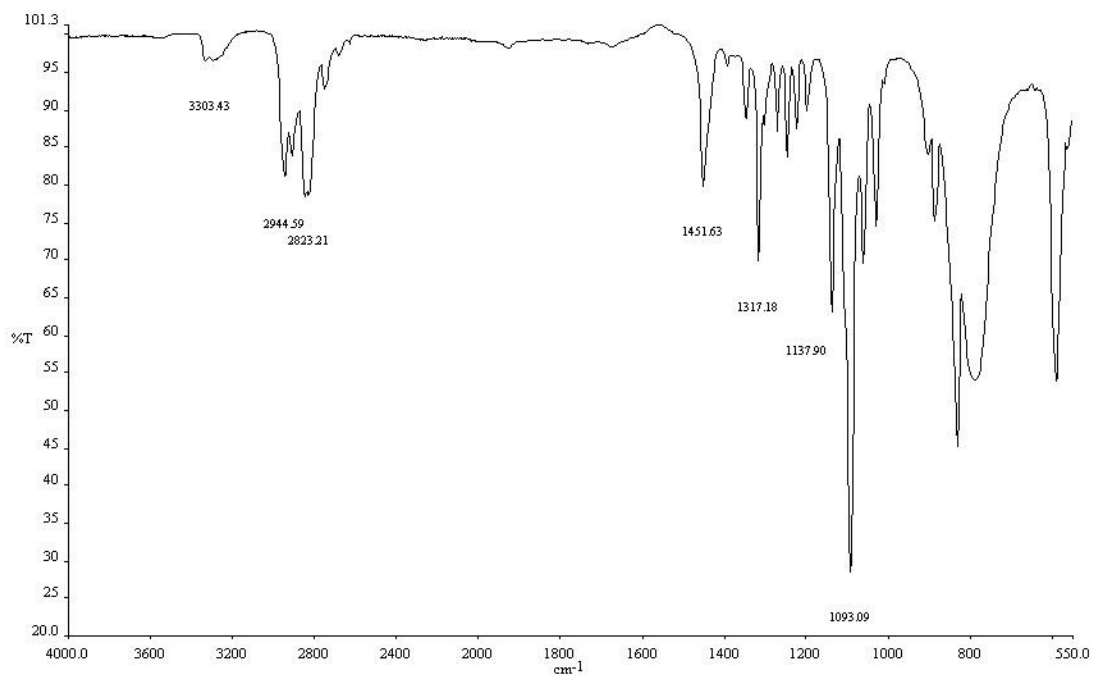


Figure A.3.1.2: FTIR spectrum of morpholine

Appendix

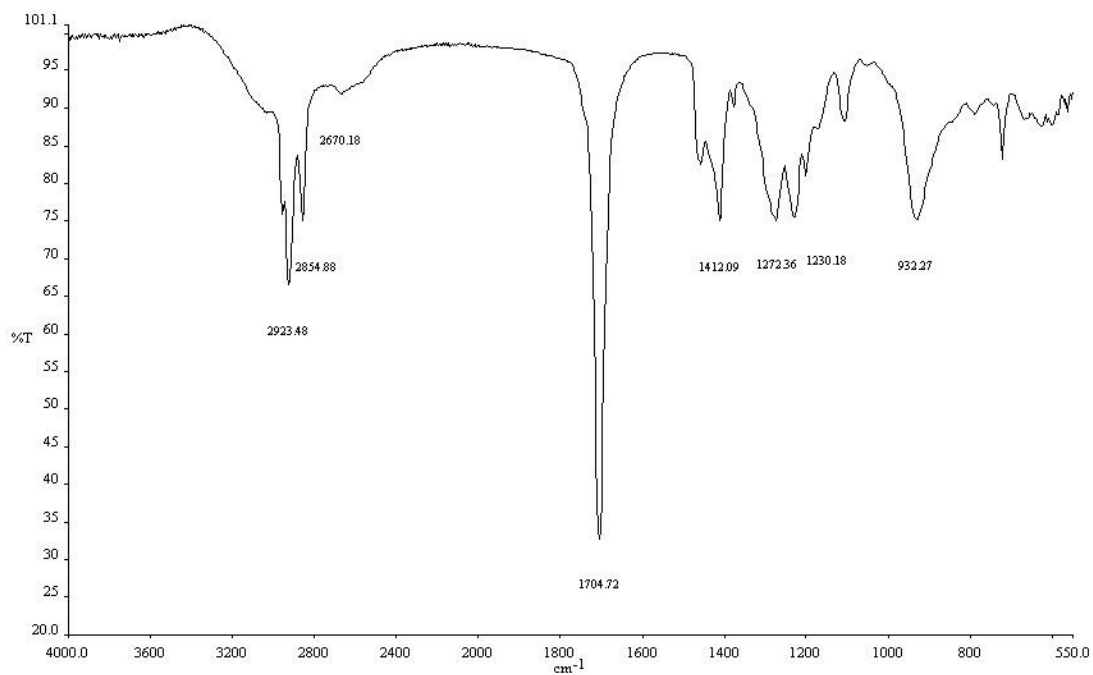


Figure A.3.1.3: FTIR spectrum of octanoic acid

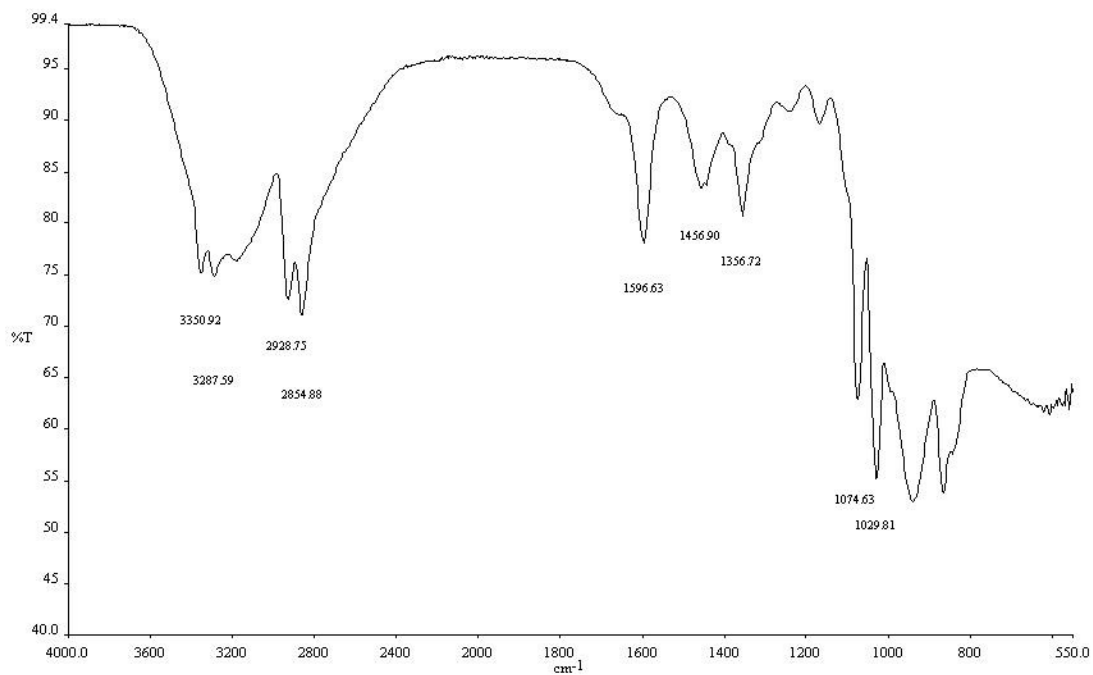


Figure A.3.1.4: FTIR spectrum of monoethanolamine 90%

Appendix

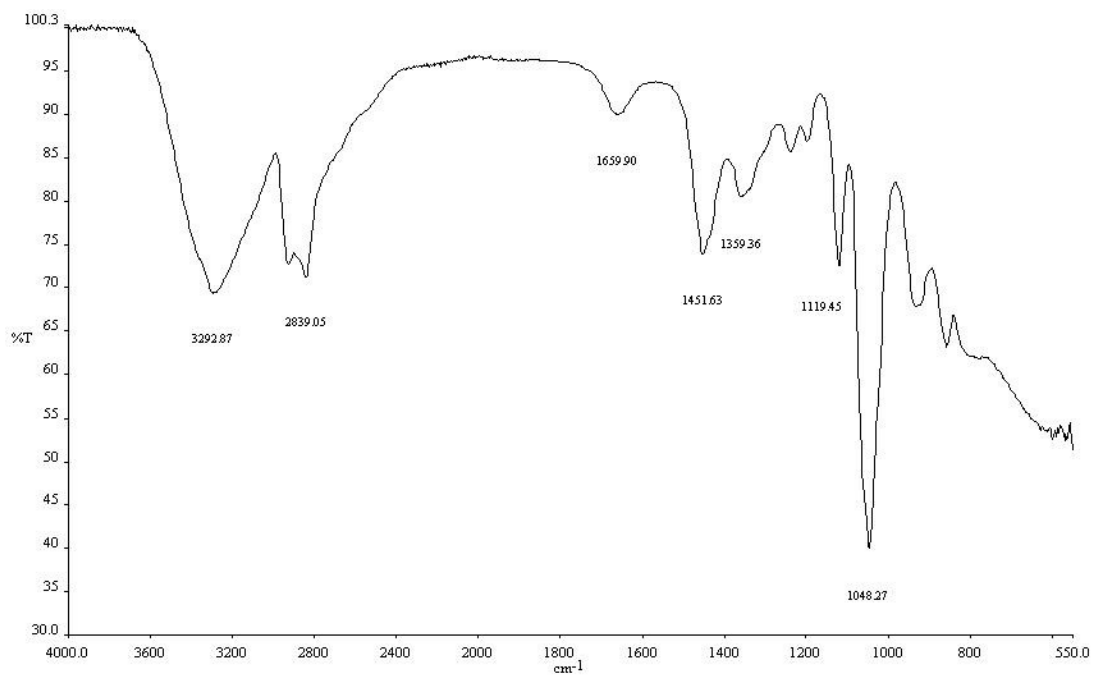


Figure A.3.1.5: FTIR spectrum of diethanolamine 88%

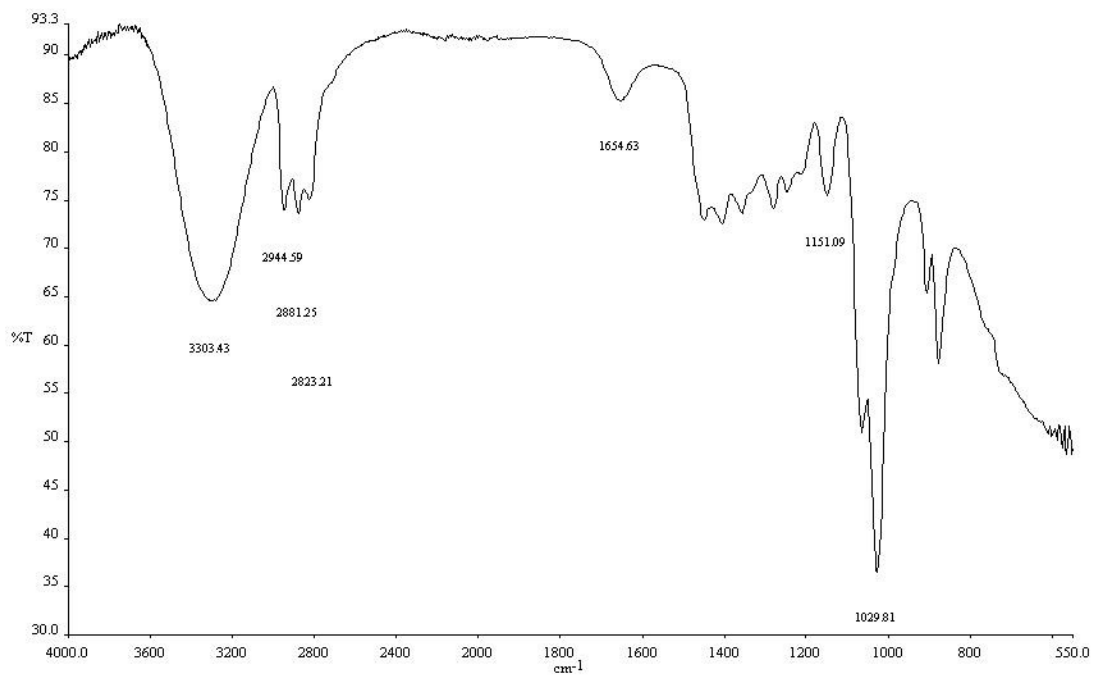
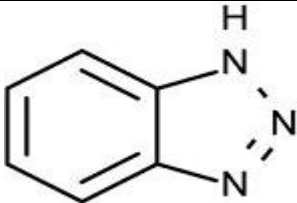
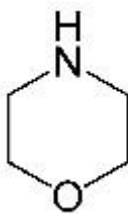
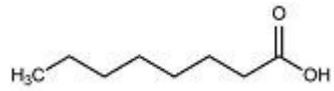
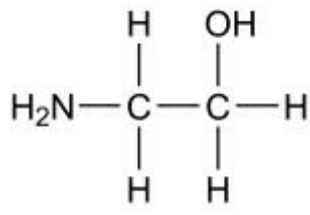


Figure A.3.1.6: FTIR spectrum of triethanolamine 90%

Compound	Structure	Bands of Interest (cm ⁻¹)	Assignment
Benzotriazole		~ 3340	N – H
		~ 1206	N – Aromatic
		~ 1003	C = CH
		~ 874	Aromatic – H
		~ 737	Aromatic – H
Morpholine		~ 3303	N – H
		~ 2944	C – H
		~ 2823	C – H
		~ 1451	C – O
		~ 1317	C – O
		~ 1137	C – O
		~ 1093	C – O
Octanoic Acid		~ 2923	COOH
		~ 2854	COOH
		~ 2670	COOH
		~ 1704	C = O
		~ 1412	C – H
		~ 1272	C – H
		~ 1230	O = C – O
		~ 932	C – O
Monoethanolamine 90%		~ 3350	O – H
		~ 3287	O – H
		~ 2928	C – H
		~ 2854	C – H
		~ 1596	N – H
		~ 1456	H ₃ C – CH ₃
		~ 1356	Scissoring bending
~ 1074	C – O		

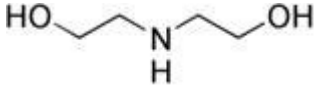
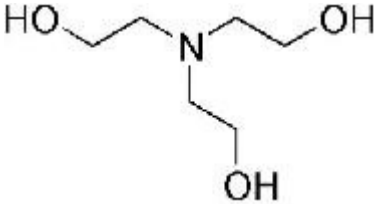
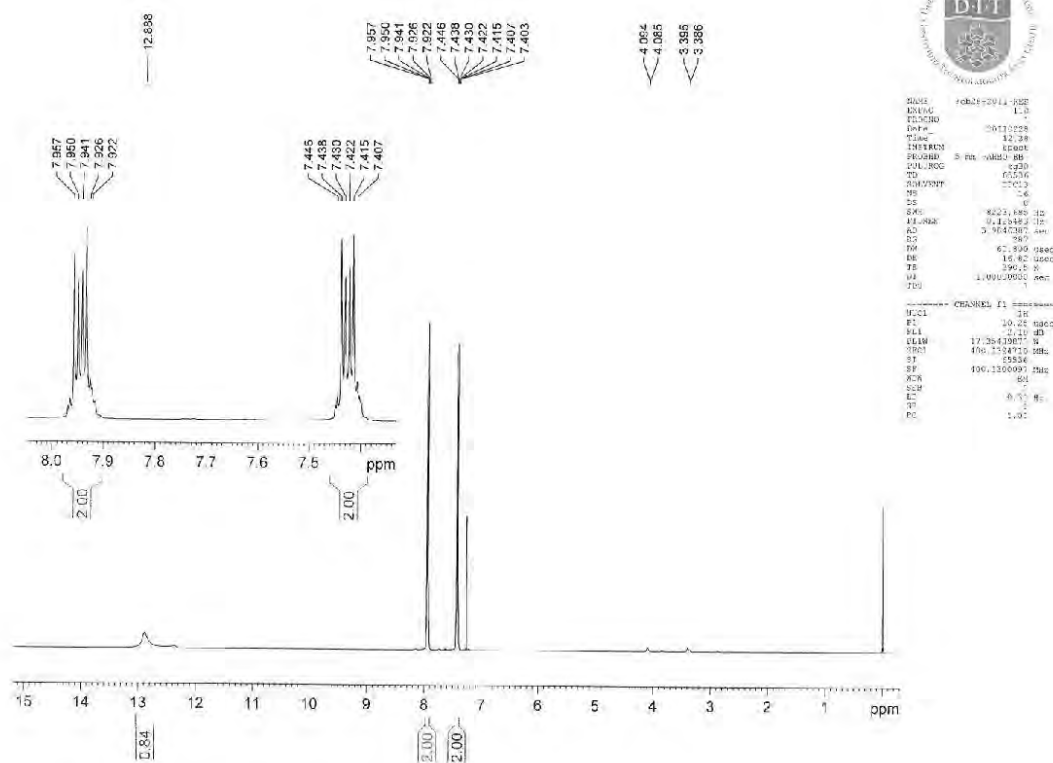
		~ 1029	C – O
Diethanolamine 88%		~ 3292	O – H
		~ 2839	N – H
		~ 1659	C – O
		~ 1451	C – O
		~ 1359	C – O
		~ 1119	C – O
		~ 1048	C – O
Triethanolamine 90%		~ 3303	O – H
		~ 2944	C – H
		~ 2881	C – H
		~ 2823	C – H
		~ 1654	C – O
		~ 1151	C – O
		~ 1029	C – O

Table A.3.1.1: MetPro VCI components structures and FTIR band assignment.

A.3.2 Characterisation of MetPro Samples – H^1 NMR AnalysisFigure A.3.2.1: H^1 NMR spectrum of benzotriazole

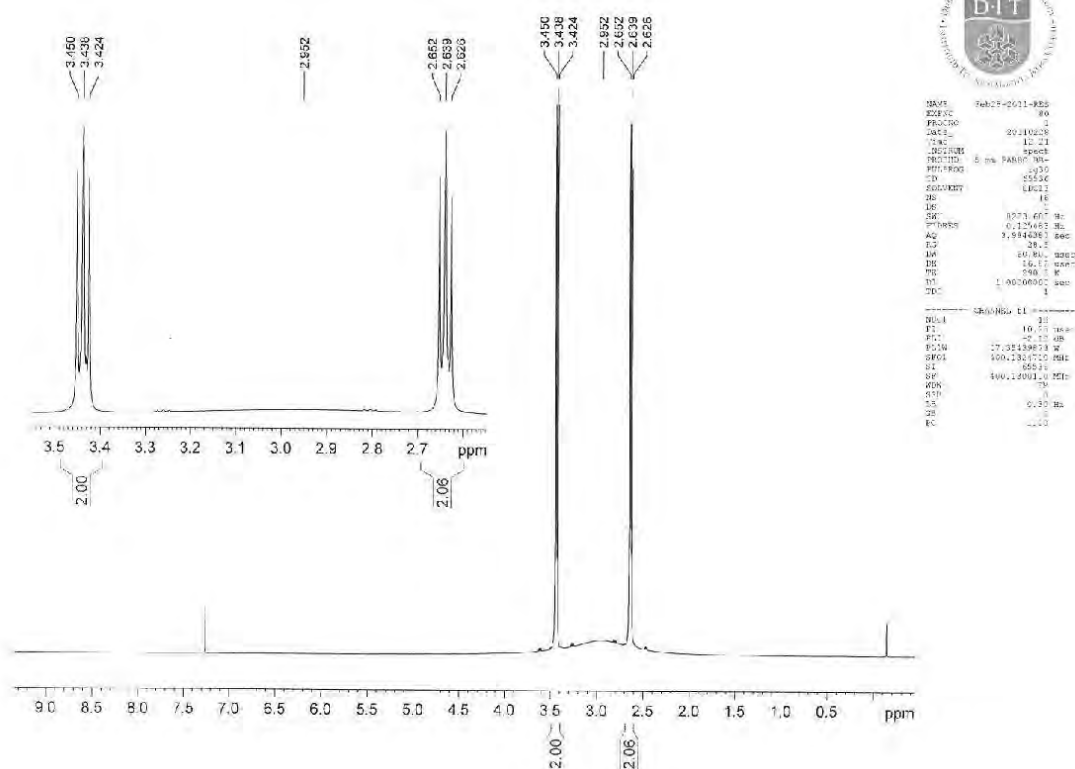


Figure A.3.2.3: ¹H NMR spectrum of monoethanolamine 90%

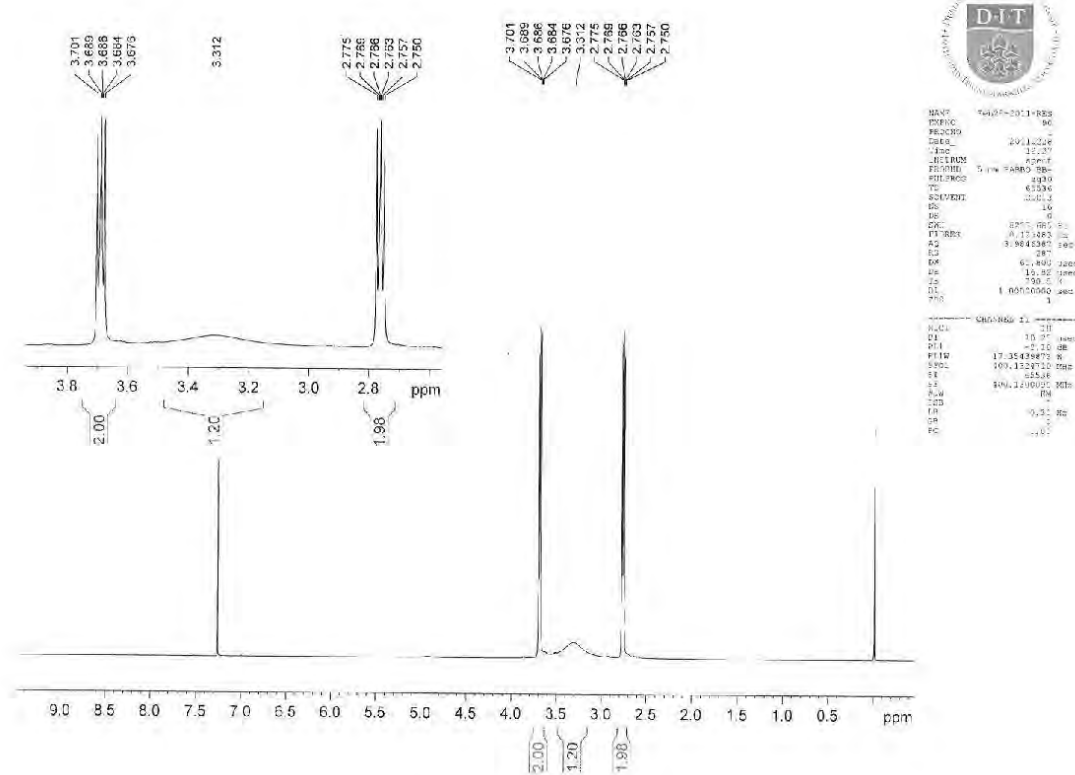
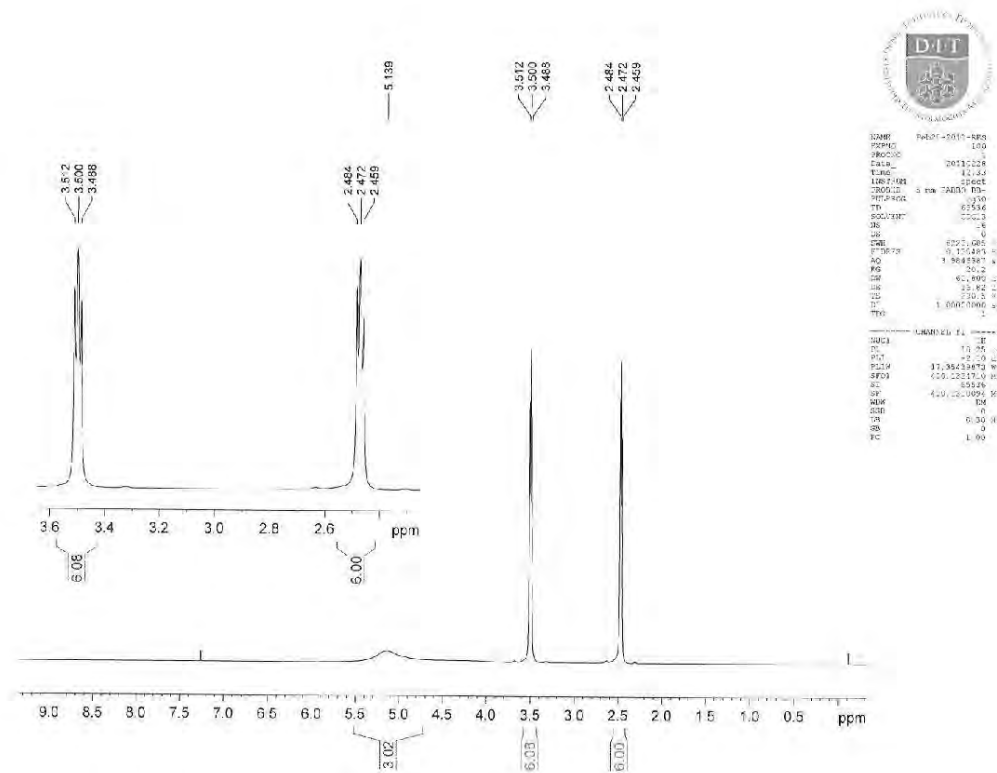


Figure A.3.3.4: ¹H NMR spectrum of diethanolamine 88%

Figure A.3.2.5: ^1H NMR spectrum of triethanolamine 90%

Compound	Structure	Peaks Assignment
Benzotriazole		12.88 ppm (1H, broad s, A) 7.95 - 7.92 ppm (2H, m, B) 7.44 - 7.40 ppm (2H, m, C)
Morpholine		1.756 ppm (1H, broad s, C) 2.78 - 2.76 ppm (4H, t, B) 3.59 - 3.57 ppm (4H, t, A)
Octanoic Acid		11.86 ppm (1H, broad s, A) 2.34 - 2.30 ppm (2H, t, B) 1.62 - 1.59 ppm (2H, t, C) 1.33 - 1.24 ppm (8H, m, D) 0.87 - 0.85 ppm (3H, t, E)

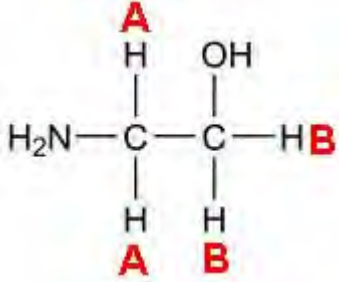
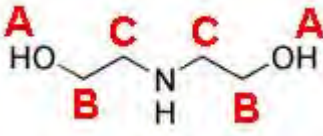
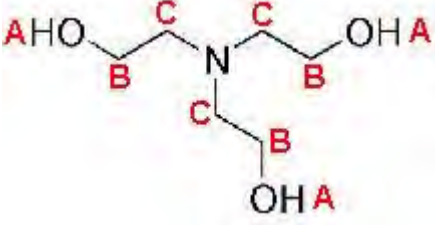
Monoethanolamine 90%		<p>2.65 - 2.63 ppm (2H, t, A) 3.45 - 3.42 ppm (2H, t, B)</p>
Diethanolamine 88%		<p>3.31 ppm (2H, broad s, A) 2.77 - 2.75 ppm (2H, t, C) 3.70 - 3.67 ppm (2H, t, B)</p>
Triethanolamine 90%		<p>5.13 ppm (3H, broad s, A) 2.48 - 2.45 ppm (6H, t, C) 3.51 - 3.48 ppm (6H, t, B)</p>

Table A.3.2.1: MetPro VCI components structures and ^1H NMR peak assignment.